DELFT UNIVERSITY OF TECHNOLOGY

FACULTY OF ELECTRICAL ENGINEERING, MATHEMATICS AND COMPUTER SCIENCE

MASTER'S THESIS

Modeling of Collection and Transmission Losses of Offshore Wind Farms for Optimization Purposes

---

Author:
Athanasios PAPADOPOULOS

Supervisor:
Dr. Eng. Pavol BAUER

A thesis submitted in fulfilment of the requirements
for the degree of Master of Science Sustainable Energy Technology

in the

Department of Electrical Sustainable Energy

February 2015

Declaration of Authorship

I, Athanasios PAPADOPOULOS, declare that this thesis titled, 'Modeling of Collection and Transmission Losses of Offshore Wind Farms for Optimization Purposes' and the work presented in it are my own. I confirm that:

- This work was done wholly or mainly while in candidature for a research degree at this University.
- Where any part of this thesis has previously been submitted for a degree or any other qualification at this University or any other institution, this has been clearly stated.
- Where I have consulted the published work of others, this is always clearly attributed.
- Where I have quoted from the work of others, the source is always given. With the exception of such quotations, this thesis is entirely my own work.
- I have acknowledged all main sources of help.
- Where the thesis is based on work done by myself jointly with others, I have made clear exactly what was done by others and what I have contributed myself.

Signed: ____

Date: ____

"The good life is one inspired by love and guided by knowledge."

Bertrand Russell, *What I believe,* 1925

DELFT UNIVERSITY OF TECHNOLOGY

Abstract

Faculty of Electrical Engineering, Mathematics and Computer Science
Department of Electrical Sustainable Energy

Master of Science Sustainable Energy Technology

Modeling of Collection and Transmission Losses of Offshore Wind Farms for Optimization Purposes

by Athanasios PAPADOPOULOS

Despite the recent technological improvements, the cost of offshore wind energy has not yet reached competitive levels. Optimization tools designed to reduce the overall losses in offshore wind farms (OWFs) may reduce its cost of energy. Hence, fast and accurate loss models are necessary for the optimization of the OWFs design.

The aim of this thesis is the development of such models to calculate the power losses in the OWF cables, transformers and converters of the collection and transmission systems (HVAC or HVDC). The models need to capture the main steady-state loss sources while being computationally light for the optimization process. All the proposed models consider the main sources of losses during steady-state operation as well as their dependence to temperature. The cable model considers the type of soil surrounding it whereas the converter model takes into account the IGBT datasheet information to compute the power losses.

A 640 MW OWF situated at 50, 100 and 150 km from shore is designed and employed to showcase the joint operation of the models and assess the impact of different variables such as the type of soil or the voltage level of the collection system to the power losses. In addition, the proposed models are compared against standard models (in which temperature dependence is not considered) for both the HVDC and HVAC transmission schemes.

The higher precision of the proposed models means designers may better predict the OWFs profitability.

Acknowledgements

I want to express my deepest gratitude to Prof. Pavol Bauer for trusting me with this interesting and exciting subject and for giving me the chance to work with a group of passionate engineers and brilliant people.

I would like to thank, from the bottom of my heart, Silvio Fragoso Rodrigues for an excellent collaboration. His poised and methodical approach to the project provided a most suitable working environment. The countless meetings we had and his invaluable feedback were of paramount importance towards the completion of my thesis. Another thanks for all the good laughs we had. I am glad that I have shared with him the feelings of excitement and fulfilment after the achievement of each of the several milestones of the project.

I am deeply grateful to Todor Todorcevic for his extremely useful advice on power electronics and his priceless feedback regarding my converter model. The passion with which he talks about his field of studies and communicates his knowledge has always been a huge motivation boost for me.

I would also like to sincerely thank Rodrigo Teixeira Pinto for letting us use his power flow solver and for the patience he showed regarding my many questions.

I am enormously grateful to my father, my mother and my sister for their love and encouragement. Thank you for believing in me and for supporting me both financially and emotionally through all these years.

Lastly, I want to thank each and every one of my friends in Delft. I will always treasure the memories of all the great times we had together.

Contents

List of Figures

List of Tables

Abbreviations

ADCC	Active Diode Clamped Converter
CCS	Carbon Capture and Storage
CHB	Cascaded H-Bridge Converter
COP	Coefficient Of Performance
DCC	Diode Clamped Converter
emf	Electromotive Force
EPR	Ethylene Propylene Rubber
EWEA	European Wind Energy Association
FCC	Flying Capacitor Converter
FEED	Front End Engineering and Design
GHG	Greenhouse Gases
GWEC	Global Wind Energy Council
IEA	International Energy Agency
IEC	International Electrotechnical Commission
IGBT	Insulated Gate Bipolar Transistor
IPCC	Intergovernmental Panel on Climate Change
LCC	Line Commutated Converter
LPC	Levelized Production Cost
LPOF	Low Pressure Oil Filled
MMC	Modular Multilevel Converter
mmf	Magnetomotive Force
NFPA	National Fire Protection Association
NLC	Near Level Control
OWF	Offshore Wind Farm
PD-PWM	Phase-disposition Pulse Width Modulation
PS-PWM	Phase-Shifted Carrier Pulse Width Modulation

PV	Photovoltaics
PWM	Pulse Width Modulation
SCFF	Self Contained Fluid Filled
SCOF	Self Contained Oil Filled
SHE	Selective Harmonic Elimination
SM	Submodule
SPC	Submarine Power Cable
SV-PWM	Space Vector Pulse Width Modulation
VSC	Voltage Source Converter
XLPE	Cross-Linked Polyethylene

Physical Constants

Constant mass temperature coefficient of copper at 0 °C	α_0^{Cu}	$=$	$4.26 \times 10^{-3}\ (K^{-1})$
Constant mass temperature coefficient of copper at 20 °C	α_{20}^{Cu}	$=$	$3.93 \times 10^{-3}\ (K^{-1})$
Constant mass temperature coefficient of aluminium at 20 °C	α_{20}^{Al}	$=$	$4.03 \times 10^{-3}\ (K^{-1})$

Symbols

A_a	Armour cross-sectional area	(mm^2)
a_n	Phase shift angle of circulating n-th harmonic	(rad)
B_p	Cable segment shunt susceptance	(Ω)
C	SM's capacitance	(F)
C_{arm}	Total arm capacitance	(F)
C_{effL}	Lower arm effective capacitance	(F)
C_{effU}	Upper arm effective capacitance	(F)
C_p	Cable segment shunt capacitance per m	(F/m)
c	Distance between conductor and cables axes	(mm)
d_c	Conductor diameter	(mm)
D_a	Armour outer diameter	(mm)
d_a	Armour mean diameter	(mm)
D_e	Cable outer diameter	(mm)
D_i	Insulation outer diameter	(mm)
D_s	Sheath outer diameter	(mm)
d_s	Sheath mean diameter	(mm)
E_{con}	Dissipated energy due to conduction	(J)
E_{off,I_{Dts},R_G}	Switch-off energy for I_{Dts} and R_G	(J)
$E_{off,I_{Dts},R_{G,Dts}}$	Switch-off energy for I_{Dts} and $R_{G,Dts}$	(J)
$E_{off,i_{arm},T}$	Switch-off energy for i_{arm} at T °C	(J)
$E_{off,i_{arm},T_{Dts}}$	Switch-off energy for i_{arm} at T_{Dts} °C	(J)
E_{on,I_{Dts},R_G}	Switch-on energy for I_{Dts} and R_G	(J)
$E_{on,I_{Dts},R_{G,Dts}}$	Switch-on energy for I_{Dts} and $R_{G,Dts}$	(J)
$E_{on,i_{arm},T}$	Switch-on energy for i_{arm} at T °C	(J)
$E_{on,i_{arm},T_{Dts}}$	Switch-on energy for i_{arm} at T_{Dts} °C	(J)
E_{rec,I_{Dts},R_G}	Reverse recovery energy for I_{Dts} and R_G	(J)

$E_{rec,I_{Dts},R_{G,Dts}}$	Reverse recovery energy for I_{Dts} and $R_{G,Dts}$	(J)
$E_{rec,i_{arm},T}$	Reverse recovery energy for i_{arm} at $T\,^{\circ}$C	(J)
$E_{rec,i_{arm},T_{Dts}}$	Reverse recovery energy for i_{arm} at $T_{Dts}\,^{\circ}$C	(J)
E_{rec,R_G}	Reverse recovery energy for R_G	(J)
$E_{rec,R_{G,Dts}}$	Reverse recovery energy for $R_{G,Dts}$	(J)
$E_{rec,T}$	Reverse recovery energy at $T\,^{\circ}$C	(J)
$E_{rec,T_{Dts}}$	Reverse recovery energy at $T_{Dts}\,^{\circ}$C	(J)
E_{sw,R_G}	Switch-on or off energy for R_G	(J)
$E_{sw,R_{G,Dts}}$	Switch-on or off energy for $R_{G,Dts}$	(J)
$E_{sw,T}$	Switch-on or off energy at $T\,^{\circ}$C	(J)
$E_{sw,T_{Dts}}$	Switch-on or off energy at $T_{Dts}\,^{\circ}$C	(J)
e_v	MMC AC terminal phase voltage	(V)
f	System frequency	(Hz)
f_s	Sampling frequency	(Hz)
f_sw	SM switching frequency	(Hz)
G	Geometric factor	$(-)$
$\bar{G}$	Geometric factor	$(-)$
I_{AC}	MMC AC terminal RMS current	(A)
i_{arm}	MMC arm current	(A)
i_{armL}	MMC lower arm current	(A)
i_{armU}	MMC upper arm current	(A)
I_c	Conductor current	(A)
$I_{c,Max}$	Maximum conductor current	(A)
$I_{c,R}$	Rated conductor current	(A)
$I_{c,Rprel}$	Preliminary rated conductor current	(A)
i_c	Collector current	(A)
i_{cc}	Circulating current	(A)
$\overline{I}_{ch}$	Charging current	(A)
$\overline{I}_{ch,c}$	Capacitive charging current	(A)
$\overline{I}_{ch,in}$	Input charging current	(A)
$\overline{I}_{ch,out}$	Output charging current	(A)
$\overline{I}_{ch,r}$	Resistive charging current	(A)
$\widehat{I}_{cc,n}$	Amplitude of circulating n-th harmonic	(A)

i_d	Diode current	(A)
I_{DC}	MMC DC terminal current	(A)
I_{Dts}	Datasheet semiconductor's current	(A)
$I_{ind,Nom}$	Nominal inductor current	(A)
$\overline{I}_{in}$	Input current	(A)
$\overline{I}_{in,L}$	Input line current referred to the secondary	(A)
$\overline{I}_{in,L,pr}$	Input line current referred to the primary	(A)
$\overline{I}_{in,L,sec}$	Input line current referred to the secondary	(A)
I_{legAC}	MMC RMS AC leg current	(A)
I_{legDC}	MMC DC leg current	(A)
I_{legRMS}	MMC RMS leg current	(A)
$I_{legRMS,Nom}$	MMC nominal RMS leg current	(A)
I_{OC}	Transformer open circuit test current	(A)
$\overline{I}_{out}$	Output current	(A)
I_{SC}	Transformer short circuit test current	(A)
$\overline{I}_{SE,L}$	Transformer series impedance current	(A)
i_v	MMC AC terminal current	(A)
K	Cable inductance constant	$(-)$
$K_{t,T}$	IGBT conduction temperature correction factor	$(-)$
$K_{d,T}$	Diode conduction temperature correction factor	$(-)$
L_1	Distance from seabed to cable axis	(mm)
L_2	Distance from seabed to center of trefoil cable group	(mm)
L_{armL}	Lower arm inductance	(H)
L_{armU}	Upper arm inductance	(H)
L_{d,R_G}	Diode switching gate resistance correction factor	$(-)$
$L_{d,T,rec}$	Diode switching temperature correction factor	$(-)$
L_s	Cable segment inductance per m	(H/m)
$L_{t,R_G,off}$	IGBT switching-off gate resistance correction factor	$(-)$
$L_{t,R_G,on}$	IGBT switching-on gate resistance correction factor	$(-)$
$L_{t,T,off}$	IGBT switching-off temperature correction factor	$(-)$
$L_{t,T,on}$	IGBT switching-on temperature correction factor	$(-)$
$L_{V_{ceDC}}$	Off-state collector-emitter DC voltage correction factor	$(-)$
$L_{V_{dDC}}$	Off-state diode DC voltage correction factor	$(-)$

m_a	Modulation index	$(-)$
n	Number of cable load-carrying conductors	$(-)$
N_L	Lower arm inserted SMs	$(-)$
n_L	Lower arm insertion index	$(-)$
$N_{Parallel}$	Number of IGBTs in parallel per SM switch	$(-)$
N_{Series}	Number of IGBTs in series per SM switch	$(-)$
N_{SM}	Number of SMs per arm	$(-)$
N_U	Upper arm inserted SMs	$(-)$
n_U	Upper arm insertion index	$(-)$
P_{AC3ph}	MMC AC terminal three-phase active power	(W)
P_{con}	Dissipated power due to conduction	(W)
p_{con}	Instantaneous dissipated power due to conduction	(W)
P_{con3ph}	MMC three-phase conduction losses	(W)
$P_{cool3ph}$	MMC three-phase cooling losses	(W)
P_{DC}	MMC DC terminal power	(W)
$P_{gate3ph}$	MMC three-phase controllers' losses	(W)
P_{heat}	Dissipated power per IGBT module	(W)
$P_{heat,Diode}$	Diode dissipated power per IGBT module	(W)
$P_{heat,IGBT}$	IGBT dissipated power per IGBT module	(W)
$P_{heat,Max}$	Maximum dissipated power per IGBT module	(W)
$P_{heat,Nom}$	Nominal dissipated power per IGBT module	(W)
P_{ind3ph}	MMC three-phase inductors' losses	(W)
P_{load}	Transformer load losses	(W)
P_{loss}	Cable segment power losses	(W)
$P_{no-load}$	Transformer no-load losses	(W)
P_{OC}	Transformer open circuit test power	(W)
P_{out}	Active Power at the output	(W)
P_{SC}	Transformer short circuit test power	(W)
P_{sw3ph}	MMC three-phase switching losses	(W)
P_{tot3ph}	MMC three-phase total losses	(W)
Q	Rate of heat extraction	(W)
Q_{out}	Reactive Power at the output	(VAr)
R_{AC}^{20}	Conductor AC resistance per m at 20 °C	(Ω/m)

$R_{AC}^{\theta_c}$	Conductor AC resistance per m at θ_c °C	(Ω/m)
$R_{AC}^{\theta_{c,Max}}$	Conductor AC resistance per m at $\theta_{c,Max}$ °C	(Ω/m)
$R_{AC,t}^{20}$	Total cable AC resistance per m at 20 °C	(Ω/m)
$R_{AC,t}^{\theta_c}$	Total cable AC resistance per m at θ_c °C	(Ω/m)
R_a^{20}	Armour AC resistance per m at 20 °C	(Ω/m)
$R_a^{\theta_a}$	Armour AC resistance per m at θ_a °C	(Ω/m)
$R_a^{\theta_{a,Max}}$	Armour AC resistance per m at $\theta_{a,Max}$ °C	(Ω/m)
R_{armL}	Lower arm resistance	(Ω)
R_{armU}	Upper arm resistance	(Ω)
R_C	Excitation branch resistance	(Ω)
R_{ce}	On-state collector-emitter resistance	(Ω)
R_{DC}^{20}	Conductor DC resistance per m at 20 °C	(Ω/m)
$R_{DC}^{\theta_c}$	Conductor DC resistance per m at θ_c °C	(Ω/m)
$R_{DC}^{\theta_{c,Max}}$	Conductor DC resistance per m at $\theta_{c,Max}$ °C	(Ω/m)
R_d	On-state diode resistance	(Ω)
R_{eqp}	Equivalent series resistance referred to the primary	(Ω)
R_{eqs}	Equivalent series resistance referred to the secondary	(Ω)
R_{eqs}^{θ}	Equivalent series resistance at θ °C referred to the secondary	(Ω)
$R_{eqs}^{\theta_{Test}}$	Equivalent series resistance at θ_{Test} °C referred to the secondary	(Ω)
R_G	IGBT gate resistance	(Ω)
$R_{G,Dts}$	Datasheet IGBT gate resistance	(Ω)
R_{indAC}^{20}	Inductor AC resistance at 20 °C	(Ω)
$R_{indAC}^{\theta_i}$	Inductor AC resistance at θ_i °C	(Ω)
R_{indDC}^{20}	Inductor DC resistance at 20 °C	(Ω)
$R_{indDC}^{\theta_i}$	Inductor DC resistance at θ_i °C	(Ω)
R_p	Insulation resistance per m	(Ω/m)
R_s	Total cable segment resistance at θ_c °C	(Ω)
R_{sh}^{20}	Sheath AC resistance per m at 20 °C	(Ω/m)
$R_{sh}^{\theta_{sh}}$	Sheath AC resistance per m at θ_{sh} °C	(Ω/m)
$R_{sh}^{\theta_{sh,Max}}$	Sheath AC resistance per m at $\theta_{sh,Max}$ °C	(Ω/m)
$R_{th,C-H}$	Case to heatsink thermal resistance per m^2	(K/W)
$R_{th,H}$	Heatsink thermal resistance per m^2	(K/W)
$R_{th,J-C}$	Junction to case thermal resistance per m^2	(K/W)

$R_{th,J-C,Diode}$	Diode junction to case thermal resistance per m^2	(K/W)
$R_{th,J-C,eq}$	Equivalent junction to case thermal resistance per m^2	(K/W)
$R_{th,J-C,IGBT}$	IGBT junction to case thermal resistance per m^2	(K/W)
s	Cable segment length	(m)
s_0	Axial separation between two conductors	(mm)
s_1	Axial separation between two cables	(mm)
T	MMC semiconductors' operating temperature	(°C)
t	Insulation thickness between conductors	(mm)
T_1	Thermal resistance per m between conductor and sheath	$(K\ m/W)$
t_1	Insulation thickness between conductor and sheath	(mm)
T_2	Thermal resistance per m between sheath and armour	$(K\ m/W)$
t_2	Bedding thickness between sheath and armour	(mm)
T_3	Thermal resistance per m of external serving	$(K\ m/W)$
t_3	External serving thickness	(mm)
T_4	Thermal resistance per m between cable surface and environment	$(K\ m/W)$
T_{Dts}	Semiconductors' Dts temperature	(°C)
T_t	Total cable thermal resistance per m	$(K\ m/W)$
$T_{t,R}$	Total rated cable thermal resistance per m	$(K\ m/W)$
$T_{t,x}$	Total cable thermal resistance per m	$(K\ m/W)$
U_0	Conductor phase voltage	(V)
U_D	Converter DC terminal voltage	(V)
V_AC	MMC AC terminal line to line voltage	(V)
v_{armL}	Lower arm voltage	(V)
v_{armU}	Upper arm voltage	(V)
V_C	SM capacitor voltage	(V)
$V_{CAv,Nom}$	Nominal average SM capacitor voltage	(V)
V_{ceDC}	Off-state collector-emitter DC voltage	(V)
$V_{ceDC,Dts}$	Datasheet Off-state collector-emitter DC voltage	(V)
$V_{CE,Nom}$	Nominal off-state collector-emitter voltage	(V)
V_{ce0}	On-state zero-current collector-emitter voltage	(V)
v_{ce}	On-state collector-emitter voltage	(V)
$v_{ce,@150\,^{\circ}\mathrm{C}}$	On-state collector-emitter voltage at 150 °C	(V)
$v_{ce,@T}$	On-state collector-emitter voltage at T °C	(V)

$v_{ce,@T_{Dts}}$	On-state collector-emitter voltage at T_{Dts} °C	(V)
v_{CL}	Sum of lower arm capacitors' voltage	(V)
v_{CLk}	Lower arm k-th capacitor's voltage	(V)
v_{CU}	Sum of upper arm capacitors' voltage	(V)
v_{CUk}	Upper arm k-th capacitor's voltage	(V)
V_{DC}	MMC DC terminal voltage	(V)
$V_{DC,Nom}$	MMC DC terminal nominal voltage	(V)
V_{d0}	On-state zero-current diode voltage	(V)
v_d	On-state diode voltage	(V)
$v_{d,@150\,^{\circ}\mathrm{C}}$	On-state diode voltage at 150 °C	(V)
$v_{d,@T}$	On-state diode voltage at T °C	(V)
$v_{d,@T_{Dts}}$	On-state diode voltage at T_{Dts} °C	(V)
$\overline{V}_{in}$	Input phase voltage	(V)
$\overline{V}_{in,Ph}$	Input phase voltage referred to the secondary	(V)
$\overline{V}_{in,Ph,pr}$	Input phase voltage referred to the primary	(V)
$\overline{V}_{in,Ph,sec}$	Input phase voltage referred to the secondary	(V)
V_{OC}	Transformer open circuit test voltage	(V)
$\overline{V}_{out}$	Output phase voltage	(V)
$\overline{V}_{out,Ph}$	Output phase voltage referred to the secondary	(V)
v_{ref}	Reference signal	(V)
$\widehat{V}_{ref}$	Amplitude of reference signal	(V)
v_{rip}	Allowed percent arm voltage ripple	(V)
V_{SC}	Transformer short circuit test voltage	(V)
v_x	Ratio of dry over moist soil thermal resistivity	$(-)$
v_θ	Temperature coefficient	$(-)$
W	Work needed for heat extraction	(W)
W_d	Dielectric loss per m	(W/m)
W_I	Ohmic cable loss per m	(W/m)
$W_{I,R}$	Rated ohmic cable loss per m	(W/m)
W_t	Total cable loss per m	(W/m)
X_{eq}	Transformer equivalent series reactance	(Ω)
X_M	Excitation branch reactance	(Ω)
X_s	Cable segment reactance	(Ω)

X_{sh}	Sheath reactance per m	(Ω/m)
$\overline{Y}_E$	Excitation branch admittance	(Ω)
y_p	Proximity effect factor	$(-)$
y_s	Skin effect factor	$(-)$
$\overline{Z}_{SE}$	Transformer series impedance	(Ω)
$\overline{Z}_t$	Total cable segment series impedance	(Ω)

α	Transformer voltage ratio	$(-)$
α_{θ}^{Cu}	Constant mass temperature coefficient of copper at $\theta\,^{\circ}\mathrm{C}$	(K^{-1})
$\alpha_{\theta_{Test}}^{Cu}$	Constant mass temperature coefficient of copper at $\theta_{Test}\,^{\circ}\mathrm{C}$	(K^{-1})
$\Delta\theta_{cr}$	Critical drying soil temperature rise	(K)
$\Delta\theta_d$	Dielectric loss temperature rise	(K)
$\Delta\theta_{d,R}$	Rated dielectric loss temperature rise	(K)
$\Delta\theta_{d,x}$	Dielectric loss temperature rise	(K)
$\Delta\theta_{\max}$	Maximum conductor temperature rise	(K)
δ	Dielectric loss angle	(rad)
δ_a	Armour equivalent thickness	(mm)
ε	Insulation material relative permittivity	$(-)$
θ_a	Armour temperature	$(^{\circ}\mathrm{C})$
$\theta_{a,Max}$	Cable armour maximum temperature	$(^{\circ}\mathrm{C})$
θ_C	IGBT module case temperature	$(^{\circ}\mathrm{C})$
θ_c	Conductor temperature	$(^{\circ}\mathrm{C})$
$\theta_{c,Amb}$	Cable ambient temperature	$(^{\circ}\mathrm{C})$
$\theta_{c,Max}$	Conductor maximum temperature	$(^{\circ}\mathrm{C})$
θ_i	MMC inductor temperature	$(^{\circ}\mathrm{C})$
$\theta_{i,Max}$	MMC inductor maximum temperature	$(^{\circ}\mathrm{C})$
θ_J	IGBT module junction temperature	$(^{\circ}\mathrm{C})$
$\theta_{m,Amb}$	MMC ambient temperature	$(^{\circ}\mathrm{C})$
$\theta_{m,Max}$	MMC IGBT maximum temperature	$(^{\circ}\mathrm{C})$
θ_{sh}	Sheath temperature	$(^{\circ}\mathrm{C})$
$\theta_{sh,Max}$	Cable sheath maximum temperature	$(^{\circ}\mathrm{C})$
θ_t	Transformer windings temperature	$(^{\circ}\mathrm{C})$
$\theta_{t,Amb}$	Transformer ambient temperature	$(^{\circ}\mathrm{C})$

$\theta_{t,Max}$	Maximum windings temperature	(°C)
$\theta_{t,Rise}$	Maximum windings temperature rise	(°C)
$\theta_{t,Test}$	Short circuit test windings' temperature	(°C)
λ_1	Sheath/screen loss factor	$(-)$
$\lambda_1^{'}$	Sheath/screen loss factor due to circulating currents	$(-)$
$\lambda_1^{''}$	Sheath/screen loss factor due to eddy currents	$(-)$
λ_2	Armour loss factor	$(-)$
$\lambda_2^{'}$	Armour loss factor due to circulating currents	$(-)$
$\lambda_2^{''}$	Armour loss factor due to eddy currents	$(-)$
μ_{st}	Steel relative permeability	$(-)$
ρ	Thermal resistivity of soil	$(K\ m/W)$
ρ_{dry}	Thermal resistivity of dry soil	$(K\ m/W)$
ρ_f	Thermal resistivity of filler material	$(K\ m/W)$
ρ_i	Thermal resistivity of insulation	$(K\ m/W)$
ρ_{moist}	Thermal resistivity of moist soil	$(K\ m/W)$
ρ_{sa}	Thermal resistivity of bedding between sheath and armour	$(K\ m/W)$
ρ_{se}	Thermal resistivity of serving	$(K\ m/W)$
ϕ	Power angle	(rad)
$\phi_{\overline{V}_{in}}$	Input voltage angle	(rad)
$\phi_{\overline{V}_{out}}$	Output voltage angle	(rad)
ω	System angular speed	(rad/s)

Dedicated to my parents…

Chapter 1

Introduction

During the last decades, human activity has caused a steep increase of atmospheric concentrations of several gases (carbon dioxide, methane, nitrous oxide etc) and subsequent alterations on the global climate. The consequences of the rapid climate change are already evident around the world [32]. Under these circumstances, humanity has to take action to decelerate the change and ensure a viable future. The principal pathway of cost-effectively stabilizing the concentrations of the aforementioned gases is reducing the carbon intensity of electricity generation [32]. A means of achieving this, is reinforcing the share of the low-carbon electricity supply through the use of renewable energy sources [3].

Wind energy is considered as an important contributor to the future energy mix [3]. Offshore wind energy is also a very promising field of focus due to several advantages such as the availability of higher-quality wind resources and the lack of space related constraints [3]. The last decade, a lot of effort has been put towards the reduction of the costs related to the deployment of wind energy. Regarding inland wind energy projects, a significant cut in costs has already been achieved due to market competition and technological advancements [2]. Conversely, the costs of offshore wind projects have increased substantially since the early $2000s$ driven both by rising underlying costs (commodity prices rises, currency fluctuations) and by more specific reasons such as supply chain bottlenecks, lack of competition, sub-optimal reliability and the move to deeper water regions [10].

1.1 Defining the Problem

In this context, there is a need for decreasing the costs involved in the development of Offshore Wind Farms (OWF). Up until today, the offshore wind industry has used products and processes that were initially developed for other fields such as the oil and gas industry. Developing products and processes specifically for offshore wind applications provides the opportunity to reduce capital and operating costs and increase power production [10]. Opportunities for cost reduction are derived from several factors such as [10] [33]:

- Introduction of larger, more reliable turbines which generate more power with lower operating costs
- Greater competition among the industry at key supply markets (turbines, support structures and installation)
- Greater activity at the front end of the project during the Front End Engineering and Design (FEED) process
- Exploitation of economies of scale and acceleration of procedures through standardization and learning by doing
- Optimization of current installation methods
- Mass-production of support structures for use in deeper waters (greater than 35 m)

An important factor that can contribute to significant cost reduction of future offshore wind projects is the improvement of the FEED. Many vital decisions that influence the whole project are taken at its early stages during this process. The use of software tools for multi-variable optimization of the wind farm layout in combination with the use of geophysical data of the site during FEED can prevent installation overruns and cut down costs [10] [33].

With multi-variable optimization, the wind farm array layout can be optimized with respect to several factors such as the wake effect, array electrical cost, support structure cost, consenting constraints, and construction and operational costs. In addition, an improved knowledge of the seabed at the project site can lead to cost reductions in electrical array construction preventing conservative over-design or late design changes [10] [33]. For these reasons, the development of fast and reliable software tools for optimizing the OWF layout is a vital step to the direction of making offshore wind energy a cost competitive technology.

1.2 Framework of Thesis

The work realized for the present thesis is part of a greater project for the fulfillment of the Doctor of Philosophy (PhD) degree of Silvio Fragoso Rodrigues in collaboration with Prof. Pavol Bauer and the Department of Electrical Sustainable Energy of the Faculty of Electrical Engineering, Mathematics and Computer Science.

The main objective of the project is the development of a multi-objective optimization method for the design of large and far offshore wind farms. This tool aims to contribute to the reduction in wind energy costs by determining optimized electrical systems for specific offshore cases.

Previous evaluations have shown that different electrical systems give substantially different contributions to the Levelized Production Cost (LPC), not only due to different investment costs but also due to differences in losses and failure rates. Therefore it is important to develop and apply validated tools to quantify the Levelized Production Costs.

Ultimately, this tool can provide wind farm developers and transmission system operators with recommendations on design directions and cost reduction options of wind farm electrical systems.

The project is performed within the even wider project 'Far and Large Offshore Wind (FLOW)' which is supported by the Ministry of Economic Affairs, Agriculture and Innovation of the Netherlands within the $EOS-LT$ program of Agentschap-NL ($P201101-005-ECN$). The opinion expressed by the authors do not necessarily reflect the position of the Ministry of Economic affairs, nor does it involve any responsibility on its part.

1.3 Objectives

The objective of the present thesis is the development of models capable of calculating the power losses of the electrical infrastructure of an OWF including all the components from the wind generators' transformers till the power transformer of the onshore substation which connects the OWF to the grid. These are the MVAC Submarine Power Cables (SPC) used for the collection system as well as the HVAC or HVDC SPCs employed for the export system, the AC/DC power converters of both the offshore and onshore substations in case of HVDC transmission and the transformers of the substations.

The models are meant to be incorporated in the multi-variable optimization tool. Therefore, they need to comply with a number of requirements:

- High computational speed
- Capture of averaged steady-state operation
- Modularity
- Exclusive use of code
- No need of simulation software

Furthermore, there are additional requirements that are model-sensitive. The SPC models need to take into account the fluctuation of characteristics of the surrounding soil (temperature, thermal resistivity) across the cable's length. The converter model needs to be modular, take into consideration the IGBT module's datasheet and incorporate the impact of the operating temperature on the power losses. In addition, the transformer model needs also to include the operating temperature impact.

The final objective of the thesis is the combined use of the aforementioned models in a case-study of an OWF in order to display their capabilities and sensitivity to the ambient conditions.

1.4 Structure of Thesis

The remainder of the thesis is organized as follows: In Chapter 2 some general information regarding the climate change and the role of the renewable energy sources is provided. In addition, an overview of the current and future status of wind energy on a global scale as well as a summary of the offshore wind energy industry's directions are included.

In Chapter 3, a thorough description of the design of SPCs is given and their thermal and electrical behavior are explained. Furthermore, the models of cables for AC and Dc transmission are presented and an assessment of them through examples is provided.

Chapter 4 is dedicated to the model of the power converter. Initially, the available technologies of AC/DC converters are briefly presented and the reason why the Modular Multilevel Converter (MMC) is the technology of focus is given. Consequently, the operation of the MMC is examined and the respective model is presented. Finally, an assessment of the model based on a comparison with an existing model is given.

Chapter 5 includes descriptions of transformers' operation principle, most important components and origins of power losses. In addition, the transformers' equivalent circuit and the methodology of deriving it are introduced. Lastly, the model of the transformer is presented.

In Chapter 6, the case study is presented. An OWF is designed and its power losses are evaluated by using the models presented in this report. In addition, the impact of variables such as the soil thermal resistivity and the voltage level of the collection system are assessed. Consequently, comparisons between HVAC and HVDC transmission with respect to power losses are included. Lastly, the proposed models are compared against standard models (in which temperature dependence is not considered) in order to assess the impact of the implementation of the conductors' and semiconductors' temperature variation.

Lastly, Chapter 7 summarizes the conclusions of the thesis and provides some recommendations for future work.

Background knowledge, explanations regarding calculation methodologies and descriptions of components' dimensioning are presented in the Appendices of the Thesis. There are four distinct appendices: the three first refer to the models of SPCs, AC/DC power converters and transformers, while the last one is dedicated to the case study.

Chapter 2

A World that changes

2.1 Climate Change and Human Activity

The last decades, the climate of the Earth experiences a series of dramatic changes. The atmosphere and oceans' temperature rises, the amounts of snow and ice diminish and sea level increases [1]. According to the Intergovernmental Panel on Climate Change (IPCC) the global warming is an undeniable fact. Each of the last three decades was successively warmer than any preceding decade since 1850 (Figure 2.1) [1].

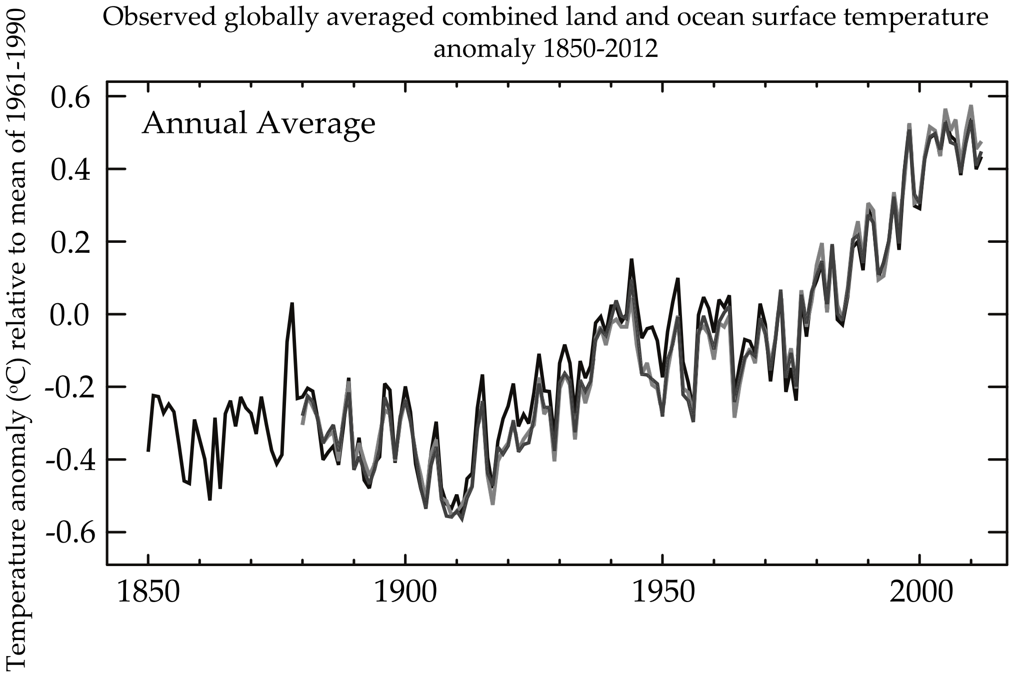

FIGURE 2.1: Annual values of observed global mean combined land and ocean surface temperature anomalies, from 1850 to 2012 from three data sets [1]

The impacts of these changes are already evident around the globe. In many regions, changing precipitation or melting snow and ice affect the local hydrological system and hence the water resources in terms of quantity and quality. Furthermore, many species are forced to change their areas of inhabitation, seasonal activities and migration patterns which affect negatively their populations. Climate changes also influence human activities. Crop yields over a wide range of regions decline, raising concerns related to future food security. Finally, extreme weather phenomena such as heat waves, droughts, cyclones, wildfires become more common around the world [34].

Generally, the drivers of climate change are both natural and anthropogenic [1]. However, according to IPCC, the main contributor towards the rise of the global average temperature is the increase in anthropogenic greenhouse gases (GHG) concentrations [34]. The concentrations of carbon dioxide, methane, and nitrous oxide in the atmoshpere have risen to levels unprecedented in at least the last $800,000$ years. The concentration of carbon dioxide, which is the main GHG, has increased by 40% to over 390 *ppm* since pre-industrial times, primarily from fossil fuel emissions and secondarily from net land use change emissions (Figure 2.2) [1].

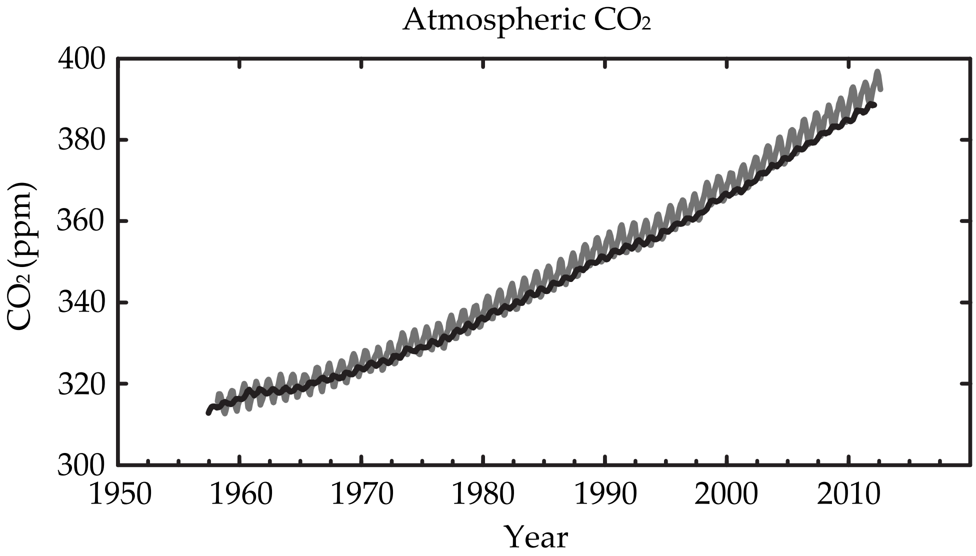

FIGURE 2.2: Atmospheric concentration of carbon dioxide from Mauna Loa (grey line) and South Pole (black line) since 1958 [1]

2.2 The role of Renewable Energy

According to IPCC, a key factor of cost-effectively stabilizing the carbon dioxide concentrations at $430 - 530$ *ppm* by 2100 is reducing the carbon intensity of electricity generation [32]. This can be achieved by reinforcing the share of the low-carbon electricity supply through the use of renewable and nuclear energy and the implementation of carbon capture and storage (CCS) for conventional power plants. In 2013, the low-carbon power supply share was 33.6% (11.5% nuclear and 22.1% renewable energy including hydropower [2]). This share needs to rise up to more than 80% by 2050. In addition, fossil fuel power generation without CCS needs to be abandoned entirely by 2100 [32].

Except from having a large potential to mitigate climate change, renewables can provide wider benefits. They can contribute to social and economic development, make energy more accessible in developing countries, increase energy supply security and reduce negative impacts on the environment and health [3].

In this context several countries around the world adopt policies regarding the reduction of their GHG emissions. According to a study, published by the Global Legislators' Organization and the Grantham Research Institute at the London School of Economics, sixty-six countries accounting for the 88% of the global emissions have already adopted such policies or are working towards this direction [35].

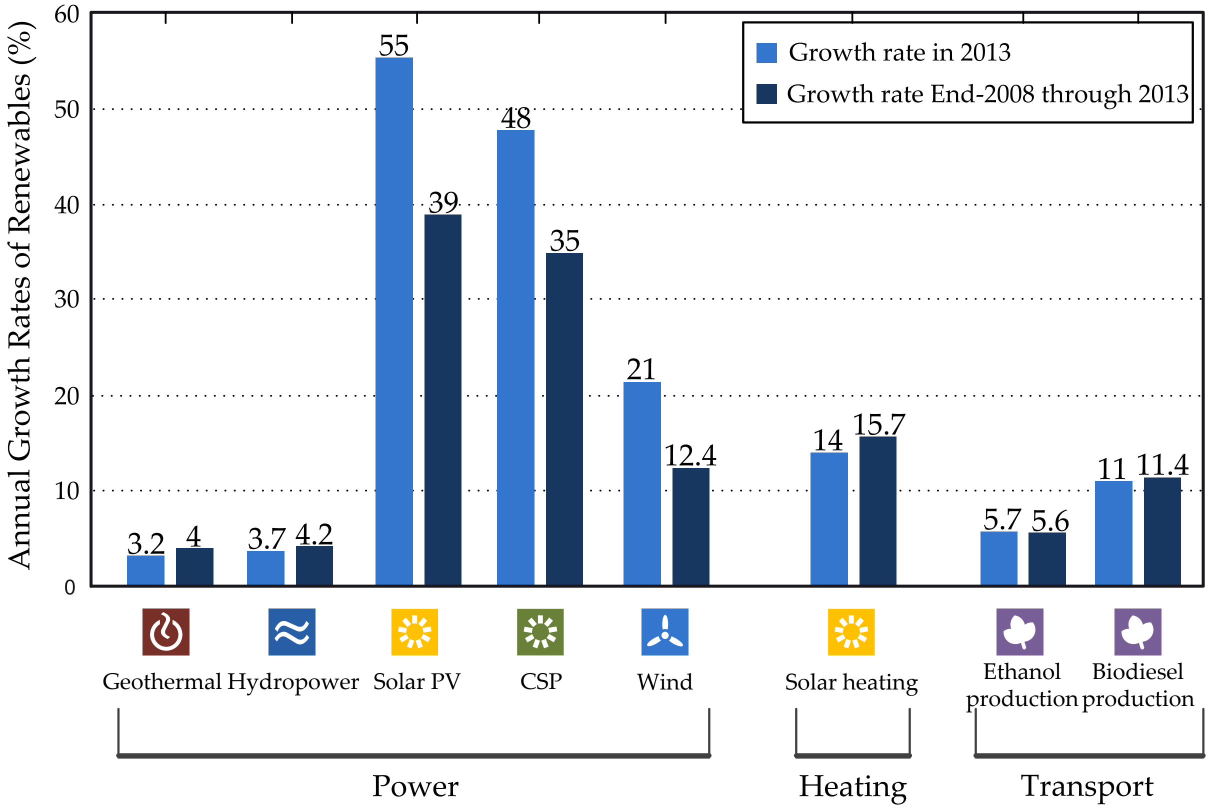

Figure 2.3: Average annual growth rates of renewable energy capacity and biofuels production, End-2008 - 2013 [2]

With a series of policies supporting them, renewables have become a major point of focus for the reduction of carbon emissions. The years 2009 through 2013 installed capacity and output of most renewable energy technologies increased with high rates (Figure 2.3). Solar photovoltaics (PV) had the steepest capacity growth rates while wind energy is the sector that experienced the largest capacity installation [2]. In 2013, renewables made up more than 56% of net additions to global electric generating capacity from all sources [2].

The latest available data regarding the share of renewables in the global energy consumption and the global electricity production is shown in Figure 2.4. Renewable energy covered an estimated 19% of global final energy consumption. Of this total share, traditional biomass, which corresponds to cooking and heating needs in remote and rural areas of developing countries, accounted for about 9%, while modern renewables increased their share to approximately 10% [2].

More specifically, regarding the electricity generation in 2013, renewables form an estimated 26.4% of the world's power generating capacity. This capacity contributed to the global production of electricity with an estimated 22.1%. Hydropower provided about 16.4%. While renewable capacity increases at a high rate each year, renewable electricity's share to the global electricity generation is increasing more slowly. This is because overall demand keeps rising rapidly. In addition, much of the deployed renewable capacity (solar PV, wind) is variable [2].

2.3 Current and Future Status of Wind Energy

Wind energy is considered as an important alternative for near-term (2020) and long-term (2050) GHG emissions' reduction. While, wind energy is used over a range of different applications, its primary use, which is relevant to climate change mitigation, is the generation of electricity from grid-connected wind turbines, deployed either on- or offshore [3].

According to a number of surveys, the global potential for wind energy could exceed the current global electricity production [3]. Although there is no standardized methodology for the calculation of this potential, several studies indicate that it could lie between 70 EJ/yr $(19,400TWh/yr)$ (onshore only) to a high of 450 EJ/yr $(125,000TWh/yr)$ (onshore and near-shore). This is approximately equal to one to six times the global electricity production in 2008 [3].

Regarding offshore wind potential, it is estimated to range from 15 EJ/yr to 130 EJ/yr $(4,000-37,000\ TWh/yr)$ when only considering relatively shallower and near-shore applications [3].

During the last decade, capital costs of wind energy have seen a significant reduction due to market competition and technological advancements [2]. The average turbine rating in $1980s$ was 50 kW and by 2000 it had increased to 2 MW. At present, sizes of $5-10$ MW are achievable [5]. In addition, developments regarding the rotor and tower design resulted to rotor diameters of over 100 m whereas the respective figure in the $1980s$ was around 15 m (Figure 2.5) [3] [5]. Furthermore, advancements in drive train designs and power electronics as well as

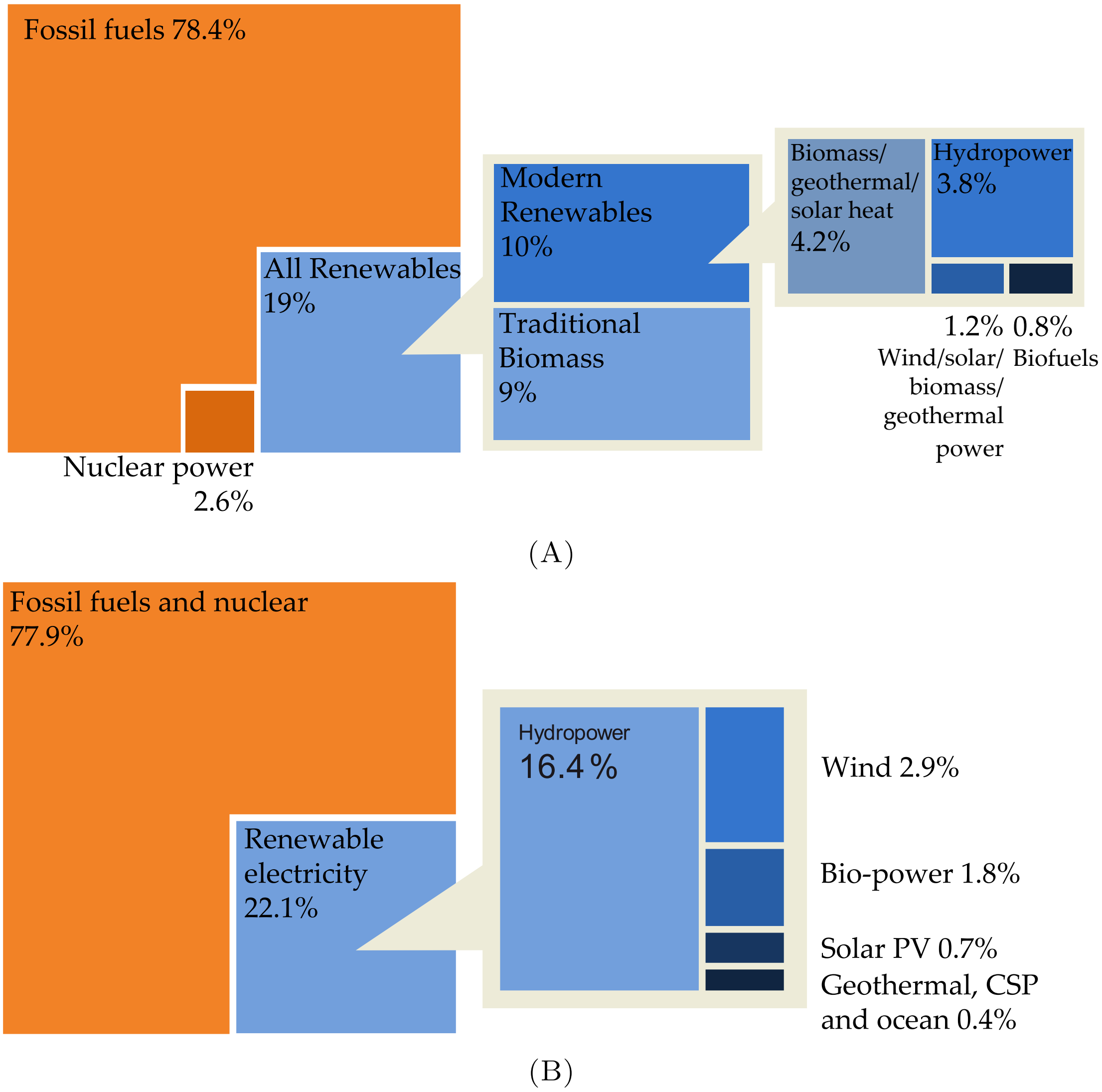

FIGURE 2.4: (A) Estimated renewable energy share of global final energy consumption (2012) (B) Estimated renewable energy share of global electricity production in (End-2013) [2]

the production of greater volumes have enhanced and continue to enhance the competitiveness of wind power [5].

This decrease in costs made wind-generated electricity cost competitive, or nearly so, on a per kWh basis with new coal- or gas-fired plants, even without compensatory support schemes, in several markets [2]. These advancements led to rapid market development and drove the global installed wind power capacity from 17 GW in 2000 to 360 GW in 2014 (Figure 2.6) [2] [4].

Wind energy is expected to have an even brighter future. According to the combined forecasts of International Energy Agency (IEA) and the Global Wind Energy Council (GWEC) the global installed capacity is anticipated to reach 750 GW by the end of 2020 and to double again in 2030 to about 1550 GW (Figure 2.7) [5].

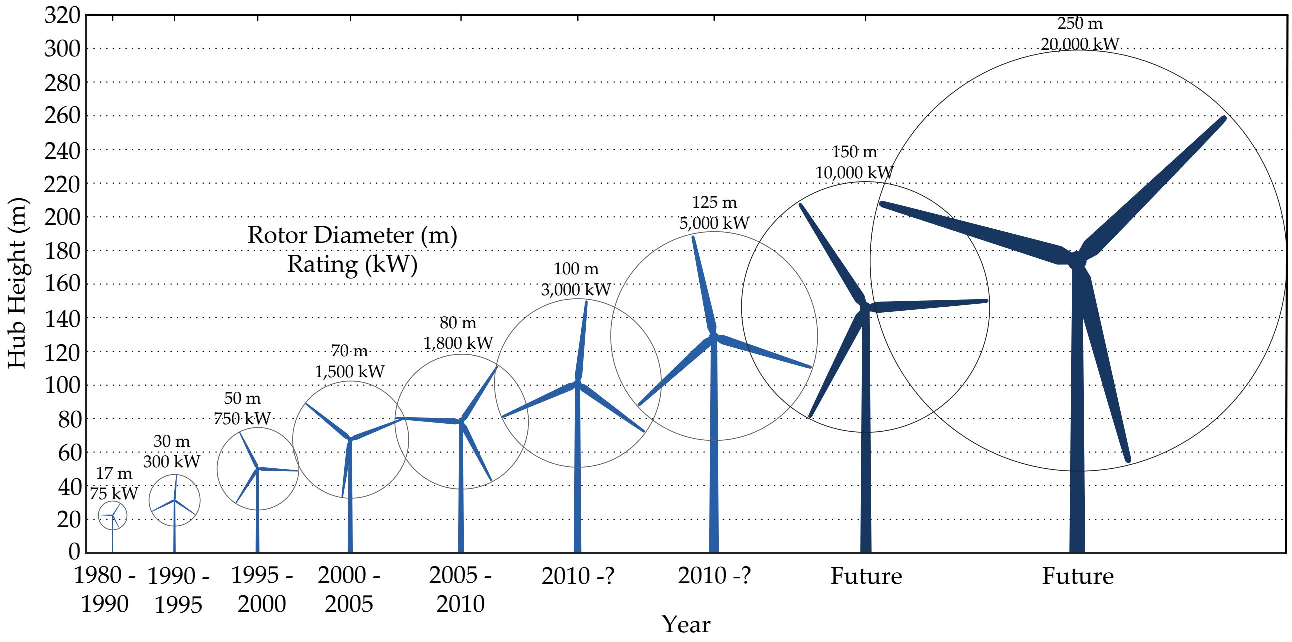

FIGURE 2.5: Growth in size of typical commercial wind turbines [3]

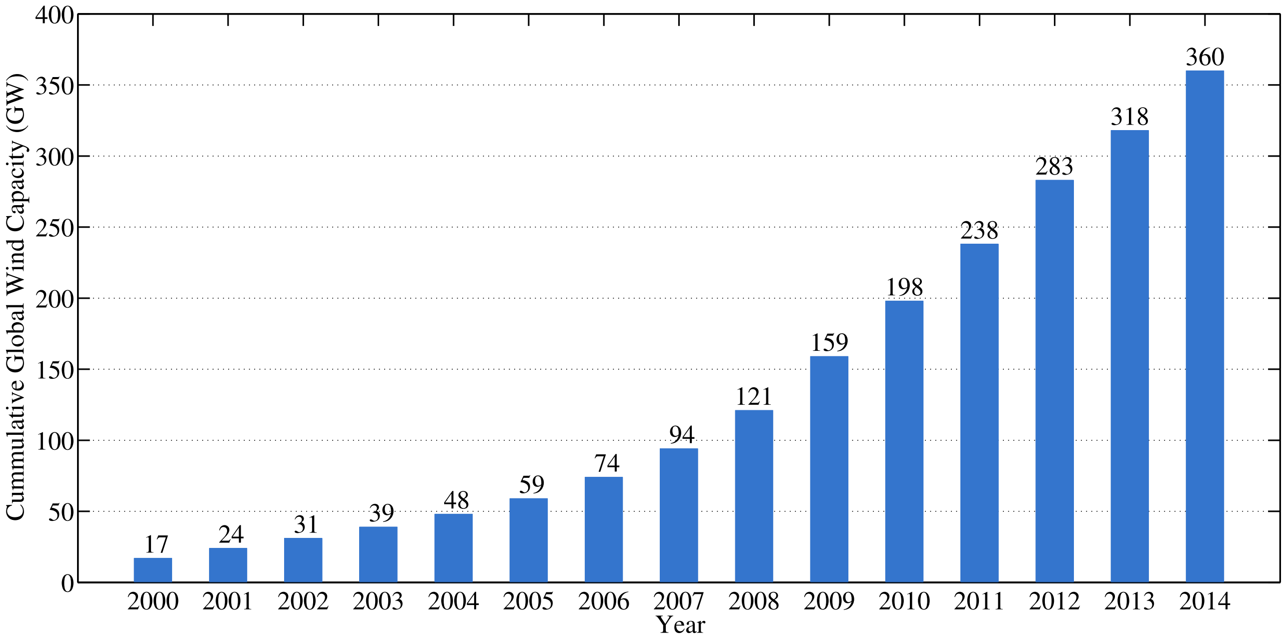

FIGURE 2.6: Wind power total world capacity 2000 – 2014 [2] [4]

2.4 Industry Trends of Offshore Wind Energy

The initial driver for the deployment of offshore wind energy is the exploitation of available wind resources in regions where onshore wind energy development is restrained by different factors such as limited wind potential or land use conflicts. In addition, offshore locations provide higher-quality wind resources (higher average wind speeds, lower wind shear etc), allow the deployment of even larger turbines due to the lack of land-based transportation constraints and hence decrease costs through economies of scale [3].

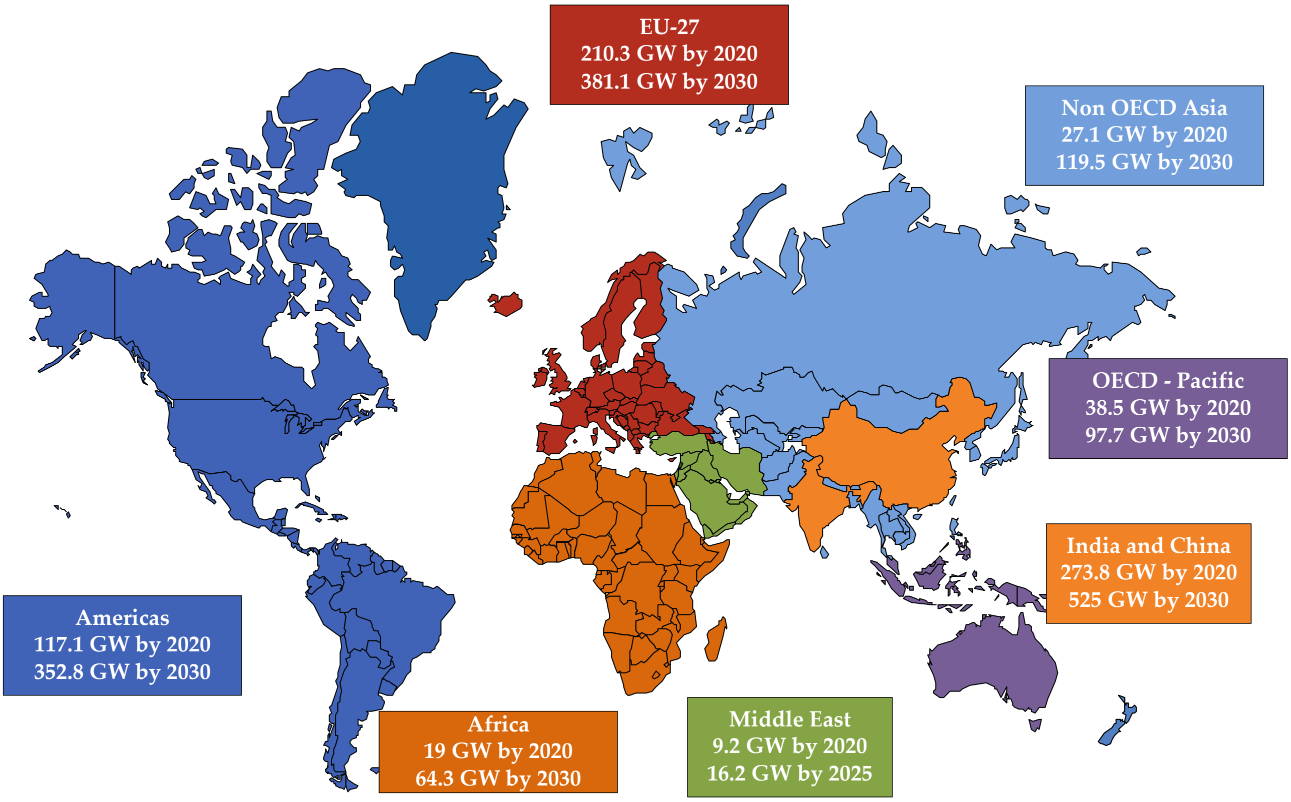

FIGURE 2.7: Projection of global cumulative wind energy growth 2020 – 2030 [5]

The first offshore wind project, the Vindeby wind farm in Denmark, was delivered twenty-three years ago in 1991 [36]. It consists of eleven turbines with a total installed capacity of 4.95 MW and is located approximately 2 km from shore at an average depth of 4 m [6].

Since then, the accumulated experience and the technological advancements have allowed the construction of larger turbines (Figure 2.5) and projects of larger installed capacities. In addition, projects have started moving towards more distant locations from shore and deeper waters [36]. Figure 2.8 summarizes trends of the offshore industry during the last 15 years [6–9].

More specifically, Figure 2.8A shows the maximum, minimum and average installed capacities per year of already delivered and planned projects. It is seen that the OWFs capacities grew significantly during the last decade. The average project capacity in 2014 is approximately 330 MV which is an almost tripled growth compared to the average capacity in 2011 of 116 MW [6–8].

Furthermore, the number of turbines per project as seen in Figure 2.8B is certainly larger for contemporary projects compared to the ones of the previous decade. However, it is a figure that varies significantly since it depends both on the total project capacity and the rated power of the turbines [6–8].

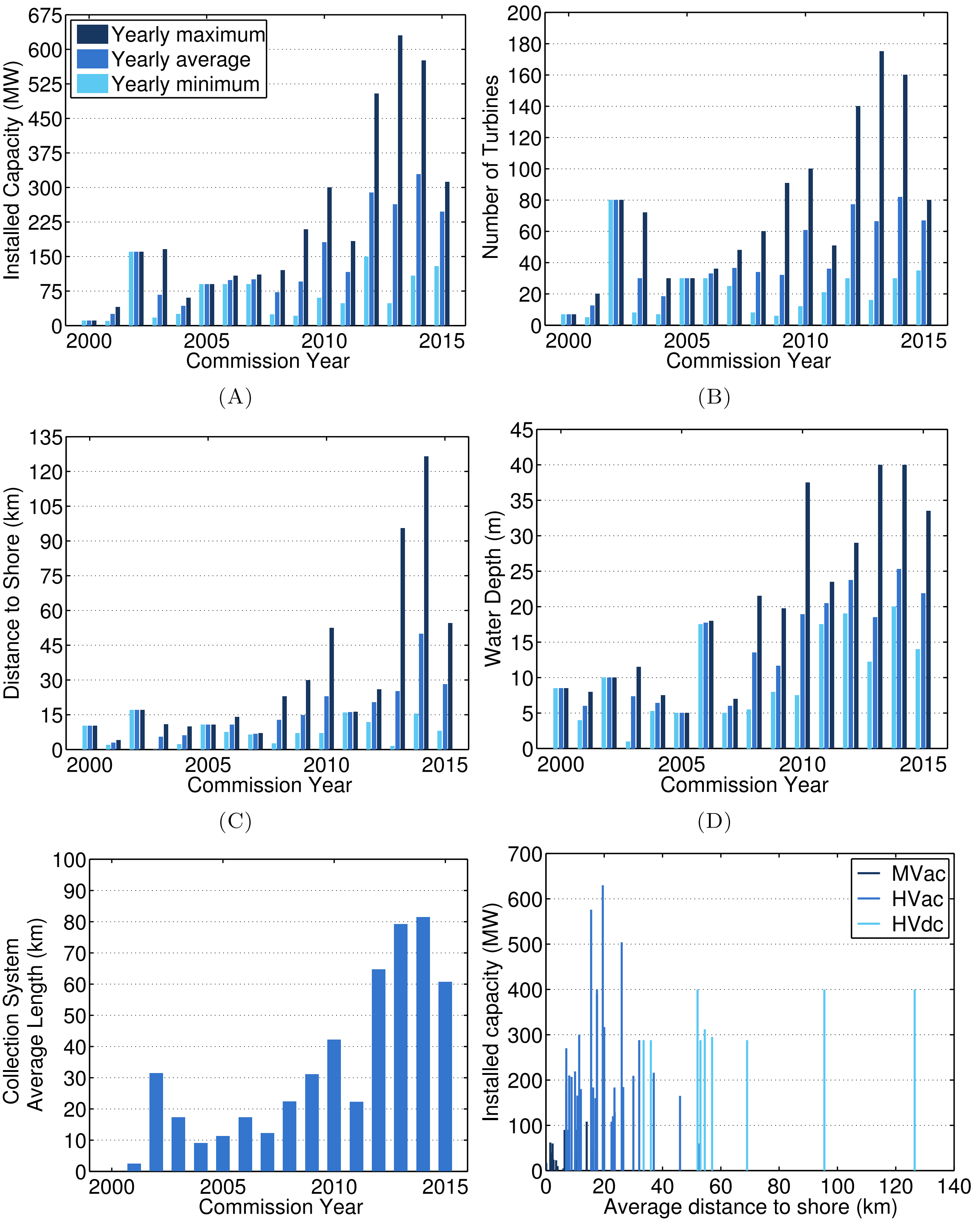

(A) (B) (C) (D) (E) (F)

FIGURE 2.8: Yearly statistics for commissioned and under construction European offshore wind projects composed of five or more turbines [6–9]

Regarding the distance from land (Figure 2.8C), it is evident that the industry has been moving further offshore. This trend is expected to continue for the coming years allowing the exploitation of richer wind resources. Naturally, moving further from shore means that the water depth also increases (Figure 2.8D) [6–8].

Finally, the average length of the collection system per project (Figure 2.8E) seems to peak in 2014 and is expected to decrease in the coming years mainly because of the use of larger turbines.

The first offshore projects used MVAC for transmitting the produced power since their installed capacity was relatively small and they were located close to shore and the grid (Figures 2.8A, 2.8C). In fact MVAC transmission has been used for distances lower than 15 km and capacities up to 100 MW (Figure 2.8F). As the industry started moving further offshore and building larger OWFs, HVAC transmission became the norm for distances between 10 km and approximately 40 km from shore. For distances longer than 40 km and capacities larger than 200 MW HVDC transmission is the usual choice of the industry due to the lower power losses which compensate for the initial costs of the converter equipment [6–8].

Furthermore, regarding the cost of offshore wind energy, it can be seen form Figure 2.9 that the capital costs of offshore wind projects have increased substantially since the early 2000s. This increase is driven both by rising underlying costs (commodity prices rises, currency fluctuations) and by more specific reasons such as supply chain bottlenecks, lack of competition, sub-optimal reliability and the move to deeper water regions [10].

However, the most recent projects show that the costs may be stabilizing. Despite the increasing water depth in which new projects are developed, recently announced wind farm capital cost lies between £3 m/MW and £3.5 m/MW (Figure 2.9). This is a result of many factors such as a better understanding of the key risks in offshore wind construction, oversupply in the general wind turbine market and larger projects leading to greater economies of scale [10].

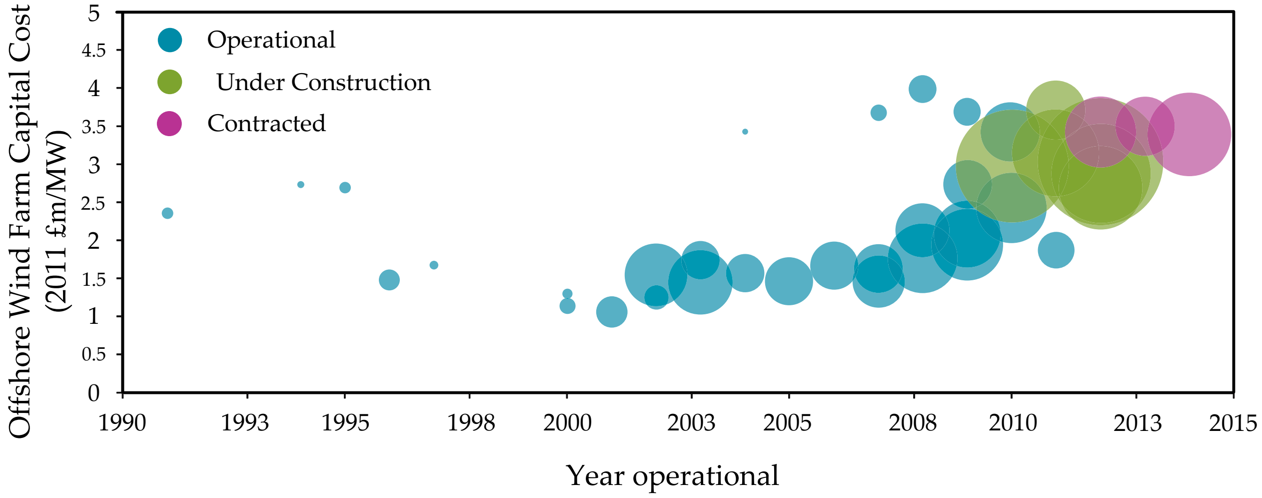

FIGURE 2.9: European offshore wind farm capital costs by year (Note: The bubble diameter is proportional to the wind farm capacity) [10]

Today, the global installed offshore wind power capacity is, still, only a fraction of the total wind power capacity (Figure 2.10) with more than 90% of it located in European waters such as the North Sea, the Baltic Sea and the Atlantic Ocean. However, offshore wind energy has started gaining traction primarily in China followed by Japan, South Korea, Taiwan and the United States [36]. The largest operational offshore wind project, as of 2014, is the 'London Array 1' in the UK which consists of 175 turbines with a total installed capacity of 630 *MW* [6].

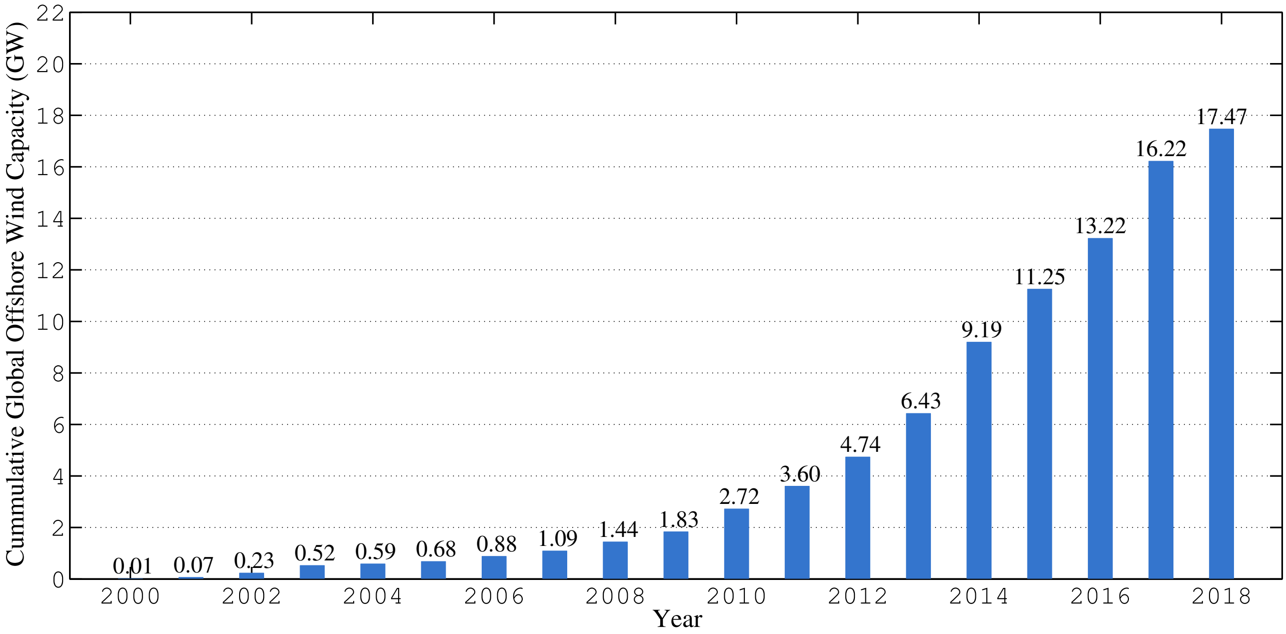

FIGURE 2.10: Offshore wind power total world capacity 2000 – 2018 (Installed and planned) [6–9]

According to the European Wind Energy Association (EWEA), offshore wind power has the potential to become the prime electricity source for Europe in the future. By 2020, 40 *GW* of offshore wind capacity could be operational in Europe, while 150 *GW* could be online by 2030 [37]. This figure could be skyrocketed to 460 *GW* by 2050 contributing an astonishing 50% of the European electricity demand. However, for these predictions to become reality, certain technological advancements are required in order to exploit even deeper waters. In addition, a supportive legislative framework is necessary [37].

Chapter 3

Submarine Power Cables

3.1 Introduction

As the installation of OWF is driven further offshore and the installed power increases, the total length of SPC, used for the infield connections and the transmission of the generated power to the onshore grid, rises (Figure 2.8). Therefore, the power losses related to the electrical connections become more and more significant regarding the total efficiency of the OWF. The model for the calculation of the power losses of SPCs, presented in this report, makes use of existing models and standards published by the International Electrotechnical Commission (IEC).

In this chapter, firstly, an overview of the design characteristics of power cables is given in Section 3.2. Then, the thermal and electrical properties of power cables are presented (Section 3.3). Finally, the model for calculating the electric power losses of AC and DC cables is explained and an assessment of the model through examples is provided in Section 3.4.

3.2 Design Characteristics of Submarine Power Cables

SPCs are complex products with several layers of different materials that serve various purposes. In this section, the different layers that compose an SPC are presented. In addition some examples of various SPCs are shown for a better visualization of their construction.

3.2.1 Conductor

The conductor (or conductors) of SPCs are made of either copper or aluminium. Despite the fact that copper is a more expensive material than aluminium, it is used for the majority of SPCs, since its higher conductivity allows the manufacturing of cables with smaller cross-sectional area [11] [31]. The conductor can have different shapes depending on the application of the cable. The most common conductor profiles are shown in Figure 3.1.

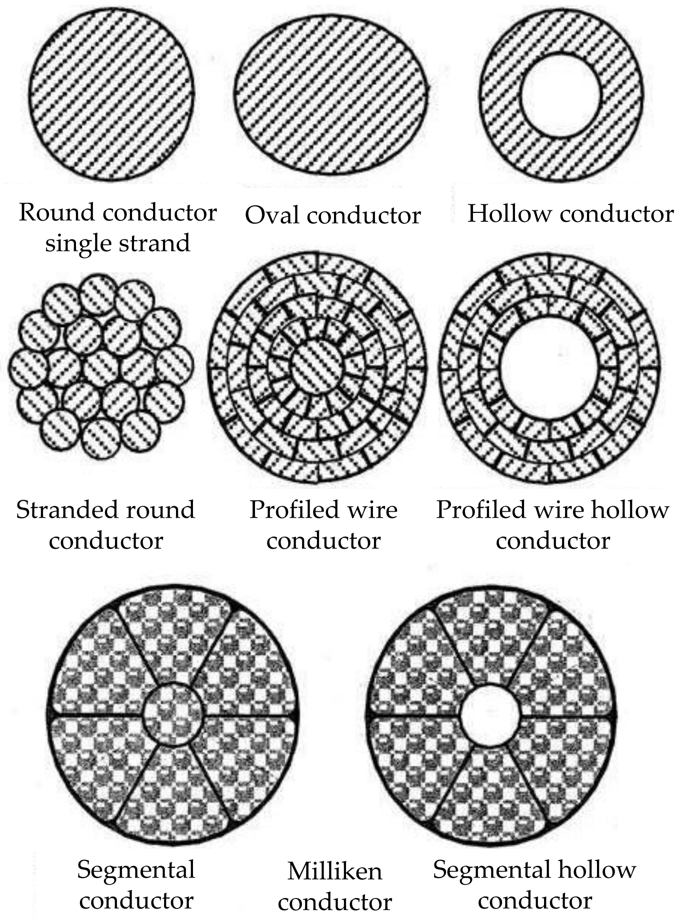

Figure 3.1: Typical conductor profiles of Submarine Power Cables [11]

3.2.1.1 Solid Conductors

Solid conductors are single uniform wires which have very smooth surface and good longitudinal water tightness [11]. The manufacturing of such conductors is simple but it is limited to cross-sectional areas up to approximately 400 mm^2 and voltage levels of about 150 kV [11]. Larger sizes of solid conductors become too rigid to install, form and terminate. Therefore, for cables of larger cross-sections and current carrying capability stranded conductors are employed [12].

3.2.1.2 Stranded Conductors

Stranded conductors are the most common conductors used in SPC and are employed for both DC and AC cables. These conductors consist of a central wire surrounded by layers of helically laid wires. Each layer is laid in the opposite direction of the previous one and consists of 6 additional wires as shown in Figure 3.2. The distance in which a strand performs a full revolution around its layer is called the length of lay [12].

During the manufacturing process the strands are compressed in order to reduce the interstices between them. Proper compression can lead to filling factors of 92%, however this procedure requires cold working of the wires which results to a reduction of the electric conductivity of the material [11].

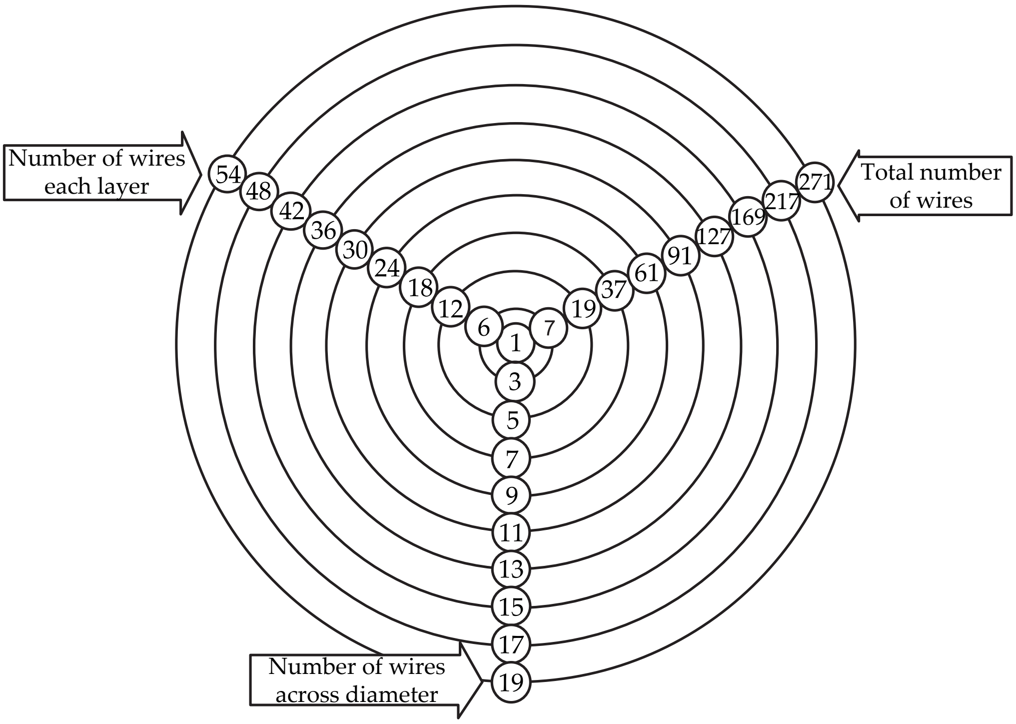

FIGURE 3.2: Concentric stranding relationships [12]

3.2.1.3 Profiled wire Conductors

Profiled conductors consist of wire sectors whose cross-section resembles the keystone of an arch as it is seen in Figure 3.1. The individual wires can be assembled together to form a perfect circular cross-section and can achieve filling factors of more than 96% [11]. The conductor surface is smooth and since cold working is not involved, the material retains its electric conductivity. Profiled wire conductors are most often used for large HVDC cables [11].

3.2.1.4 Milliken Conductors

This type of conductors was introduced by Milliken in the $1930s$ aiming to reduce the impact of the skin effect, an electromagnetic phenomenon effecting conductors under AC loading according to which the current density tends to concentrate towards the outer part of the conductor (explained further in Section 3.3.2).

The conductors consist of several segments which are electrically separated by a thin layer of insulation. In addition, since every segment is composed of a number of stranded wires, each individual wire changes its radial position with respect to the central axis of the cable from close to the center to far from the center as the wire proceeds along the conductor. These techniques reduce the skin effect and the resistance, increasing the current carrying capability of the cable [12]. The results become more effective with an increasing number of segments. Usually five or six segments are employed but there are designs with nine segments as well [11].

Because of the more complicated design, the cost of Milliken conductors is higher compared to the standard stranded conductors. Therefore they are only used for very large cross-sections (more than 1200 mm^2) [11].

3.2.1.5 Hollow Conductors

Hollow conductors are used in cables that are filled with usually a low viscosity oil. The fluid serves as part of the cable's insulation. The hollow center allows the fluid to flow easily allowing pressure control in case of thermal expansion [11].

3.2.2 Insulation System

The insulation system of a cable provides a barrier against the electric potential difference between the conductors of the cable and adjacent conducting surfaces [11]. The insulation has to be mechanically durable and retain its voltage blocking capabilities irrespectively of temperature variations for the whole lifetime of the cable. The materials used for the insulation system are composed of either synthetic or natural polymers [12]. Regarding contemporary SPCs, there are only a few different materials used for this purpose. Some of them and their operation temperature is shown in Table 3.1.

Today, the most common materials used for SPC is the Cross-Linked Polyethylene (XLPE) for both AC and DC application and the mass-paper combination employed in DC applications [11]. In the following sections these two types of insulation are briefly presented. In addition, for completion purposes, some information is given regarding other types of insulation that have been used in the past but are gradually being abandoned.

Cable Insulation Materials	
Material	Maximum Operation Temperature (°C)
Low Density Polyethylene	70
Cross-linked Polyethylene	90
Ethylene Propylene Rubber	90
Mass-paper	50 – 55
Oil-paper	85 – 90

Table 3.1: Operational temperature of cable insulation materials [11]

3.2.2.1 Polyethylene

Polyethylene is a hydrocarbon polymer composed exclusively of carbon and hydrogen [12]. Although it was used as an electric insulation material for power cables in the past, it was subsequently replaced by XLPE which can withstand higher operational temperatures [11].

3.2.2.2 Cross-linked Polyethylene (XLPE)

Cross-linked polyethylene is derived from polyethylene that has been further processed. Cross-linking is a chemical procedure according to which different polymer chains are connected together [12]. Cross-linking upgrades certain properties of the polyethylene such as its endurance at elevated temperatures [12].

During its early days of manufacturing XLPE faced reliability issues as a cable insulator due to a phenomenon called water-treeing. Under the combined influence of water, electric field and impurities, damage tree-like patterns would start growing in the material and eventually lead to an electric breakdown. However today's modern techniques have rendered it as a first-choice insulation material for both land and submarine cables [11].

A modern XLPE insulation can exhibit an excellent dielectric value and a long lifetime while being resistant against water-treeing. Achieving these characteristics demands the use of a semi-conductive screen on both the inner and outer surface of the insulation. In this way a smooth surface is provided on both surfaces of the insulation making it to be distributed evenly throughout the cable length. The semi-conductive layer is made of PE-based co-polymers blended up with 40% carbon black [11].

Regarding HVDC, standard XLPE is unsuitable because of space charge phenomena appearing under DC loading. However, nowadays, there are HVDC cables using extruded XLPE insulation that overcome successfully this challenge.

3.2.2.3 Ethylene Propylene Rubber (EPR)

As its name suggests, Ethylene Propylene Rubber (EPR) is a copolymer composed of ethylene and propylene. Nowadays, because of the fact that EPR presents higher dielectric losses under AC loading than XLPE it is not preferred by cable manufacturers for high voltage applications. However there are still cables with EPR insulation in service [11].

3.2.2.4 Mass-Paper

Cables with mass-impregnated insulation is a well-proven technology that is in use today for HVDC submarine applications for voltage levels up to 500 kV [11].

The insulation consists of layers of paper from conifer cellulose pulp which is vacuum-dried and impregnated with an impregnation compound such as mineral oil based compounds. In addition semi-conducting screens of carbon black paper at the inner and outer surface of the paper insulation provide a smooth surface for the paper layers [11].

Mass-impregnated cables can be used practically for any cable length but only for DC applications. Between the paper layers, there are inherently small voids. Under an alternating electric field these gaps allow successive partial discharges to take place which can lead to the breakdown of the insulation [11].

3.2.2.5 Oil-Paper

Another insulation approach used for both AC and DC cables is the use of a fluid in combination with paper. The cables that have this kind of insulation are found under different names such as Low Pressure Oil Filled (LPOF), Self Contained Fluid Filled (SCFF) or Self Contained Oil Filled (SCOF). The paper insulation consists usually of layers of conifer cellulose pulp paper while an improvement is the use of paper layers reinforced with polymeric films. Regarding the fluid, traditionally a low viscosity oil was used but today synthetic fluids are employed [11].

During operation, the fluid has to maintain a pressure between an allowed interval since this pressure affects the dielectric ability of the insulation. Changes in pressure may be caused due to thermal expansion of the fluid which depends on the cable's loading or even because of a possible damage of the cable's protective layers. For this reason, pressure feeding systems are needed at the terminals of the cable. Regarding SPCs of this type, the fluid flows through the opening at the center of the hollow conductor [11].

3.2.2.6 Gas-Paper

Similar to the fluid filled cables, this insulation design employs nitrogen gas instead of a fluid. The pressurized gas fills the gaps between the paper layers and suppresses the formation of partial discharges. For this reason these cables can be used for both AC and DC applications [11] [38].

3.2.3 Swelling agents

A SPC needs to be longitudinally watertight to avoid water mitigation after an accident or fault. For this reason special materials, that swell when they come in contact with water, are added between the layers of the cable. These swelling agents usually are in the form of powder, tapes or yarns [12]. They are used mainly for cables with extruded insulation since the oil-filled and mass-impregnated cables are considered to be inherently watertight [11].

3.2.4 Sheath

All SPCs have a sheath over their insulation layers to provide protection against radial infusion of water into the cable [11]. An additional duty of the metallic layers of the sheath is handling and providing a low resistance path for the charging current in case of AC loading or for fault currents [12]. Regarding high voltage SPCs, the sheath is usually metallic with additional layers of polymeric jackets. The metals commonly used for this propose, are lead or lead alloys, copper or aluminium [11]. The polymeric jackets are intended to protect the metallic layer against corrosion and abrasions [11].

Medium voltage cables on the other hand, usually employ only polymeric sheaths in combination with a water absorbing agent [11]. While polymeric sheaths can block water effectively, some water vapour can diffuse through them. In case of medium voltage cables where the strength of the electric field around the conductor is not that high (compared to high voltage cables) this amount of vapour can be effectively blocked by the water absorbing agent and does not create any problems [11].

3.2.5 Armour

The armour of an SPC provides tension stability during its installation and mechanical protection from external factors such as fishing equipment or anchors [11]. It is composed of metal wires that are placed helically around the cable with a certain length of lay. The length of lay is a design parameter that affects certain properties of the cable such as bending stiffness, tensional stability and torsion balance [11].

There are different armour configurations depending on the application. The armour can have one or two layers of wires while the wires can be round or flat. Regarding three-core AC cables and DC cables, the metal used for the armour wires is usually mild steel which is a magnetic material. This means that, during AC loading, it concentrates the magnetic field and generates losses due to induced electromotive forces. However, in case of three-core cables the magnetic fields of the three phases cancel each other out significantly allowing the use of mild steel in the armour. Regarding single-core SPCs intended to be used under AC loading other solutions are applied. An alternative is the use of non magnetic materials such as bronze, brass, copper, aluminium or even stainless steel. Another approach is the use of a massive copper screen grounded at both ends of the cable. The magnetic field of the generated induced current that flows in the screen cancels the field generated from the conductor current. In this way the losses at the armour can be avoided but the losses at the screen get higher [11] [39].

The armour is usually laid on a fabric-tape bedding in order the underlying layers to be protected [11].

3.2.6 Corrosion Protection

In order to protect the external layers of the cable against corrosion of sea salt, different measures are employed. The steel wires of the armour can be coated with a layer of zinc or an individual polymeric sheath. In addition, a layer of bituminous compound is usually added on top of the armour layer [11].

3.2.7 Outer Serving

The outermost layer of an SPC is the external serving which protects the anti-corrosion layer against damages from external factors. The serving usually consists of extruded polymeric or wound yarn layers [11].

3.2.8 Examples

For a visualization of the different layers of an SPC, some examples of typical cable configurations are shown in the following figures.

1. Conductor: copper, circular stranded compacted

2. Conductor screening: extruded semi-conductive compound

3. Insulation: XLPE

4. Insulation screening: extruded semi-conductive compound

5. Screen: copper wires and copper helix, swelling powder or tape

6. Laminated sheath: aluminum tape bonded to overlaying PE sheath plus conductive coating

7. Fibre optic cable, optional

8. Fillers: polypropylene strings

9. Binder tapes

10. Bedding: polypropylene strings or polyester tape

11. Armour: galvanized round steel wires

12. Serving: bituminous compound, hessian tapes, polypropylene strings with coloured stripe

Figure 3.3: Typical design of a MVAC SPC with XLPE insulation (Courtesy of Nexans) [13]

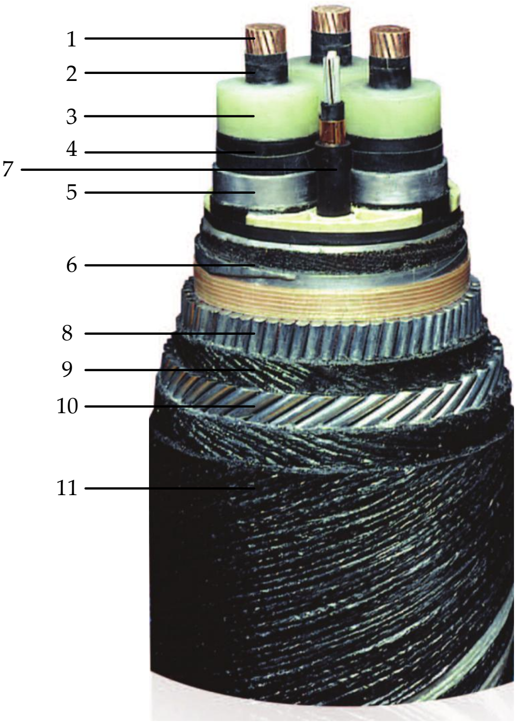

1. Conductor: copper, circular stranded compacted

2. Conductor screening: extruded semi-conductive compound

3. Insulation: XLPE

4. Insulation screening: extruded semi-conductive compound

5. Sheath: Lead alloy bonded to overlaying PE jacket

6. Laminated sheath: aluminum tape bonded to overlaying PE sheath plus conductive coating and swelling tape

7. Fibre optic cable, optional

8. Armour: galvanized round steel wires

9. Bedding: polypropylene yarn

10. Armour: galvanized round steel wires

11. Serving: bituminous compound, polypropylene yarn

Figure 3.4: Typical design of a HVAC SPC with XLPE insulation (Courtesy of ABB) [11]

1. Conductor: copper, circular stranded compacted

2. Conductor screening: extruded semi-conductive compound

3. Insulation: XLPE

4. Insulation screening: extruded semi-conductive compound

5. Sheath: Swelling tapes

6. Sheath: lead alloy bonded to overlaying PE jacket

7. Armour: galvanized round steel wires

8. Serving: bituminous compound, polypropylene yarn

Figure 3.5: Typical design of a HVDC SPC with XLPE insulation (Courtesy of ABB) [14]

Figure 3.6: Typical design of a HVDC fluid-filled SPC (Courtesy of PRYSMIAN) [15]

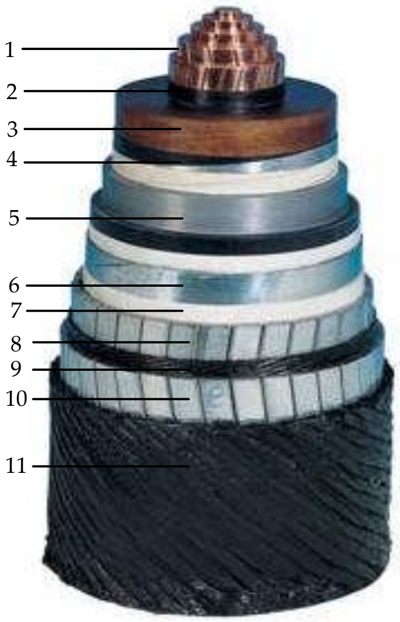

Figure 3.7: Typical design of a HVDC mass-impregnated SPC (Courtesy of PRYSMIAN) [15]

3.3 Thermal and Electrical Behavior of Power Cables

During the operation of an AC power cable, heat is produced because of ohmic and dielectric losses. The heat is generated at the conductors (W_c), the insulation (W_d) as well as the sheath (W_s) and armour (W_a) of the cable. Then it dissipates from the interior of the cable towards the surroundings. A graphical representation of this phenomenon for a three-core AC cable is presented in Figure 3.8.

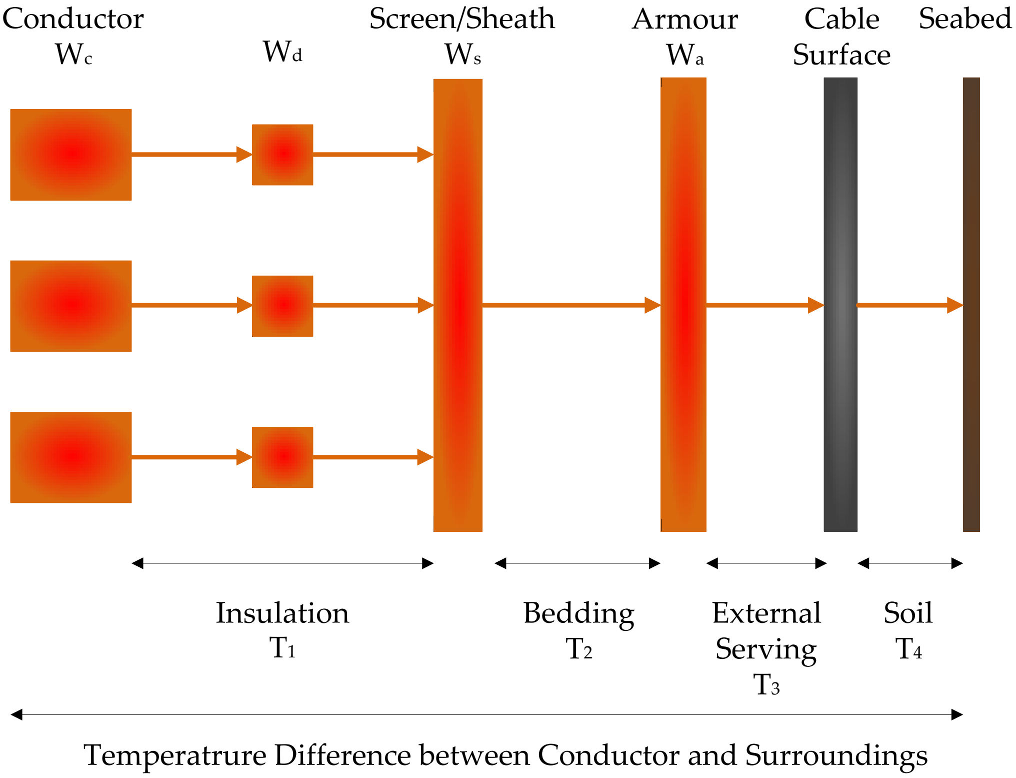

FIGURE 3.8: A graphical representation of heat dissipation in a three-core AC cable

The generated heat and, consequently, the temperature of the conductor depend on the current flowing in the cable. As the loading of the cable increases, larger amount of heat is produced and the operating temperature rises. Therefore, the maximum current through a cable is confined by its temperature limit which is usually imposed by the insulation material. The temperature of the conductor has to be kept lower than this temperature limit. Regarding the DC power cables, the same phenomenon takes place but the heat generation is caused only by ohmic losses at the conductor since there are no sheath, armour or dielectric losses under DC loading.

According to the IEC, the maximum temperature rise of the conductor above the ambient temperature for an AC power cable is given by the following expression [27]:

$$\Delta\theta_{c,Max} = (I_{c,Max}^2 R_{AC}^{\theta_{c,Max}} + \frac{1}{2}W_d)T_1 + [I_{c,Max}^2 R_{AC}^{\theta_{c,Max}}(1+\lambda_1) + W_d]nT_2 + \\ + [I_{c,Max}^2 R_{AC}^{\theta_{c,Max}}(1+\lambda_1+\lambda_2) + W_d]n(T_3+T_4) \quad (3.3.1)$$

Where:

- $\Delta\theta_{c,Max}$: Maximum conductor temperature rise above the ambient temperature (K)
- $I_{c,Max}$: Maximum current of conductor (A)
- $R_{AC}^{\theta_{c,Max}}$: AC resistance per m of the conductor at $\theta_{c,Max}$ °C (Ω/m)
- W_d: Dielectric loss per m for the insulation surrounding one conductor (W/m)
- T_1: Thermal resistance per m between one conductor and the sheath $(K\ m/W)$
- T_2: Thermal resistance per m between the sheath and the armour $(K\ m/W)$
- T_3: Thermal resistance per m of the external serving of the cable $(K\ m/W)$
- T_4: Thermal resistance per m between the cable surface and the surrounding medium $(K\ m/W)$
- n: Number of load-carrying conductors in the cable $(-)$
- λ_1: Loss factor for the sheath or screen $(-)$
- λ_2: Loss factor for the armour $(-)$

Considering that $W_c = I_{c,Max}^2 R_{AC}^{\theta_{c,Max}}$, $W_s = \lambda_1 W_c$ and $W_a = \lambda_2 W_c$, the equation 3.3.1 can be visualized by means of an equivalent thermal circuit. The heat sources are analogous to electrical current sources while the thermal resistances are analogous to electrical resistances. The temperature difference is the driving force which indicates the direction of the heat flow and it is analogous to an electrical potential difference. The thermal circuit that corresponds to a three-core AC cable is shown in Figure 3.9.

The equation 3.3.1 can be rewritten as follows in order to express the maximum permissible current [27]:

$$I_{c,Max} = \left[\frac{\Delta\theta_{c,Max} - W_d\left[\frac{1}{2}T_1 + n(T_2+T_3+T_4)\right]}{R_{AC}^{\theta_{c,Max}}T_1 + nR_{AC}^{\theta_{c,Max}}(1+\lambda_1)T_2 + nR_{AC}^{\theta_{c,Max}}(1+\lambda_1+\lambda_2)(T_3+T_4)}\right]^{0.5} \quad (3.3.2)$$

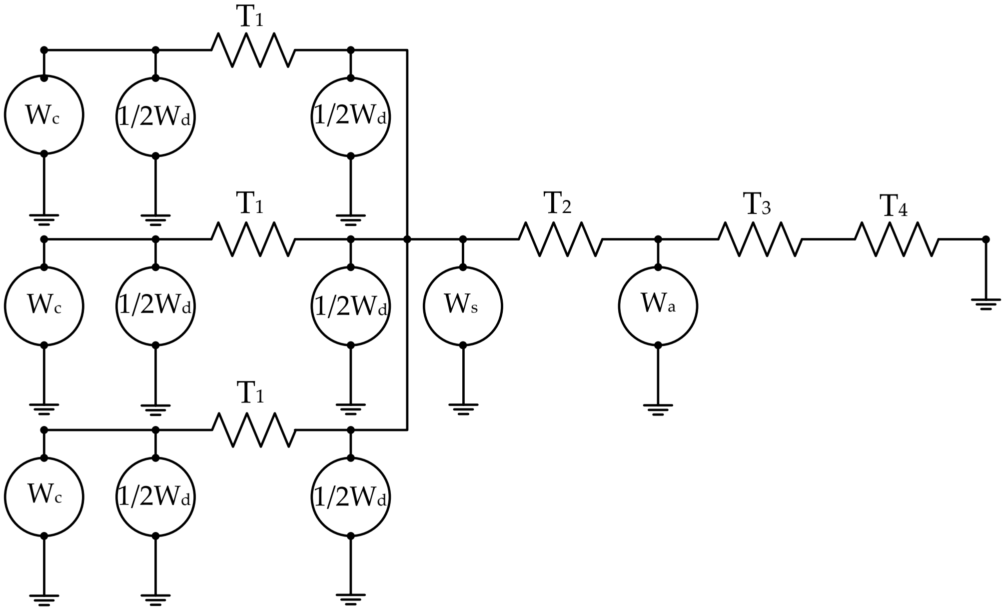

Figure 3.9: The thermal circuit of a three-core AC cable

The equation 3.3.2 is applicable when drying-out of the soil surrounding the cable does not occur, which is the most common situation regarding submarine power cables [28]. The soil drying-out is unusual since submarine power cables are laid at a depth of approximately 1 m below the seabed and at that depth the soil is saturated with water [40].

However, in some cases, the soil surrounding the cable can partially dry out. This phenomenon can be modeled by employing a two-zone approximate physical model of the soil [27]. The zone adjacent to the cable is dried out and therefore has a higher thermal resistivity than the outer zone that retains the site's thermal characteristics. The boundary between the two zones is considered to be an isotherm. The partial drying-out of the soil is taken into account by modifying equation 3.3.2 as follows [27]:

$$I_{c,Max} = \left[\frac{\Delta\theta_{c,Max} - W_d\left[\frac{1}{2}T_1 + n(T_2 + T_3 + v_x T_4)\right] + (v_x - 1)\Delta\theta_{cr}}{R_{AC}^{\theta_{c,Max}} T_1 + nR_{AC}^{\theta_{c,Max}}(1+\lambda_1)T_2 + nR_{AC}^{\theta_{c,Max}}(1+\lambda_1+\lambda_2)(T_3 + v_x T_4)} \right]^{0.5} \tag{3.3.3}$$

Where:

- v_x: Ratio of dry over moist soil thermal resistivity $(-)$
- $\Delta\theta_{cr}$: Critical drying soil temperature rise (K)

Regarding the DC power cables, similar expressions can be derived by eliminating the terms due to AC specific losses from equations 3.3.2 and 3.3.3. For a single-core HVDC power cable, for which partial drying-out does not occur, the maximum permissible current is given by the following expression [11]:

$$I_{c,Max} = \left[\frac{\Delta\theta_{c,Max}}{R_{DC}^{\theta_{c,Max}}(T_1 + T_2 + T_3 + T_4)}\right]^{0.5} \tag{3.3.4}$$

Where:

- $R_{DC}^{\theta_{c,Max}}$: The DC resistance per m of the conductor at $\theta_{c,Max}$ °C (Ω/m)

Similarly, when drying-out of the soil occurs, the equation 3.3.4 can be expressed as follows:

$$I_{c,Max} = \left[\frac{\Delta\theta_{c,Max} + (v_x - 1)\Delta\theta_{cr}}{R_{DC}^{\theta_{c,Max}}(T_1 + T_2 + T_3 + v_x T_4)}\right]^{0.5} \tag{3.3.5}$$

3.3.1 Thermal Resistance of Power Cables

According to *IEC* 60287, the thermal resistance of a power cable can be divided in 4 consecutive thermal resistances, namely T_1, T_2, T_3 and T_4. As already defined in equation 3.3.1, T_1 is the thermal resistance between the conductor and the sheath, T_2 is the one between the sheath and the armour, T_3 corresponds to the external serving of the cable and T_4 is the thermal resistance of the surrounding medium.

IEC 60287 provides equations for the calculation of these thermal resistances for several cable types and formations. Some of them are summarized in Appendix A.1.

3.3.2 DC and AC Resistance of the Conductor

The DC resistance of a conductor at a temperature θ_c can be derived by the following equation [27]:

$$R_{DC}^{\theta_c} = R_{DC}^{20}[1 + \alpha_{20}(\theta_c - 20)] \tag{3.3.6}$$

Where:

- $R_{DC}^{\theta_c}$: DC resistance per m of the conductor at θ_c °C (Ω/m)
- R_{DC}^{20}: DC resistance per m of the conductor at 20 °C (Ω/m)

- α_{20}: Constant mass temperature coefficient at 20 °C (K^{-1})
- θ_c: Temperature of the conductor (°C)

The calculation of the AC resistance of a conductor is more complicated because of two phenomena that take place during AC loading. The first is the skin effect which is a result of the alternating magnetic field developed in and around the conductor when AC current flows through it. During loading, the center of the conductor is enveloped by a greater magnetic flux than the outer part. Hence, the self-induced counter electromotive force (emf) is greater towards the center of the conductor [31]. Therefore, the net driving electromotive force is reduced at the central part of the conductor cross-section. This fact drives the current density to be higher closer to the surface of the conductor and lower at the center of the conductor [12]. In other words, a variable current distribution across the cross-sectional area of the conductor is created and it leads to the reduction of the useful conductor area and the increase of the effective conductor resistance [11].

The second electromagnetic phenomenon is the proximity effect and it is a result of the impact that neighboring conductors have on each other. If there are two adjacent conductors carrying currents towards the same direction, the two halves of the conductors that are close together are penetrated by a larger magnetic flux than the remote halves. Thus, the current density tends to be higher at the part of the cross-sectional area of the conductor which is physically further away from the adjacent conductors [11]. Taking into account these two effects, the AC resistance of a conductor can be expressed as follows:

$$R_{AC}^{\theta_c} = R_{DC}^{\theta_c}(1 + y_s + y_p) \tag{3.3.7}$$

Where:

- $R_{AC}^{\theta_c}$: AC resistance per m of the conductor at θ_c °C (Ω/m)
- $R_{DC}^{\theta_c}$: DC resistance per m of the conductor at θ_c °C (Ω/m)
- y_s: Skin effect factor ($-$)
- y_p: Proximity effect factor ($-$)

Combining the equations 3.3.6 and 3.3.7, another expression can be derived for the AC resistance of the conductor:

$$R_{AC}^{\theta_c} = R_{AC}^{20}[1 + \alpha_{20}(\theta_c - 20)] \tag{3.3.8}$$

The calculation of the skin and proximity effect factors for a three-core or three single-core cables, according to *IEC* 60287, is shown in Appendix A.2.

3.3.3 Inductance of Power Cables

An AC current through a conductor generates a time-varying magnetic flux which by its turn causes the generation of an induced emf in the conductor. The proportionality constant between the emf and the rate of change of the current is the self inductance of the conductor. In addition, in case there are other conductors in the vicinity of the current-carrying conductor a voltage is also induced in them. The proportionality constant between this voltage and the rate of change of the current is the mutual inductance of the conductors [41]. Therefore, the measured inductance of a conductor is a combination of both its self inductance and its mutual inductance with neighboring conductors.

Consequently, the inductance of the conductor (or conductors) of a cable is a quantity that depends on different parameters related to its geometry, its size and the distance between adjacent conductors. Cabling manufacturers usually disclose in the cable's datasheet a calculated value of the inductance of the cable's conductor (or conductors) under specific conditions and in a specific configuration.

Analytical expressions for the calculation of the inductance of a three-core or three single-core cables are presented in Appendix A.3.

3.3.4 Capacitance and Dielectric Losses of Power Cables

In case of AC power cables having a metallic screen around the conductor, a capacitance is created between the conductor and the screen/sheath and a charging current flow through it, when the cable is energized. The molecules of the material act as electric dipoles and realign each time the direction of the magnetic field changes. The work required for this realignment leads to consumption of power and subsequent heat generation [39]. This power loss is called dielectric loss and is given by the following expression [27]:

$$W_d = 2\pi f C_p U_0^2 \tan\delta \tag{3.3.9}$$

Where:

- W_d: Dielectric loss per m (W/m)

- f: System frequency (Hz)
- C_p: Capacitance per m (F/m)
- U_0: Conductor phase voltage (V)
- $\tan\delta$: Dielectric loss factor ($-$)

The loss factor is given by IEC 60287 for different insulation materials. As with the cable's inductance, cabling manufacturers usually disclose in the cable's datasheet calculated values of the capacitance and the dielectric losses of the cable. The derivation of the dielectric losses relationship and an analytical expression for the calculation of the cable's capacitance are presented in Appendix A.4.

3.3.5 Screen/Sheath and Armour Losses of Power Cables

Screen and armour losses are only applicable for AC cables. It is known that an alternating current flowing through a conductor creates an alternating magnetic field which induces a voltage to conductors located in its proximity. This induced voltage can cause the generation of circulating and eddy currents in the metallic parts of the cable, namely the metallic screen or sheath and the armour in case they are part of a closed circuit loop [12].

Induced circulating currents are produced when the screen/sheath is grounded at both ends of the cable. This is the usual case for three-core cables. Regarding single-core cables, sheath losses depend on the sheath bonding arrangement i.e. the way in which the sheaths of the three single-core cables are linked. Generally, there are three main options: single-point bonding (at the one end of the cables), two-point or solid bonding (at both ends of the cables) and cross bonding (at several points of the cables) [39]. However, when it comes to submarine applications, the common practice is the bonding of the sheaths at both ends [11]. These currents are expressed by the factor $\lambda_1^{'}$.

The eddy currents are locally driven in the screen/sheath as a result of the induced electromotive force (emf) from the AC current flowing through the conductor. Their amplitude is strongly dependent by the thickness of the screen/sheath, while the materials and the geometric factors play also an important role. The loss factor corresponding to the eddy currents is denoted as $\lambda_1^{''}$. In most cases $\lambda_1^{''}$ is less significant than $\lambda_1^{'}$ and can be neglected. The total screen/sheath loss factor is expressed as follows:

$$\lambda_1 = \lambda_1^{'} + \lambda_1^{''} \tag{3.3.10}$$

Similarly, $\lambda_2^{'}$ and $\lambda_2^{''}$ stand for the loss factors because of circulating and eddy currents in the armour of the cable. The total armour loss factor is:

$$\lambda_2 = \lambda_2^{'} + \lambda_2^{''} \tag{3.3.11}$$

Finally, the total AC resistance of the cable at a temperature θ_c can be expressed as a function of the AC resistance of the conductor at the same temperature multiplied by an expression corresponding to the screen/sheath loss and the armour loss factors:

$$R_{AC,t}^{\theta_c} = R_{AC}^{\theta_c}(1 + \lambda_1 + \lambda_2) \tag{3.3.12}$$

Where:

- $R_{AC,t}^{\theta_c}$: Total AC resistance per m of the cable at $\theta_c\,$°C (Ω/m)
- $R_{AC}^{\theta_c}$: AC resistance per m of the conductor at $\theta_c\,$°C (Ω/m)
- λ_1: Loss factor for the sheath or screen $(-)$
- λ_2: Loss factor for the armour $(-)$

IEC 60287 provides analytical expressions for the calculation of the screen/sheath and armour loss factors for several cable types. Indicatively, some of them are disclosed in Appendix A.5. In addition, Appendix A.6 presents the calculation of the screen/sheath and armour resistances which are necessary for the derivation of these loss factors.

3.4 Modeling the Cable Power Losses

3.4.1 Introduction

The goal of the model presented in the following section is to calculate the power losses of a SPC single-core or three-core, AC or DC. The model is developed with certain design criteria:

- High computational speed
- Soil temperature dependency
- Soil thermal resistivity dependency

- Modularity
- Exclusive use of code
- No need of external software

A power cable can be modeled as a transmission line taking into account its own specific electrical characteristics. An overhead transmission line which is less than 240 km long can be modeled by a lumped element pi model as shown in Figure 3.10, [42]. This means that the series impedance (due to line resistance and inductance) as well as the shunt admittance (due to shunt capacitance and conductance) are summed up to single electrical components. The lumped pi model is also applicable for an underground or submarine cable less than 100 km [43].

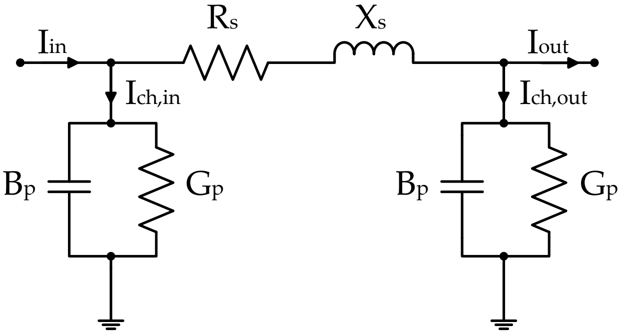

FIGURE 3.10: Lumped element Pi Model of a Power Cable

Transmission lines longer than this limit have to be modeled by means of the distributed element model. According to this model the line parameters are distributed continuously throughout the line and can be regarded as infinitesimal small elements [42].

The proposed model aims to combine the accuracy of the distributed element model and the ease of calculation of the lumped element model. The cable is divided in a number of cable segments. Each segment is modeled as a pi model, as in Figure 3.10.

The core of the model, which calculates the cable power losses, is based on a method derived by Anders and Brakelmann in [28]. The full method developed by Anders and Brakelmann is explained in detail in Appendix A.7.

In the next sections, the operation of the model is explained thoroughly (Section 3.4.2) and the modifications to the Anders and Brakelmann's method are presented (Section 3.4.3). Finally the operation of the model is assessed and its capabilities are shown through examples in Section 3.4.4.

3.4.2 Model

Anders and Brakelmann model the cable power losses as a function of the conductor current and some parameters linked to the nominal loading conditions while considering the impact of temperature. Starting from equation 3.3.2 Anders and Brakelmann derived the following expression for the calculation of the cable's losses:

$$W_t = W_d + W_{I,R}\left(\frac{I_c}{I_{c,R}}\right)^2 v_\theta \tag{3.4.1}$$

Where:

- W_t: Total losses per m (W/m)
- W_d: Dielectric losses per m (W/m)
- $W_{I,R}$: Nominal ohmic losses per m (W/m)
- I_c: RMS current of the conductor (A)
- $I_{c,R}$: Nominal RMS current of the conductor (A)
- v_θ: Temperature coefficient $(-)$

This expression corresponds to a cable under AC loading but the same methodology can be applied for a DC cable by eliminating the AC specific variables (capacitive and inductive reactances, screen/sheath and armour loss factors, dielectric losses).

Two consequent cable segments are presented in Figure 3.11. It is seen that the current and voltage at the output of the first segment are the input current and input voltage respectively for the second segment. However, variables such as the length of the segment, the temperature of its surroundings or the thermal resistivity of the soil around it, are related only to the specific segment. The inputs and outputs of the model are summarized in Tables 3.2 and 3.3 respectively.

The calculations performed by the model are summarized in Figure 3.12. Firstly, an analysis of the electrical circuit is realized. The susceptance due to the shunt capacitance and the reactance due to the series inductance of the segment are calculated:

$$B_p = 2\pi f(C_p/2)s \tag{3.4.2}$$

$$X_s = 2\pi f L_s s \tag{3.4.3}$$

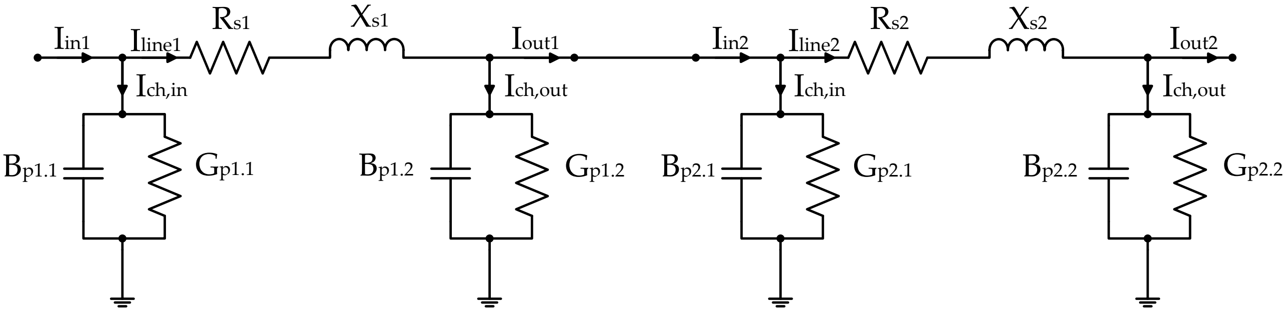

FIGURE 3.11: Two adjacent cable segments

Model Inputs	
$\overline{V}_{in}$	Phase voltage at the input (V)
$\overline{I}_{in}$	Current at the input (A)
C_p	Capacitance of the cable per m (F/m)
L_s	Inductance of the cable per m (H/m)
R_{AC20}	AC resistance of the conductor at 20 °C (Ω/m)
a_{20}	Constant mass temperature coefficient at 20 °C (K^{-1})
s	Length of the cable segment (m)
f	Frequency of the system (Hz)
$tan(\delta)$	Dielectric loss factor ($-$)
$I_{c,Rprel}$	Preliminary value of the rated current of the cable (A)
$\theta_{c,Max}$	Maximum operating temperature of the conductor (°C)
$\theta_{c,Amb}$	Temperature of the soil (°C)
ρ_{moist}	Thermal resistivity for moist soil ($K\ m/W$)
ρ_{dry}	Thermal resistivity for dry soil ($K\ m/W$)
$\Delta\theta_{cr}$	Critical temperature rise of the soil (K)
λ_1	Loss factor for the sheath or screen ($-$)
λ_2	Loss factor for the armour ($-$)
T_1	Thermal resistance per m between one conductor and the sheath ($K\ m/W$)
T_2	Thermal resistance per m between the sheath and the armour ($K\ m/W$)
T_3	Thermal resistance per m of the external serving of the cable ($K\ m/W$)
T_4	Thermal resistance per m between the cable surface and the surrounding medium ($K\ m/W$)

TABLE 3.2: Model Inputs

Model Outputs	
$\overline{V}_{out}$	Phase voltage at the output (V)
$\overline{I}_{out}$	Current at the output (A)
P_{out}	Real Power at the output (W)
Q_{out}	Reactive Power at the output (VAr)
P_{loss}	Power losses of the cable segment (W)
θ	Conductor temperature (°C)
$I_{c,R}$	Rated current of the cable (A)

TABLE 3.3: Model Outputs

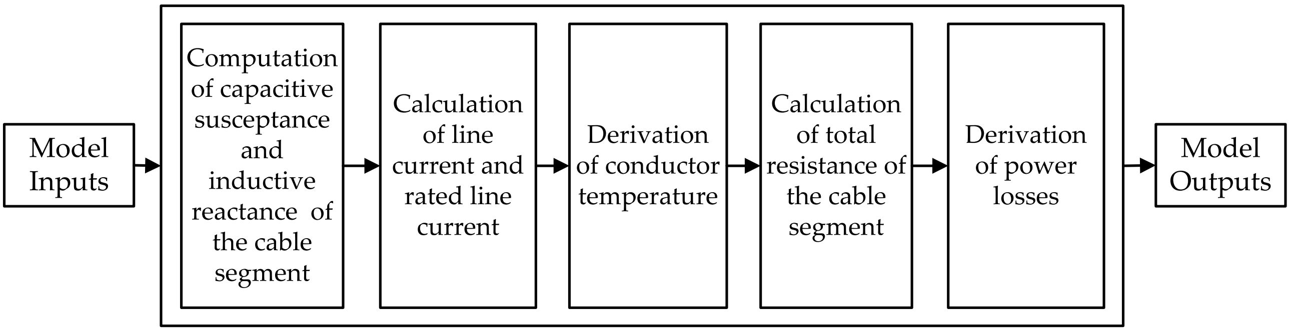

FIGURE 3.12: Procedure of model calculations

Where:

- B_p: Shunt susceptance of the cable segment (Ω)
- f: System's frequency (Hz)
- C_p: Shunt capacitance per m of the cable segment (F/m)
- s: Length of the cable segment (m)
- X_s: Reactance of the cable segment (Ω)
- L_s: Inductance per m of the cable segment (H/m)

The capacitance is divided by two because the half of it is considered to be connected at the input branch and the other half at the output branch of the pi model. Then, the charging current, that flows at the input shunt branch of the pi model, and the current which flows through the series impedance are determined:

$$\overline{I}_{ch,in} = B_p V_{in}\sqrt{1+(\tan\delta)^2}\angle\phi_{\overline{V}_{in}} + \pi/2 - \delta \tag{3.4.4}$$

$$\overline{I}_c = \overline{I}_{in} - \overline{I}_{ch,in} \tag{3.4.5}$$

Where:

- $\overline{I}_{ch,in}$: Charging current (A)
- $\overline{B}_p$: Shunt susceptance of the cable segment (Ω)
- V_{in}: Magnitude of input voltage (V)
- $\tan\delta$: Dielectric loss factor $(-)$

- $\phi_{\overline{V}_{in}}$: Angle of input voltage (rad)
- δ: Dielectric loss angle (rad)
- $\overline{I}_c$: Conductor current (A)
- $\overline{I}_{in}$: Input current (A)

Then, the rated current of the cable segment is calculated by an iterative method (Figure 3.13). Initially, an estimation for the rated current is made. For example, the value of the rated current given by the manufacturer can be used as a starting point. Then it is determined whether there is soil drying-out or not and the respective equation is used for a more accurate calculation of the rated current that corresponds to the specific properties of the surroundings. This new value of the rated current is used again to check if there is drying-out or not and the procedure starts again. After some iterations an accurate value of the rated current is derived.

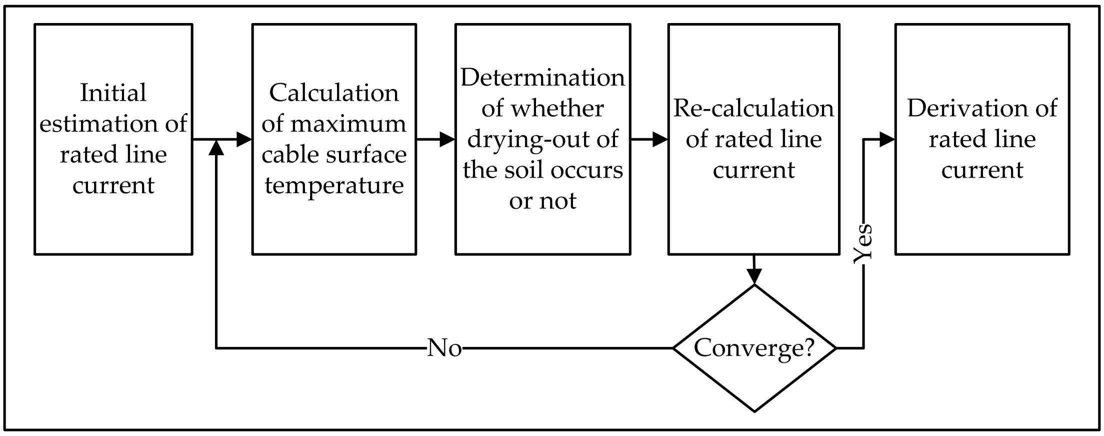

Figure 3.13: Calculation of the rated current

Consequently, for calculating the total phase impedance, the value of the phase resistance of the cable is needed. This means that the temperature of the conductor has to be calculated. The procedure is summarized in Figure 3.14.

Firstly the cable surface temperature is calculated for the rated current. If there is no drying-out for the rated current then this is the case for the whole range of current. Knowing that there is no drying-out the conductor temperature for current I_c is calculated.

In case there is soil drying-out for the rated current, it has to be identified if there is drying-out for current I_c or not. The potential soil drying-out for current I_c is identified through a slightly altered version of the equation 3.3.2 which is the following:

$$I_c = \left[\frac{\Delta\theta_c - W_d \left[\frac{1}{2}T_1 + n(T_2 + T_3)\right]}{R_{AC}^{\theta_c}T_1 + nR_{AC}^{\theta_c}(1+\lambda_1)T_2 + nR_{AC}^{\theta_c}(1+\lambda_1+\lambda_2)(T_3)} \right]^{0.5} \tag{3.4.6}$$

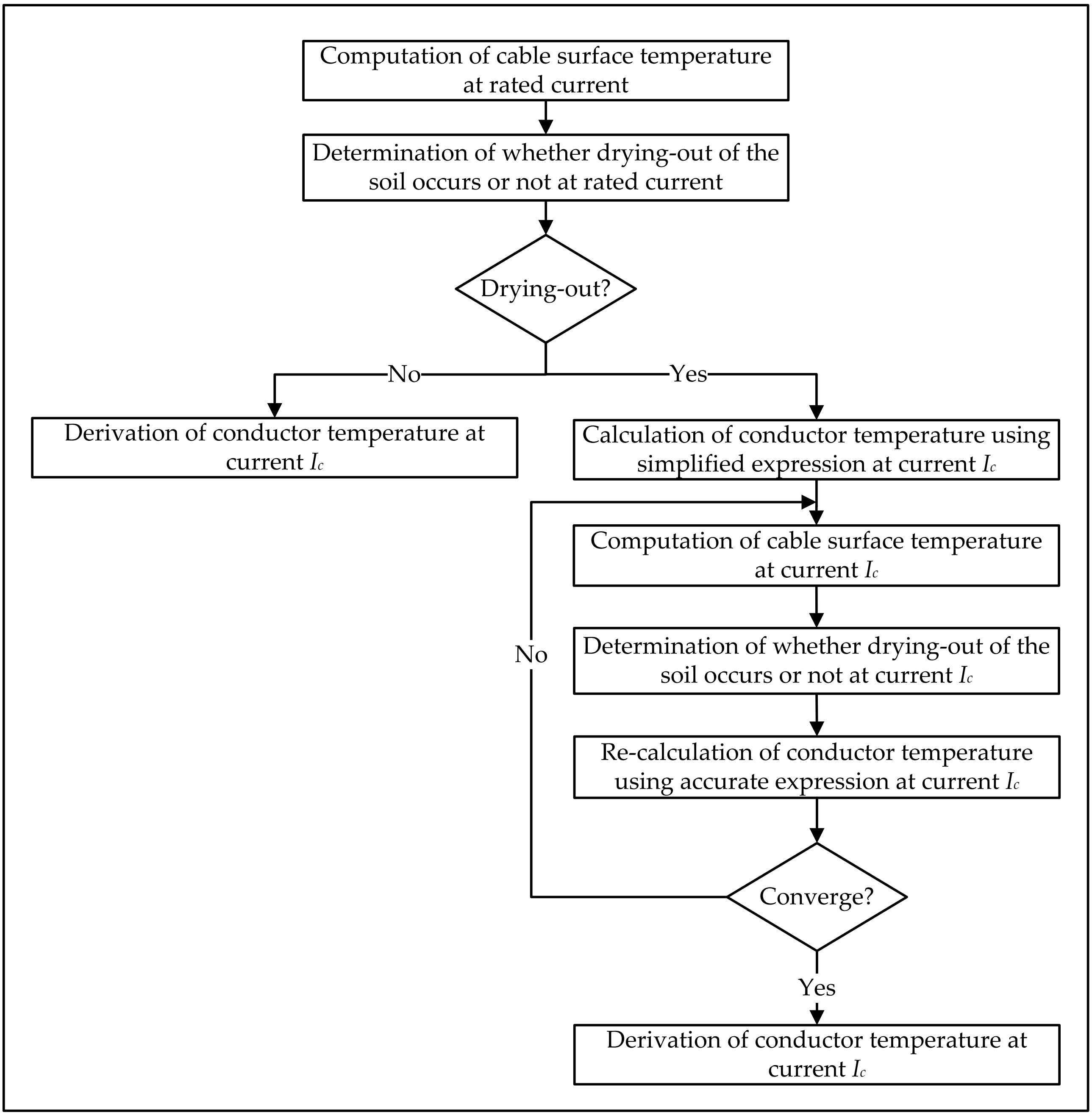

FIGURE 3.14: Calculation of the conductor temperature

The difference in this equation is that the thermal resistance of the surrounding soil T_4 is not included and therefore the temperature rise $\Delta\theta_c$ corresponds to the difference between the conductor temperature and the external cable surface temperature. By calculating the cable surface temperature the temperature difference between the cable surface and the surrounding soil can be compared to the critical temperature difference above which drying-out occurs. Evidently, this calculation can be easily realized for the rated current since the conductor temperature for rated conditions is known. However a problem appears regarding the cable surface temperature calculation at a different current. As it is seen from the equation 3.4.6 the conductor temperature, which is the initial calculation objective, is needed.

For this reason, the cable surface temperature for current I_c is determined using an iterative method. An estimation for the conductor temperature is made by using a simple equation [44]:

$$\theta_c = \theta_{c,Amb} + (\theta_{c,Max} - \theta_{c,Amb})\left(\frac{I_c}{I_{c,R}}\right)^2 \tag{3.4.7}$$

Where:

- θ_c: Conductor temperature (°C)
- $\theta_{c,Amb}$: Ambient soil temperature (°C)
- $\theta_{c,Max}$: Maximum operating temperature (°C)
- I_R: Rated current of the cable (A)

The value of the conductor temperature calculated using the above equation is used for the determination of the cable surface temperature. Then it is determined whether drying-out occurs or not. Consequently, the more sophisticated expression of Anders and Brakelmann (A.7.28 in Appendix A.7) is used for the conductor temperature and the calculation sequence is repeated. This procedure accomplishes an accurate calculation of the conductor temperature by taking into account a potential soil drying-out.

Another issue is the fact that the value of the dielectric losses is also required for the calculations of the conductor temperature and hence the phase impedance. As it is seen from equation A.4.6, the dielectric losses are determined using the voltage magnitude across the capacitance. However, since the phase impedance is not known, the voltage at the output branch cannot be calculated. This can be easily solved by taking that the total capacitance of the cable segment is connected at the input branch of the pi model. This alteration introduces a negligible error especially in case the length of the cable segment is small.

Having acquired an accurate value for the conductor temperature, the total phase impedance can be determined:

$$R_s = R_{AC}^{20}[1 + \alpha_{20}(\theta_c - 20)](1 + \lambda_1 + \lambda_2)s \tag{3.4.8}$$

$$\overline{Z}_t = R_s + jX_s \tag{3.4.9}$$

Where:

- R_s: Total AC resistance of the cable segment at θ_c °C (Ω)

- R_{AC}^{20}: AC resistance per m of the conductor at 20 °C (Ω/m)
- α_{20}: Constant mass temperature coefficient of copper at 20 °C (K^{-1})
- θ_c: Temperature of the conductor (°C)
- λ_1: Screen/sheath loss factor ($-$)
- λ_2: Armour loss factor ($-$)
- s: Length of the cable segment (m)
- $\overline{Z}_t$: Total series impedance of the cable segment (Ω)
- X_s: Reactance of the cable segment (Ω)

Then, the voltage and the current at the output can be derived:

$$\overline{V}_{out} = \overline{V}_{in} - \overline{I}_c \overline{Z}_t \tag{3.4.10}$$

$$\overline{I}_{ch,out} = B_p V_{out} \sqrt{1 + (\tan\delta)^2} \angle \phi_{\overline{V}_{out}} + \pi/2 - \delta \tag{3.4.11}$$

$$\overline{I}_{out} = \overline{I}_c - \overline{I}_{ch,out} \tag{3.4.12}$$

Furthermore the active and reactive power at the output of the pi model are calculated:

$$P_{out} = V_{out} I_{out} \cos\varphi \tag{3.4.13}$$

$$Q_{out} = V_{out} I_{out} \sin\varphi \tag{3.4.14}$$

Where:

- $\overline{V}_{out}$: Output voltage (V)
- $\overline{I}_{ch,out}$: Output charging current (A)
- V_{out}: Magnitude of output voltage (V)
- $\phi_{\overline{V}_{out}}$: Angle of output voltage (rad)
- $\overline{I}_{out}$: Output current (A)
- I_{out}: Magnitude of output current (A)

- P_{out}: Real Power at the output (W)
- ϕ: Power angle (rad)
- Q_{out}: Reactive Power at the output (VAr)

Finally, the total power losses of the cable segment are determined by using the equation 3.4.1.

3.4.3 Alterations in Anders and Brakelmann's Methodology

The two iteration procedures for the calculation of the rated current and the conductor temperature (Figures 3.13 and 3.14 respectively) are the main modifications to Anders and Brakelmann's methodology. The implementation of these two procedures eliminates the need of using any additional software.

More specifically, regarding the rated current of the cable, its value can be derived through equation 3.3.2 or 3.3.3 for AC loading and 3.3.4 or 3.3.5 for DC loading. It is clear that these equations require knowing whether drying-out of the soil occurs or not. This can be determined only if the rated current is known, which leads to a calculation deadlock. Anders and Brakelmann use a standard cable rating software to determine the rated current. However this can be avoided by making an initial estimation of the segment rated current and by using the first iterative method.

A similar problem also rises regarding the calculation of the conductor temperature. According to the method presented by Anders and Brakelmann, it is necessary to know whether drying-out of the soil for a current I_c occurs or not to calculate the conductor temperature and the cable losses. But this requires the conductor temperature leading again to a calculation deadlock. In order to overcome this issue, Anders and Brakelmann propose two options. Either a standard rating software can be used to determine the current for which drying-out of the soil occurs, or the concept of soil drying-out can be assumed that does not occur at all [28]. The model presented here, shifts this limitation by making an initial estimation of the conductor temperature corresponding to current I_c and by using the second iterative.

3.4.4 Model Assessment

To assess the alterations to the model, the example of the Anders and Brakelmann paper is reproduced. In addition, the same cable is used to show the response of the model to changes of the cable surroundings (type and temperature of soil). Finally, the difference between AC and DC loading is presented.

Anders and Brakelmann used a 145 kV three-core armoured cable with XLPE insulation. The soil properties used for the example are listed in Table 3.4 and the characteristics of the cable are summarized in Table 3.5.

Soil Properties		
Variable	Unit	Value
$\theta_{c,Amb}$	(°C)	15
$\Delta\theta_{cr}$	(K)	35
ρ_{moist}	$(K\ m/W)$	0.6
ρ_{dry}	$(K\ m/W)$	1.8

Table 3.4: Soil Properties of Numerical Example [28]

Cable Properties		
Variable	Unit	Value
$I_{c,R}$	(A)	966
C_p	$(\mu F/km)$	0.236
L_s	$(\mu H/km)$	0
$R_{AC}^{\theta_{c,Max}}$	(Ω/km)	0.033
λ_1	$(-)$	0.123
λ_2	$(-)$	0.210
T_1	$(K\ m/W)$	0.754
T_2	$(K\ m/W)$	0.040
T_3	$(K\ m/W)$	0.047
T_4	$(K\ m/W)$	0.299
W_d	(W/m)	0.52

Table 3.5: Cable Properties of Numerical Example [28]

The values of the model inputs are summarized in Table 3.6. The power factor is assumed equal to unity, therefore the angles of the input voltage and current are zero. The inductance is assumed to be equal to zero as according to the example. The conductor AC resistance at 20 °C can be calculated from the AC resistance at the maximum operating temperature (90 °C for the XLPE insulation). The constant mass temperature coefficient is given by IEC 60287 for copper. The frequency of the system is 50 Hz while the dielectric loss factor is also given by IEC 60287 and it is equal to 0.001 for cables over 18/30 kV using unfilled XLPE as insulation. The preliminary value of the rated current is needed for the iterative procedure in the model and is assumed equal to 700 A. This proved not to have an impact on the calculations since a wide range of values have been given as inputs, both lower and higher than the 966 A of the example and the iterative method converged to the same value of the rated current. The maximum operating temperature is 90 °C. The soil properties remain the same as in the example. Finally, the sheath/screen and the armour factors as well as the values of the thermal resistances are also given in the example.

The model calculates the rated current equal to 966.32 A which is practically the same as the example of Anders and Brakelmann. In addition the same graphs which are presented in their

Model Inputs		
Variable	Unit	Value
$\overline{V_{in}}$	(kV)	$145/\sqrt{3}$
$\overline{I_{in}}$	(A)	miscellaneous
C_p	$(\mu F/km)$	0.236
L_s	$(\mu H/km)$	0
R_{AC}^{20}	(Ω/km)	0.0258
α_{20}	(K^{-1})	3.9310^{-3}
s	(m)	1
f	(Hz)	50
$tan(\delta)$	$(-)$	0.001
I_{Rprel}	(A)	700
$\theta_{c,Max}$	(°C)	90
$\theta_{c,Amb}$	(°C)	15
ρ_{moist}	$(K\ m/W)$	0.6
ρ_{dry}	$(K\ m/W)$	1.8
$\Delta\theta_{cr}$	(K)	35
λ_1	$(-)$	0.123
λ_2	$(-)$	0.210
T_1	$(K\ m/W)$	0.754
T_2	$(K\ m/W)$	0.040
T_3	$(K\ m/W)$	0.047
T_4	$(K\ m/W)$	0.299

TABLE 3.6: Model Inputs of Numerical Example [28]

paper are reproduced for a direct comparison. The graphs of the total three-phase losses are given in Figures 3.15A and 3.15B. For the rated current, Anders and Brakelmann report total losses equal to 124.58 W/m while the proposed model calculated 124.3 W/m. The model is also accurate for currents lower than the rated one as it is seen by comparing the two graphs.

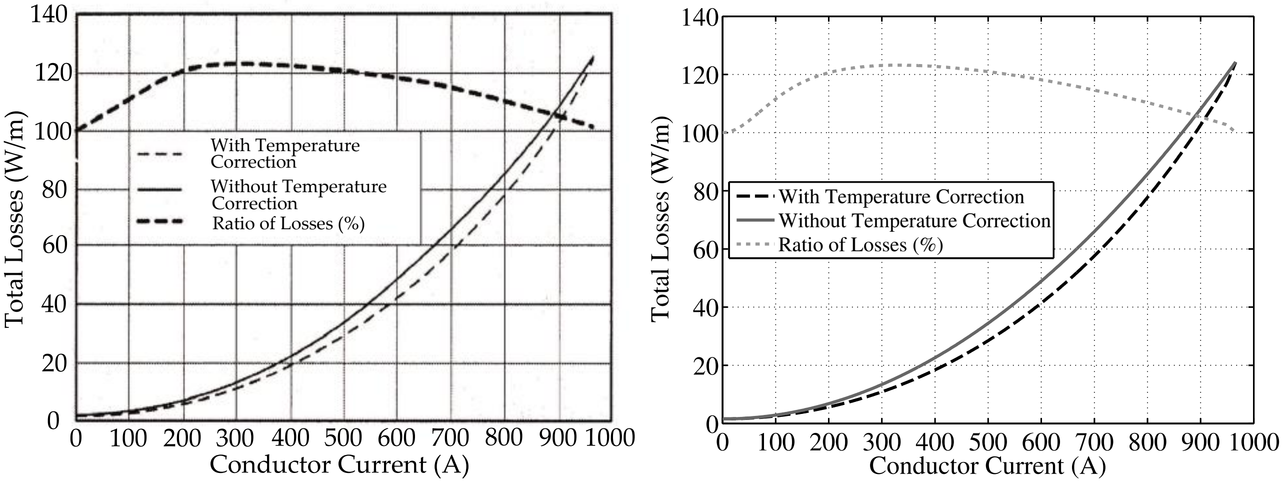

(A) (B)

FIGURE 3.15: Total 3-phase losses (W/m): (A) Anders and Brakelmann (B) Matlab Model

Another point of comparison is the variation of the conductor temperature with respect to the conductor current. According to Anders and Brakelmann calculations, when the cable is just energized and no current is flowing, the conductor temperature is 15.8 °C due to the present dielectric losses. This value has been confirmed by the proposed model. At rated current the conductor temperature rises to its maximum operational, 90 °C. The conductor temperature at currents close to the rated one, is a result of the effect of the soil drying-out. The higher thermal soil resistivity leads to a decrease of the heat dissipation rate and a subsequent increase of the temperature rate.

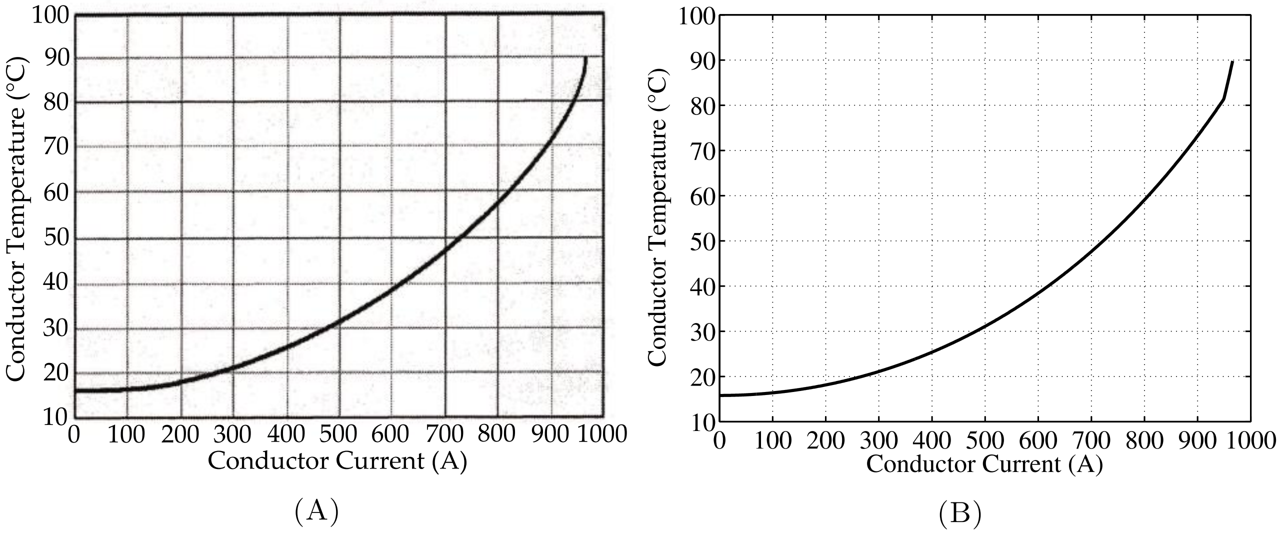

(A)

(B)

FIGURE 3.16: Conductor temperature (°C): (A) Anders and Brakelmann (B) Matlab Model

The response of the model to changes of the characteristics of its surroundings can also be verified by applying the model for different soil temperatures and thermal resistivities. The conductor temperature rise for three ambient temperature values (10 °C, 15 °C and 20 °C is presented in Figure 3.17A, while the comparative graph of the total three-phase losses that correspond to these temperatures is shown in Figure 3.17B.

The conductor temperature is higher than the ambient temperature when no current flows through the cable due to the dielectric losses. As the cable current increases, the conductor temperature rises in a similar way for all three cases until it reaches its maximum temperature. The cable can be loaded with a larger current when the soil temperature is lower. In addition, a lower soil temperature causes drying-out of the soil to occur at a higher loading. This happens since a larger current is required in order the the cable to reach its critical temperature difference, above which drying-out occurs.

Regarding the losses graph, it is seen that the losses decrease when the ambient temperature is lower. This is logical due to the fact that the ohmic resistance of the cable is larger at higher temperatures. In addition, the cable's rated current increases when the soil temperature is lower.

A similar test is realized for the thermal resistivity of the soil. Some typical values of the thermal resistivity of common submarine soils are summarized in Table 3.7 [11]. The thermal resistivity of the wet soil in the example of Anders and Brakelmann is equal to 0.6 $K\ m/W$ which most

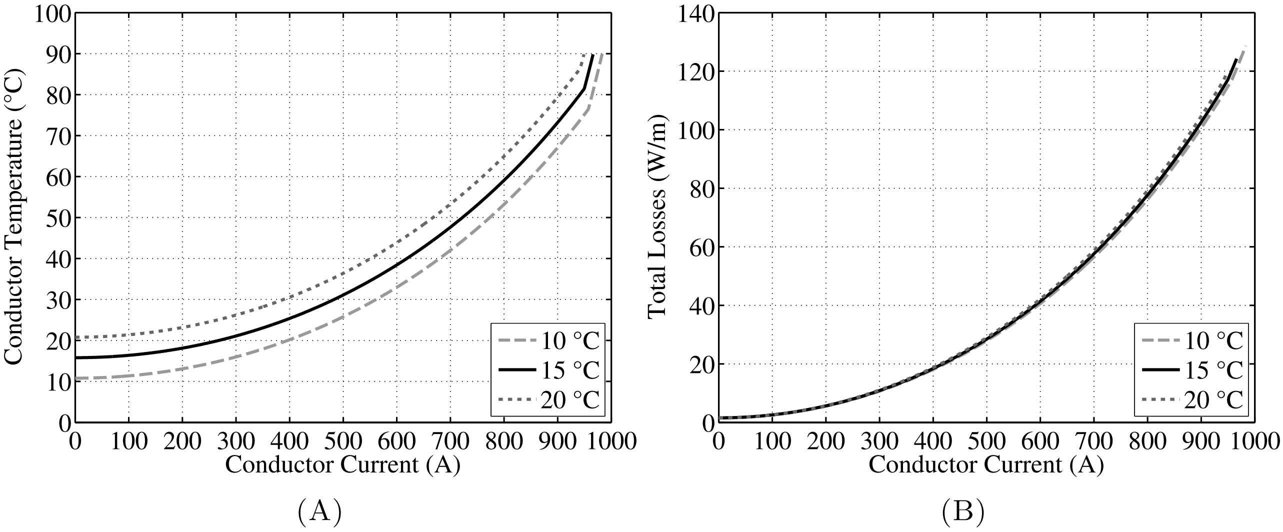

Figure 3.17: Impact of ambient temperature (A) Conductor temperature (°C) (B) Total 3-phase losses (W/m)

Thermal resistivity of some submarine soils ($K\ m/W$)	
Gravel	$0.33 - 0.55$
Sand	$0.2 - 0.67$
Clay/silt	$0.56 - 2.5$

Table 3.7: Thermal resistivity of some submarine soils [11]

probably relates to a sandy soil. Two other values for the soil resistivity (0.33 $K\ m/W$ i.e. gravel and 1.8 $K\ m/W$ i.e. clay) are chosen to compare with the initial example. It is assumed that the corresponding dry soil resistivity is three times higher than the one of the moist soil as in the example of Anders and Brakelmann. A different soil thermal resistivity leads to a change of the thermal resistance of the surroundings T_4.

	Thermal resistivity (moist) ($K\ m/W$)	**Thermal resistivity (dry)** ($K\ m/W$)	**Thermal resistance** ($K\ m/W$)
Gravel	0.33	0.99	0.164
Sand	0.6	1.8	0.299
Clay/silt	1.8	5.4	0.897

Table 3.8: Thermal resistivities of example cases

The conductor temperature variation with respect to the current of the cable is displayed in Figure 3.18A for the three types of soil, while the comparison of losses for the three cases is shown in Figure 3.18B. It is seen that the larger thermal resistivity of the soil leads the conductor to reach its maximum operating temperature at a lower current since it's more difficult to dissipate heat. In addition the drying-out of the soil begins at lower temperature. Furthermore, a larger soil thermal resistivity corresponds to a higher conductor temperature for the same current.

The fact that the ohmic resistance of the cable is larger at higher temperatures leads to higher losses.

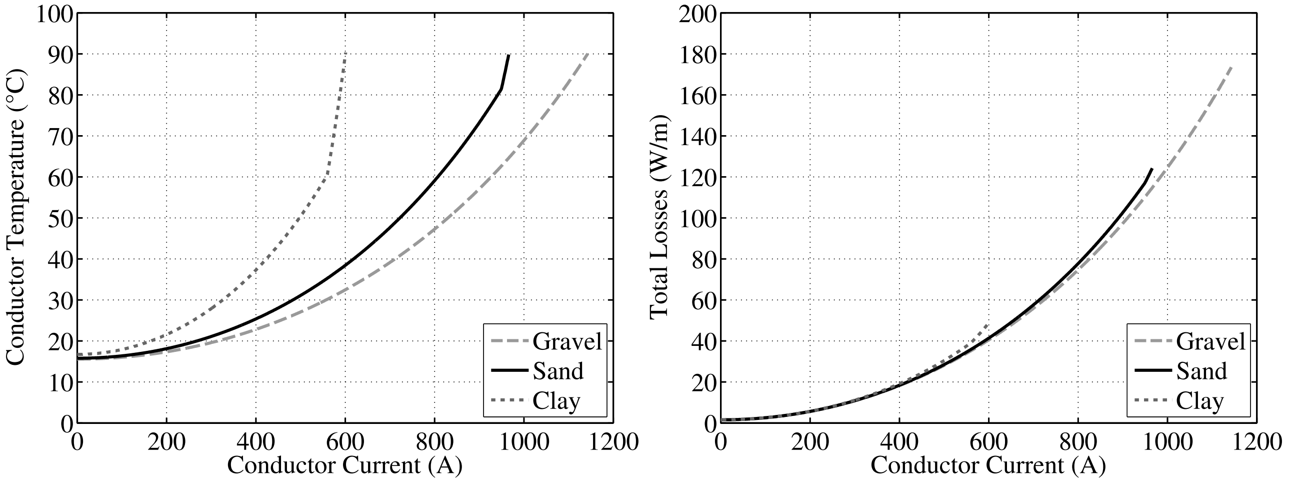

(A) (B)

Figure 3.18: Impact of type of soil (A) Conductor temperature (°C) (B) Total 3-phase losses (W/m)

Finally, a last test shows the difference between AC and DC loading. The AC related variables (capacitive and inductive reactances, screen/sheath and armour loss factors, dielectric losses) are deactivated. In this way, the model calculated the power losses of the cable under DC loading. In reality, three-core cables are only employed for AC transmission. However, the same cable is used under DC loading in order to evaluate the impact on the losses on equal terms.

The conductor temperature variation with respect to the current of the cable is displayed in Figure 3.19A and the comparison of losses for the two cases is shown in Figure 3.19B. It is seen that the temperature of the conductor is lower under DC loading. This is expected since under DC loading less heat is generated, since the DC resistance is lower than the AC resistance and there are no dielectric losses. In fact, under DC loading, the cable surface temperature never exceeds the critical temperature above which drying out occurs. This is why there is no change in the slope of the DC loading curve. Furthermore, because of the lower amount of generated heat, the rated DC current is higher. The losses are higher under AC loading. The absence of the skin and proximity effects' impact as well as the lack of screen/sheath and armour losses results to a lower conductor resistance under DC. Finally, the dielectric losses are null under DC loading. This is also evident from the fact that the losses under DC loading are zero for zero current.

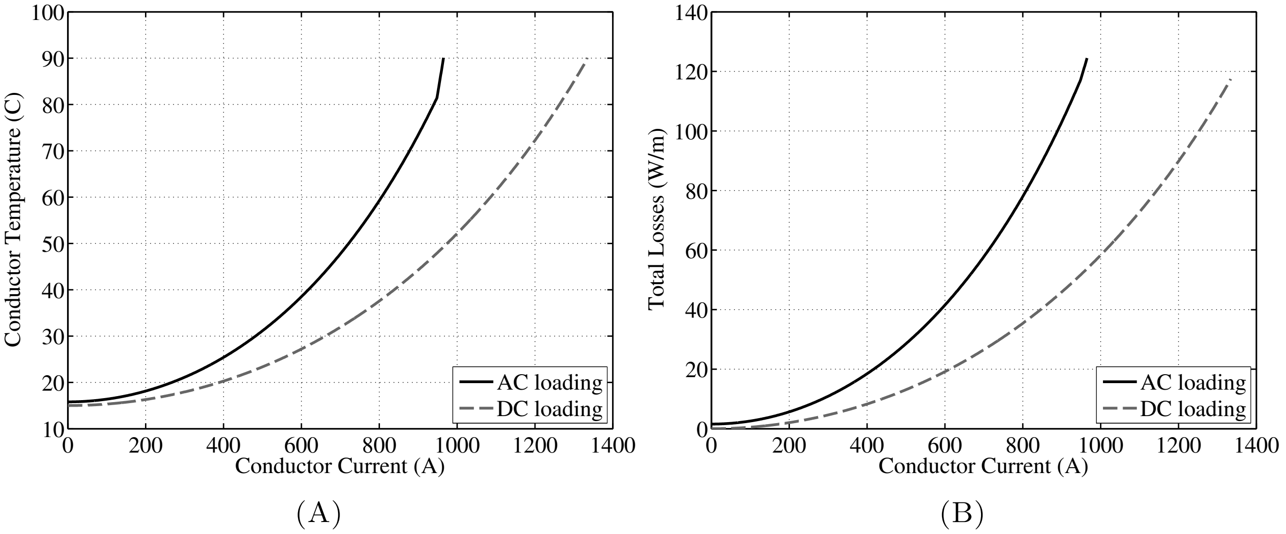

(A) (B)

FIGURE 3.19: Impact of loading (A) Conductor temperature (°C) (B) Total losses (W/m)

Chapter 4

Modular Multilevel Converters

4.1 Introduction

Until recently, OWFs were deployed at locations closer to the shore and HVAC cables were used for the transmission of power to the inland grid. However as OWFs are installed further from shore limitations arise regarding the use of HVAC transmission: long submarine and underground HVAC cables require reactive power compensation which sometimes is cumbersome to be implemented.

Therefore, the HVDC transmission seems a more feasible option for long distances. Indeed, recent studies indicate that the HVDC transmission is economically more efficient than the HVAC alternative for distances above 70 km [29] while the industry seems to choose HVDC for distances longer than 40 km and capacities larger than 200 MW (Figure 2.8F). In this context, the converters required for HVDC transmission come to the fore and become the object of intense study.

The HVDC converter technology can be divided into two main categories: the conventional Line Commutated Converters (LCC) and the relatively novel Voltage Source Converters (VSC).

In Section 4.2, after a brief introduction to the two technologies, an overview of the different types of multilevel converters is given. Consequently, it is explained why the topology of the MMC was modeled in this thesis. Then, the structure and the steady-state operation principle of the MMC is presented in Section 4.3. Finally, the model for the calculation of the power losses of a MMC is presented and assessed in Section 4.4.

4.2 Converter Technologies for HVDC Applications

4.2.1 Line Commutated Converters (LCC)

The LCC is regarded as the traditional HVDC converter technology since its first application was in 1954 [29] and its wider introduction during the 1970s [45]. The term line commutated indicates that the converter relies on the line voltage of the AC system to perform the commutation from one switching device (thyristor) to its adjacent one.

Figure 4.1 shows an LCC in its most basic form which is a 6-pulse bridge of thyristors also known as a Graetz bridge. However, because the Graetz bridge generates harmonic distortion at both the DC and AC terminals an alternative configuration is used in practice: a 12-pulse bridge which connects two 6-pulse bridges in parallel on the AC side and in series on the DC side (see Figure 4.2). The two bridges are phase shifted 30 degrees on the AC side, using transformers with two different secondary windings. Usually, the winding connected to the one bridge is wye-connected while the other is delta-connected [16].

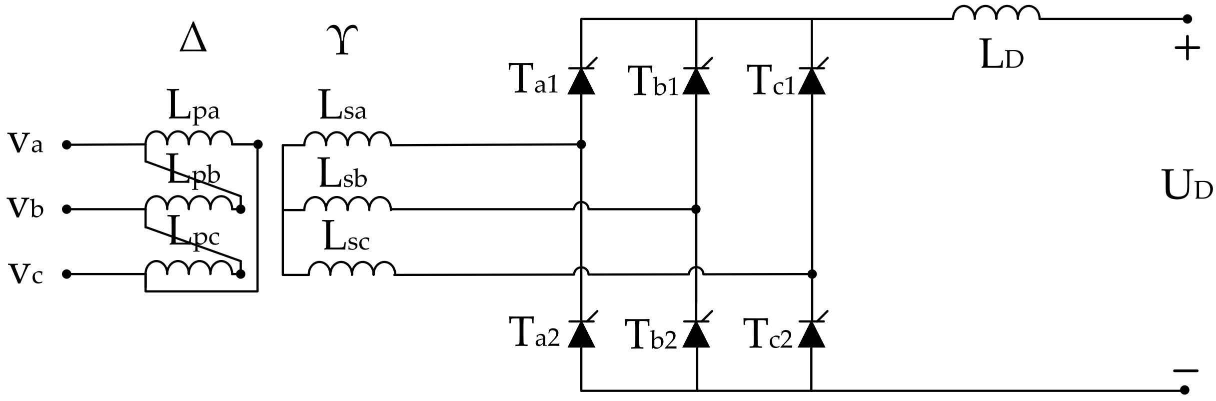

Figure 4.1: Three-phase full-wave rectifier or Graetz bridge [16]

The LCC is still the technology that can achieve the highest power levels making it the most suitable for bulk power transmission. In addition, LCCs are extremely efficient presenting losses of approximately 0.7% per converter [45]. However, the LCCs have a number of disadvantages. First of all, as already mentioned, the switching of thyristors rely on the external AC system, requiring the AC system, to which the HVDC converter is connected, to always contain synchronous machines in order to provide the commutating voltage [45]. Moreover, both in inverter and rectifier modes, the converter absorbs a varying amount of reactive power from the grid, rising the need for adjustable reactive compensation [45].

In addition, the current direction is fixed, therefore the only way of reversing the direction of power flow is by changing the voltage polarity. Consequently, XLPE cables cannot be used in combination with LCCs since they do not have the ability of handling the stress originated from

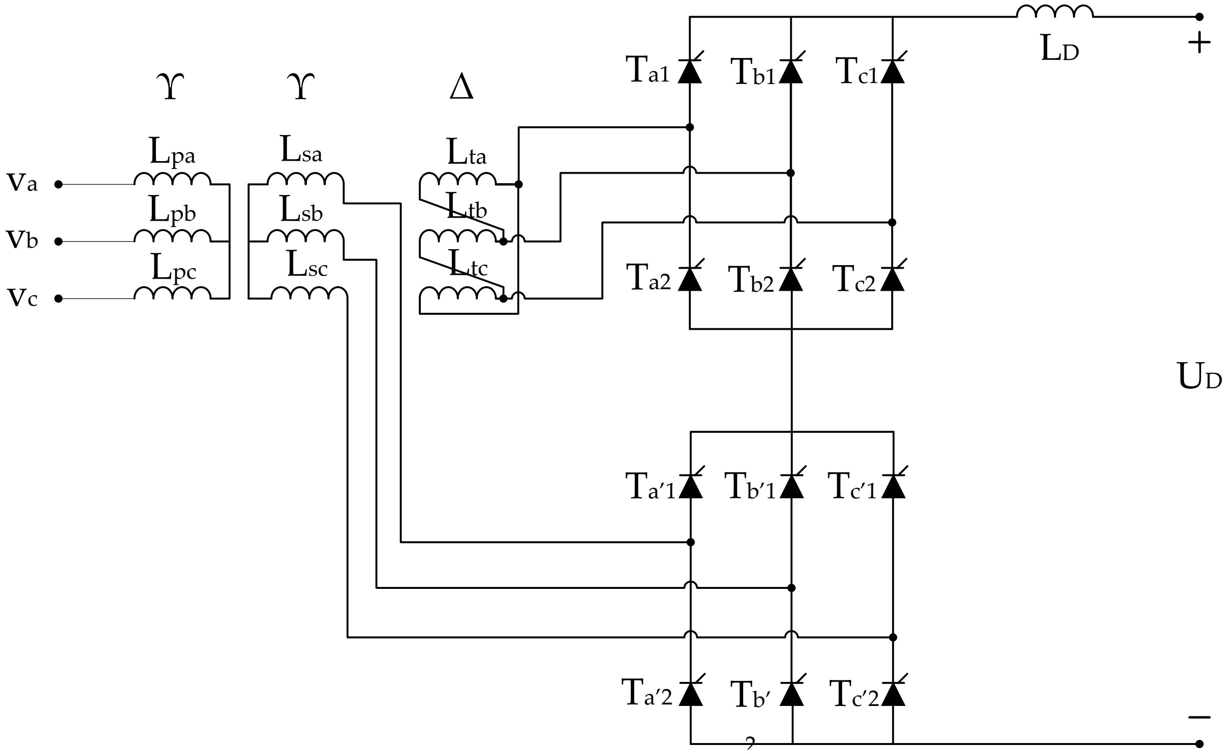

FIGURE 4.2: Three-phase 12-pulse rectifier configuration [16]

the change of voltage polarity [29]. Instead, mass impregnated cables are employed which are heavier, larger and more expensive [45]. Finally, LCCs usually have a minimum active power output 5% below rated power which makes them unsuitable for power transmission applications where there are large variations of the transmitting power such as an OWF [45].

4.2.2 Voltage Source Converters (VSC)

The VSCs were introduced in 1997 by ABB [29] [45]. The major difference between the VSCs to and LCCs is that their switching devices are Insulated Gate Bipolar Transistors (IGBTs) which unlike thyristors are self-commutated and can be switched on and off by a control signal. The term voltage-source converter is assigned to this type of converters because the voltage at the DC side has fixed polarity and is usually constant since it is smoothed by a large capacitance. This type of converters allow fast and decoupled control of bidirectional active and reactive power flow [29]. Consequently, no reactive power compensation is needed which leads to a more compact station configuration in comparison with a LCC [45]. Furthermore, a VSC can handle the full range of active power, giving the ability of black starting and making it suitable for power transmission of varying magnitude [29] [45]. Finally, instead of changing the voltage polarity as with LCCs, power flow reversal with VSCs is realized by changing the current direction. Therefore, XLPE cables can be employed in HVDC systems with VSCs [29].

The first VSCs were two or three level systems meaning that they could generate two 4.3 or three voltage levels at the AC side. The main disadvantages of these VSCs are the high switching losses, the significant insulation requirements of the adjacent transformer, as well as the need of substantial filtering. In addition, in order the switching valves to be able to handle high voltage levels, several IGBTs have to be connected in series and be switched simultaneously. This is a challenging task and requires sophisticated gate drive circuits [45]. The efficiency of such converters is in the range of 98% [29].

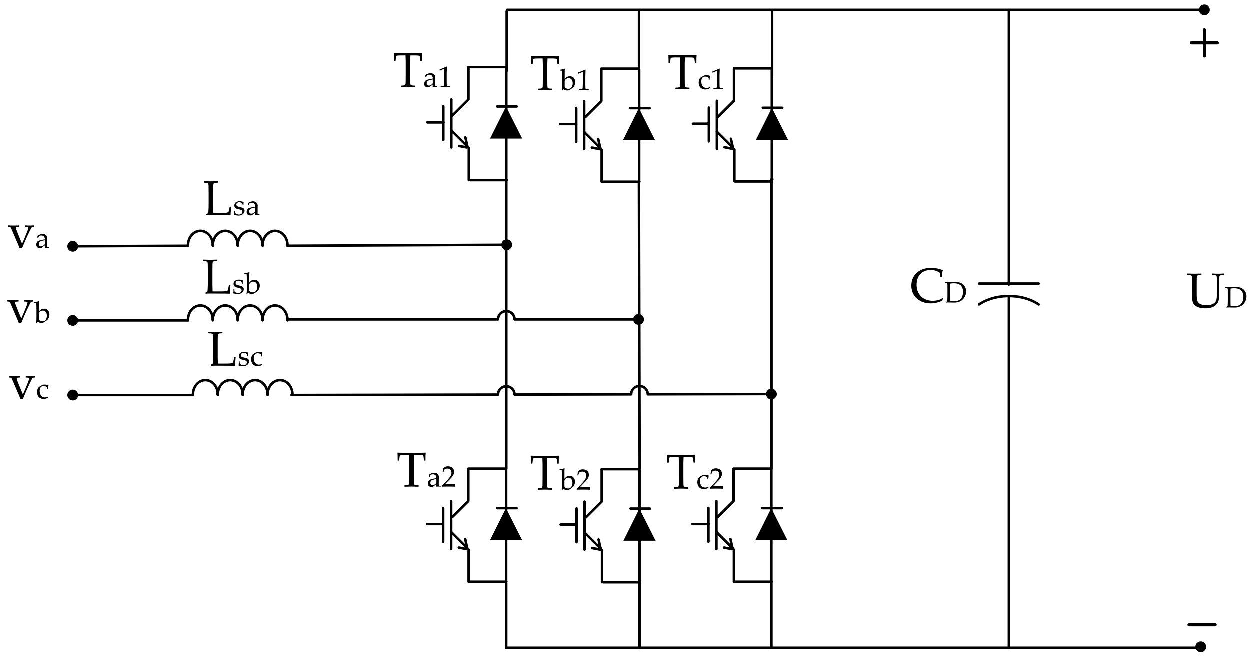

Figure 4.3: Three-phase 2-level voltage source converter configuration [16]

4.2.3 Multilevel Converters

The need to improve the voltage waveform and reduce switching losses of the traditional VSCs configurations has led to the development of multilevel converters. Several different configurations of multilevel converters have been developed. Some of the most well known are the Diode Clamped Converter (DCC), the Flying Capacitor Converter (FCC) and the Cascaded H-Bridge Converter (CHB) [16]. However, all of them present some limitations regarding bulk power transmission, which were overcome with the introduction of the Modular Multilevel Converter (MMC). In the last years, some hybrid systems, that combine the MMC with the traditional two-level VSC, have been proposed [17].

A brief overview of the different types of converters are presented in the next sections.

4.2.3.1 The Diode Clamped Converter (DCC)

The Diode Clamped Converter, in its 3-level version, was introduced in 1981 by Nabae, Takahashi and Akagi [16]. A 6-level inverter is given in Figure 4.4. The three phases of the inverter share a common DC bus, which is divided in six levels by five capacitors. Thanks to the clamping diodes the voltage across each IGBT is equal to the capacitors' voltage. In general, a n-level DCC has $n-1$ capacitors on the DC bus and can produce n-level output phase voltage and $(2n-1)$-level output line voltage [16].

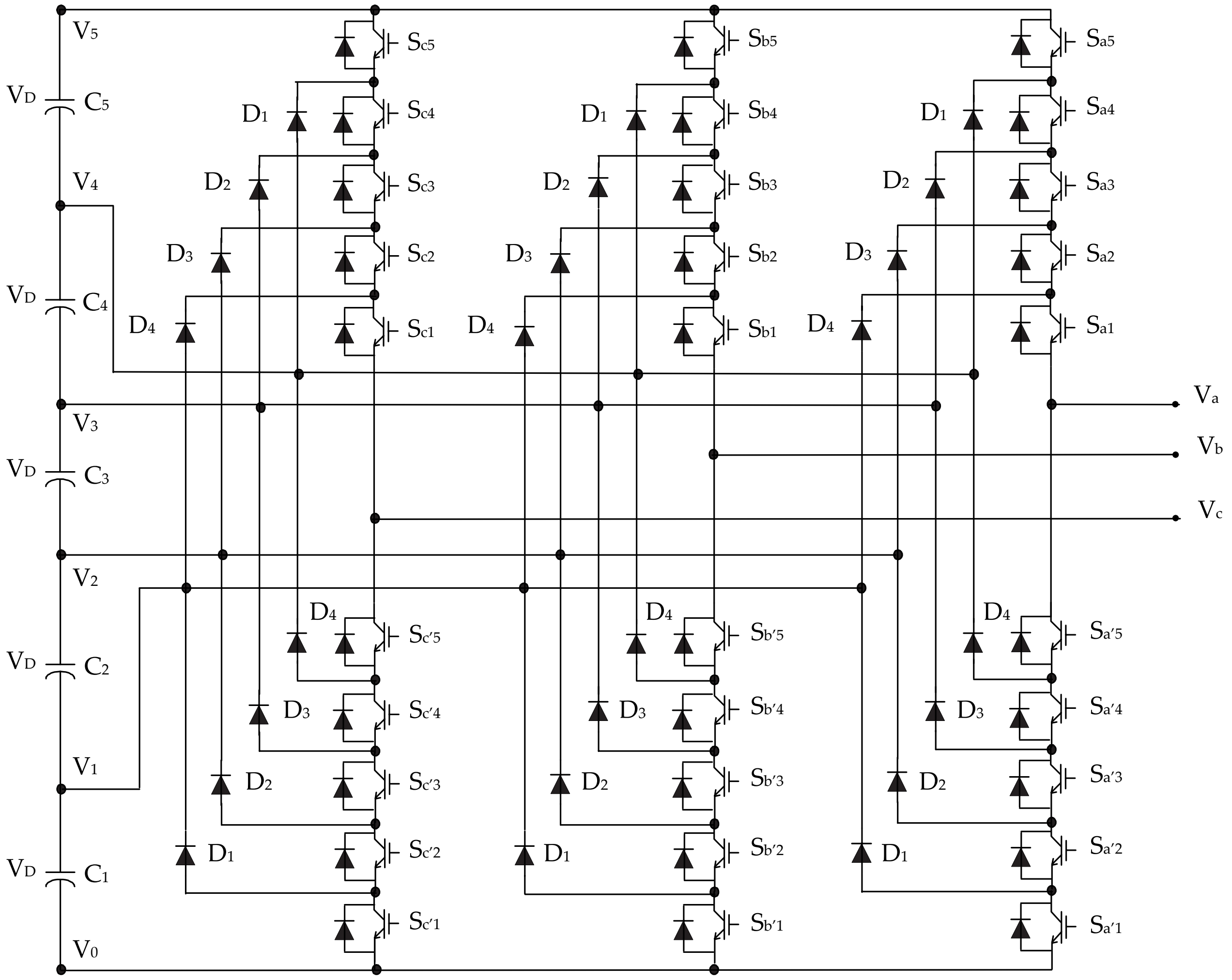

FIGURE 4.4: Three-phase 6-level Neutral Point Clamped Converter [16]

Among the advantages of this topology is the low requirement in capacitances since all of the phases use a common DC bus. In addition, the capacitors can be pre-charged as a group. Lastly, the DCC displays a highly efficient operation for applications that employ fundamental switching [16].

However this configuration has several drawbacks. First of all, it becomes too cumbersome for more than three or five levels due to the complex voltage balancing of the DC link [29]. Furthermore, the number of the clamping diodes increases quadratically with the number of levels, which also introduces complexity with increasing number of levels [16]. Another drawback of the DCC is the uneven distribution of switching losses between the IGBTs. This can be solved by a modified version called the Active DCC (ADCC) [29]. In an ADCC the clamping is realized using active components such as IGBTs instead of diodes. In this way the switching losses can be equally distributed in expense of an even more complex configuration [46].

The DCC configuration has been proposed for a number of applications. Firstly, it can be used as an interface between HVDC and AC transmission lines. Moreover, it can serve as a variable speed drive for high-power medium-voltage motors. Finally, it can used in the field of static Var compensation [16].

4.2.3.2 The Flying Capacitor Converter (FCC)

The Flying Capacitor Converter (FCC) was introduced in 1992 by Meynard and Foch [16]. This topology is very similar to the DCC with the exception that instead of clamping diodes, the configuration uses capacitors. In Figure 4.5 a three-phase, 6-level FCC, using thyristors, is shown. The VSC FCC employs IGBTs instead, but apart from that the configuration is identical. The voltage increment between two adjacent capacitor steps gives the size of the voltage steps in the output waveform [16]. A n-level converter of this type utilizes $n-1$ DC link capacitors and $(n-1)(n-2)/2$ auxiliary capacitors per phase in case they have the same voltage rating as the switches.

The FCC has phase redundancies meaning that it can produce most of the different voltage levels through more than one switching combinations, giving the flexibility of balancing the voltage of the capacitors. In addition, it has the ability of controlling the active and reactive power independently, while the large number of capacitor makes the converter capable of withstanding short duration outages or deep voltage sags [16].

On the other hand, monitoring and balancing the voltages of such a large amount of capacitors is a complex procedure [29] while pre-charging them at the same voltage level is also a difficult task. Also, switching utilization and efficiency are poor for real power transmission. Lastly, in comparison with the DCC, it is a larger and more expensive configuration since the capacitors both more costly and bulky than clamping diodes. Packaging is also more difficult in converters with a high number of levels.

The FCC configuration finds application in the field of motor drivers [47]. In addition, another application of the FCC mentioned in the literature is static Var generation [16].

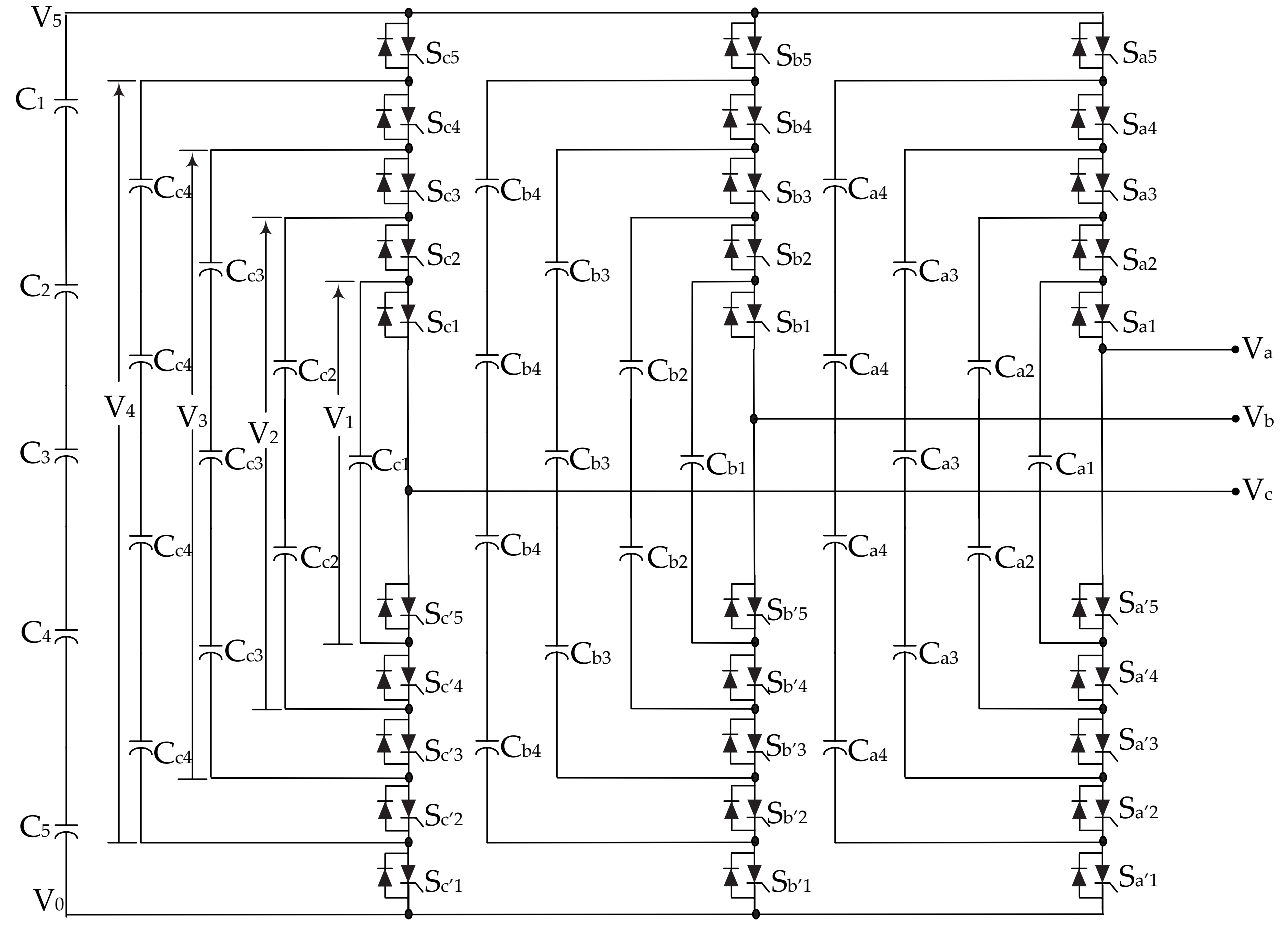

Figure 4.5: Three-phase 6-level Flying Capacitor Converter [16]

4.2.3.3 The Cascaded H-Bridge Converter (CHB)

The Cascaded H-Bridge converter (CHB) is a modular converter whose each phase consists of a number of two-level full bridge converters or H-bridge cells connected in series. Each H-bridge cell includes two pairs of switches with anti-parallel diodes and needs a separate DC source in case of inverter operation, or a separate power output in case of rectifier operation. A phase of such a converter, operating as an inverter, is presented in Figure 4.6. In this case, the H-bridge cells can produce three different voltage levels $(+V(DC), 0, -V(DC))$ depending on the different combinations of the conducting switches. The summation of the AC outputs of the cells shape the total AC voltage waveform. The number of voltage levels n that comprise the AC waveform is related to the number of the separate DC sources s according to the equation $n = 2s + 1$ [16].

The main advantage of the CHB is that it is modular which makes the configuration versatile and flexible while being cheaper and faster to be built. However, the need of separate DC sources (inverter operation) or outputs (rectifier operation) limit its application to products that already have multiple DC sources or outputs readily available [16].

The CHB can be employed for applications such as static Var compensation, acting as an interface of renewable energy sources or battery-based systems [16]. However it is not a practical

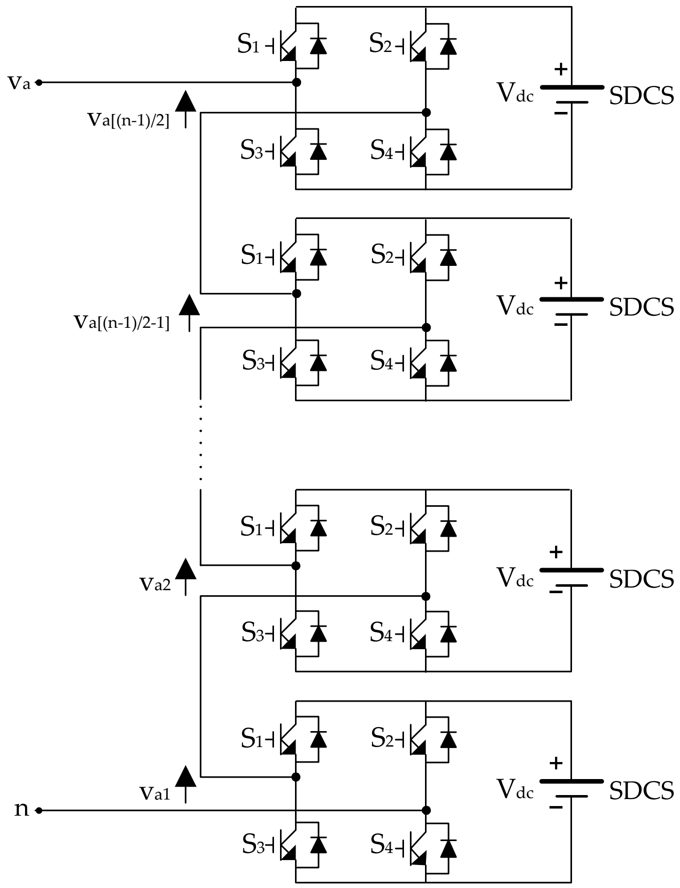

FIGURE 4.6: Single-phase structure of a Cascaded H-Bridge Inverter [16]

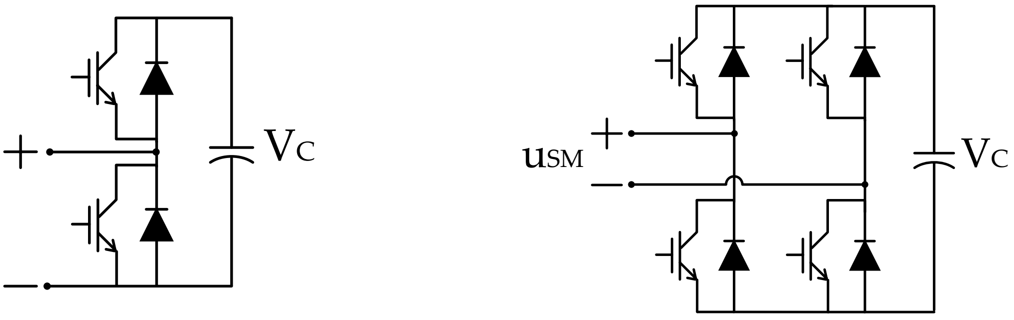

(A)

(B)

FIGURE 4.7: MMC SMs: (A) Half-bridge (B) Full-bridge

configuration regarding bulk HVDC power transmission.

4.2.3.4 The Modular Multilevel Converter (MMC/M2C)

The Modular Multilevel Converter (MMC/M2C) was introduced by Lesnicar and Marquardt in 2003 in [48]. A MMC consists of a number of identical but individually controllable submodules (SMs). The SMs can be either 2-level full-bridge converters capable of producing three different voltage levels $(-V_C, 0, +V_C)$ or 2-level half-bridge converters capable of producing two voltage levels $(+V_C, 0)$. A representation of the two types of SMs is shown in Figure 4.7.

However, because using full-bridge SMs requires the double number of switching components compared to the half-bridge ones, the later is the prevailing and commercialized technology [45]. A three-phase n-level MMC can be seen in Figure 4.8. By appropriate switching of the IGBTs, a SM can be inserted or bypassed meaning that either its capacitor's voltage contributes to the arm voltage or not, respectively. For example in inverter operation, by properly manipulating the number of SMs that are inserted, the output voltage waveform at the AC side has a staircase sinusoidal shape which is very close to the desired sinusoidal waveform. The accuracy of the staircase waveform depends on the number of the SMs.

The MMC topology is highly modular. The voltage level determines the number of SMs needed and the technology can be scaled up to the highest transmission voltages. In addition, redundancy can be easily achieved by including more SMs than strictly needed. In case of a faulty SM, this can be easily bypassed and one of the backup SMs can replace it. Another advantage is that the MMC is capable of synthesizing a high quality sinusoidal voltage waveform, reducing the high harmonics' filters requirements. Furthermore, the switching frequency of the individual IGBTs is decreased from $1-2\ kHz$ for the 2- and 3-level converters to typically $100-150\ Hz$ in the MMC, reducing the converter losses to about 1% [29]. However, it requires more complex control systems and more advanced modulation strategies compared to 2- or 3-level converters [49].

In the last years the MMC topology is becoming widely used in power system applications such as HVDC transmission, flexible alternating current transmission systems (FACTS) and electric railway supply [49].

4.2.3.5 Hybrid Multilevel Converters

As previously mentioned in section 4.2.2, the main disadvantages of two-level VSCs are the high switching losses and the high insulation requirements of the adjacent transformer and the substantial harmonics filtering needs. The MMC addresses these issues but it requires a high number of semiconductors and distributed capacitances. In this context, a hybrid converter has been proposed which combines the features of the 2-level VSC and the MMC configurations [29].

The basic concept of such a converter is the utilization of a 2-level converter, operating at a low switching frequency, as the workhorse of the conversion and the addition of a relatively small multilevel converter which is used in refining the voltage waveform in order to eliminate the harmonics generated by the 2-level converter [29]. In other words the MMC is used as a an active filter or wave-shaping circuit [17].

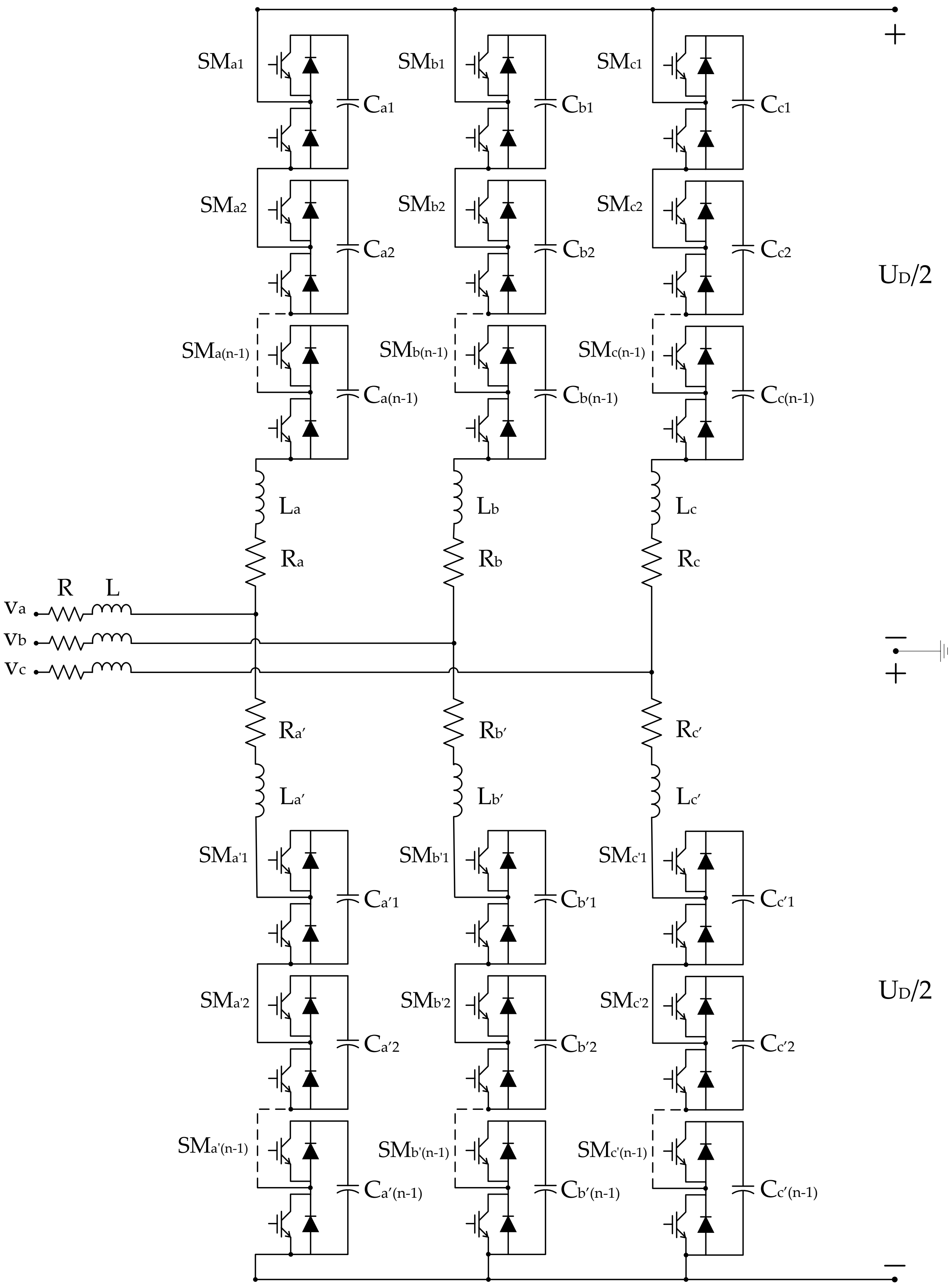

FIGURE 4.8: Three-phase n-level Modular Multilevel Converter

The wave-shaping circuit might be series or parallel connected to the 2-level converter. The switches of the 2-level converter are essentially strings of IGBTs while the wave-shaping circuit uses strings of half or full-bridge submodules (as seen in Figure 4.7). These strings of components are depicted in the following schematics as shown in Figure 4.9.

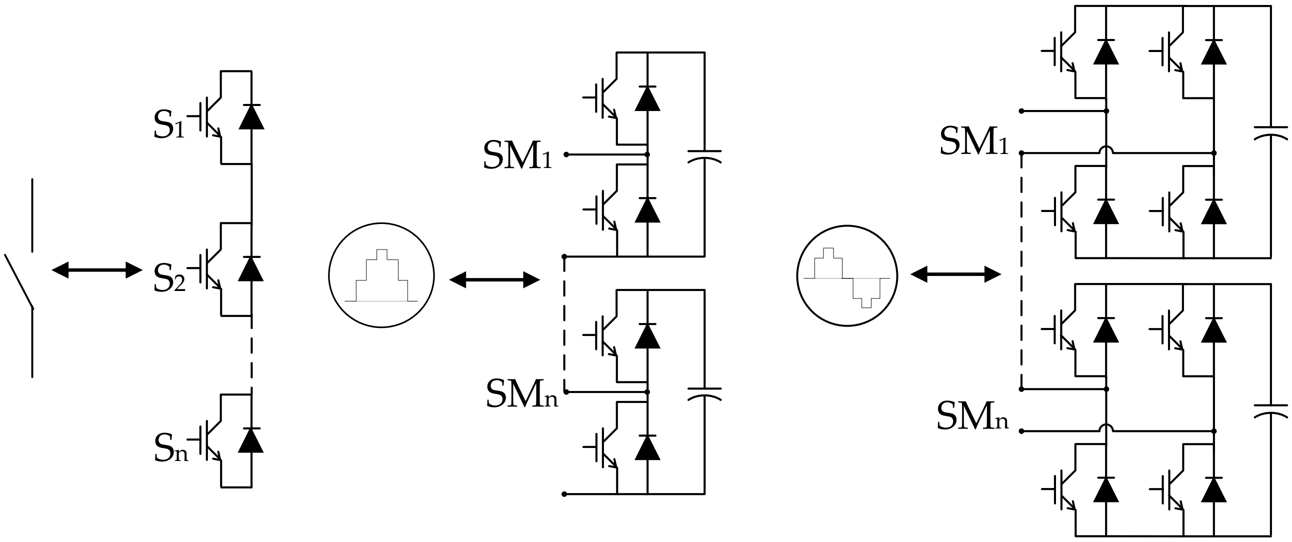

FIGURE 4.9: Graphical representation of building blocks of hybrid multilevel converters [17].

Series Circuits The wave-shaping circuit can be connected in series at both the AC or DC sides of the hybrid converter. In Figure 4.10 the wave-shaping circuit is placed on the AC side of the 2-level converter.

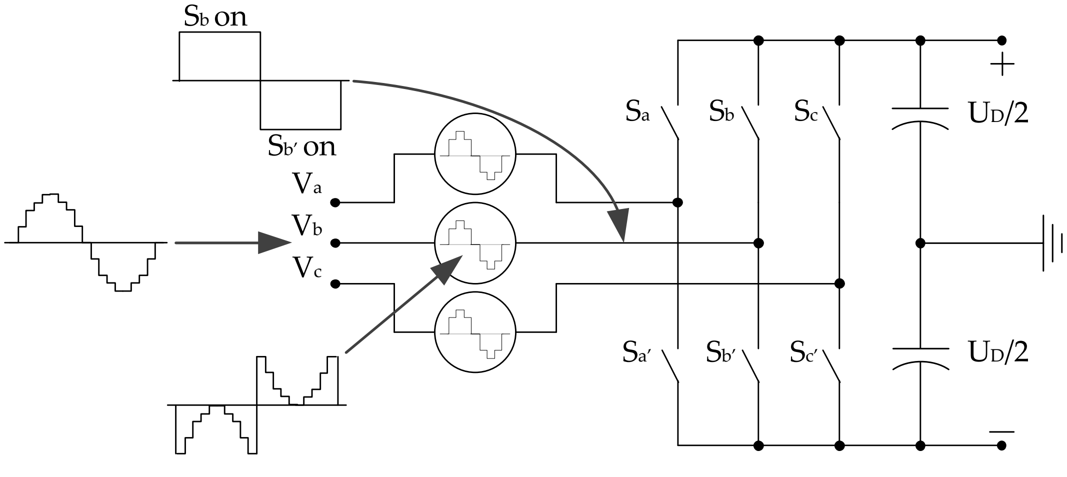

FIGURE 4.10: Wave-shaping circuit connected in series on AC side of a 2-level converter[17].

In this configuration the wave-shaping circuit takes up the difference between the output of the 2-level converter and the desired (staircase sinusoidal) output voltage. This allows the 2-level converter to switch at a much lower frequency than would be acceptable in the absence of the wave-shaping circuit. The voltage produced by the wave-shaping circuit is symmetrical, therefore full-bridge cells are required. A disadvantage of this topology is the fact that the 2-level converter is hard-switched resulting in quite high switching losses, although not as high as a simple 2-level converter. Moreover, careful synchronization between the 2-level converter and wave-shaping converter is required to avoid high voltage spikes from appearing in the combined output voltage waveform [17] [50].

Another topology is derived by placing the wave-shaping converter on the DC side as shown in Figure 4.11. With this configuration, when a switch of the 2-level converter conducts, its adjacent the wave-shaping string is connected to the AC terminal and behaves similarly to the MMC. However, since the complementary switch is off, there is no current circulating between phases resulting to a more efficient utilization of the current ratings of the semiconductor devices.

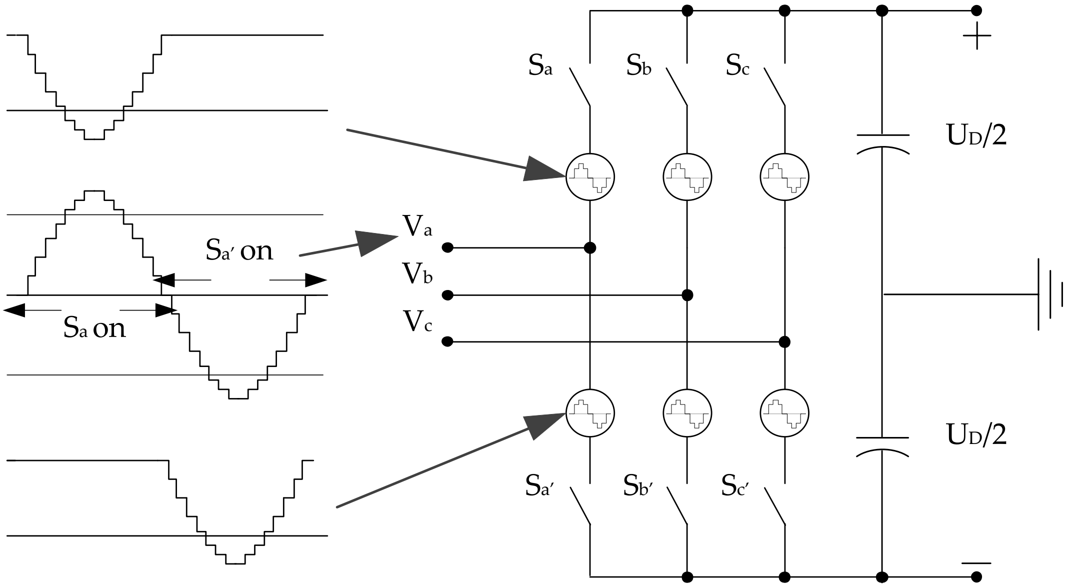

Figure 4.11: Wave-shaping circuit connected in series on DC side of a 2-level converter [17].

Another advantage of this converter is that the wave-shaping converter can adjust the voltage and current on the series connected IGBTs during the switching periods resulting to soft-switching operation. This leads to negligible switching losses and more simplified design of the valve. Lastly, since the wave-shaping circuit is connected in series with the IGBTs' string, the voltage of each arm of the converter is shared between these to components resulting in a lower number of required cells compared to an equivalent MMC [17] [51].

Parallel Circuits The wave-shaping circuit can also be connected in parallel to each full-bridge of the 2-level converter. This configuration employs half-bridge SMs since the DC voltage is unipolar. The principle of operation of a single-phase of this converter is shown in Figure 4.12.

The topology exploits the fact that any ripple present on the DC side is transferred directly to the AC side. The string of half-bridge SMs on the DC side, produce a rectified voltage sine wave as shown in Figure 4.12. The resulting AC voltage is slightly distorted, depending on the

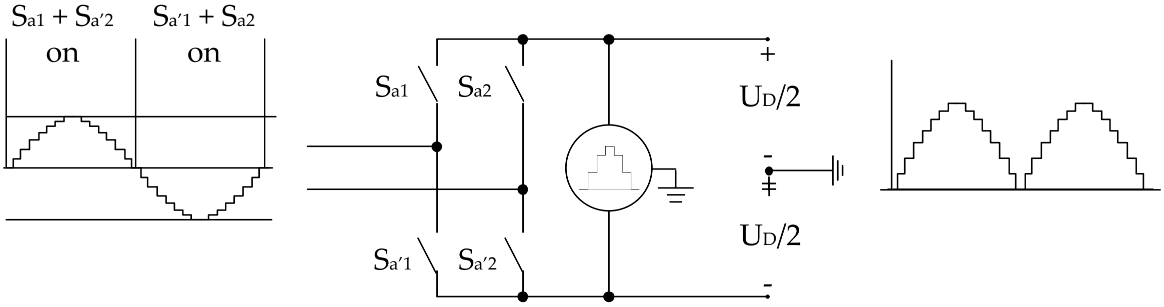

FIGURE 4.12: Full-bridge with active DC capacitor [17].

number of SMs used in the wave shaping circuit. The full three-phase topology is presented in Figure 4.13.

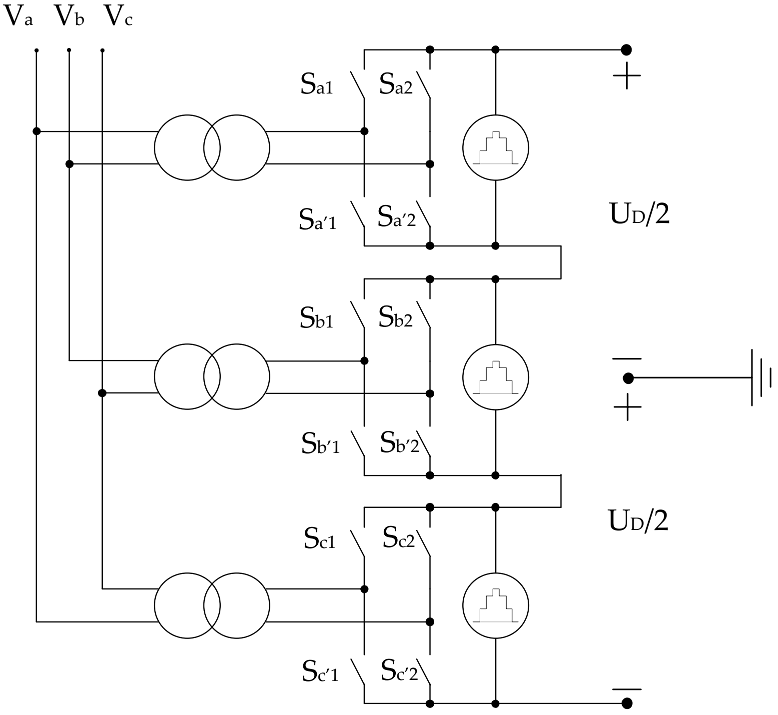

FIGURE 4.13: Parallel circuit with wave-shaping circuit on DC side [17].

A major advantage of this circuit is that the three wave-shaping circuits are outside the main current path. Therefore, compared to the MMC configuration, a substantially lower number of SMs with smaller capacitors is needed. In addition, the wave-shaping circuits can control the voltage of the full-bridges' IGBTs enabling them to be soft-switched an thus reducing the switching losses to zero [17]. On the other side, a large 6th harmonic component is present at the DC side but it can be easily removed using either phase filters or by using active techniques such as adding zero-sequence triple harmonics to the waveforms generated by the three wave-shaping circuits [29]. Another drawback of the topology is that it requires three single-phase transformers as it is shown in Figure 4.13 [17] [52].

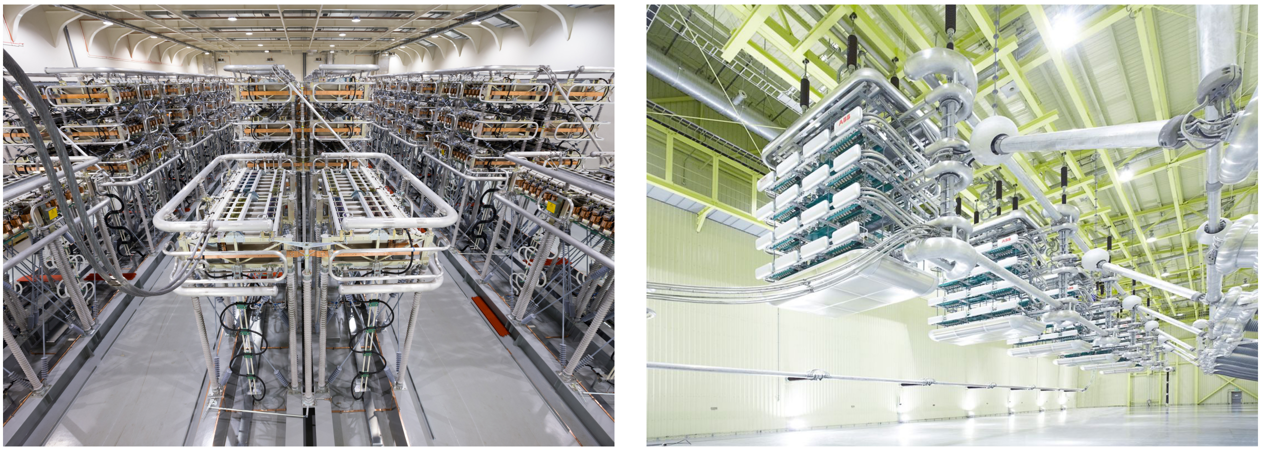

(A) (B)

Figure 4.14: MMCs: (A) Siemens ”HVDC PLUS” MMC [18] (B) ABB ”HVDC Light” MMC [19]

4.2.3.6 The MMC and the Offshore Wind Industry

In the previous section, the different multilevel topologies have been briefly presented. The last two, namely the Modular Multilevel Converter and the Hybrid Multilevel Converter, are the ones that are most suitable for bulk power transmission applications. This is the reason why these two topologies have already been commercialized. In 2010 Siemens installed its first MMC with half-bridge SMs under the name ”HVDC PLUS” (Figure 4.14A), while ABB updated their ”HVDC Light” (Figure 4.14B) product to a similar configuration [45]. In addition, in 2010 Alstom Grid introduced their line of hybrid multilevel converters under the name ”MaxSine” [17] [50] [51] [52] [53].

As it is shown in Table 4.1, all delivered or still under development Offshore Wind projects, utilizing HVDC transmission, make use of the MMC technology. More specifically, three Offshore Wind projects installed in 2013 and another three scheduled to be delivered in 2014 and 2015 were commissioned either to Siemens or ABB. On the other hand, Alstom Grid is in the final stages of completing a HVDC system in inland Sweden using their MaxSine technology. Since the MMC technology is more widely used by the Offshore Wind Industry, the MMC is the topology that is further studied and modeled.

4.3 The MMC Explained

4.3.1 Basic Structure and Operation Principle

A typical configuration of a three-phase n-level MMC is displayed in Figure 4.8 and is reproduced here for the sake of continuity in Figure 4.15. A n-level MMC is capable of producing n

Overview of Selected VSC-HVDC Projects				
Installation	Installed	Manufacturer	Rated Power[MW]	Converter topology
Gotland	1999	ABB	50	2-level
Murraylink	2002	ABB	220	3-level
Estlink	2006	ABB	350	2-level
BorWin1 (OWF)	2009	ABB	400	2-level
Trans Bay Cable Project	2010	Siemens	400	ML
BorWin2 (OWF)	2013	Siemens	800	ML
HelWin1 (OWF)	2013	Siemens	576	ML
DolWin1 (OWF)	2013	ABB	800	ML
SylWin1 (OWF)	2014	Siemens	864	ML
South-West Link	2014	Alstom	1440	ML
HelWin2 (OWF)	2015	Siemens	800	ML
Dolwin2 (OWF)	2015	ABB	900	ML

Table 4.1: List of VSC-HVDC projects [29]

different voltage levels. Each phase is called leg and is composed of an upper and lower arm. Each arm is constituted by $n-1$ submodules (SM). The n voltage levels can be achieved by properly inserting or bypassing the SMs. In addition, each arm includes an inductor, which is usually a standard air-core type inductor, for limiting parasitic currents and fault currents [54]. During each instant there are $n-1$ SMs conducting in every phase leg while the average voltage at the terminals of the SMs is equal to $U_D/(n-1)$.

As it has already been stated, the fundamental building block of a MMC in its most common form, is a half-bridge submodule (SM). The SM is basically constituted by two IGBTs with antiparallel diodes and a capacitor. It has four operating states, depending on the current direction and whether the SM is inserted or bypassed. These states are summarized in Figures 4.16, 4.17.

When the SM is inserted meaning that its capacitor contribute in the arm voltage, the upper IGBT ($T1$) is conducting, while the lower IGBT ($T2$) is blocking. The current may pass through the capacitor in both directions. The capacitor is charging when the current is positive, and discharging when the current is negative. The voltage across the sub-module is in both current directions equal to the capacitor voltage. When the SM is bypassed, the upper IGBT ($T1$) is blocking, while the lower IGBT ($T2$) is conducting. In this case the capacitor does not contribute to the circuit and the voltage at the SM terminals is zero.

In Figure 4.18 a simple one-phase 3-level MMC is shown. The three voltage levels which this configuration can produce are: $+U_D/2$, $-U_D/2$ and 0.

The voltage level $+U_D/2$ is reached when the two upper SMs, 1 and 2, are bypassed. Similarly, for the negative output, $-U_D/2$, the two lower SMs (3 and 4) are bypassed. The zero voltage level is achieved when one SM of the upper and one of the lower arm are bypassed. When two SMs are conducting, the average voltage at the terminals of the SMs is $U_D/2$. Figure 4.19

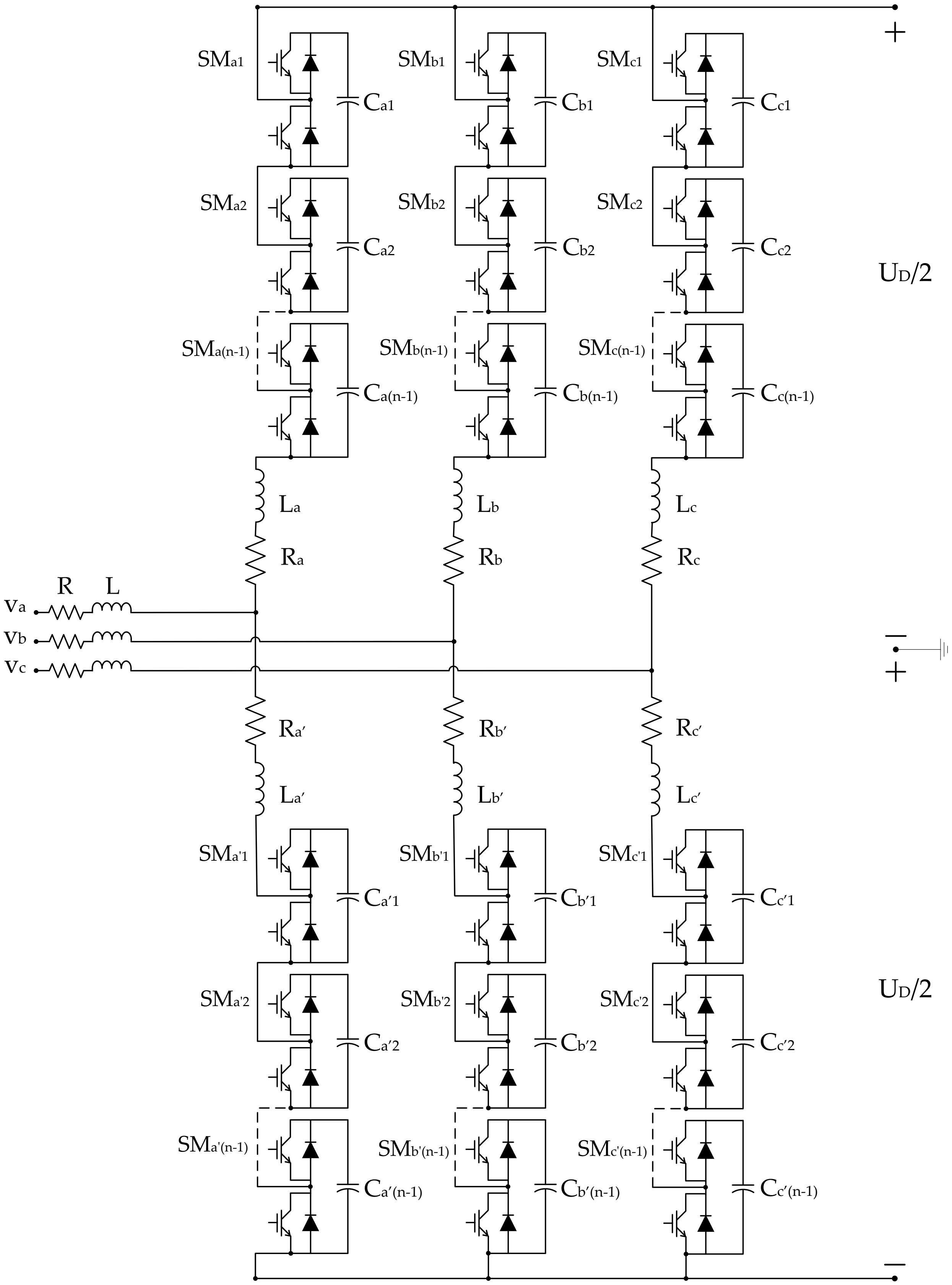

FIGURE 4.15: Three-phase n-level Modular Multilevel Converter

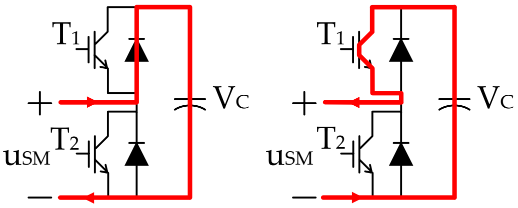

FIGURE 4.16: Operating states when the SM is ON

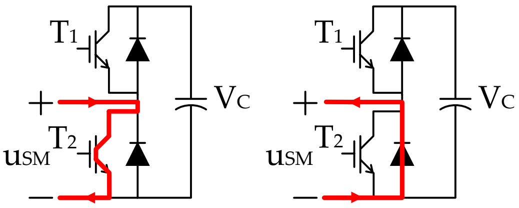

FIGURE 4.17: Operating states when the SM is OFF

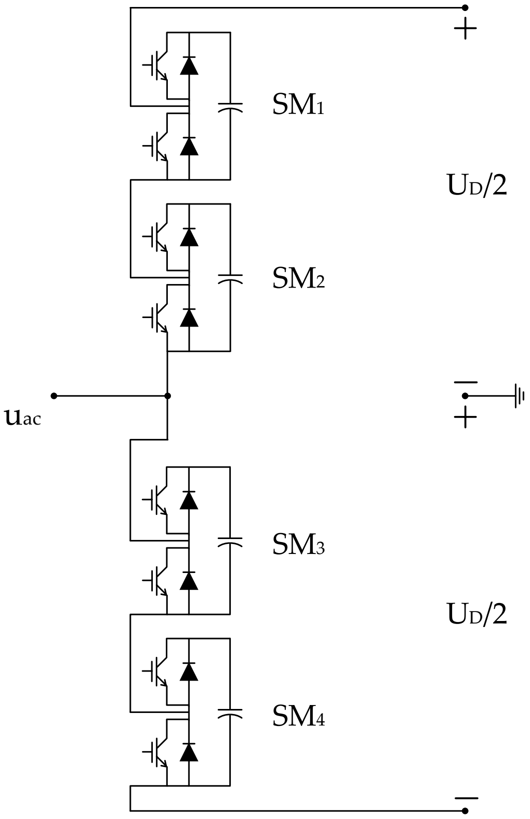

FIGURE 4.18: Scheme of a one-phase 3-level Modular Multilevel Converter

shows a graphical representation of how the different voltage levels are achieved while Table 4.2 sums the redundancies of the voltage levels.

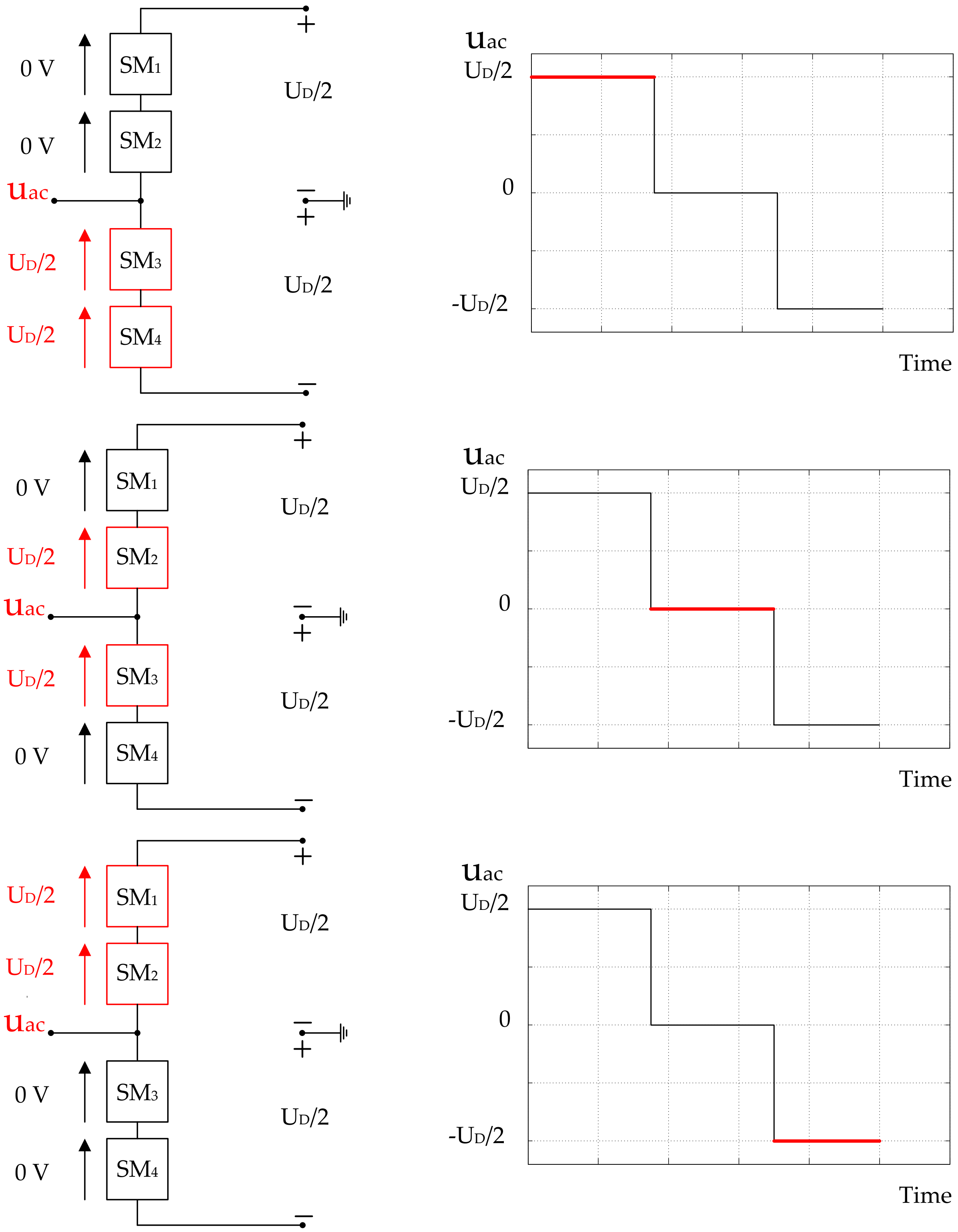

FIGURE 4.19: Generation of voltage levels in a 3-level MMC

Voltage levels of a 3-level MMC				
$u_{ac}(V)$	SM_1	SM_2	SM_3	SM_4
$U_D/2$	OFF	OFF	ON	ON
0	OFF	ON	ON	OFF
0	OFF	ON	OFF	ON
0	ON	OFF	ON	OFF
0	ON	OFF	OFF	ON
$-U_D/2$	ON	ON	OFF	OFF

Table 4.2: Redundancies of the voltage levels of a 3-level MMC

4.3.2 Modulation Technique

Modulation of a power converter is the process of determining the exact time instants for changing the state of each individual switch [55]. There are several Pulse Width Modulation (PWM) techniques that have been proposed for the MMC configuration during the last years. Some of the most well-known are the Phase-disposition PWM (PD-PWM) [56], the phase-shifted carrier PWM (PS-PWM) [57], the space vector modulation (SV-PWM) [48] and the improved selective harmonic elimination (SHE) proposed in [58].

However, as the number of levels increase these techniques become highly complex and computationally very intense [59] [60] [61]. Therefore, more straight-forward, staircase type techniques like the Near Level Control (NLC) modulation have been proposed [62] [63]. Finally, another technique called Direct Modulation is almost identical to the NLC and was introduced in [64]. Because of its simplicity and its solid performance [61] [65] Direct Modulation is the technique chosen to be implemented in the model presented in this thesis.

4.3.2.1 The Direct Modulation Technique

Direct modulation is carried out by simply varying the number of submodules that are connected in each arm in a sinusoidal manner. This is realized by using a reference signal which is identical to the voltage at the AC side of the converter:

$$v_{ref} = \widehat{V}_{ref} \cos(\omega t) \tag{4.3.1}$$

The modulator tries to follow the amplitude of this reference signal as closely as possible and determines the number of SMs that have to be inserted at the upper and the lower arm through the calculation of the insertion indices:

$$n_U = \frac{1 - m_a \cos(\omega t)}{2} \tag{4.3.2}$$

$$n_L = \frac{1 + m_a \cos(\omega t)}{2} \tag{4.3.3}$$

Where m_a is the modulation index:

$$m_a = \frac{2\widehat{V}_{ref}}{U_D} \tag{4.3.4}$$

Where:

- $\widehat{V}_{ref}$: Amplitude of the reference signal (kV)
- U_D: Total DC voltage at the DC side of the MMC (kV)

It is seen that the insertion indices vary from 0 to 1. When the insertion index of an arm equals 0, all of the SMs of the arm are bypassed, while when it is equal to 1, all the SMs of the arm are inserted. Therefore, the number of SMs that have to be inserted at the upper and lower arm is given by the equation 4.3.5. Examples of the modulation technique are shown in Figure 4.20 for a 5-level and a 21-level MMC.

$$N_U = round(N_{SM} * n_U) \tag{4.3.5}$$

$$N_L = round(N_{SM} * n_L) \tag{4.3.6}$$

Where:

- N_{SM}: The number of SMs per arm of the MMC $(-)$

4.3.3 Capacitor Balancing Control

During the MMC operation, the capacitor of an inserted SM is charging or discharging depending on the direction of the current. As a result, the voltage of the capacitor varies in time. To ensure the proper operation of the MMC and avoid unequal stresses on the power devices, the capacitors have to be kept at the same voltage level. Hence, a capacitors' voltage balancing control is required. The modulation controller must not only produce the required AC voltage, it also has to ensure voltage balancing among the capacitors. In other words, the modulator

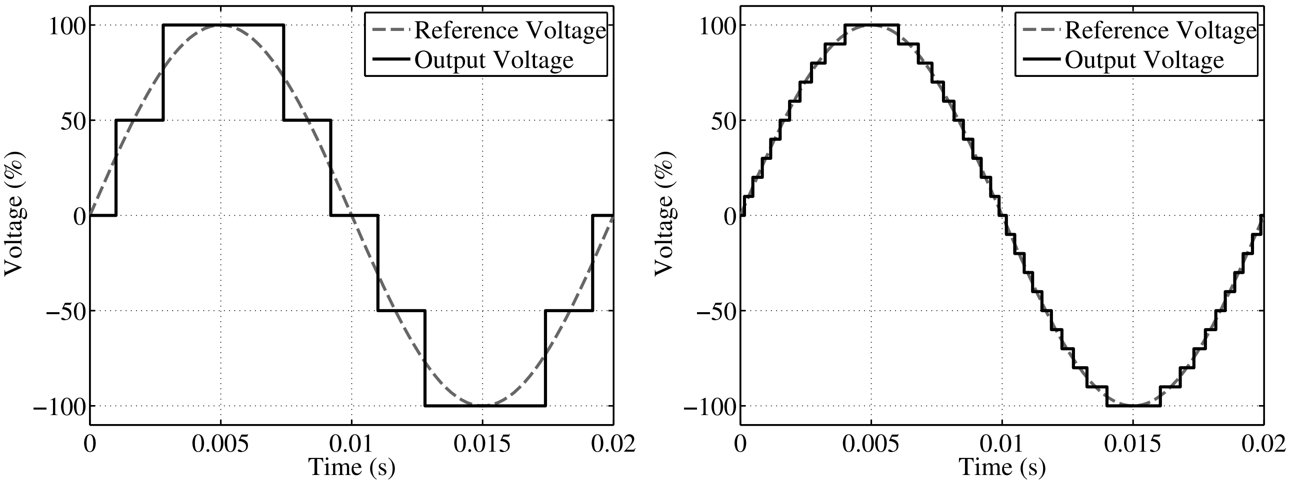

(A) (B)

Figure 4.20: Direct Modulation for (A) 5 voltage levels and (B) 21 voltage levels

has to constantly calculate the number of SMs that need to be inserted, and then decide which SMs have to switched on or off.

The most common method in the literature is the use of a selection algorithm which was initially introduced by Lesnicar and Marquardt in [48]. According to this selection algorithm, the capacitor voltages of each arm are measured periodically with a sampling rate in the millisecond range. Then the values are listed and sorted in ascending order. The sign of the arm current and the number of submodules that have to be on dictate which submodules will be selected. If the arm current is positive, the submodules with the lowest capacitor voltages will be switched on in order to charge. If the arm current is negative, the submodules with the highest capacitor voltages will be switched on, since the negative arm current discharges the capacitors. With this selection algorithm, all capacitor voltages of an arm are balanced, and they lie within a small voltage interval.

Improvements to this selection algorithm have been proposed to alter the switching actions and consequently minimize the switching losses. According to [60], the efficiency of the algorithm can be improved by including a trigger control that activates the algorithm only when the number of the submodules that have to be inserted changes. As a result, switching of the SMs is not realized at every sampling time point. According to another approach [63], when a SM needs to be inserted, the algorithm is only applied to the currently bypassed SMs. Accordingly, when a SM needs to be bypassed, the controller will take into consideration only the SMs that are on and will pick one to go off. Finally, in [20], the controller is optimized by introducing a voltage limit check. The capacitors' voltages that exceed a specific limit are regulated quickly. At the same time, the switching states of the capacitors whose voltages is within the set limits, are maintained to some degree to reduce switching frequency of the power semiconductors. A generalized visual representation of how the modulator operates is given in Figure 4.21.

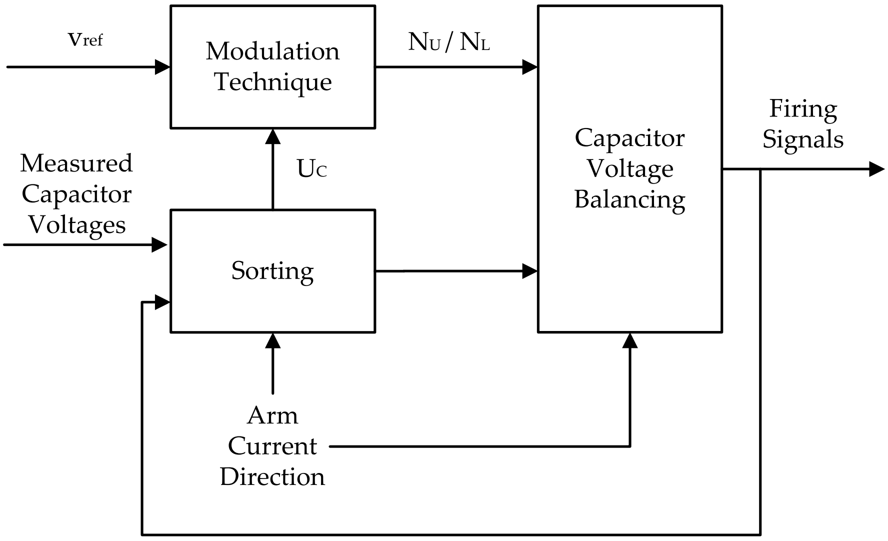

FIGURE 4.21: Modulation and Capacitor Balancing Control, [20]

There are some other, not so common techniques that have appeared in the literature. According to a technique introduced in [66], the voltage balancing of the capacitors can be divided in three different steps: the averaging control, the individual-balancing control and the arm-balancing control. The first step forces the average voltage of each leg, which equals the sum of its capacitors' voltages, to constantly try reaching a set value. The second step forces each individual capacitor to also follow a set value. The final step tries to mitigate the voltage difference between the upper and the lower arm of each leg of the converter. Finally, the balancing of the capacitors' voltage can be realized by switching the semiconductors using a pre-calculated pulse pattern as suggested in [67]. According to this method switching angles can be estimated in such a way that balancing will occur slowly in the range of several fundamental periods, while a number of harmonics can be eliminated from the output signal. It is shown that this can be done at the fundamental switching frequency without measuring the capacitor voltages or using any other form of feedback control.

However, for the purposes of the model presented here, it is assumed that the capacitor voltages are always balanced. Nonetheless, a voltage ripple is taken into account for the dimensioning of the IGBTs as it will be explained later.

4.3.4 General Analysis of the Arm Current of a MMC

A simple way of understanding the internal dynamics of a MMC is by considering a continuous model of the converter presented in [64]. In order such a continuous model to be established two assumptions are made. The first one is that the switching frequency is assumed to be very high relatively to the frequency of the produced output voltage. This implies infinite switching frequency of the converter's switches. The second one is that the steps' resolution in the output voltage is very small compared to the amplitude of the output voltage. This second assumption is equivalent to having an infinite number of modules in each arm.

These two basic assumptions reduce significantly the complexity of this study, as all the converter voltages can be regarded to have a continuous variation, and not any discrete step changes. However as proven in [21], the continuous model is also applicable for a relatively small number of submodules, as well as for a considerably low switching frequency.

The SMs of an arm can be considered as a varying capacitance since the number of inserted capacitors depends on the SMs being inserted each instant. Therefore, a phase leg of the MMC can be represented according to Figure 4.22.

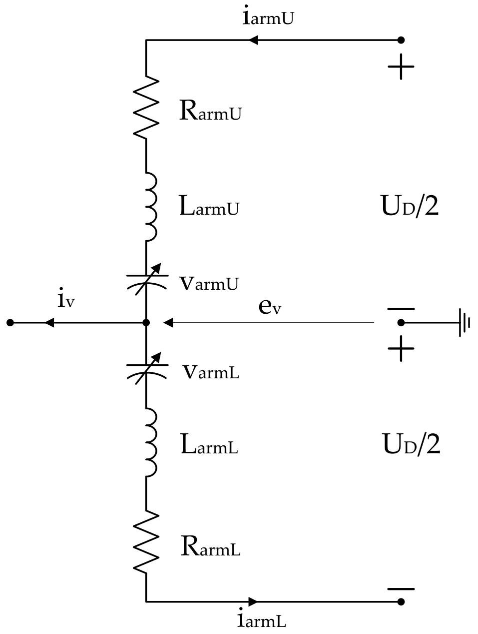

FIGURE 4.22: Single-phase model of a MMC with varying capacitors substituting the SMs of each arm

Applying the Kirchhoff voltage law to the upper and lower arm, the relations 4.3.7 and 4.3.8 are derived.

$$\frac{U_D}{2} = R_{armU} i_{armU} + L_{armU} \frac{d}{dt} i_{armU} + v_{armU} + e_v \tag{4.3.7}$$

$$\frac{U_D}{2} = R_{armL} i_{armL} + L_{armL} \frac{d}{dt} i_{armL} + v_{armL} - e_v \tag{4.3.8}$$

The arm voltages in the upper arm v_{armU} and lower arm v_{armL} can be assumed to be equal to the sum of the upper and lower capacitors' voltages, that are inserted each moment, respectively.

$$v_{armU} = n_U v_{CU} \tag{4.3.9}$$

$$v_{armL} = n_L v_{CL} \tag{4.3.10}$$

Where:

- n_U: Insertion index for the upper arm $(-)$
- n_L: Insertion index for the lower arm $(-)$
- v_{CU}: Sum of the N_{SM} capacitors' voltages of the upper arm (V)
- v_{CL}: Sum of the N_{SM} capacitors' voltages of the lower arm (V)

The sums of all the capacitors' voltages of the two arms can be expressed according to the equations 4.3.11, 4.3.12.

$$v_{CU} = \sum_{k=1}^{N_{SM}} v_{CUk} \tag{4.3.11}$$

$$v_{CL} = \sum_{k=1}^{N_{SM}} v_{CLk} \tag{4.3.12}$$

Where:

- N_{SM}: Number of SMs per arm of the MMC $(-)$
- v_{CUk}: k-th capacitor's voltage of the upper arm (V)
- v_{CLk}: k-th capacitor's voltage of the lower arm (V)

In addition, since the capacitors of one phase leg have the same capacitance C, an effective capacitance can be defined with respect to the insertion indices. The effective capacitance can be easily derived by considering how the inserted capacitance of an arm varies in time. If a SM of an arm is inserted while all the others are bypassed, the inserted capacitance equals the capacitance of this SM's capacitor. If two SMs are inserted, then there are two capacitors connected in series and assuming that these two capacitors are identical, the inserted capacitance is now the half. The total capacitance of an arm is defined in 4.3.13 while the effective capacitances of the upper and lower arms are derived in 4.3.14 and 4.3.15.

$$C_{arm} = \frac{C}{N_{SM}} \tag{4.3.13}$$

$$C_{effU} = \frac{C}{N_{SM}n_U} \tag{4.3.14}$$

$$C_{effL} = \frac{C}{N_{SM}n_L} \tag{4.3.15}$$

The variation of the v_{CU} and v_{CL} voltages is given by equations 4.3.16, 4.3.17.

$$\frac{d}{dt}v_{CU} = \frac{i_{armU}}{C_{effU}} \tag{4.3.16}$$

$$\frac{d}{dt}v_{CL} = \frac{i_{armL}}{C_{effL}} \tag{4.3.17}$$

The currents flowing in the arms of a MMC are defined such that a positive current is charging the capacitors. That is, a positive upper arm current flows from the positive DC terminal to the AC terminal, and a positive lower arm current flows from the AC terminal to the negative DC terminal. With the defined directions of the arm currents, it becomes obvious that the AC-side current i_v must be equal to the difference between the upper and lower arm current. The mean value i_{cc} of the upper and lower arm current is referred to as circulating current.The upper arm current i_{armU} and lower arm current i_{armL} must then satisfy the following equations [67]:

$$i_v = i_{armU} - i_{armL} \tag{4.3.18}$$

$$i_{cc} = \frac{i_{armU} + i_{armL}}{2} \tag{4.3.19}$$

From equations 4.3.18, 4.3.19, it is derived that:

$$i_{armU} = i_{cc} + \frac{i_v}{2} \tag{4.3.20}$$

$$i_{armL} = i_{cc} - \frac{i_v}{2} \tag{4.3.21}$$

In addition, assuming that the current at the AC side is purely sinusoidal, it can be expressed as shown in 4.3.22 [68].

$$i_v = \widehat{I}_v \cos(\omega t + \varphi) \tag{4.3.22}$$

Where:

- $\widehat{I}_v$: Amplitude of AC current (A)
- ω: Angular frequency of the system (rad/s)
- φ: Power angle (rad)

Considering equal the arm parameters, it is applicable that $R_{arm} = R_{armU} = R_{armL}$ and $L_{arm} = L_{armU} = L_{armL}$. Subtracting 4.3.8 from 4.3.7 and using equations 4.3.16, 4.3.17 as well as the current definitions 4.3.18, 4.3.19, the dynamics of a phase leg of a MMC can be summarized in the following first-order differential equation system:

$$\frac{d}{dt}\begin{bmatrix} i_{cc} \\ v_{CU} \\ v_{CL} \end{bmatrix} = \begin{bmatrix} -\frac{R_{arm}}{L_{arm}} & -\frac{n_U}{2L_{arm}} & -\frac{n_L}{2L_{arm}} \\ \frac{n_U}{C_{arm}} & 0 & 0 \\ \frac{n_L}{C_{arm}} & 0 & 0 \end{bmatrix} \begin{bmatrix} i_{cc} \\ v_{CU} \\ v_{CL} \end{bmatrix} + \begin{bmatrix} \frac{U_D}{2L_{arm}} \\ \frac{n_U}{2C_{arm}} i_v \\ -\frac{n_L}{2C_{arm}} i_v \end{bmatrix} \tag{4.3.23}$$

4.3.5 Circulating Current Suppression

In steady state the circulating current can be expressed as [67]:

$$i_{cc} = \frac{I_{DC}}{3} + \sum_{n=1}^{\infty} \widehat{I}_{cc,n} \cos(n\omega t + a_n) \tag{4.3.24}$$

Where:

- I_{DC}: Current at the DC side of the MMC (A)
- $\widehat{I}_{cc,n}$: Amplitude of n-th harmonic (A)
- a_n: Phase shift angle of n-th harmonic (rad)

The circulating current has a DC component which is responsible for the power delivery from or to the DC side of the converter [68]. Since the current of the DC link is split evenly between the three phases of the converter, the DC component of the circulating current is equal to the one third of the DC link current [60]. In addition, because of the fact that the capacitors' voltages vary in time, harmonic components are created in the circulating current [69].

In [70], it is shown that all odd-order harmonics of the circulating current have amplitudes equal to zero, assuming that the AC side current is purely sinusoidal. In addition, among the existing even-order harmonics, the second harmonic has the greatest contribution in the circulating current [70]. This second-order harmonic component distorts the arm currents increasing the power losses and raises the ripple of the capacitors' voltages, affecting the ratings of the switches and the capacitors [54] [60].

There are several methods of suppressing the aforementioned harmonic component. There are methods that make use of an active control over the modulated voltage [21], [64], [71], while the use of a passive filter has also been proposed [54] [72]. Finally, as it is shown in [68], the harmonics can be greatly suppressed by properly dimensioning the capacitance and the inductance of the converter.

An example of suppressing the harmonic component of the circulating current using an active controller is shown in Figure 4.23. The controller is switched on at 0.4 seconds, consequently the circulating current reaches its average value which is equal to its DC component.

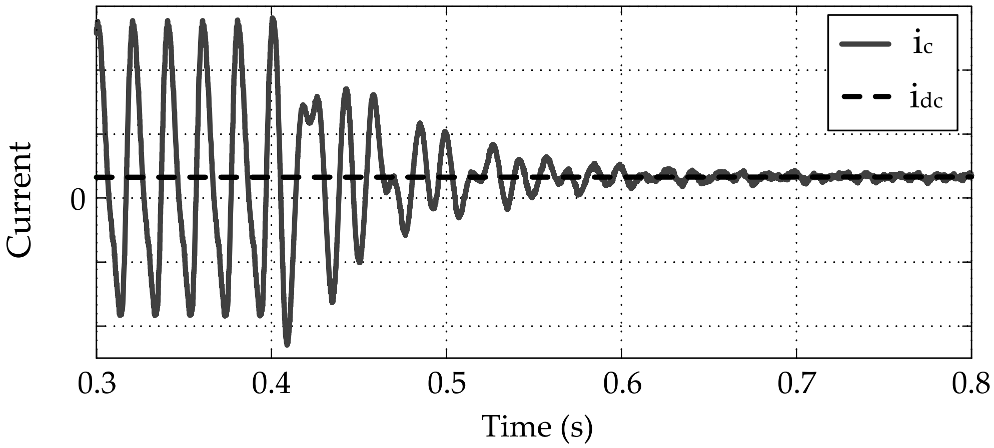

FIGURE 4.23: Circulating current harmonics' suppression using active control, [21]

Due to the existence of several techniques to eliminate the harmonic content, in this thesis it is assumed that there are no harmonics involved in the circulating current.

4.4 Modeling the MMC Power Losses

4.4.1 Introduction

The model presented in this section calculates the power losses of MMC while avoiding the need for a full dynamic simulation model of the converter. The design criteria for this model are:

- High computational speed
- Capture of averaged steady-state operation
- Temperature dependency
- Modularity
- Exclusive use of code
- Use of IGBT module's datasheet

The power losses of a MMC are mainly due to conduction and switching losses. In addition, the losses of control electronics, gate drivers, inductors and cooling system also contribute to the total losses. The calculation of the conduction and switching losses of an IGBT require the use of its datasheet. The model developed based on the $FZ1000R33HL3$ IGBT module produced by Infineon. The model needs as inputs the rated voltage and current of the IGBT as well as several of its characteristic graphs.

Furthermore, the model incorporates the impact of the semiconductors' temperature on the losses. It is assumed that the junction temperature of the semiconductors varies linearly with respect to the RMS current flowing through the converter. Their temperature is equal to the ambient temperature when no current flows and it reaches its maximum value at full load.

The model captures the average operation of the MMC by using some assumptions:

- All semiconductors are identical
- Capacitors' voltages are balanced
- There are no harmonics involved in the circulating current
- Switching occurs uniformly in a fundamental period
- Switching is instantaneous compared to a fundamental period

- The semiconductors' temperature varies linearly with the current

The method according to which the losses of the different components of the MMC are determined is explained in Section 4.4.2. Finally the operation of the model is assessed and its capabilities are shown through examples in Section 4.4.3.

4.4.2 Model

The model needs a number of input variables which are related to the rated data of the converter or retrieved from the IGBTs' datasheets. Furthermore there are input variables that are based on the user's preference. Tables 4.3 and 4.4 show the inputs and the outputs of the model respectively.

Initially, preliminary calculations are conducted to determine the number and configuration (series and/or parallel connected) of IGBT modules that are needed for every switch of a SM. The calculations are thoroughly presented in Appendix B.1.

For deriving the power losses, the arm currents need to be known. However, only the current at the input side is known, which is the DC side in case of inverter operation or the AC side in case of rectifier operation. To bypass this deadlock an iterative procedure is employed. This procedure is shown in Figure 4.24.

Firstly, it is assumed that the losses are equal to 1%, and the currents at both sides of the MMC are calculated. Then, these values are used in the calculation of the power losses of the converter. This new value of the losses is used to re-calculate the currents' values. For the derivation of the arm currents only the losses that have an impact on them are considered. These are the losses corresponding to components of the main electrical circuit of the MMC (conduction, switching and inductors' losses).

Then, the additional losses are calculated (gate controllers' and cooling system losses) and added to the conduction, switching and inductors' losses for the derivation of the total losses.

This process is initially applied for the rated values of the converter in order to determine the rated losses. The rated losses are needed for the implementation of the temperature impact on the power losses. Then, the MMC efficiency curve is obtained by sweeping the values across its power range.

More specifically, in case of inverter operation, the power at the DC side is taken as an input. Assuming power losses of 1% the DC, AC and RMS value of the leg current are calculated according to equations 4.4.1-4.4.4. When the MMC operates as a rectifier the power and hence

Inputs	
$P_{DC,Nom}$	Nominal power at the DC side of the MMC (W)
$P_{AC3ph,Nom}$	Nominal active power at the AC side of the MMC (W)
$Q_{AC3ph,Nom}$	Nominal reactive power at the AC side of the MMC (VAr)
$IRopFlag$	Flag variable determining Inverter or Rectifier operation $(-)$
V_{DC}	Voltage at the DC side of the MMC (V)
m	Modulation index $(-)$
P_{DC}	Lowest possible power at the DC side of the MMC (W)
P_{AC3ph}	Lowest possible power at the AC side of the MMC (W)
$Step$	Accuracy resolution of the efficiency curve calculation (W)
phi	Power angle at the AC side of the MMC (rad)
f	Frequency of the system (Hz)
f_{sw}	Switching frequency of a SM (Hz)
N_{SM}	Number of SMs per arm $(-)$
v_{rip}	Allowed percent arm voltage ripple (%)
$V_{CE,Nom}$	Nominal collector-emitter voltage of the IGBT module (V)
$R_{th,J-C,IGBT}$	IGBT junction to case thermal resistance of the IGBT module (k/W)
$R_{th,J-C,Diode}$	Diode junction to case thermal resistance of the IGBT module (k/W)
$R_{th,C-H,IGBT}$	IGBT case to heatsink thermal resistance of the IGBT module (k/W)
$R_{th,C-H,Diode}$	Diode case to heatsink thermal resistance of the IGBT module (k/W)
$R_{th,H}$	Heatsink thermal resistance of the IGBT module (k/W)
$\theta_{m,Max}$	Maximum operating temperature of the IGBT module (°C)
$\theta_{m,Amb}$	Ambient temperature (°C)
$\theta_{i,Max}$	Maximum operating temperature of the inductor (°C)
$I_{ind,Nom}$	Nominal current of a SM's inductor (A)
R^{20}_{indDC}	DC resistance of a SM's inductor at 20 °C (Ω)
R^{20}_{indAC}	AC resistance of a SM's inductor at 20 °C (Ω)
α_{20}	Constant mass temperature coefficient at 20 °C (K^{-1})
COP	Coefficient of Performance of the Cooling System $(-)$
R_{Gon}	On gate resistance of the IGBT module (Ω)
R_{Goff}	Off gate resistance of the IGBT module (Ω)
R_{Grec}	Diode gate resistance of the IGBT module (Ω)
$I_C = f(V_{CE})$	Collector current vs collector-emitter voltage characteristic $(-)$
$E_{on} = f(I_C)$	Switching on losses vs collector current characteristic $(-)$
$E_{off} = f(I_C)$	Switching off losses vs collector current characteristic $(-)$
$E_{on} = f(R_G)$	Switching on losses vs gate resistor characteristic $(-)$
$E_{off} = f(R_G)$	Switching off losses vs gate resistor characteristic $(-)$
$I_D = f(V_D)$	Diode current vs diode voltage characteristic $(-)$
$E_{rec} = f(I_D)$	Reverse recovery energy vs diode current characteristic $(-)$
$E_{rec} = f(R_G)$	Reverse recovery energy vs gate resistor characteristic $(-)$

Table 4.3: Model Inputs

Outputs	
P_{con}	Conduction losses (W)
P_{sw}	Switching losses (W)
P_{ind}	Inductors' losses (W)
P_{gate}	Gate controllers' losses (W)
P_{cool}	Cooling system losses (W)
P_{tot}	Total losses (W)
I_{out}	Current at the output (A)

TABLE 4.4: Model Outputs

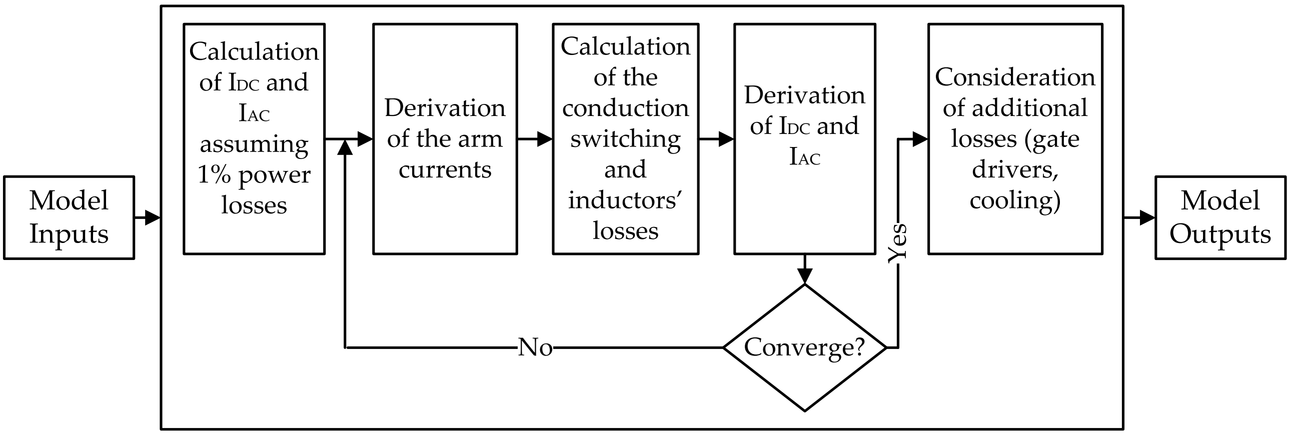

FIGURE 4.24: Iterative process calculating the Power Losses and Arm Currents

the current at the AC side is known. Therefore, the same equations are applied inversely.

$$I_{DC} = \frac{P_{DC}}{V_{DC}} \tag{4.4.1}$$

$$P_{AC3ph} = (1 - 0.01)P_{DC} \tag{4.4.2}$$

$$I_{AC} = \frac{P_{AC3ph}}{\sqrt{3}V_{AC}\cos(\varphi)} \tag{4.4.3}$$

$$I_{legRMS} = \sqrt{\left(\frac{I_{DC}}{3}\right)^2 + \left(\frac{I_{AC}}{2}\right)^2} \tag{4.4.4}$$

Where:

- I_{DC}: Current at the DC side of the converter (A)
- P_{DC}: Power at the DC side of the converter (W)
- V_{DC}: Voltage at the DC side of the converter (V)

- P_{AC3ph}: Three-phase active power at the AC side of the converter (W)
- I_{AC}: Line current at the AC side of the converter (A)
- V_{AC}: Line to line voltage at the AC side of the converter (V)
- φ: Power angle of the converter (rad)
- I_{legRMS}: RMS current at a leg of the converter (A)

Consequently, the iteration loop begins. The losses of the main circuit components are determined as explained in the next sections (4.4.2.1 - 4.4.2.3) and updated values for the AC current (Inverter operation) or the DC current (Rectifier operation) are calculated using equations 4.4.5 and 4.4.6 respectively. Then, the arm currents' values are updated. It is observed that after three iteration loops the currents and losses converge to their final values.

$$P_{AC3ph} = P_{DC} - (P_{con3ph} + P_{sw3ph} + P_{ind3ph}) \tag{4.4.5}$$

$$P_{DC} = P_{AC3ph} - (P_{con3ph} + P_{sw3ph} + P_{ind3ph}) \tag{4.4.6}$$

Finally, the additional losses are determined as shown in Section 4.4.2.4 and the total losses are derived using equation 4.4.7.

$$P_{tot3ph} = P_{con3ph} + P_{sw3ph} + P_{ind3ph} + P_{gate3ph} + P_{cool3ph} \tag{4.4.7}$$

Where:

- P_{tot3ph}: Total losses (three-phase) (W)
- P_{con3ph}: Conduction losses (three-phase) (W)
- P_{sw3ph}: Switching losses (three-phase) (W)
- P_{ind3ph}: Inductors' losses (three-phase) (W)
- $P_{gate3ph}$: Gate controllers' losses (three-phase) (W)
- $P_{cool3ph}$: Cooling system losses (three-phase) (W)

4.4.2.1 Conduction Losses

The dissipated energy due to conduction over a fundamental period of an IGBT module is given by equations 4.4.8 and 4.4.9 for the IGBT switch and the antiparallel diode respectively. The derivation of these expressions is summarized in Appendix B.2.

$$E_{con} = \int_{0}^{T} K_{t,T}(V_{ce0} \cdot i_c + R_{ce0} \cdot {i_c}^2)dt \tag{4.4.8}$$

$$E_{con} = \int_{0}^{T} K_{d,T}(V_{d0} \cdot i_d + R_{d0} \cdot {i_d}^2)dt \tag{4.4.9}$$

Where:

- $K_{t,T}$: Temperature correction factor $(-)$
- V_{ce0}: On-state zero-current collector-emitter voltage at datasheet's temperature (V)
- i_c: Collector current (A)
- R_{ce}: On-state collector-emitter resistance at datasheet's temperature (Ω)
- $K_{d,T}$: Temperature correction factor $(-)$
- V_{d0}: On-state zero-current diode voltage at datasheet's temperature (V)
- i_d: Diode current (A)
- R_d: On-state diode resistance at datasheet's temperature (Ω)

The conduction losses are calculated in two parts. Firstly, some preliminary calculations are realized to determine necessary parameters of the IGBT module. Secondly, the conduction losses of the semiconductors of the MMC are derived. During the first part, the IGBT parameters (V_{ce0}) and (R_{ce}), the diode parameters (V_{d0}) and (R_d), as well as the temperature correction factors $K_{t,T}$ and $K_{d,T}$ are derived. The correction factors are given in equations 4.4.10 and 4.4.11 and can be derived using the IGBT module's datasheet graphs shown in Figure 4.25. For values of collector-emitter voltage lower than 0.625 the curves are projected until the center of the axes.

$$K_{t,T} = \frac{v_{ce,@T}}{v_{ce,@T_{Dts}}} \tag{4.4.10}$$

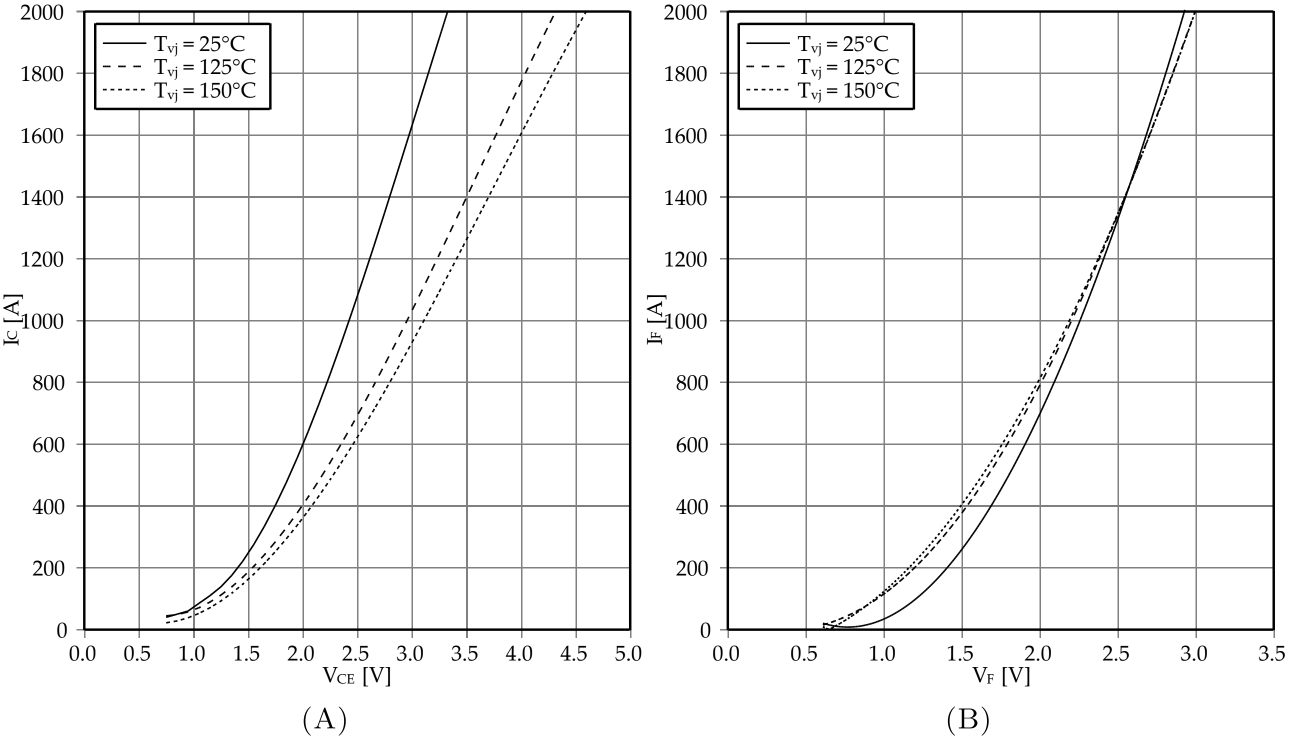

FIGURE 4.25: FZ1000R33HL3: (A) Collector current vs collector-emitter voltage characteristic (B) Diode current vs diode voltage characteristic [22]

$$K_{d,T} = \frac{v_{d,@T}}{v_{d,@T_{Dts}}} \tag{4.4.11}$$

Where:

- $v_{ce,@T}$: On-state collector-emitter voltage at operation temperature T (V)
- $v_{ce,@T_{Dts}}$: On-state collector-emitter voltage at datasheet's temperature (V)
- $v_{d,@T}$: On-state diode voltage at operation temperature T (V)
- $v_{d,@T_{Dts}}$: On-state diode voltage at datasheet's temperature (V)

The calculation of the correction factors needs the junction's operation temperature of the semiconductors. It is assumed that the junction temperature varies linearly with respect to the RMS value of the leg current as shown in 4.4.12.

$$\theta_J = \theta_{m,Amb} + \frac{I_{legRMS}}{I_{legRMS,Nom}}(\theta_{m,Max} - \theta_{m,Amb}) \tag{4.4.12}$$

Where:

- $\theta_{m,Amb}$: MMC ambient temperature (°C)

- $\theta_{m,Max}$: Maximum operating temperature of the IGBT module (°C)
- I_{legRMS}: RMS current at a leg of the converter (A)
- $I_{legRMS,Nom}$: Nominal RMS current at a leg of the converter (A)

Regarding the IGBT correction factor, in Figure 4.25A it is seen that the $I_C = f(V_{CE})$ curve is given for three temperatures namely 25 °C, 125 °C, 150 °C. Initially, the V_{CE} corresponding to the RMS leg current I_{legRMS} is determined for the three given curves by linear interpolation. Then, depending on where the calculated junction temperature θ_J lies with respect to the three given temperatures, a second linear interpolation (or extrapolation) is realized. Therefore the V_{CE} corresponding to both the specific RMS leg current and junction temperature is derived and the correction factor $K_{t,T}$ is calculated. In a completely analogous procedure using the diode's $I_D = f(V_D)$ curves, the factor $K_{d,T}$ is determined. A summary of this procedure is given in Figure 4.26.

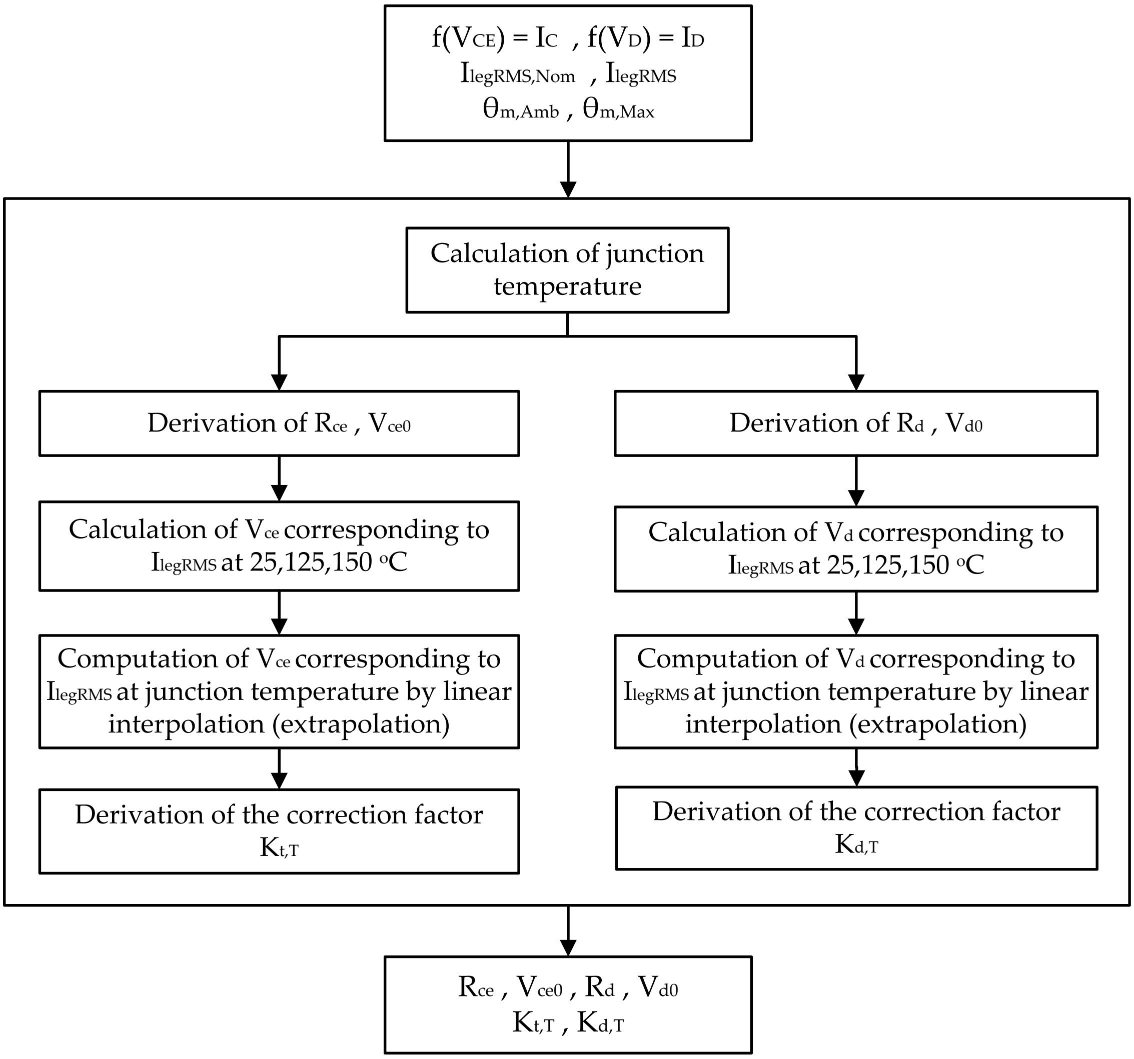

FIGURE 4.26: Calculation of temperature correction factors

During the second part, the conduction losses are calculated. The period of the system (0.02 *sec*) is sampled. For each of the sampling points the number of inserted SMs and the direction of current are determined. Then the dissipated energy due to conduction is calculated for all the time intervals between the sampling points using equations 4.4.8, 4.4.9. In order to be ensured that the calculation includes all the voltage levels, the sampling frequency has to be at least two times the number of the SMs of an arm times the fundamental frequency [73]. Therefore, the sampling frequency is:

$$f_s = 3N_{SM}f \tag{4.4.13}$$

Where:

- N_{SM}: Number of SMs in each arm $(-)$
- f: System's frequency (Hz)

The number of SMs, that are inserted during the time intervals between the sampling instants, is calculated using the modulating reference signal V_{ref} and the insertion indices. The direction of the current is derived from the expressions 4.4.14 and 4.4.15 in case of inverter operation and the expressions 4.4.16 and 4.4.17 for rectifier operation. This separation between the two operation modes is important because, although the RMS value of the arm currents is the same, their direction of flow determines the semiconductors that conduct each instant.

$$i_{armU} = \frac{I_{DC}}{3} + \frac{1}{2}\widehat{I}_{AC}\cos(\omega t + \varphi) \tag{4.4.14}$$

$$i_{armL} = \frac{I_{DC}}{3} - \frac{1}{2}\widehat{I}_{AC}\cos(\omega t + \varphi) \tag{4.4.15}$$

$$i_{armU} = -\frac{I_{DC}}{3} - \frac{1}{2}\widehat{I}_{AC}\cos(\omega t + \varphi) \tag{4.4.16}$$

$$i_{armL} = -\frac{I_{DC}}{3} + \frac{1}{2}\widehat{I}_{AC}\cos(\omega t + \varphi) \tag{4.4.17}$$

Finally, the conduction losses are calculated by simply multiplying the dissipated energy for a fundamental period times the fundamental frequency. The procedure is summarized in Figure 4.27.

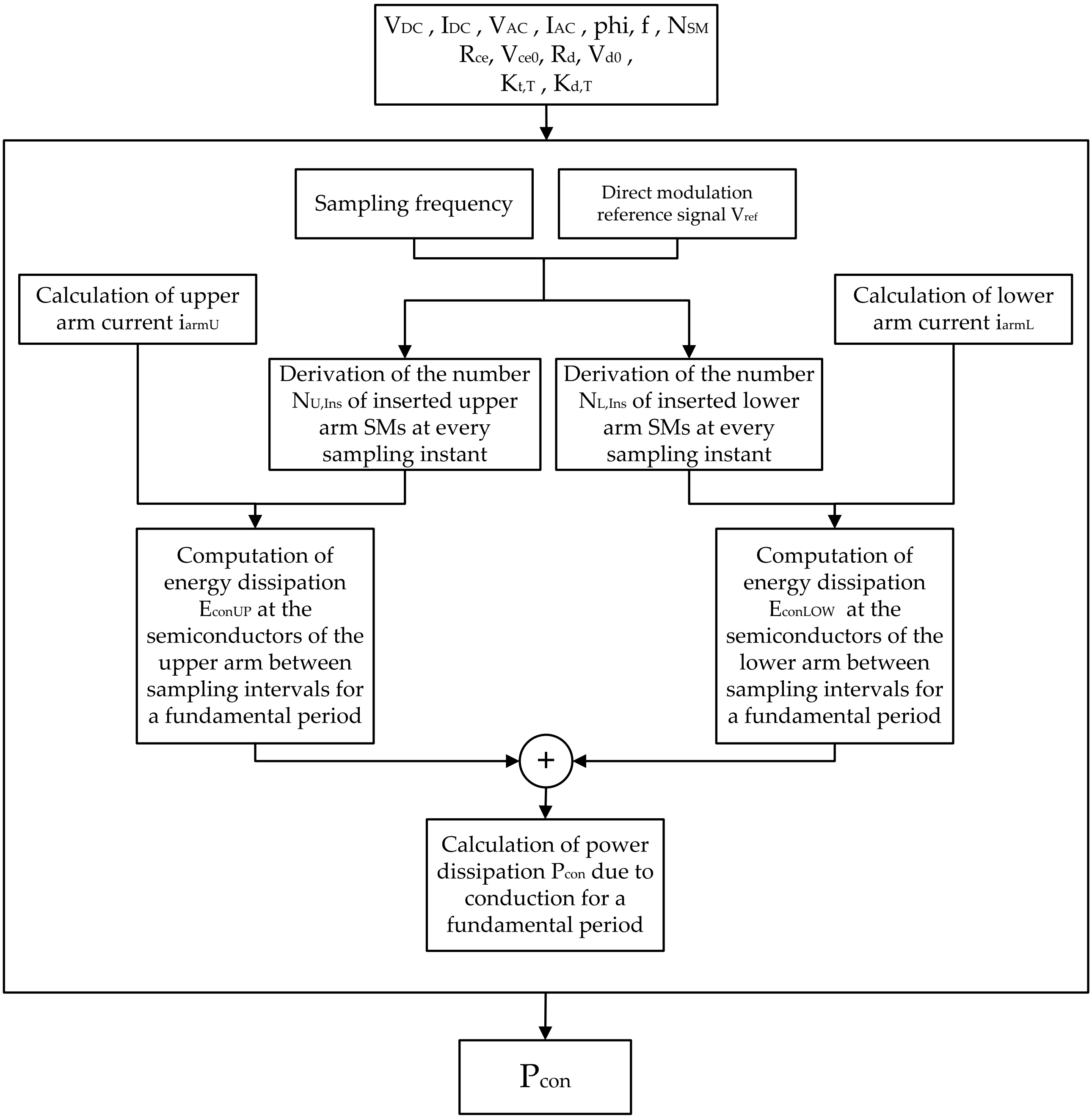

FIGURE 4.27: Calculation of the conduction losses

4.4.2.2 Switching Losses

The calculation of the switching losses of the MMC is done without knowing the exact moment when a switching occurs. This has the advantage of not needing to employ a controller for the balancing of capacitors' voltages.

The switching pattern is derived by using only one variable which is the approximate switching frequency of the SMs. Using this variable, the number of switching incidents (switch-ons and switch-offs), that occur during a fundamental period (0.02 sec) of the arm current is determined. For example, for a switching frequency equal to 200 Hz, 4 switch-ons and 4 switch-offs occur during a fundamental period. Half of the switching incidents are dispersed uniformly throughout the positive semi-period of the AC component of the arm current while the other half throughout the negative semi-period. Figure 4.28 shows how the switching incidents are distributed throughout a fundamental period for a switching frequency of 200 Hz.

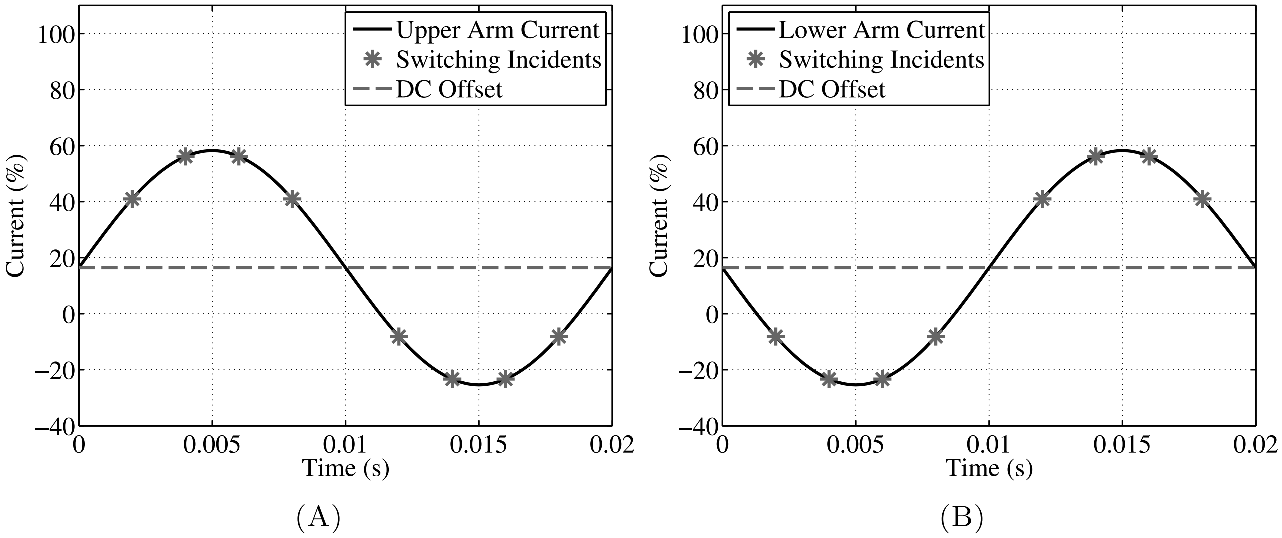

FIGURE 4.28: Current and switching incidents for switching frequency of $200Hz$: (A) Upper arm (B) Lower arm

Although the timing of the switching incidents is determined, the pattern gives no indication whether these are switch-ons or switch-offs. Therefore, the losses are calculated for two fundamental periods. For the first one it is assumed that the first switching incident is a switch-on of the SM, while for the second period the first switching incident is a switch-off. This is mathematically equal to the calculation of one period where all the switching incidents are switch-ons and another period where all the incidents are switch-offs. Having determined when the switching incidents occur and knowing the direction of the current, it can be determined which component of the SM switches on or off.

If the current is positive when the submodule is switched on then:

- one IGBT switches off (hard)
- one IGBT switches on (soft) (no losses)
- one diode switches on (hard) (no losses)

If the current is negative when the submodule is switched on then:

- one diode switches off (hard) (reverse recovery losses)
- one IGBT switches off (soft) (no losses)
- one IGBT switches on (hard)

If the current is positive when the submodule is switched off then:

- one diode switches off (hard) (reverse recovery losses)
- one IGBT switches off (soft) (no losses)
- one IGBT switches on (hard)

If the current is negative when the submodule is switched off then:

- one IGBT switches off (hard)
- one IGBT switches on (soft) (no losses)
- one diode switches on (hard) (no losses)

The dissipated energy during switching is read from the IGBT module's datasheet for specific values of temperature, gate resistance and collector-emitter voltage. Three correction factors are defined to determine the switching loss for different values of these variables, as explained in Appendix B.3.

The temperature correction factor for the IGBT $L_{t,T}$ and for the diode $L_{d,T}$ are calculated using the graphs of the switching losses with respect to the collector's current (Figure 4.29).

In addition, since these graphs give curves corresponding only to two high temperatures, the introduction of a curve for a lower temperature is necessary. This is realized by using another IGBT module's datasheet namely the $IKW40N120H3$ of Infineon. For this module there is data provided about the switching losses at 25 °C, 125 °C and 150 °C. The expressions $E_{sw,25^{\circ}\mathrm{C}}/E_{sw,125^{\circ}\mathrm{C}}$ for the IGBT and $E_{rec,25^{\circ}\mathrm{C}}/E_{rec,125^{\circ}\mathrm{C}}$ for the diode are used as a scaling factor to introduce the curves of switch on, switch off and reverse recovery losses at 25 °C.

Only the procedure for the calculation of switch-on loss of the IGBT will be explained in detail since the switch off and the reverse recovery loss are computed in analogous fashion.

First, for each of the instantaneous values of the arm current at the switching instants, the switch-on loss is calculated for the three temperatures from the respective curve using linear interpolation. Then, a second linear interpolation (or extrapolation) is realized between these three values in order the loss for the specific junction temperature to be determined. The junction temperature is derived in the same way as explained in section 4.4.2.1. The result is a one-dimensional table with a number of cells equal to the switching instants. Each cell has the value of the switch on loss corresponding to the instantaneous arm current at each instant and the junction temperature of the semiconductor.

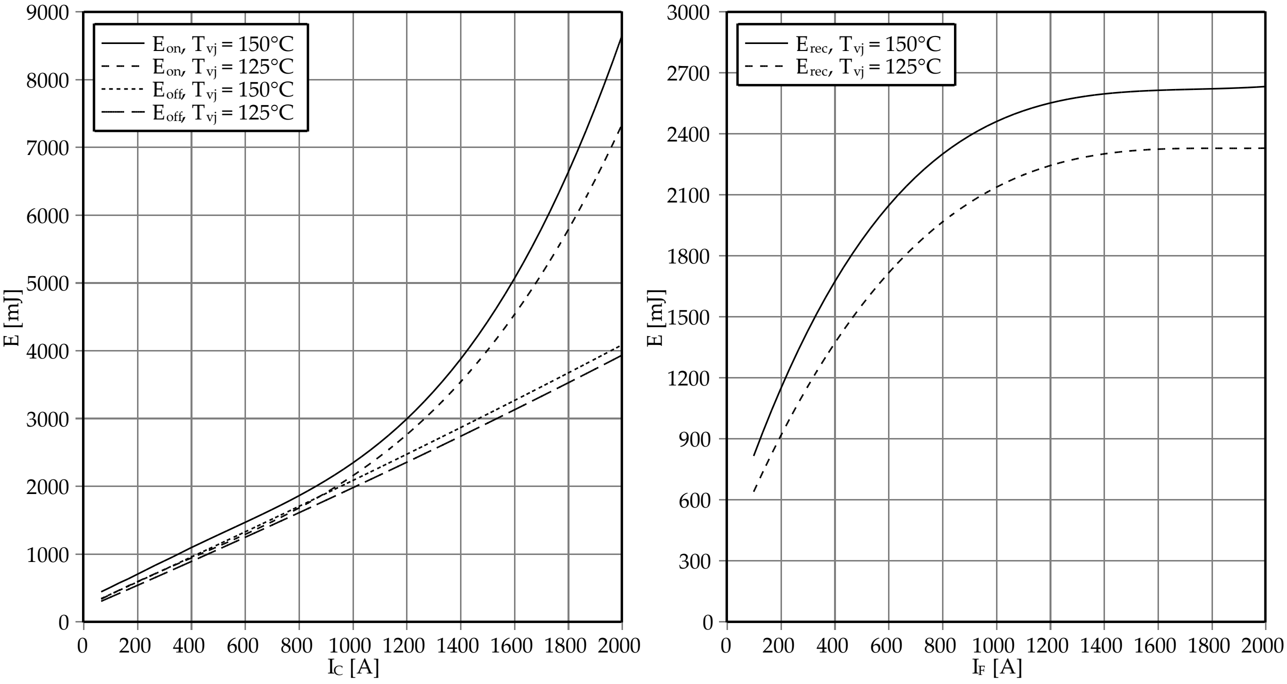

(A) (B)

FIGURE 4.29: FZ1000R33HL3: (A) IGBT switching losses vs collector current characteristic (B) Diode reverse recovery losses vs diode current characteristic ($R_{Gon} = 0.75\Omega$, $R_{Goff} = 4.1\Omega$, $V_{CE} = 1800V$)[22]

After producing the same table for the switch-off loss and the reverse recovery loss, the temperature correction factors are derived according to expressions 4.4.18 - 4.4.20.

$$L_{t,T,on} = \frac{E_{on,i_{arm},T}}{E_{on,i_{arm},T_{Dts}}} \tag{4.4.18}$$

$$L_{t,T,off} = \frac{E_{off,i_{arm},T}}{E_{off,i_{arm},T_{Dts}}} \tag{4.4.19}$$

$$L_{d,T,rec} = \frac{E_{rec,i_{arm},T}}{E_{rec,i_{arm},T_{Dts}}} \tag{4.4.20}$$

Where:

- $E_{on,i_{arm},T}$: Switch-on energy at a specific arm current and junction temperature (J)
- $E_{on,i_{arm},T_{Dts}}$: Switch-on energy at a specific arm current and the datasheet junction temperature (J)
- $E_{off,i_{arm},T}$: Switch-off energy at a specific arm current and junction temperature (J)
- $E_{off,i_{arm},T_{Dts}}$: Switch-off energy at a specific arm current and the datasheet junction temperature (J)

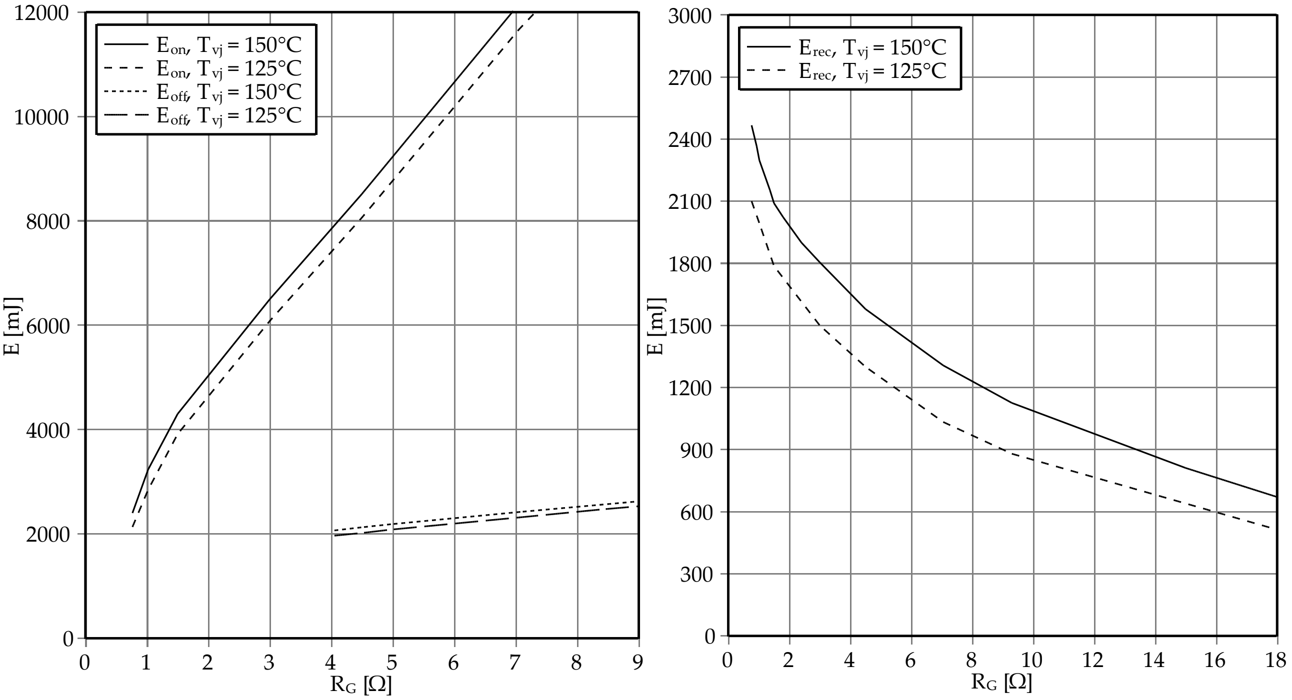

(A) (B)

FIGURE 4.30: FZ1000R33HL3: (A) IGBT switching losses vs gate resistance characteristic (B) Diode reverse recovery losses vs gate resistance characteristic ($I_C = 1000A$, $V_{CE} = 1800V$)[22]

- $E_{rec,i_{arm},T}$: Reverse recovery energy at a specific arm current and junction temperature (J)
- $E_{rec,i_{arm},T_{Dts}}$: Reverse recovery energy at a specific arm current and the datasheet junction temperature (J)

Consequently, the correction gate resistance factors L_{t,R_G} for the IGBT and L_{d,R_G} for the diode are calculated using the graphs shown in Figure 4.30). A single linear interpolation is realized for each of the three factors in which the respective loss that corresponds to the value of the gate resistance specified by the user is determined. Then the factors can be calculated as shown in 4.4.21

$$L_{t,R_G,on} = \frac{E_{on,I_{Dts},R_G}}{E_{on,I_{Dts},R_{G,Dts}}} \tag{4.4.21}$$

$$L_{t,R_G,off} = \frac{E_{off,I_{Dts},R_G}}{E_{off,I_{Dts},R_{G,Dts}}} \tag{4.4.22}$$

$$L_{d,R_G} = \frac{E_{rec,I_{Dts},R_G}}{E_{rec,I_{Dts},R_{G,Dts}}} \tag{4.4.23}$$

Where:

- E_{on,I_{Dts},R_G}: Switch-on energy at datasheet's current and specific gate resistance (J)
- $E_{on,I_{Dts},R_{G,Dts}}$: Switch-on energy at datasheet's current and the datasheet gate resistance (J)
- E_{off,I_{Dts},R_G}: Switch-off energy at datasheet's current and specific gate resistance (J)
- $E_{off,I_{Dts},R_{G,Dts}}$: Switch-off energy at datasheet's current and the datasheet gate resistance (J)
- E_{rec,I_{Dts},R_G}: Reverse recovery energy at datasheet's current and specific gate resistance (J)
- $E_{rec,I_{Dts},R_{G,Dts}}$: Reverse recovery energy at datasheet's current and the datasheet gate resistance (J)

The last factor to be calculated is $L_{V_{DC}}$ corresponding to the DC collector-emitter voltage. All the graphs of the datasheet regarding the switching losses have been produced by applying a DC voltage of 1800 V to the collector-emitter. Therefore they have to be adjusted to the DC voltage that is applied during the MMC operation. This voltage is equal to the average SM capacitor's voltage divided by the number of switches that are connected in series. The factor is the same for the three different kinds of switching losses and it is derived as shown in 4.4.24. A visual representation of the procedure of calculating the correction factors is shown in Figure 4.31.

$$L_{V_{ceDC}} = \frac{V_C/N_{Series}}{V_{ceDC,Dts}} \tag{4.4.24}$$

Where:

- V_C: SM capacitor's voltage (V)
- N_{Series}: Number of IGBT modules in series composing a SM's switch $(-)$
- $V_{ceDC,Dts}$: Datasheet collector-emitter DC voltage (V)

Since all of the three correction factors are determined the switching losses can be deduced as shown below:

$$E_{on} = E_{on,i_{arm},T_{Dts}}\ L_{t,T,on}\ L_{t,R_G,on}\ L_{V_{ceDC}} \tag{4.4.25}$$

$$E_{off} = E_{off,i_{arm},T_{Dts}}\ L_{t,T,off}\ L_{t,R_G,off}\ L_{V_{ceDC}} \tag{4.4.26}$$

$$E_{off} = E_{rec,i_{arm},T_{Dts}}\ L_{d,T}\ L_{d,R_G}\ L_{V_{ceDC}} \tag{4.4.27}$$

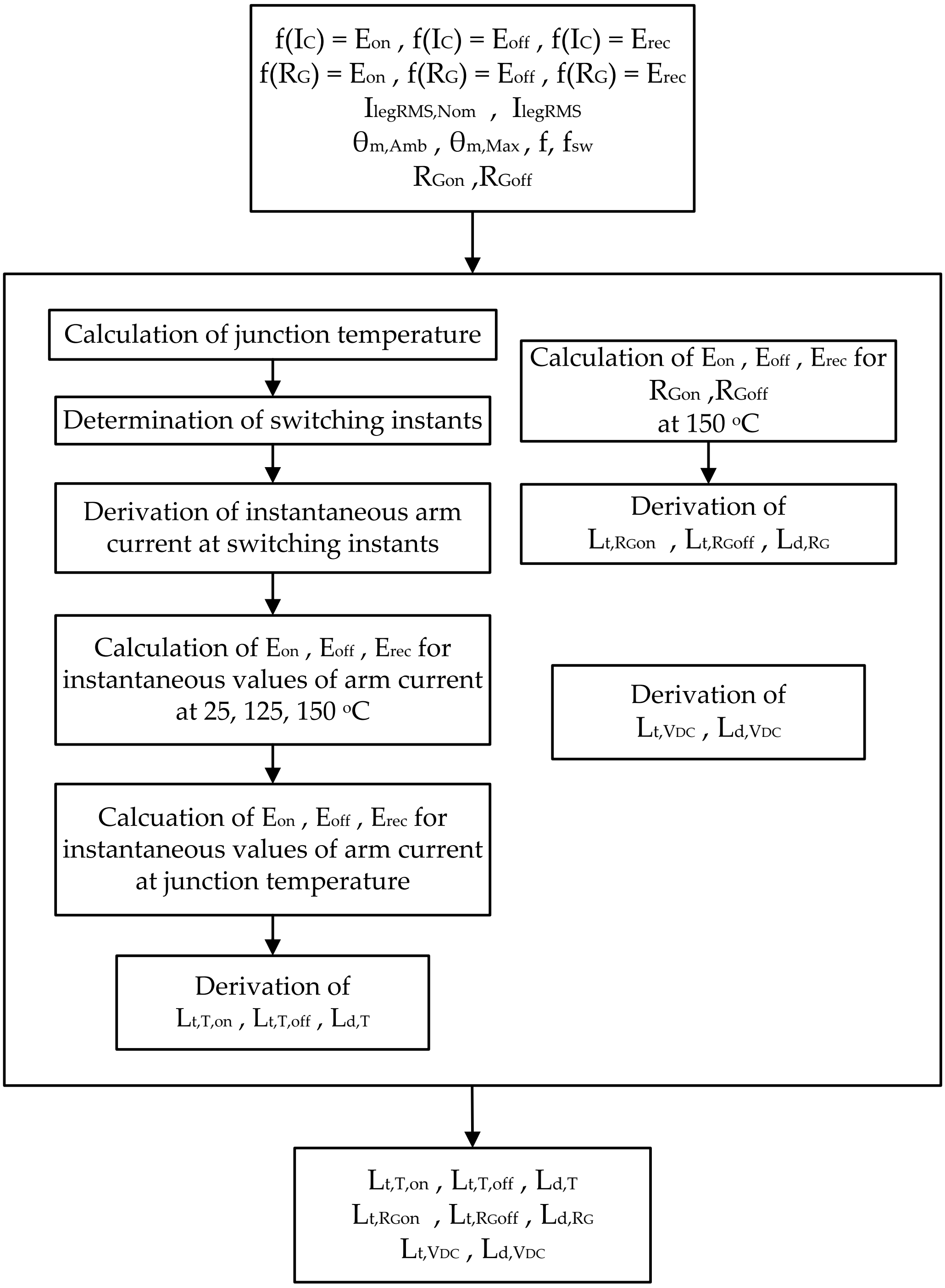

FIGURE 4.31: Calculation of temperature, gate resistance and DC voltage correction factors

After the losses are calculated for two periods as previously explained, they are added and divided by two in order to derive the average total switching loses of a fundamental period. This value is then multiplied by the fundamental frequency to derive the switching power losses in watts. The procedure is summarized in Figure 4.32.

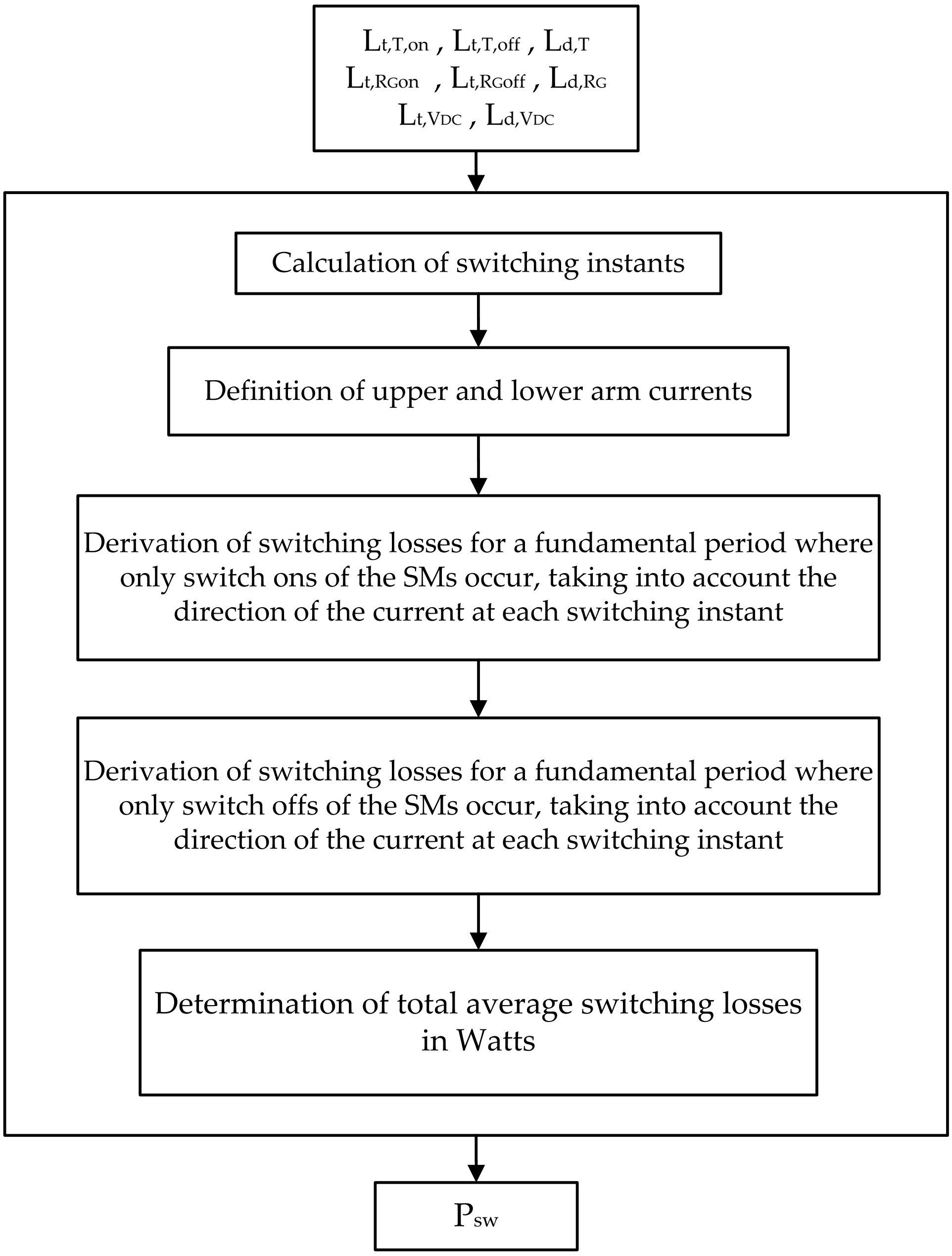

Figure 4.32: Calculation of the Switching Losses

4.4.2.3 Inductors' Losses

Each arm of an MMC has an air-core type inductor, for limiting parasitic currents and fault currents [54]. The resistance of these inductors is a source of ohmic losses which has to be taken into account in the calculation of the total losses.

The current that flows though the upper and lower inductor of each leg is the upper and lower arm current respectively. Because of the currents' magnitude several inductors are connected in parallel. In addition, the arm inductor is considered to be split into smaller inductors connected at each SM. The model requires as inputs the rated current and the DC and AC resistance at 20 °C of one of the smaller inductors connected in parallel at each SM and calculates the total arm inductance and the corresponding ohmic losses.

In addition, the model takes into account the AC and DC resistances' dependence on the temperature variation:

$$R^{\theta_i}_{indDC} = R^{20}_{indDC}[1 + \alpha_{20}(\theta_i - 20)] \tag{4.4.28}$$

$$R^{\theta_i}_{indAC} = R^{20}_{indAC}[1 + \alpha_{20}(\theta_i - 20)] \tag{4.4.29}$$

Where:

- $R^{\theta_i}_{indDC}$: DC resistance of an arm inductor at θ_i °C (Ω)
- R^{20}_{indDC}: DC resistance of an arm inductor at 20 °C (Ω)
- a_{20}: Constant mass temperature coefficient at 20 °C (K^{-1})
- θ_i: Temperature of the conductor (°C)
- $R^{\theta_i}_{indAC}$: AC resistance of an arm inductor at θ_i °C (Ω)
- R^{20}_{indAC}: AC resistance of an arm inductor at 20 °C (Ω)

It is assumed that the inductors' temperature varies similarly to the junction temperature of the semiconductors, which is linearly dependent to the RMS current flowing through them. Their temperature is equal to the ambient temperature when no current flows and it reaches its maximum value at full load.

Consequently, the losses are calculated. As seen from equations 4.3.20 - 4.3.24, the arm current has DC and an AC component. Therefore the ohmic losses of an arm inductor per phase are given by the following expression:

$$P_{ind} = I^2_{legDC}R^{\theta_i}_{indDC} + I^2_{legAC}R^{\theta_i}_{indAC} = \left(\frac{I_{DC}}{3}\right)^2 R^{\theta_i}_{indDC} + \left(\frac{I_{AC}}{2}\right)^2 R^{\theta_i}_{indAC} \tag{4.4.30}$$

Where:

- I_{legDC}: DC current at a leg of the converter (A)
- I_{legAC}: RMS value of AC current at a leg of the converter (A)
- I_{DC}: Current at the DC side of the converter (A)
- I_{AC}: Line current at the AC side of the converter (A)

4.4.2.4 Additional Losses

Apart from the semiconductors and the inductors, other components of the converter also contribute to the total power losses. These are the losses of the control electronics and the gate drivers of the SMs and the power demands of the cooling system of the converter.

Gate Drivers' Losses These are losses corresponding to the control electronics and gate drivers. According to [23] these losses can be taken equal to 50 W per voltage level:

$$P_{gate3ph} = 3 \cdot 2N_{SM} \cdot 50 \tag{4.4.31}$$

Where:

- N_{SM}: Number of SMs per arm ($-$)

Cooling System Losses Large converters need a cooling system for the dissipation of the generated heat due to the power losses of the semiconductors. In its most common configuration, this system consists of a single cooling circuit which circulates a cooling agent between the IGBT modules and the outdoor heat exchangers (Figure 4.33. The cooling medium is usually water or a mixture of water and ethylene or propylene glycol when sub-zero temperatures are involved [74].

The coolant is passed from the manifolds to the heat sink of the IGBT modules through pipes made of XLPE in order to provide high dielectric strength against the high voltage stresses on the module. The electrical conductivity of the coolant is important for the operation of the system. Therefore, a portion of the coolant continuously passes through a de-ionizer to maintain its conductivity and consequently the leakage currents in the cooling circuit at very low levels [74].

Furthermore, to ensure high reliability of the system, critical components (pumps, heat exchangers) can be duplicated. A bypass valve prevents very low temperature coolant to circulate

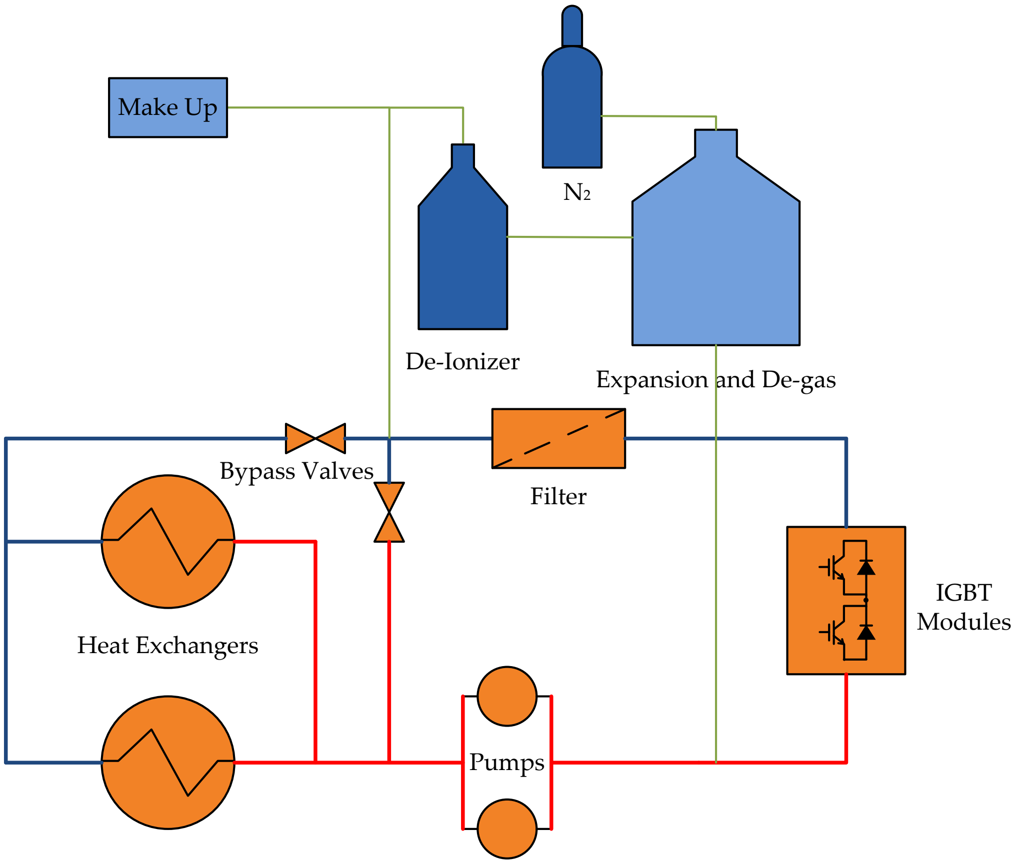

FIGURE 4.33: Typical cooling system of a MMC

through the IGBT modules avoiding the risk of condensation on the modules during the start up of the system. Once the heat sinks of the modules and the coolant have warmed up, the valve changes to allow full cooling from the outdoors heat exchangers [74].

Finally, an expansion vessel under a nitrogen blanket is used for adjusting changes in the coolant quantity during operation. A de-gasifier removes the small amount of gas produced by electrolytic action on the cooling agent [74].

It is evident that the cooling system of a large MMC is a quite complex configuration. Consequently, it is very difficult to determine its power requirements without knowing exact figures regarding the components of the system (power consumption of the pumps, the control scheme of the heat exchangers' fans etc).

For this reason an approximate calculation is conducted based on the concept of the coefficient of performance (COP) of the cooling system. The COP is the ratio of the extracted heat over the power needed to achieve this extraction [75]:

$$COP = \frac{Q}{W} \tag{4.4.32}$$

Where:

- Q: Rate of heat extraction from the system (W)
- W: Work needed for heat extraction (W)

It is assumed that the only devices cooled by the cooling system are the semiconductors, since the inductors of the MMC are dimensioned in such a way that do not require additional cooling than the natural convection of air. Having calculated the power losses of the semiconductors as explained in the previous sections (Sections 4.4.2.1, 4.4.2.2) and assuming a COP for the cooling configuration, its power requirements are determined using equation 4.4.32.

4.4.3 Model Assessment

In order to evaluate the behavior of the model and its results, it is compared to another average operation model developed by Allebrod, Hamerski and Marquardt and presented in [23]. For this reason, Marquardt's model is transferred in Matlab and the results of [23] are reproduced as an assessment for the correct operation of the Matlab code. Consequently, a number of comparisons of the two models are made.

There are some differences between the models. Firstly, Marquardt's model considers that the semiconductors operate at their maximum junction temperature. Secondly the gate resistance is not taken into account in the switching losses calculation. In addition, it calculates the conduction and switching losses using a different approach which is based on analytical expressions of the average currents flowing through the four semiconductors of a SM.

Furthermore, Marquardt's model assumes that both conduction and switching losses are directly proportional to the power and hence the current. Although this is a fair assumption for the conduction losses, this is not the case for the switching losses. As it can be seen from the IGBT module's datasheet (Figure 4.29), the switching losses are considerable even for very low values of current.

In addition, the proposed model considers the inductors' ohmic losses as well as the power demands of the cooling system. The additional losses of the control electronics and gate drivers as described in section 4.4.2.4, are taken into account by both models in the same fashion.

Therefore, several comparisons are conducted. For the first comparison, the switching losses for the proposed model are modeled in the same manner as in Marquardt's model. In addition, the junction temperature and the gate resistance impact and the inductors' and cooling losses are deactivated on the presented model. For the second comparison, the switching losses for the proposed model are calculated based on the original graphs of the IGBT module's datasheet.

After the first two comparisons with Marquardt's model, additional capabilities of the proposed model are shown through comparisons that only involve the later. In the third comparison, the two cases of having the temperature impact activated or not are assessed. During the forth comparison, with the temperature variation activated, the inductors' losses are taken into account. In the fifth comparison the cooling losses are activated in addition to the previous comparison. Finally, the sixth comparison shows the impact of the gate resistance on the switching and thus the total losses.

In the first and second comparison, results are presented for both inverter and rectifier operation, but for the rest of the comparisons only results of inverter operation are shown for economy of space.

4.4.3.1 Reproduction of Marquardt's Model

The properties of the MMC presented in [23] are shown in Table 4.5 while the characteristics of the semiconductors are summed in Table 4.6.

Converter Properties		
Variable	Unit	Value
$P_{DC,Nom}$	(W)	$335 \cdot 10^6$
V_{DC}	(V)	$300 \cdot 10^3$
m	$(-)$	0.95
$cos(\phi)$	(rad)	0.88
f	(Hz)	50
f_{sw}	(Hz)	150
N_{SM}	$(-)$	125

TABLE 4.5: Converter properties of the numerical example presented in [23]

Semiconductors' Characteristics				
Semi	IGBT T_1	IGBT T_2	Diode D_1	Diode D_2
$V_{ce0}(V)$	1.8	1.8	-	-
$R_{ce}(m\Omega)$	2.4	1.6	-	-
$V_{d0}(V)$	-	-	1.8	1.8
$R_d(m\Omega)$	-	-	3.0	2.0
$E_{on}(J)$	4.0	4.0	-	-
$E_{off}(J)$	2.7	2.7	-	-
$E_{rec}(J)$	-	-	0.5	0.5

TABLE 4.6: Characteristics of the semiconductors in [23]

Figures 4.34 and 4.35 show the losses of each semiconductor of a SM, in inverter operation, as presented in [23] and reproduced respectively. In addition, Figure 4.36 shows the efficiency curve of the inverter as presented in [23] and reproduced respectively. It can be seen that the reproduced figures are identical to the original ones. The same accuracy is achieved for the Rectifier operation.

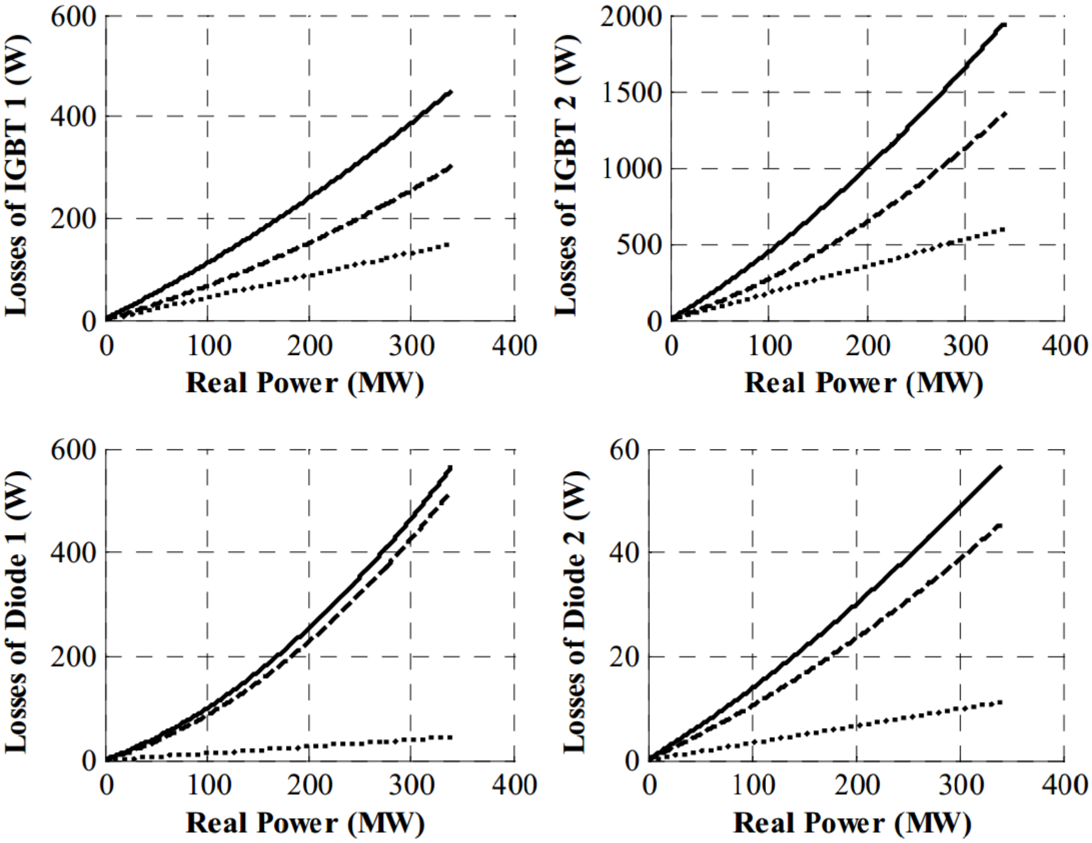

Figure 4.34: Semiconductor's losses as presented in [23]

4.4.3.2 First Comparison: Comparing on the same basis

The accurate reproduction of the results published in [23] show that the Matlab code of Marquardt's model works as intended. Consequently, its performance can be compared to the proposed model of this thesis. A different numerical example is realized for this reason, since in the numerical example presented in [23] the semiconductors are not identical but they have different resistances as seen in Table 4.6. This is against the assumption, on which the proposed model is developed, that all IGBT modules are identical.

A 510 MVA MMC, which uses the $FZ1000R33HL3$ IGBT module, is employed to compare both models. The properties of the converter are summarized in Table 4.7. A detailed list of all the characteristics of the converter is provided in Appendix B.5.

In order to implement the same approach as Marquardt's model for the switching losses, the switching losses' curves retrieved from the IGBT's datasheet are shifted downwards until they become equal to zero for zero current. As a result the switching losses become directly proportional to the power and hence the current for the proposed model similarly to the Marquardt's approach. Figures 4.37 and 4.38 show the efficiency and losses for inverter and rectifier operation respectively. The losses are expressed as percentages of the rated active power of the

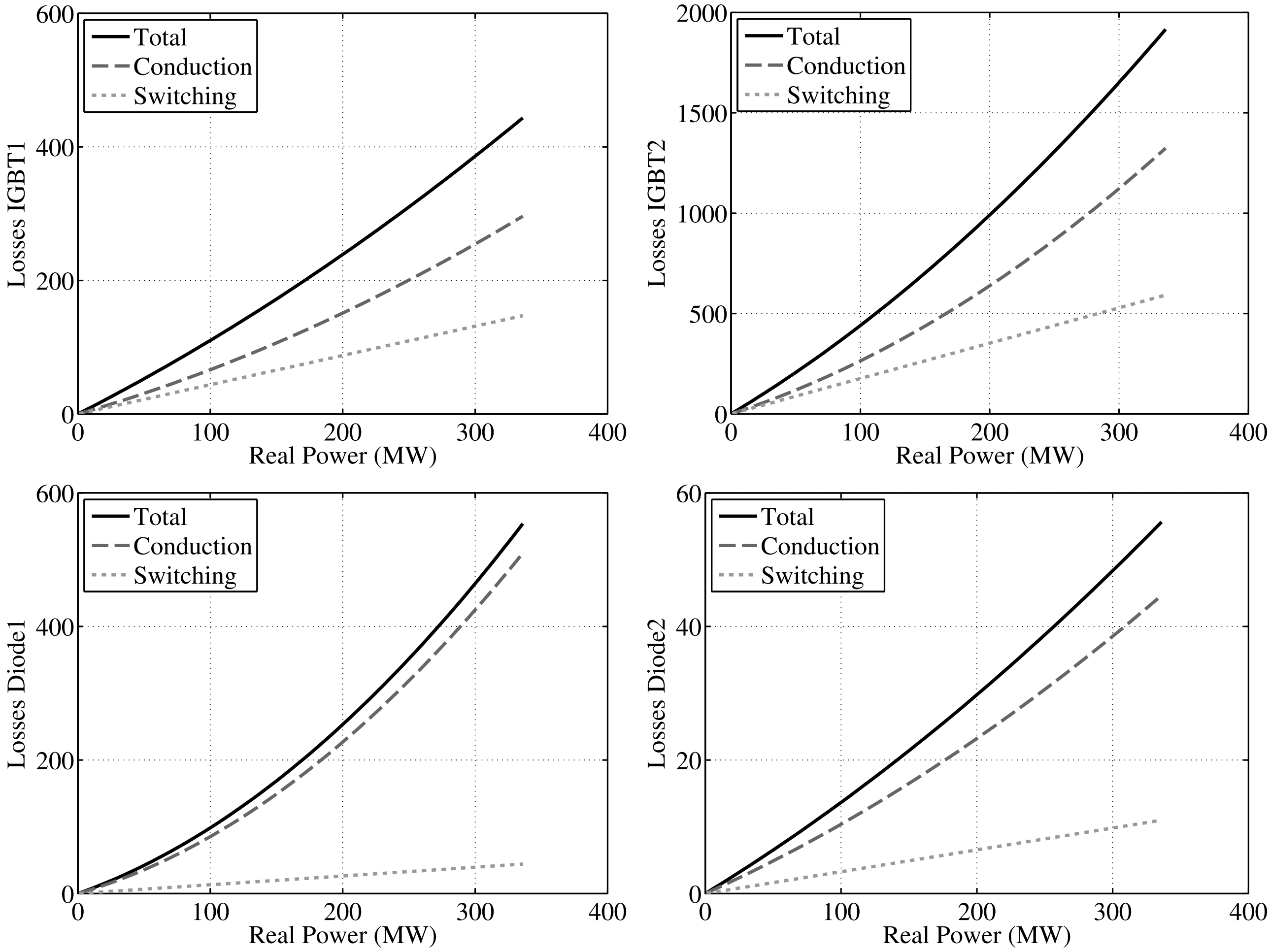

FIGURE 4.35: Semiconductor's losses reproduced

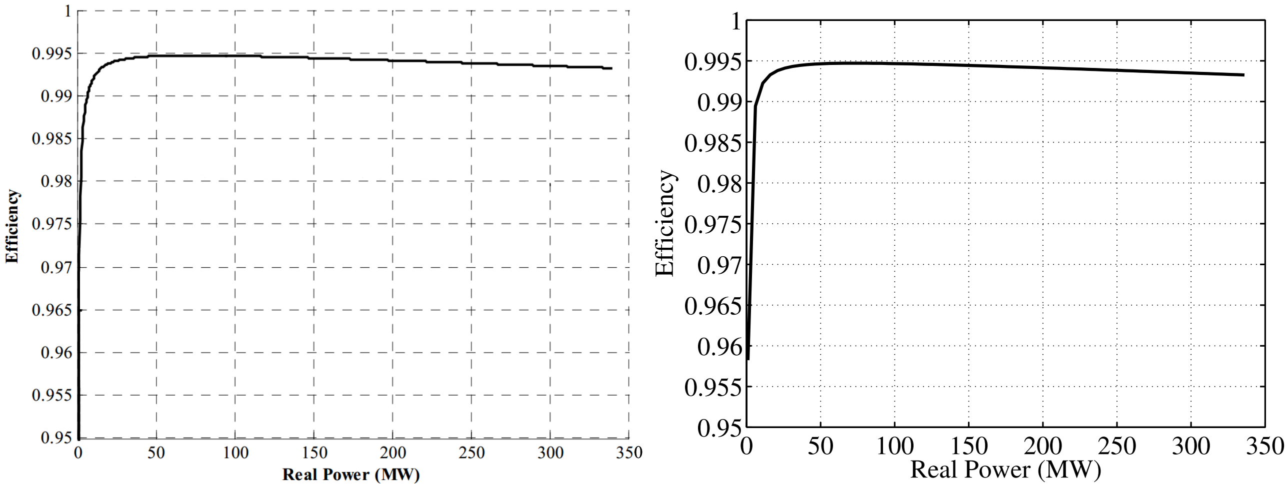

(A)

(B)

FIGURE 4.36: Inverter efficiency: (A) As presented in [23] (B) Reproduced

Converter Properties		
Variable	Unit	Value
$P_{DC,Nom}$	(W)	$500 \cdot 10^6$
$P_{AC,Nom}$	(W)	$500 \cdot 10^6$
$Q_{AC,Nom}$	(VAr)	$100 \cdot 10^6$
V_{DC}	(V)	$450 \cdot 10^3$
m	$(-)$	0.8
$cos(\phi)$	(rad)	0.98
f	(Hz)	50
f_{sw}	(Hz)	150
N_{SM}	$(-)$	38

Table 4.7: Converter properties of the new numerical example

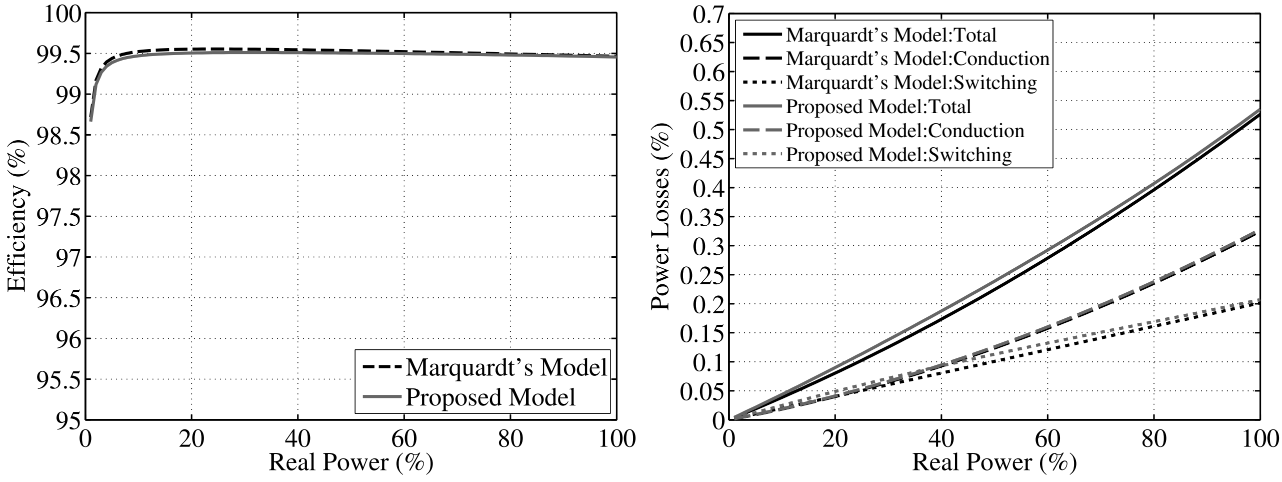

(A) (B)

Figure 4.37: Using the same approach for the switching losses in inverter operation: (A) Comparison of efficiency curves (B) Comparison of losses curves

converter. Tables 4.8 and 4.9 show the difference in efficiency between the two models for some specific power levels.

Inverter operation: Comparison of Efficiency curves						
Power (%)	10	20	40	60	80	100
Marquardt's Model Efficiency (%)	99.52	99.55	99.54	99.52	99.49	99.46
Proposed Model Efficiency (%)	99.47	99.50	99.51	99.50	99.48	99.46
Difference (%)	0.05	0.05	0.03	0.02	0.01	0

Table 4.8: Efficiency of the inverter calculated by both models for different power levels using the same approach for the switching losses

For inverter operation, the efficiency curves calculated by both models are almost identical. A better insight of the calculations is provided in Figure 4.37B. Firstly, it is seen that the conduction losses are practically the same for both models. This is a strong indication that the conduction losses are calculated accurately. The switching losses are slightly different. This fact is the source of the insignificant but existing difference between the efficiency curves.

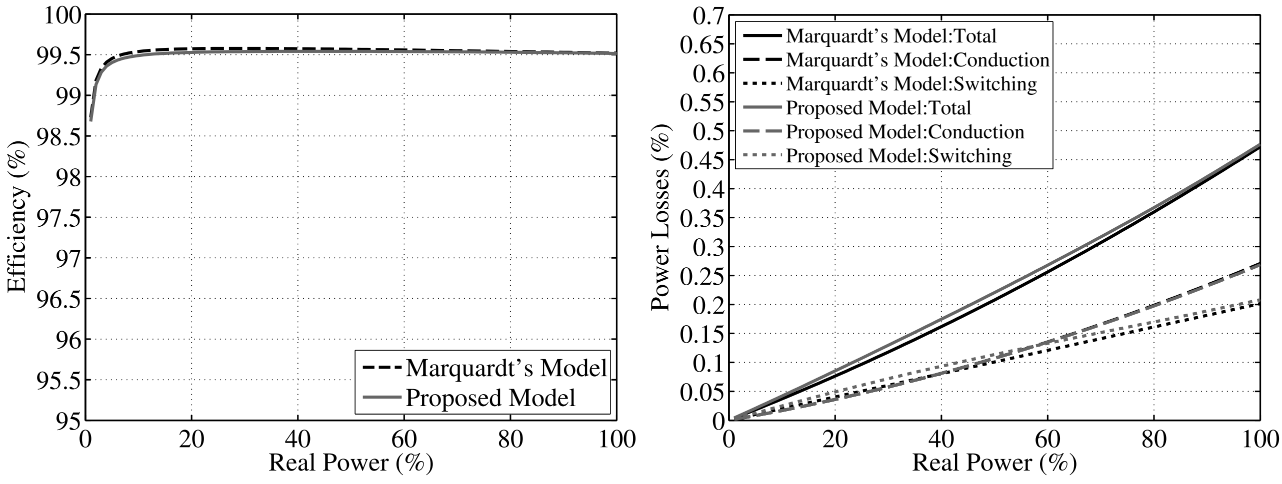

(A) (B)

FIGURE 4.38: Using the same approach for the switching losses in rectifier operation: (A) Comparison of efficiency curves (B) Comparison of losses curves

Rectifier operation: Comparison of Efficiency curves						
Power (%)	10	20	40	60	80	100
Marquardt's Model Efficiency (%)	99.54	99.57	99.57	99.56	99.54	99.52
Proposed Model Efficiency (%)	99.49	99.53	99.54	99.54	99.53	99.52
Difference (%)	0.05	0.04	0.03	0.02	0.01	0

TABLE 4.9: Efficiency of the rectifier calculated by both models for different power levels using the same approach for the switching losses

Regarding the rectifier operation, similar results to the inverter case are obtained. It can be seen that the efficiency is higher when the converter operates as a rectifier. This is a result of the different resistance of the semiconductors of the IGBT module. Depending on the direction of the current either the IGBT or the antiparallel diode conducts. Since these components have different resistances, the calculated conduction losses also differ.

4.4.3.3 Second Comparison: Calculating the Switching Losses Differently

This comparison is conducted between Marquardt's model and the proposed model with calculating the switching losses based on the original graphs of the datasheet. The efficiency and the losses, in inverter operation, are shown in Figure 4.39.

For power transmission below 20% of the rated, there is a considerable difference between the two efficiency curves. However, with increasing power, the curves converge.

The results can be explained using 4.39B. First of all, the conduction losses are again identical for both models, as expected. Regarding the switching losses, it can be seen that the rate in which they increase is similar for both models. But the switching losses calculated by the proposed model are shifted upwards compared to the ones determined by Marquardt's model.

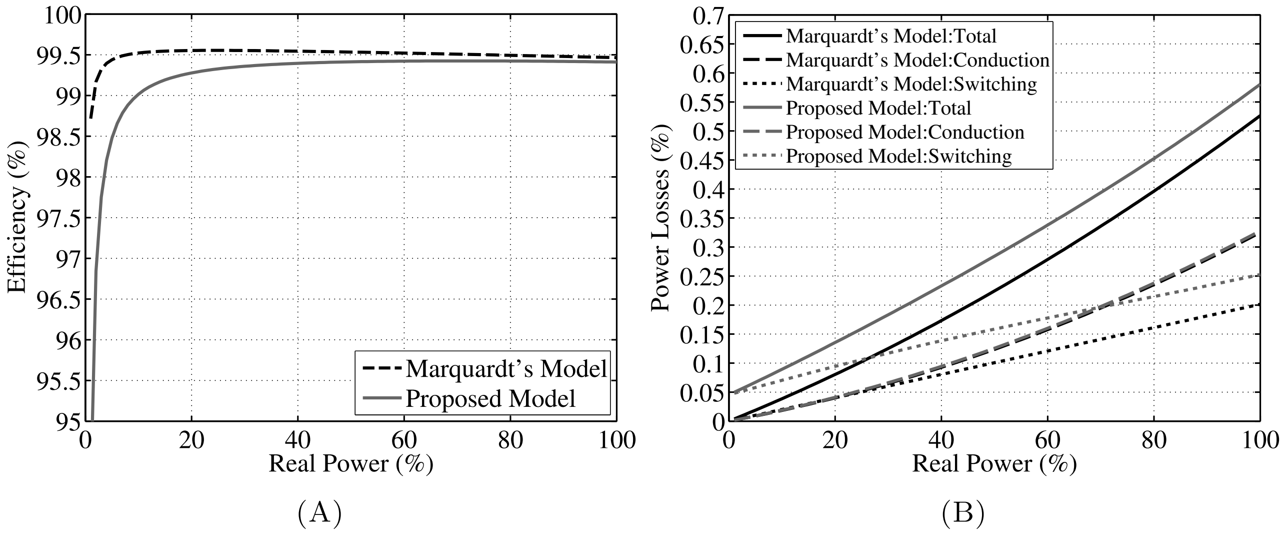

Figure 4.39: Calculating the switching losses differently in inverter operation: (A) Comparison of efficiency curves (B) Comparison of losses curves

With increasing power, the impact of the conduction losses also increases. Therefore the effect of the switching losses on the efficiency curves is gradually mitigated and the gap between them decreases.

Similar graphs for the rectifier operation are presented in Figure 4.40. As already explained, the difference in the efficiency between the inverter and rectifier operation is a result of the different resistance of the semiconductors of the IGBT module.

Tables 4.10 and 4.11 give the efficiency of the converter at different power levels calculated by both models for inverter and rectifier operation respectively.

Inverter operation: Comparison of Efficiency curves						
Power (%)	10	20	40	60	80	100
Marquardt's Model Efficiency (%)	99.52	99.55	99.54	99.52	99.49	99.46
Proposed Model Efficiency (%)	99.02	99.28	99.39	99.42	99.42	99.41
Difference (%)	0.50	0.27	0.15	0.10	0.07	0.05

Table 4.10: Efficiency of the inverter calculated by both models for different power levels

Rectifier operation: Comparison of Efficiency curves						
Power (%)	10	20	40	60	80	100
Marquardt's Model Efficiency (%)	99.54	99.57	99.57	99.56	99.54	99.52
Proposed Model Efficiency (%)	99.03	99.30	99.43	99.46	99.47	99.47
Difference (%)	0.51	0.27	0.14	0.10	0.07	0.05

Table 4.11: Efficiency of the rectifier calculated by both models for different power levels

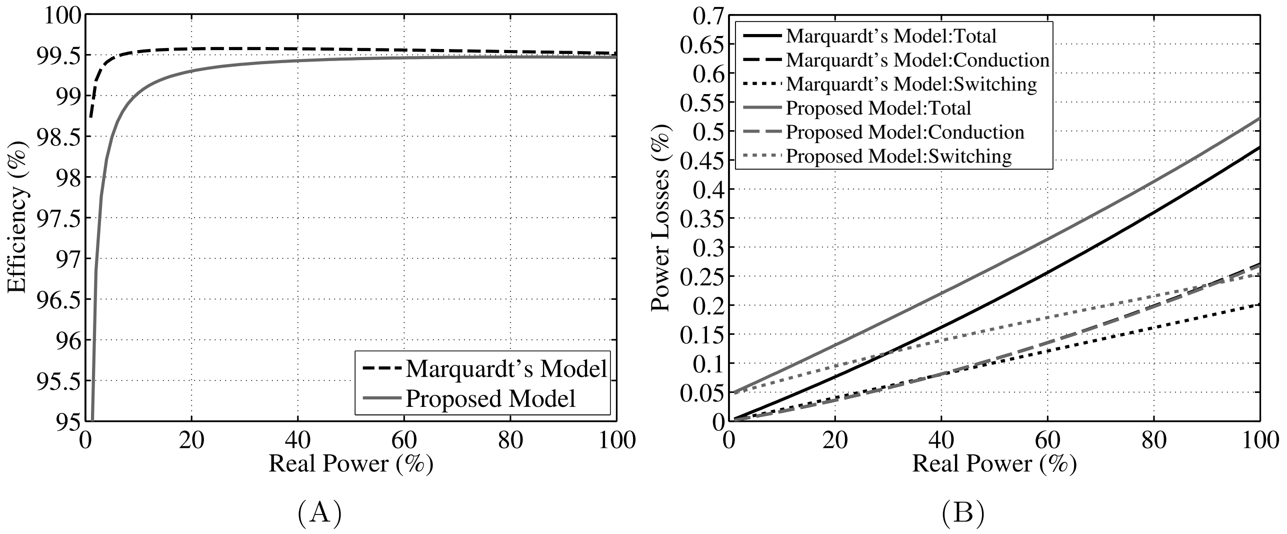

FIGURE 4.40: Calculating the switching losses differently in rectifier operation: (A) Comparison of efficiency curves (B) Comparison of losses curves

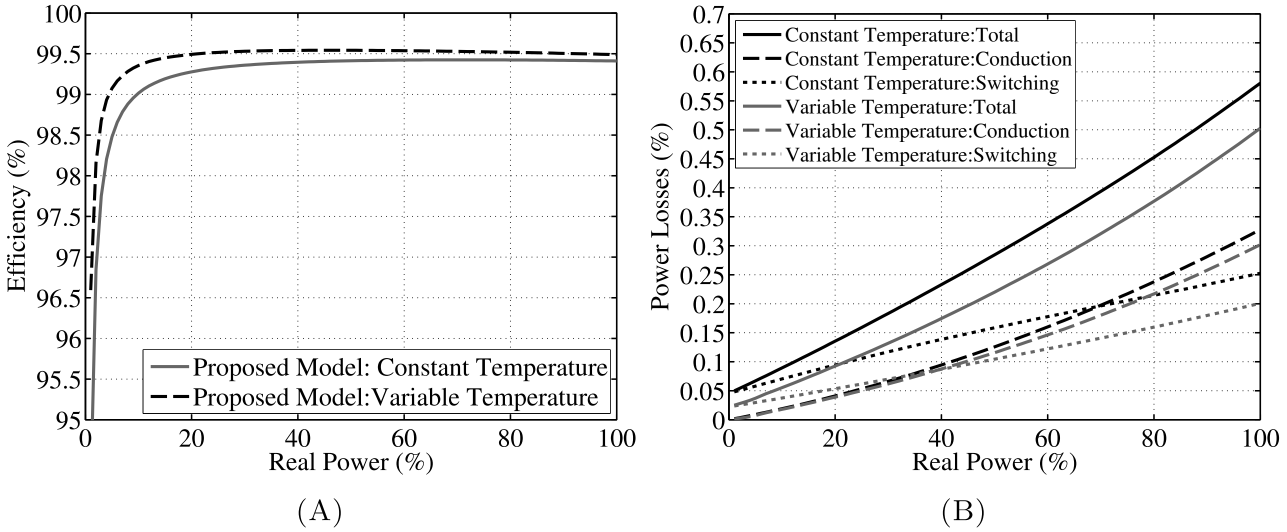

FIGURE 4.41: Activating the temperature impact in inverter operation: (A) Comparison of efficiency curves (B) Comparison of losses curves

4.4.3.4 Third Comparison: Activating the Temperature Impact

In the third comparison, the proposed model takes into account the impact of the semiconductors' temperature for the calculation of the losses. It is assumed that the temperature varies linearly from 20 °C when the RMS arm current is equal to zero to 90 °C for rated RMS arm current. Figure 4.41 shows the efficiency and losses of the proposed model when the temperature impact is deactivated (constant temperature) and when it is activated (variable temperature) for inverter operation. Table 4.12 presents the efficiency of the converter at different power levels calculated for the two scenarios.

The efficiency of the MMC is higher when the temperature impact is activated since the losses are not calculated at 150 °C. Instead they are calculated at a range of temperatures from 20 °C

Inverter operation: Comparison of Efficiency curves						
Power (%)	10	20	40	60	80	100
Proposed Model Efficiency (Constant Temperature) (%)	99.02	99.28	99.39	99.42	99.42	99.41
Proposed Model Efficiency (Variable Temperature) (%)	99.36	99.49	99.54	99.54	99.52	99.49
Difference (%)	−0.34	−0.21	−0.15	−0.12	−0.10	−0.08

Table 4.12: Efficiency of the inverter calculated by the proposed models with and without temperature variation for different power levels

to 90 °C. As seen from Figure 4.41B the conduction losses start from zero for both scenarios. However, in case of constant temperature, the losses increase more rapidly especially for lower power since there the temperature difference is more pronounced.

Furthermore, the switching losses begin at a lower value when the temperature impact is activated compared to the case of constant temperature. The curve for variable temperature follows a constantly increasing rate since for increasing power, the temperature rises and so do the switching losses. The curve for constant temperature increases vigorously in the beginning and continues to rise with a slightly decelerating rate which is a result of the combined role of the IGBT modules' switching and reverse recovery curves at 150 °C (Figures 4.29). Specifically, the rate of increase of the reverse recovery losses is sharply reduced after 600 A. Overall, The gap between the two curves increases for the largest part of the power range and becomes slightly smaller close to the rated power.

Figure 4.42A shows the temperature correction factors $K_{t,T}$ and $K_{d,T}$ regarding the conduction losses of the IGBT and the antiparallel diode respectively. Figure 4.42B presents the temperature correction factors $L_{t,T,on}$, $L_{t,T,off}$ and $L_{t,T,rec}$ corresponding to the switching on and off losses of the IGBT and the reverse recovery losses of the diode respectively.

First of all, is should be mentioned that the correction factors for conduction (expressions 4.4.10, 4.4.11) are calculated based on the respective curves at 150^oC (Figure 4.25). The ones regarding the switching (expressions 4.4.18-4.4.20) are computed based on the respective curves at 125^oC (Figure 4.29, since it does not really matter which datasheet curve is used.

Factor $K_{t,T}$ is always below 1 while factor $K_{d,T}$ is above 1 for the whole range of power. This can be explained through Figures 4.25A and 4.25B. Regarding the IGBT, for a specific value of the collector current, the curve at 25 °C corresponds to a lower collector-emitter voltage compared to the curve at 150 °C. Therefore this is the case for all temperature between 25 °C and 150 °C and the correction factor takes values lower than unity. Regarding the diode exactly the opposite is applicable and $K_{d,T}$ which drives it above unity. The shape of the curves is a result of the combination of the slope of the datasheet curves and the linear interpolation between them due to the temperature variation.

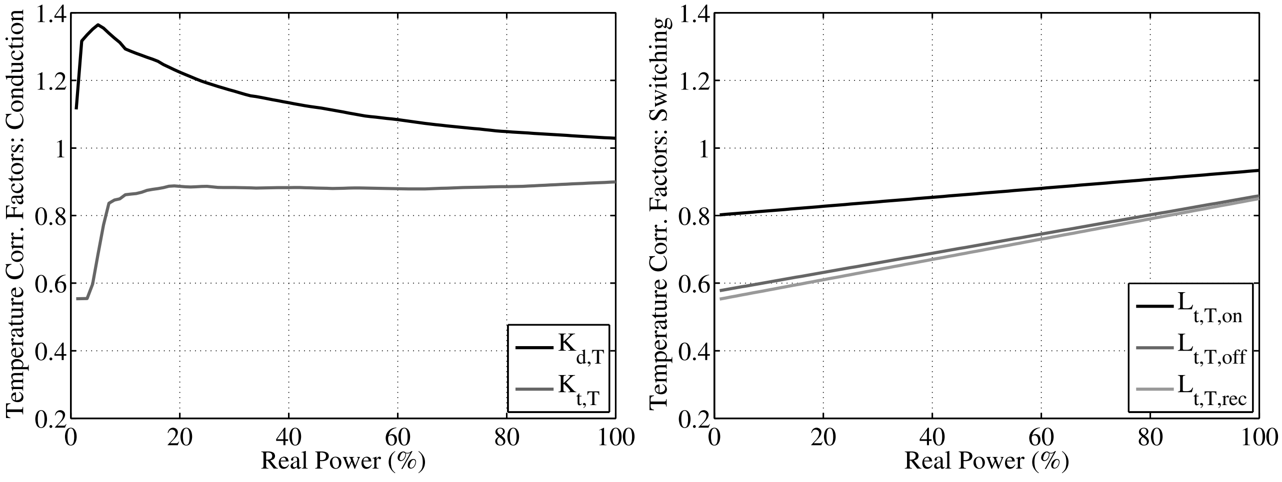

(A) (B)

Figure 4.42: Activating the temperature impact in inverter operation: (A) Temperature correction factors: Conduction (B) Temperature correction factors: Switching

The switching and reverse recovery factors are always below 1 since the switching and reverse recovery losses are higher for higher temperature (Figure 4.25). Their shape is completely linear because of the fact that the curve at 25 °C is derived by scaling down the curve at 125 °C and the temperature range is from 20 °C to 90 °C which means that the curve at 150 °C does not take part in the linear interpolation calculations.

4.4.3.5 Forth Comparison: Including the Inductor's Losses

In this section, the impact of the arm inductors' losses on the efficiency of the MMC is assessed. As mentioned before, the arm inductors limit parasitic and fault currents [54]. The arm inductance is a design parameter that depends on several variables such as the submodule capacitance and capacitor voltage, the modulation technique, the switching frequency, the optional use of a circulating current suppression technique and the limit of the fault current rise rate [68] [76]. Therefore, the losses of the MMC are calculated for different values of the arm inductances. According to [68] common values for the arm inductances are in the vicinity of 1 mH to 5 mH. Therefore four different arm inductances are assessed, namely 1 mH, 2 mH, 4 mH, 6 mH. Due to the scarcity of data regarding industrial scale inductors, their DC and AC ohmic resistances are calculated using two different online inductance calculators in combination with standards published by IEC and the National Fire Protection Association (NFPA). The calculations are thoroughly explained in Appendix B.4. Table 4.13 shows the total arm inductances and their respective resistances.

Figure 4.43 presents the efficiency of the MMC in inverter operation and the inductors' losses for the aforementioned values of arm inductance. Naturally, for larger values of the arm inductance the losses are higher since the resistance of the inductor is also higher.

Arm Inductors' Ohmic Resistances				
Total Arm Inductance (mH)	1	2	4	6
Total Arm DC Resistance at 20^oC ($m\Omega$)	71.393	104.015	150.737	187.88
Total Arm AC Resistance at 20^oC ($m\Omega$)	71.393	104.015	150.737	187.88

Table 4.13: AC and DC resistance of arm inductors for different values of arm inductance

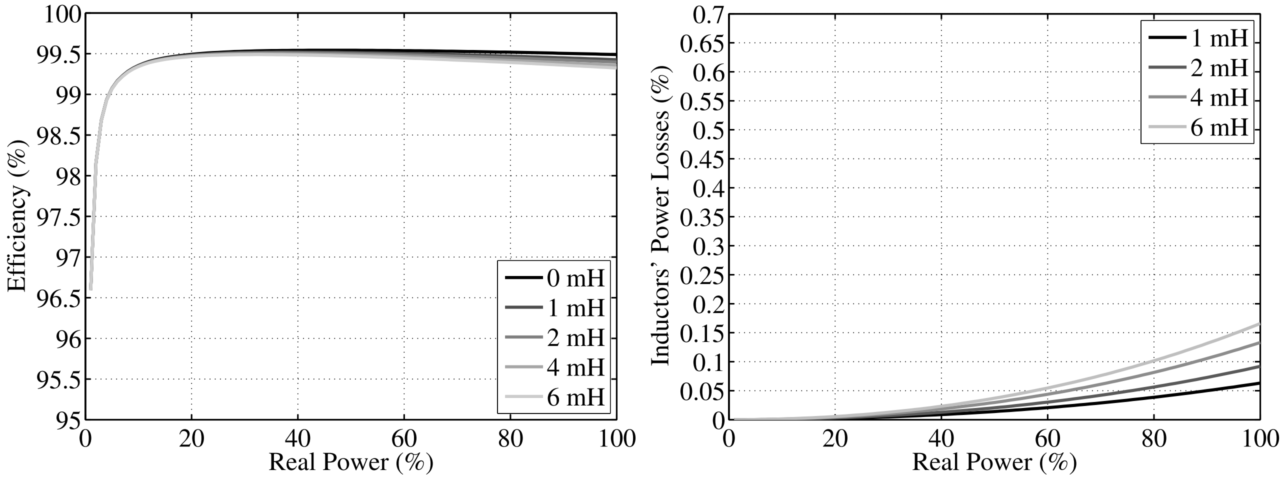

(A) (B)

Figure 4.43: Including the inductor's losses in inverter operation: (A) Efficiency for different values of arm inductance (B) Inductors' losses for different values of arm inductance

4.4.3.6 Fifth Comparison: Including the Cooling Losses

For the fifth comparison, the cooling requirements are taken into account in addition to the temperature variation impact and the consideration of an arm inductance equal to 6 mH. Due to the scarcity of information regarding cooling systems such as the one described in Section 4.4.2.4, the COP of the system is assumed equal to 20 based on similar configurations used for cooling IT applications [77].

The comparison of the efficiency curves with and without considering the cooling power requirements is shown in Figure 4.44A. In addition, Figure 4.44B presents the power losses of the MMC including the power consumption of the cooling system. Table 4.14 shows the difference between the efficiency of the two scenarios for some power levels.

It can be seen that the cooling requirements are insignificant compared to the total power losses of the MMC, which is normal considering the high COP of the cooling system.

4.4.3.7 Sixth Comparison: The Impact of the Gate Resistance

The final comparison shows the impact of the gate resistance on the switching losses. The gate resistor is an important design parameter that influences the IGBT switching time, switching

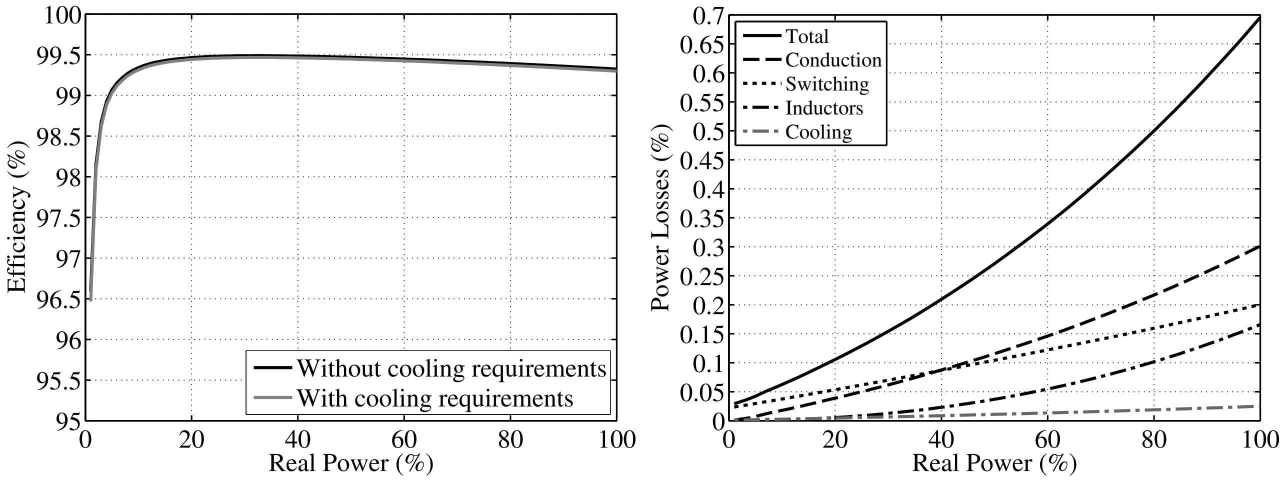

(A) (B)

Figure 4.44: Including the cooling losses in inverter operation: (A) Efficiency with and without the cooling power requirements (B) Power losses including the cooling system

Inverter operation: Comparison of Efficiency curves						
Power (%)	10	20	40	60	80	100
Proposed Model Efficiency (Without cooling) (%)	99.34	99.46	99.48	99.45	99.39	99.32
Proposed Model Efficiency (With cooling) (%)	99.31	99.44	99.46	99.42	99.37	99.30
Difference (%)	0.03	0.02	0.02	0.03	0.02	0.02

Table 4.14: Efficiency of the inverter calculated with and without cooling requirements for different power levels

losses, reverse-bias safe operating area, short-circuit safe operating area, EMI, rate of rise of current and voltage and reverse recovery current of the antiparallel diode [78].

The on and off gate resistors' values that are specified and used in the datasheet are usually the minimum values. In practice, sometimes these figures cannot be achieved due to differences between the test circuit used for the needs of the datasheet and the individual application for which the IGBT module is employed [78].

The datasheet gate resistance values of the IGBT module from Infineon, that is used for the purposes of this thesis, are to 0.75 Ω for the on gate resistance and 4.1 Ω for the off gate resistance. As it is seen from Figure 4.30, these values are indeed the minimum and as they increase the switching losses of the IGBT also increase. The reverse recovery losses follow the opposite trend but the increase of the losses regarding the IGBT are much larger. Therefore, in total, an increasing gate resistor leads to the rise of the total switching losses of the module.

Figure 4.45 shows the efficiency and the switching losses for different values of the on and off gate resistance. As expected, the losses rise as the gate resistance increases. Consequently, the efficiency of the converter decreases. Table 4.15 shows the efficiency of the converter for the datasheet values of the gate resistor compared to the efficiency achieved with a larger value of the gate resistor.

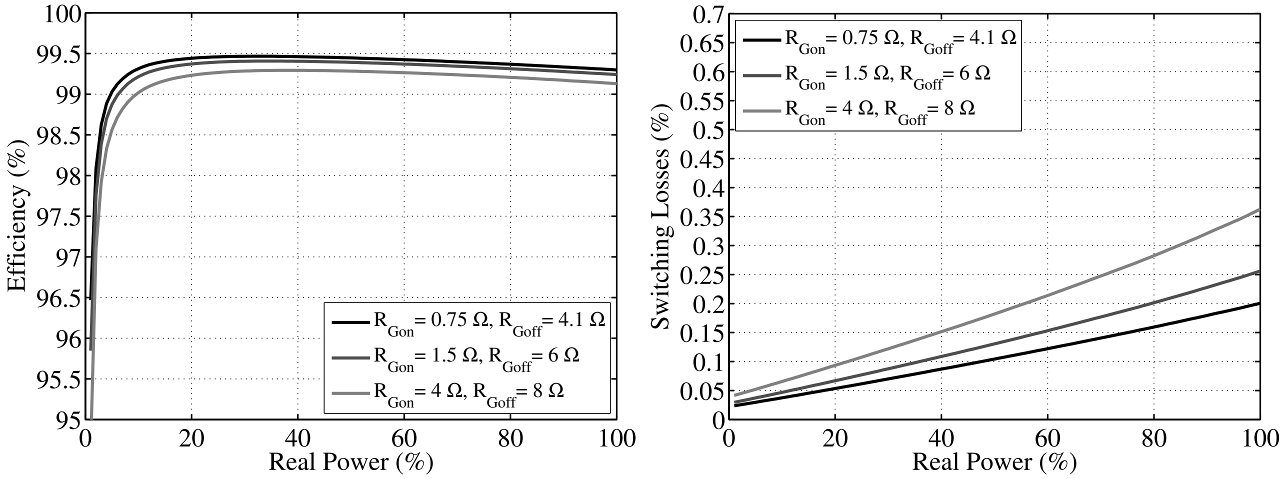

(A) (B)

Figure 4.45: The impact of the gate resistance in inverter operation: (A) Efficiency for different values of gate resistance (B) Switching losses for different values of gate resistance

Inverter operation: Comparison of Efficiency curves						
Power (%)	10	20	40	60	80	100
Proposed Model Efficiency ($R_{Gon} = 0.75\Omega$, $R_{Goff} = 4.1\Omega$) (%)	99.31	99.44	99.46	99.42	99.37	99.30
Proposed Model Efficiency ($R_{Gon} = 4\Omega$, $R_{Goff} = 8\Omega$) (%)	99.02	99.23	99.29	99.26	99.21	99.13
Difference (%)	0.29	0.21	0.17	0.16	0.16	0.17

Table 4.15: Efficiency of the inverter calculated with different gate resistance for different power levels

Chapter 5

Power Transformers

5.1 Introduction

The first practical transformer was introduced in 1884 by Zipernowsky, Deri and Blathy, a group of Hungarian engineers working for Ganz Companies in Budapest. At the same time, similar development of transformer took place in USA by Stanley and Westinghouse and in England by de Ferranti [79]. During the last century the development of transformers was phenomenal. Their operating voltage increased from several hundred volts to more than 1000 kV and their power rating from a few kVA to more than 1000 MVA [79].

Transformers have become a vital part of electrical power systems allowing the transmission of power at high voltages increasing the range of transmission and decreasing the related power losses. In a conventional power system, electric power is generated at voltages between 12 and 25 kV. Transformers step up the voltage to a range of 110 kV to nearly 1000 kV for transmission over long distances at very low losses. Transformers then step down the voltage to $12-34.5$ kV for local distribution. Finally, the voltage is stepped down again to be used safely by consumers at voltages as low as 120 V [24]. Regarding offshore wind parks, transformers are equally important since they step up the voltage of the wind generators to the voltage level of the collection system and then again to the voltage level of the transmission line.

In this chapter, initially, the operation principle and a brief introduction to the transformers' most important components is given in Sections 5.2 and 5.3 respectively. Then, the origins of power losses in transformers are explained (Section 5.4) and their equivalent electrical circuit is introduced (Section 5.5). Consequently, it is explained how the values of the elements of the equivalent circuit of a specific transformer can be determined through the open and short circuit tests (Section 5.6). Finally, in Section 5.7 the model for the calculation of the power losses of a transformer is presented.

5.2 Operation Principle

A power transformer normally consists of a pair of windings, primary and secondary, linked by a magnetic circuit or core. For the purposes of this report, the primary winding is the first winding with regards to power flow.

Regarding an ideal lossless transformer (Figure 5.1), when an AC voltage is applied to one of the windings, let it be the primary, a no-load current flows in the primary circuit which sets up an alternating magnetomotive force (mmf) and hence an alternating flux in the core. this current is also called magnetizing since it sets the magnetic flux in the core. This alternating flux links both windings and induces an electromotive force (emf) in each one of them. In the primary winding this is the back-emf and opposes the applied voltage. In the secondary winding the induced emf, is the secondary open-circuit voltage. The total voltage induced in each of the windings by the common flux is proportional to the number of turns of the windings [25]:

$$\frac{v_p}{v_s} = \frac{N_p}{N_s} = \alpha \tag{5.2.1}$$

Where:

- v_p: Voltage at the primary winding (V)
- v_s: Voltage at the secondary winding (V)
- N_p: Number of turns of the primary winding $(-)$
- N_s: Number of turns of the secondary winding $(-)$
- α: Turns ratio of the transformer $(-)$

In reality, this transformation between the primary and secondary winding is not perfect because of the transformers' internal impedance. Therefore, the output voltage of a transformer varies with the load even if the input voltage remains constant [24].

5.3 Design of Power Transformers

In this section, some of the most important components of a modern power transformer are briefly presented in order to provide the background for understanding the origins of the transformers' power losses. Short descriptions are given regarding the core and the windings, the

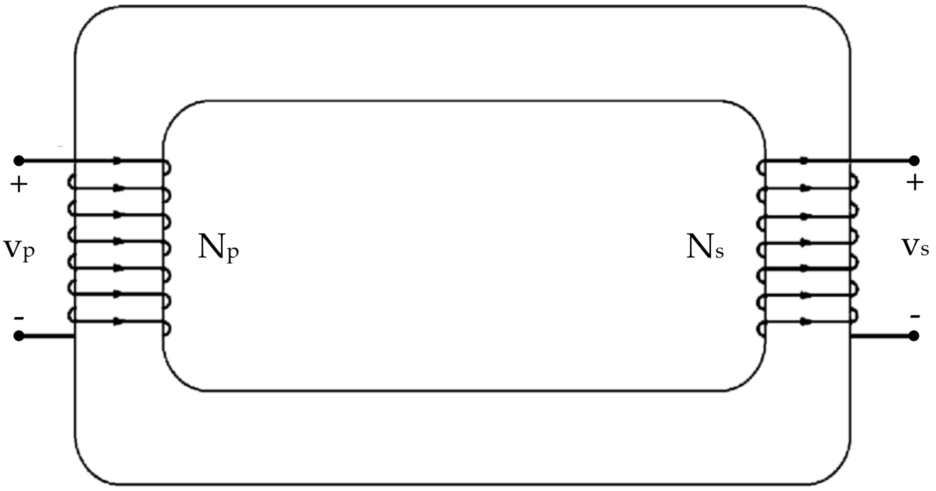

Figure 5.1: Representation of an ideal transformer [24]

insulation and cooling, the taps and the optional tertiary windings as well as the enclosure of power transformers. Finally, it is explained why oil-immersed transformers are still the most suitable for offshore wind applications.

5.3.1 Core and Windings

The role of the transformer's core is to provide a low reluctance path for the magnetic flux linking the primary and secondary windings and it is made of special steel alloys. The windings carry the load current and are almost exclusively made of high conductivity copper [25]. The turns of the LV winding usually consist of several conductors in parallel and insulated from each other in order to withstand the high currents (Figure 5.2A). In addition they are transposed to limit power losses as it is explained later. The HV windings might have ten times as many turns as the LV one in order to achieve the desirable turns ratio. For this reason, they are usually wound as disc windings as shown in Figure 5.2B [25].

There are two main types of core and windings assemblies: the shell-type and the core-type. Figure 5.3 shows three-phase transformers of both types. It is seen that the shell-type transformers have their windings enclosed by the flux-return paths of the core achieving better magnetic shielding. On the contrary, the core-type transformers have their limbs surrounded by the windings [25].

Regarding the core-type transformers, when the top and bottom yokes have the same cross section as the windings' limbs, there is no need of additional flux return paths. However, in case of large transformers it may be necessary to reduce the cross section of the upper and

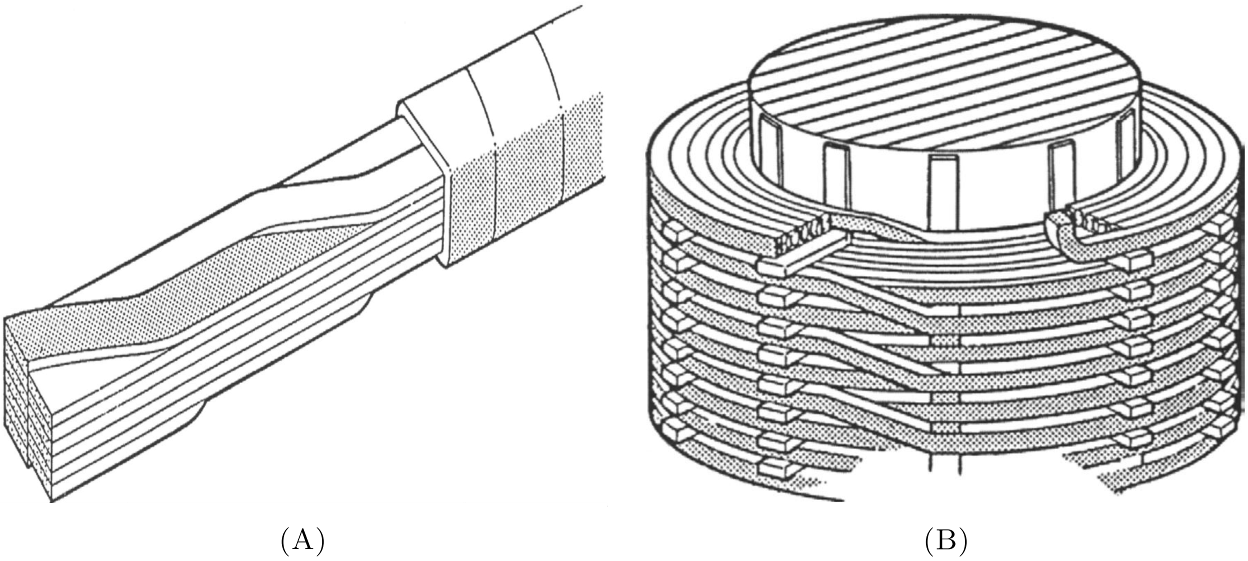

(A) (B)

Figure 5.2: Transformer Design (A) Example of LV winding conductor (B) Example of HV winding conductor [25]

lower yokes due to size restrictions. In this case, two additional flux return limbs are added to the three windings' limbs as shown in Figure 5.3 [25].

The windings of each phase are wrapped one on top of the other around a limb of the core, with the low voltage winding being innermost. In this way, the leakage flux is reduced while the issue of insulating the high voltage winding is simplified [24].

Regarding single-phase transformers, the high and low voltage windings can either be wound around the same limb or around different limbs of the core. A flux return path has to be provided in any case leading to core designs as shown in Figure 5.4.

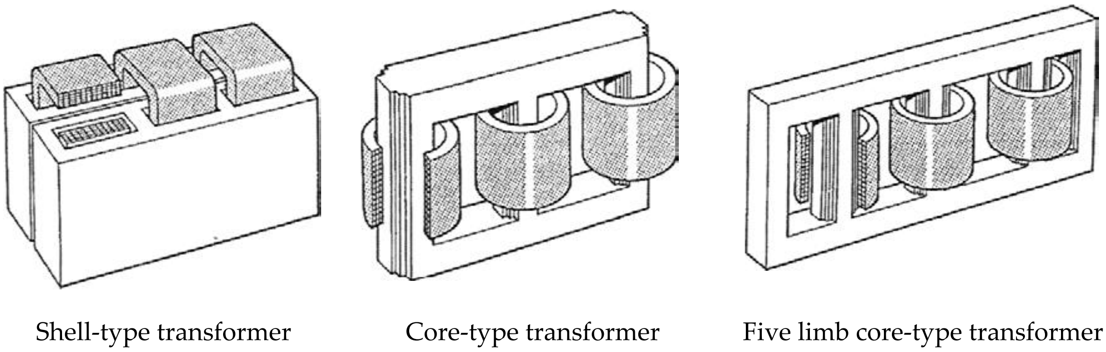

Figure 5.3: Common three-phase transformer types [25]

5.3.2 Insulation

The insulation of a power transformer includes the complete internal assembly of dielectric insulating materials. This includes parts and support structures that cover the windings, insulate

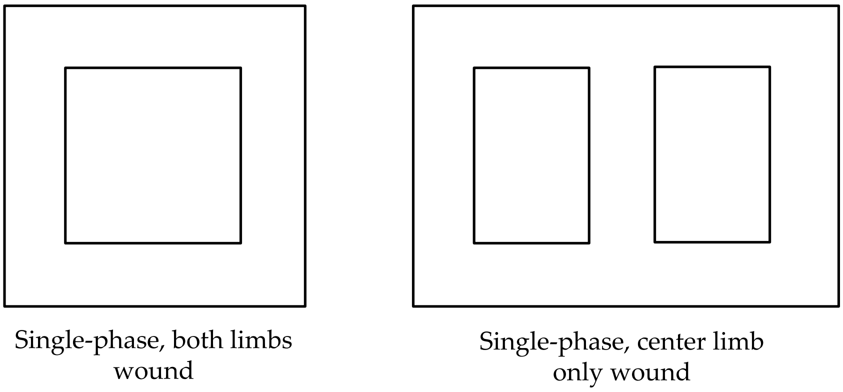

FIGURE 5.4: Common single-phase transformer cores [25]

the turns from each other, separate different winding bodies from each other as well as from the core and the enclosure [80].

There are two types of transformers with respect to their insulation: the oil-immersed and the dry-type transformers. The oil-immersed type has dominated the technology of power transformer insulation since the beginning of electrification. The last 60 years, several designs of dry-type insulation transformers have been developed and used for distribution up to some tens of MVA and moderate voltage levels [80] [81]. However, regarding large, high voltage transformers the traditional oil-filled design still prevails [80].

The insulation of oil-immersed transformers consists of the insulation fluid in combination with solid dielectric materials. Traditionally, the insulation fluid is a type of mineral oil but other fluids can be employed such as synthetic or natural esters or silicone fluids [79] [82]. In addition, the solid materials, usually employed, include different types of paper (cellulose, aramid, enamel), pressboard or even wood [79] [25].

Regarding dry-type transformers, the insulation usually consists of polyester resin. However, other materials such as silica and epoxy can be employed [25] [83].

5.3.3 Cooling

The power losses of a transformer are manifested as heat that has to be dissipated in order to keep the temperature of the device at levels that does not damage its insulation. Regarding oil-immersed transformers, the insulation fluid also acts as a primary coolant. It absorbs heat from the core and the windings and transmits it, sometimes aided by forced circulation to outer surfaces of the transformer. Figure 5.5A shows the ducts which allow the coolant to flow around the windings in an oil-immersed transformer. The outer surfaces are either naturally cooled by the ambient air or artificially cooled by water or air [25] [84].

For small dry-type transformers, the ambient air, which circulates either naturally or forced, is used as the cooling agent [25]. However, regarding larger transformers of this type a secondary cooling system using water can be employed to achieve better heat dissipation [81].

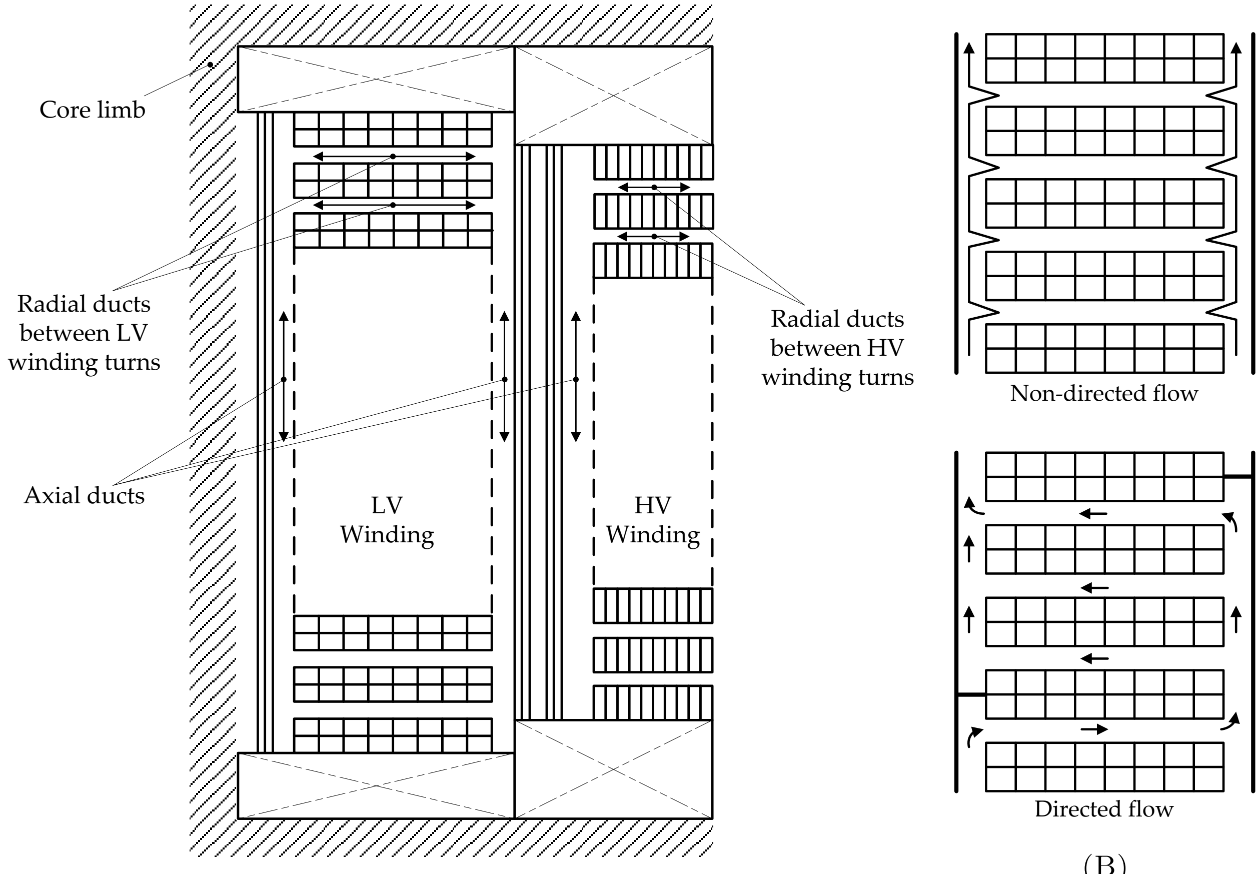

(A) (B)

FIGURE 5.5: Transformer Cooling (A) Section of LV and HV windings showing radial and axial cooling ducts (B) Directed and non-directed flow in cooling ducts [25]

According to the $IEC60076-2$ standard, the type of cooling of a transformer is specified by a code of four letters as summarized in Table 5.1. The difference between the non-directed and the directed circulation mechanism is shown in Figure 5.5B.

5.3.4 Taps and Tapchangers

In almost all real transformers, the turns ratio is not fixed but it can be adjusted between certain limits thanks to a series of taps. This adjustment may be made by tapchangers either on-load, as is the case for larger transformers, or by means of a off-load switch. In this way, it is possible to partly compensate the voltage drop at the secondary winding under varying loads [24].

Code Letters of Transformers' Cooling Systems	
Internal cooling medium	
A	Air
O	Mineral oil or synthetic insulating liquid with a fire point $\leq 300^\circ C$
K	Insulating liquid with a fire point $> 300^\circ C$
L	Insulating liquid with no measurable fire point
Circulation mechanism of internal cooling medium	
N	Natural thermosiphon flow through cooling equipment and windings
F	Forced circulation through cooling equipment, thermosiphon through windings
D	Forced circulation through cooling equipment, directed from the cooling equipment into at least the main windings
External cooling medium	
A	Air
W	Water
Circulation mechanism of external cooling medium	
N	Natural convection
F	Forced circulation (fans, pumps)

Table 5.1: Code letters specifying the cooling type of transformers according to $IEC60076-2$ [25]

However, transformers without taps are simpler, cheaper and more reliable. Therefore, whenever possible, taps should be avoided and if this is not the case, the extent of tapping range should be maintained to the minimum [25].

5.3.5 Tertiary Windings

The most usual configuration of a transformer includes only two windings: the primary and the secondary. However, sometimes, a third winding, called the tertiary, is added to the transformer. The most common reason for adding a tertiary in a three-phase transformer is to include a delta-connected winding which provides a low impedance path for third-harmonic currents [25].

In this case, a tertiary winding is intended only to magnetically interact with the primary and secondary windings so it usually does not even have external terminal connections. One corner of the Delta-connected tertiary winding is sometimes grounded internally to limit capacitively coupled voltages [26].

Other common uses of a tertiary winding include the interconnection of three circuits operating at different supply voltage and the regulation of system voltage and of reactive power by means of capacitor or reactor banks connected to its terminals [25] [26].

5.3.6 Transformer Tank

The transformer tank provides the containment for the core and the windings, supports the terminals of the electrical connections and accommodates parts of the transformer's cooling system [84].

In case of oil-immersed transformers, the tank acts as the vessel for containing the insulation fluid and caries additional components that ensure its adequate supply [84].

Regarding dry-type transformers, complete enclosure is usually not necessary. Smaller transformers can be positioned in simple steel-sheet ventilated enclosures [25]. Larger dry-type transformers are usually equipped with a support structure around their core and windings for accommodating components of their cooling system [81].

5.3.7 Power Transformers and the Offshore Wind Industry

Every wind turbine of an OWF is equipped with a transformer to step-up the voltage of the generator to the voltage level of the collection system. In addition, transformers are located on the offshore substation in order to step-up the collection system's voltage even higher to the level of the export cable that transmits the generated power to the shore. The turbines' transformer can be either fluid-filled or dry-type, while the substation's transformers are exclusively fluid-filled due to the demand of higher power ratings [82].

Regarding offshore installations, the external cooling system of the transformer is subjected to the marine environment which is humid, salty and variable in temperature. Liquid-filled transformers which are protected by their steel tanks can withstand this corrosive environment. On the other hand, dry-type transformers having exposed windings are much more sensitive to condensation, electrical creepage, partial discharges, cracks and temperature variations [85].

Therefore, the only way to protect a dry-type transformer is to employ a hermetic enclosure together with a heat exchanger and an air-treatment unit. However this design is expensive, requires extra space, consumes more energy and needs maintenance [86].

In addition, although mineral oil is not environmentally friendly, both natural and synthetic esters are officially classified as 'readily biodegradable' [82]. Therefore fluid-filled transformers using these insulation agents are capable to meet environmental concerns.

Finally, these fluids are better cooling mediums than air since they have higher specific heat, better thermal conductivity and require much lower flow rate to remove the same amount of heat. As a result fluid-immersed transformers are more efficient than their dry-type counterparts

[82]. Due to these advantages, fluid-filled transformers are still considered as the most viable option for offshore wind projects.

5.4 Sources of Losses in Power Transformers

Transformers' losses are divided into two general categories. These are the no-load losses, also known as iron or core losses, which are present whenever the transformer is energized and the load or copper losses which are result of the current flowing through the transformer [25].

The no-load losses consist of hysteresis and eddy-current losses and they originate from the alternating magnetic flux in the core of the transformer. The hysteresis losses depend on a number of parameters such as the frequency, the magnitude of the flux density and the type of core steel. These losses can be limited by increasing the number of windings' turns which reduces the induced voltage per turn and thus decreasing the peak flux density. In addition, special types of steel such as amorphous core materials with superior magnetic properties can be employed for the construction of the core [26]. Unfortunately, both of these solutions lead to other problems. Increasing the number of windings' turns leads to the utilization of a larger amount of copper while the amorphous core materials have ceramic-like properties which complicates the core manufacturing [26].

Eddy currents are induced to the core because of the alternating magnetic field and generate local ohmic losses. These losses can be effectively reduced by using thin laminated strips of steel for the assembly of the core (Figure 5.6A). Each strip has an oxide film applied on its surface which is very effective in blocking the eddy currents paths [26].

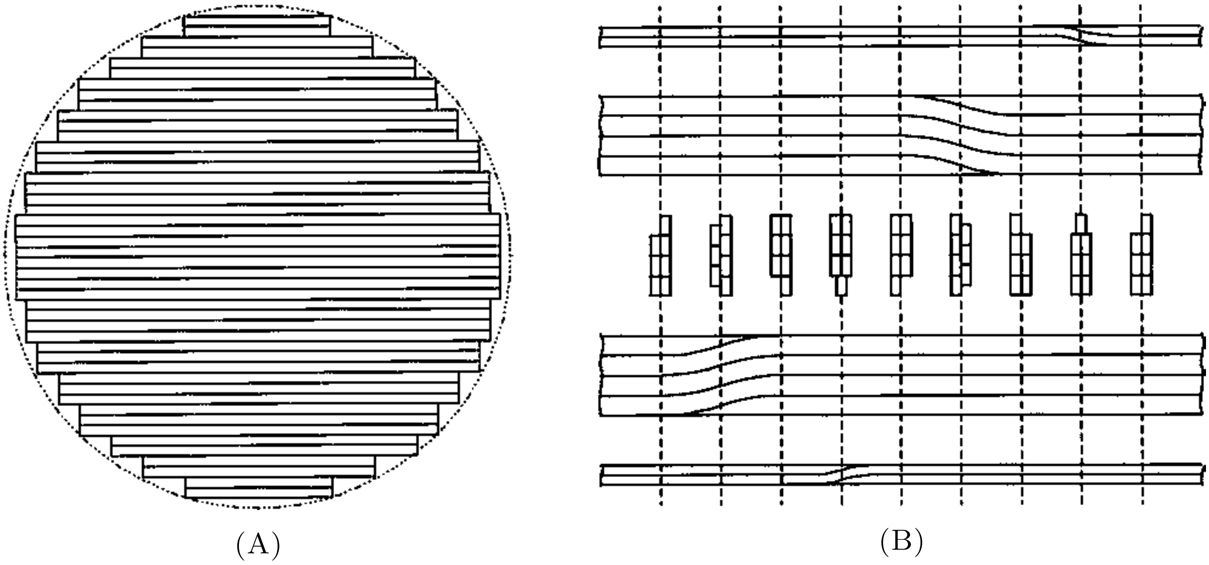
(A) (B)

FIGURE 5.6: Transformer Design (A) Cross section of circular core limb (B) Strands transposition of a seven-strand conductor used in a transformer winding [26]

The load losses consist of ohmic losses at the windings and stray losses because of eddy currents at the windings and other metallic parts of the transformer. These losses are only present during the loading of the transformer since the no-load current is so small that produces negligible resistive losses in the windings and the other metallic parts of the transformer [25].

The ohmic losses are associated with the square of the current flowing through the windings and their resistance. The AC resistance of the windings is affected from the skin and proximity effects which are explained in Section 3.3.2 [26].

As already mentioned, the alternating magnetic field causes the generation of eddy currents in metallic parts of the transformer. These eddy currents are induced around the paths surrounding the lines of magnetic flux which penetrate a conductor. Because of the fact that the magnetic field is not only present in the core of the transformer but there is always leakage flux, eddy currents are generated at the windings and other metallic parts of the transformer [25] [26]. The eddy currents are proportional to the leakage flux which is proportional to the load currents. Therefore, the eddy-current losses are proportional to the square of the load current [26]. These losses are expressed by a factor that increases the effective resistance of the windings even if they occur in metallic parts that are electrically isolated from the windings [26].

The load losses can be limited by decreasing either the effective resistance of the windings or the leakage flux [25] [26]. The reduction of the windings' resistance can be achieved by special conductor designs. The windings' conductors can be divided in several strands that are insulated from each other and are transposed in such a way that they are exposed to the same amount of leakage flux. In this way the eddy-current losses and the skin effect impact are reduced significantly. Figure 5.6B shows an example of strands' transposition of a seven-strand conductor. After seven complete transpositions, all the strands return to their initial positions [26]. The leakage flux can be limited by the implementation of flux shunts. These shunts divert the leakage flux so as to prevent its passing through the winding conductors and also made to run along the axis of the winding rather than have a large radial component as indicated shown in Figure 5.7.

5.5 Equivalent Circuit

In order to develop an accurate model of a non-ideal transformer, the power losses that occur during its operation have to be included. The points of focus regarding such a model are the following [24] [84]:

- Load (copper) losses

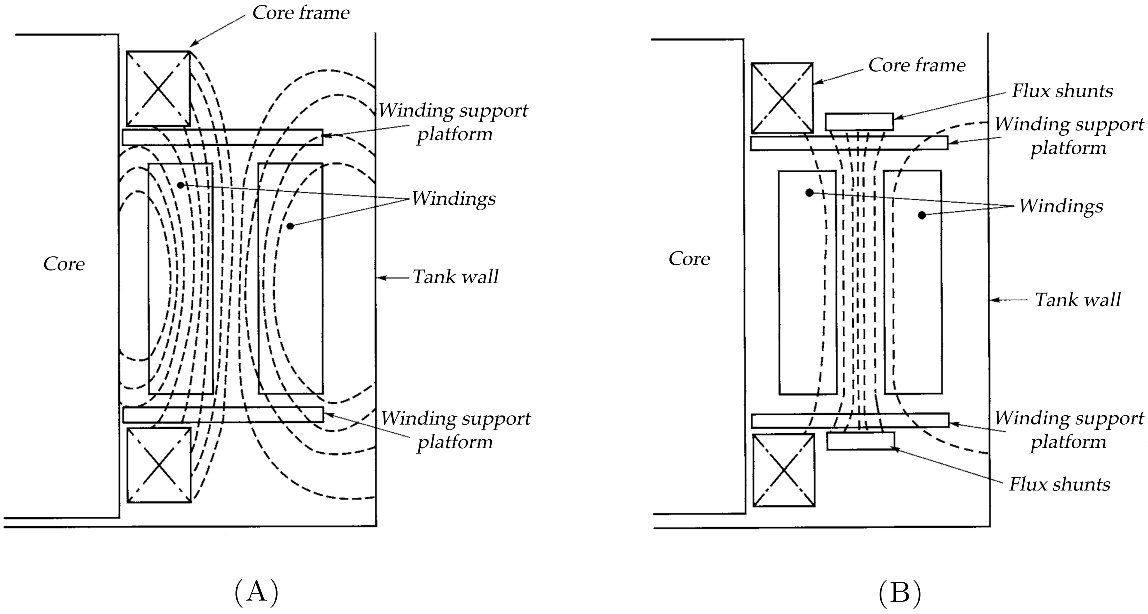

FIGURE 5.7: Limiting the leakage flux (A) Winding leakage flux paths without shunts (B) Winding leakage flux paths with shunts [25]

- No-load (core) losses
- Mutual magnetic flux
- Leakage magnetic flux

The copper losses are resistive losses in the windings and stray losses in the windings and other metallic parts of the device. Since the stray losses can be expressed as an increase of the resistance of the windings, the copper losses are modeled by placing an ohmic resistance R_p in the primary circuit and an ohmic resistance R_s in the secondary circuit of the transformer [24] [84].

As already explained in Section 5.2 a magnetizing current creates the mutual magnetic flux in the core of the transformer. This current is proportional (in the unsaturated region) to the voltage applied to the core and lags this voltage by $\frac{\pi}{2} rads$. Therefore it can be modeled by a reactance X_M connected across the primary voltage source [24] [84].

However, regarding a non-ideal transformer, the no-load current except the magnetizing component has another component which is responsible for the core losses. This current is also proportional to the voltage applied to the core and it is in phase with it. Thus, the core losses are modeled by a an ohmic resistance R_C connected in parallel to the reactance X_M [24] [84].

Finally, there is a portion of the magnetic flux linking only the primary winding and another portion linking only the secondary winding. These leakage fluxes are proportional to the primary and secondary current respectively and are responsible for a voltage drop in each circuit which can be expressed by a reactance, X_p for the primary and X_s for the secondary circuit, in series with the windings' ohmic resistances [24] [84].

Taking into consideration these components, the equivalent circuit of an non-ideal transformer is developed as shown in Figure 5.8. However this circuit is not very useful because it contains two different voltage levels. A more practical approach is referring the equivalent circuit to either the voltage level of the primary or the secondary winding using the voltage ratio as shown in Figure 5.9.

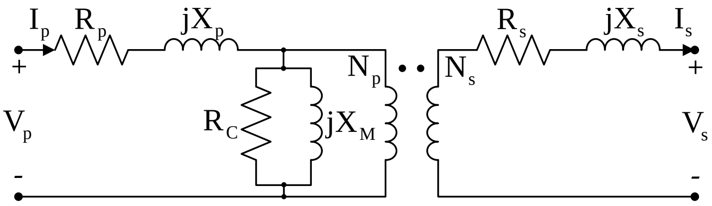

FIGURE 5.8: Equivalent circuit of a real transformer [24]

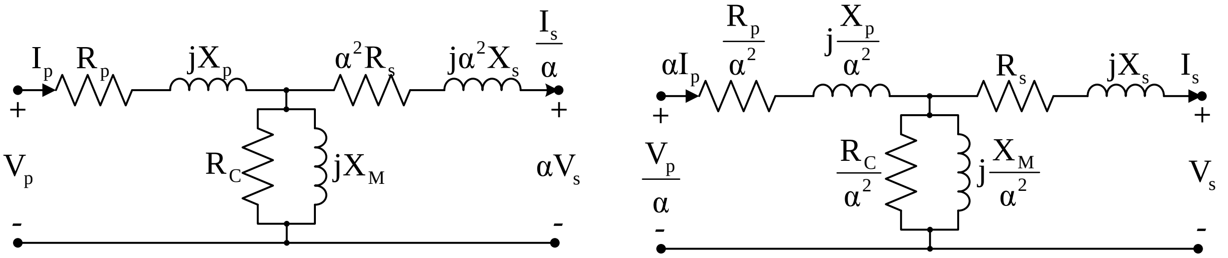

(A) (B)

FIGURE 5.9: Equivalent circuit of a real transformer (A) Referred to the primary winding voltage (B) Referred to the secondary winding voltage [24]

In reality, the current of the excitation branch is very small compared to the load current of the transformer. In addition, since the voltage drop on the leakage impedance of the primary is small, the terminal voltage is not appreciably different than the corresponding internal induced voltage. Therefore, the equivalent circuit can be simplified by moving the excitation branch to the front of the transformer. In this way, the primary and secondary impedances are left in series with each other and are combined in an equivalent series resistance R_{eq} and an equivalent series reactance X_{eq} [24] [84]. This simplified version of the equivalent circuit of the transformer is shown in Figure 5.10.

5.6 Testing of Power Transformers

Even today, the majority of power transformers are literally hand-made. There is little or no mass production involved regarding their components and every transformer is manufactured

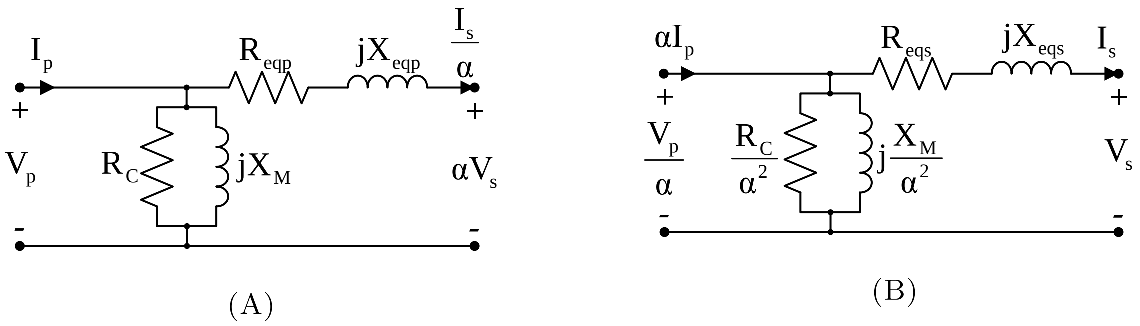

Figure 5.10: Simplified equivalent circuit of a real transformer (A) Referred to the primary winding voltage (B) Referred to the secondary winding voltage [24]

individually as an one-off. This means that every transformer is unique and several tests and measurements are required to check its design and ensure that the device is fit for service throughout its lifetime [25].

Among all these procedures, there are two that are associated with the device's power losses. These are the open circuit and the short circuit tests and through them, the impedance of the excitation branch as well as the series impedance of the primary and secondary windings can be determined. Consequently, the power losses can be estimated. The two tests, which are presented in the next sections, are explained for a single-phase transformer but they are the same in principle for three-phase transformers as well.

5.6.1 Open Circuit Test

The open circuit test is conducted by applying the rated voltage to a winding, let it be the primary, while keeping the other winding, let it be the secondary open-circuited. A voltmeter, an ammeter and a wattmeter are employed as shown in Figure 5.11.

Since the no-load current is very small compared to the full-load current, the voltage drop on the impedance of the primary winding is negligible as compared to the applied rated voltage. The wattmeter displays the summation of the total core losses and the ohmic losses of the primary winding because of the no-load current. However the later can be neglected since it is insignificant compared to the core losses [24] [84].

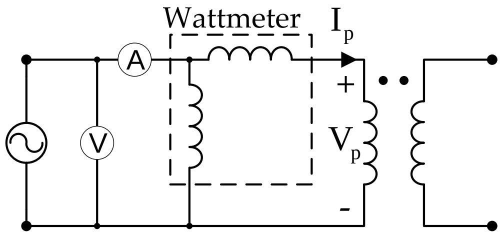

Figure 5.11: Open circuit test [24]

Using the indications P_{OC} of the wattmeter, V_{OC} of the voltmeter and I_{OC} of the ammeter, the impedance of the excitation branch is calculated. The easiest method to do so, is to consider the corresponding admittance:

$$\overline{Y}_E = \frac{1}{R_C} - j\frac{1}{X_M} \tag{5.6.1}$$

Where:

- R_C: Resistance of the excitation branch (Ω)
- X_M: Reactance of the excitation branch (Ω)

The magnitude of the excitation admittance (referred to the primary) is calculated according to equation 5.6.2. In addition, the angle of the admittance is determined through the circuit's power factor which is given by equation 5.6.3. The power factor is always lagging for a real transformer. Therefore, the angle of the current lags the angle of the voltage by $\varphi\ rads$. Finally, the admittance is given by equation 5.6.4 through which the excitation resistance and reactance are derived [24] [84].

$$\left|\overline{Y}_E\right| = \frac{I_{OC}}{V_{OC}} \tag{5.6.2}$$

$$PF = \cos\varphi = \frac{P_{OC}}{V_{OC}I_{OC}} \Rightarrow \varphi = \cos^{-1}\frac{P_{OC}}{V_{OC}I_{OC}} \tag{5.6.3}$$

$$\overline{Y}_E = \frac{I_{OC}}{V_{OC}}\angle - \varphi \tag{5.6.4}$$

5.6.2 Short Circuit Test

For the purposes of the short circuit test, one of the two windings, let it be the secondary, is now short-circuited. A voltage is applied to the other winding, in this case the primary, that causes rated currents to flow in both windings. The same configuration of the three measuring devices as for the open circuit test is employed again as shown in Figure 5.12.

The applied voltage in the primary winding is very small compared to the rated one. This means that the current flowing in the excitation branch and the core losses can be neglected. Therefore, the wattmeter displays the load losses of the two windings of the transformer [24] [84].

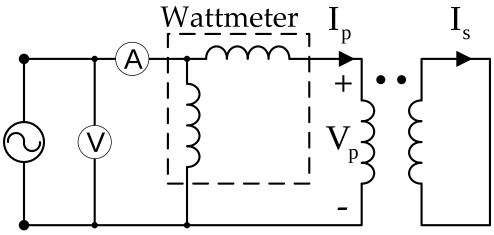

FIGURE 5.12: Short circuit test [24]

Using the indications P_{SC} of the wattmeter, V_{SC} of the voltmeter and I_{SC} of the ammeter, the summation of the series impedances (referred to the primary) of the two windings is determined. This impedance is expressed as:

$$\overline{Z}_{SE} = R_{eqp} + jX_{eqp} \tag{5.6.5}$$

Where:

- R_{eqp}: Equivalent resistance of the combined impedance of the two windings referred to the primary (Ω)
- X_{eqp}: Equivalent reactance of the combined impedance of the two windings referred to the primary (Ω)

The magnitude of the total impedance is given by equation 5.6.6, while the power factor of the circuit is derived according to equation 5.6.7. As already mentioned, this power factor is always lagging. Finally, the combined impedance of the two windings is calculated according to equation 5.6.8 [24] [84].

$$\left|\overline{Z}_{SE}\right| = \frac{V_{SC}}{I_{SC}} \tag{5.6.6}$$

$$PF = \cos\varphi = \frac{P_{SC}}{V_{SC}I_{SC}} \Rightarrow \varphi = \cos^{-1}\frac{P_{SC}}{V_{SC}I_{SC}} \tag{5.6.7}$$

$$\overline{Z}_{SE} = \frac{V_{SC}}{I_{SC}}\angle\varphi \tag{5.6.8}$$

This technique allows for the calculation of the total series impedance. There is no accurate way to separate this impedance into the primary and secondary windings impedances since it is not practically possible to apportion parts of the stray losses to each winding [24] [84].

Both of the open and short circuit tests can be performed on the secondary winding if it is more convenient due to lower voltage level or other reasons. In this case, the calculated values of the equivalent circuit will, naturally, refer to the secondary instead of the primary winding of the transformer [24].

5.7 Modeling the Transformer Power Losses

5.7.1 Introduction

The model presented in the following section calculates the power losses of a power transformer. Similarly to the cables and MMC models, the transformer model is developed according to a number of criteria:

- High computational speed
- Capture of averaged steady-state operation
- Temperature dependency
- Exclusive use of code

As already explained, the power losses of the transformer consist of two general categories: the load and the no-load losses. These are calculated using the equivalent circuit of the transformer as presented in Section 5.5. In addition, a simplified estimation regarding the cooling requirements of the transformer in terms of power consumption is included in the calculation of the total losses of the device.

Furthermore, the model incorporates the impact of the windings' temperature on the losses. It is assumed that their temperature varies linearly with respect to the RMS current flowing through the transformer. This means that their temperature is equal to the ambient temperature when no current flows and it reaches its maximum value at full load.

The model conducts the required calculations, using some assumptions:

- There is no tertiary winding
- The transformer has a fixed voltage ratio
- The windings' temperature varies linearly with the current

The model's methodology for calculating the power losses of a transformer is explained in Section 5.7.2. Finally the operation of the model is assessed in Section 5.7.3.

5.7.2 Model

In order to calculate the power losses of a transformer, the components of its equivalent circuit have to be determined. The standard procedure for acquiring these values consists of the open and short circuit tests, as already explained. For this reason, the model has the capability of deriving the equivalent circuit by using the open and short circuit tests' measurements as inputs. Alternatively, in case the values of the components are already known, they can be directly used as inputs to the model. These values need to be referred to the secondary winding with respect to power flow. Tables 5.2 and 5.3 show the inputs and the outputs of the model respectively.

Inputs	
P_{OC}	Power measurement during open circuit test ($Option1$) (W)
V_{OC}	Voltage measurement during open circuit test ($Option1$) (V)
I_{OC}	Current measurement during open circuit test ($Option1$) (A)
P_{SC}	Power measurement during short circuit test ($Option1$) (W)
V_{SC}	Voltage measurement during short circuit test ($Option1$) (V)
I_{SC}	Current measurement during short circuit test ($Option1$) (A)
$FlagWinding$	Flag variable determining the winding on which the open and short circuit tests were conducted ($Option1$) ($-$)
$R_{C,sec}$	Resistance of excitation branch referred to the secondary winding ($Option2$) (Ω)
$X_{M,sec}$	Reactance of excitation branch referred to the secondary winding ($Option2$) (Ω)
$R_{eq,sec}$	Series resistance of the windings referred to the secondary winding ($Option2$) (Ω)
$X_{eq,sec}$	Series reactance of the windings referred to the secondary winding ($Option2$) (Ω)
α	Voltage ratio (N_p/N_s) with respect to power flow ($-$)
S_{Nom}	Nominal apparent power of the transformer (VA)
S_{in}	Lowest possible apparent power of the transformer (VA)
$Step$	Accuracy resolution of the efficiency curve calculation (W)
$\overline{V}_{in,LL}$	Input line to line voltage (V)
ϕ	Input power angle (rad)
$\theta_{t,Amb}$	Ambient temperature (°C)
$\theta_{t,Test}$	Temperature at which the open and short circuit tests were conducted (°C)
$\theta_{t,Rise}$	Maximum allowed temperature rise above the ambient (°C)
a_0	Constant mass temperature coefficient at 0 °C (K^{-1})
$P_{cool,Nom}$	Nominal installed power of the cooling system (W)

Table 5.2: Model Inputs

The model calculates the input voltage and line current of a phase of the transformer by using the line to line voltage and line current at the input and taking into consideration the primary winding's connection configuration. Four different connections are available: Wye/Wye, Wye/Delta, Delta/Wye, Delta/Delta. Having these values in addition to the components of the

Model Outputs	
$\overline{V}_{in,LL}$	Output line to line voltage at the output (V)
$\overline{I}_{out,L}$	Output line current (A)
$P_{no-load}$	No-load losses (W)
P_{load}	Load losses (W)
P_{cool}	Cooling system losses (W)

Table 5.3: Model Outputs

equivalent circuit the losses can be determined. Since there is no practical method to separate the windings' impedances, the model uses the equivalent circuit of Figure 5.10.

Initially, the input phase voltage and current are referred to the primary winding. Their values referred to the secondary are derived using the following equation:

$$\overline{V}_{in,Ph,\mathrm{sec}} = \frac{\overline{V}_{in,Ph,pr}}{\alpha} \tag{5.7.1}$$

$$\overline{I}_{in,L,\mathrm{sec}} = \alpha \overline{I}_{in,L,pr} \tag{5.7.2}$$

Where:

- $\overline{V}_{in,Ph,\mathrm{sec}}$: Input phase voltage referred to the secondary (V)
- $\overline{V}_{in,Ph,pr}$: Input phase voltage referred to the primary (V)
- α: Voltage ratio $(-)$
- $\overline{I}_{in,L,\mathrm{sec}}$: Input line current referred to the secondary (A)
- $\overline{I}_{in,L,pr}$: Input line current referred to the primary (A)

The variables involved in the rest of the calculations are all referred to the secondary. For simplicity, the subscript notation 'sec', which denotes that the variable is referred to the secondary, is eliminated from the following equations. The current flowing through the combined series impedance of the two windings is given by equation 5.7.3.

$$\overline{I}_{SE,L} = \overline{I}_{in,L} - \overline{Y}_E \overline{V}_{in,Ph} \tag{5.7.3}$$

Where:

- $\overline{V}_{in,Ph}$: Input phase voltage referred to the secondary (V)

- $\overline{I}_{in,L,}$: Input line current referred to the secondary (A)
- $\overline{Y}_E$: Admittance of the excitation branch referred to the secondary (Ω)

This current is also equal to the output line current. The output phase voltage is derived using equation 5.7.4.

$$\overline{V}_{out,Ph} = \overline{V}_{in,Ph} - \overline{Z}_{SE}\overline{I}_{SE,L} \tag{5.7.4}$$

Where:

- $\overline{V}_{in,Ph}$: Input phase voltage referred to the secondary (V)
- $\overline{Z}_{SE}$: Series impedance referred to the secondary (Ω)
- $\overline{I}_{SE,L}$: Line current through the series impedance referred to the secondary (A)

5.7.2.1 No-load and Load Losses

The no-load losses depend on the voltage across the excitation branch, which is equal to the input phase voltage according to the equivalent circuit. The three-phase no-load losses are derived using the following relationship:

$$P_{no-load} = 3\frac{V_{in,Ph}^2}{R_C} \tag{5.7.5}$$

Where:

- $\overline{V}_{in,Ph}$: Input phase voltage referred to the secondary (V)
- R_C: Resistance of the excitation branch referred to the secondary (Ω)

Having calculated the current flowing the combined series impedance of the two windings, the three-phase load losses are calculated according to equation 5.7.6.

$$P_{load} = 3R_{eqs}I_{SE,L}^2 \tag{5.7.6}$$

Where:

- R_{eqs}: Resistance of the series impedance referred to the secondary (Ω)
- $I_{SE,L}$: Line current through the series impedance referred to the secondary (A)

5.7.2.2 Implementation of Temperature Impact

By calculating the load losses according to equation 5.7.6, the temperature impact on the windings' is not taken into consideration. The resistance R_{eqs} corresponds to the temperature at which the short circuit test is conducted. Therefore, a correction may be applied to the value of the resistance, in order to correspond to the actual temperature of the winding.

Since this resistance represents the load losses of the windings, it consists of two parts: the resistive losses of the windings and the stray losses at the windings and other metallic parts of the transformer. The resistive losses of the windings vary in proportion with the windings' resistance. In addition, the resistivity of the windings increases with increasing temperature since all metals, including copper, have positive temperature coefficients of resistance. Therefore the windings' resistance and consequently ohmic losses increase with increasing temperature [84].

The stray losses depend on the eddy currents which are induced by the leakage magnetic flux in the conductive parts of the transformer. These eddy currents are restricted by the lack of space or high resistivity of the conductor [84]. Therefore, the stray losses vary in the inverse proportion of the resistivity of the conductive material. Consequently, they decrease with increasing temperature [25] [84]. For simplicity in the calculations, the total stray losses are assumed to vary in the inverse proportion of the resistivity of the windings' conductor which means that they decrease with increasing winding's temperature [84].

Furthermore, the short circuit test does not give any indication about the percentage of the resistive and stray losses in the total load losses figure. The existing methods (analytical/numerical) for calculating the stray losses are too complicated with respect to the scope of this report. A fair estimation is that the resistive losses represent the 85% and the stray losses the rest 15% of the load losses [25]. Thus, the combined series resistance R_{eqs} of the windings can be expressed according to the following equation:

$$R_{eqs}^{\theta_t} = \frac{85}{100} R_{eqs}^{\theta_{t,Test}} \left[1 + \alpha_{\theta_{t,Test}}(\theta_t - \theta_{t,Test})\right] + \frac{15}{100} R_{eqs}^{\theta_{t,Test}} \frac{1}{\left[1 + \alpha_{\theta_{t,Test}}(\theta_t - \theta_{t,Test})\right]} \tag{5.7.7}$$

Where:

- $R_{eqs}^{\theta_t}$: Resistance at temperature θ_t °C (Ω)
- $R_{eqs}^{\theta_{t,Test}}$: Resistance at $\theta_{t,Test}$ (Ω)
- $\alpha_{\theta_{t,Test}}$: Constant mass temperature coefficient of copper at $\theta_{t,Test}$ °C (K^{-1})

- $\theta_{t,Test}$: Windings' temperature during the short circuit measurement (°C)

Since the temperature during the short circuit test is not known and is an input variable, the constant mass temperature coefficient of copper at this temperature is calculated using equation 5.7.8 [87].

$$\alpha_{\theta_t} = \frac{1}{\frac{1}{\alpha_0} + \theta_t} \tag{5.7.8}$$

Where:

- α_0: Constant mass temperature coefficient of copper at 0 °C (K^{-1})

In addition, as already mentioned the temperature of the windings is assumed to vary linearly with the RMS value of the current. It is equal to the ambient temperature when no current flows and equal to a maximum value for rated current. In reality, even if no current flows, in case the transformer is energized the no-load losses are present. However it is assumed that when no current flows, the cooling system keeps the temperature of the windings close to the ambient one.

For normal ambient conditions which are defined by IEC 60076 as air never below −25 °C and over 40 °C, not exceeding 30 °C on average during the warmest month and not exceeding 20 °C on average during a year, or water never exceeding 25 °C at the inlet to oil/water coolers, the permitted temperature rise of the windings are as follows [25]:

- for transformers identified as ON.. or OF.. : 65 °C
- for transformers identified as OD.. : 70 °C

Therefore, the maximum windings' temperature that corresponds to rated current is the summation of the ambient temperature and the allowed temperature rise.

$$\theta_{t,Max} = \theta_{t,Amb} + \theta_{t,Rise} \tag{5.7.9}$$

Where:

- $\theta_{t,Max}$: Maximum windings' temperature (°C)
- $\theta_{t,Amb}$: Ambient temperature (°C)
- $\theta_{t,Rise}$: Maximum allowed temperature rise above the ambient (°C)

5.7.2.3 Cooling Losses

The cooling requirements of a transformer vary with respect to its rating, its physical size and its cooling system configuration [25]. Transformers of larger rating suffer from higher losses in terms of absolute values. Therefore, the cooling system needs to dissipate larger amounts of heat which impacts the cooling input. In addition, transformers of larger tank surface are able to dissipate more heat passively needing lower amount of cooling power. Finally, the control scheme of the active components of the cooling system (fans or pumps) introduces variable power requirements.

Determining the power requirements of the transformers' cooling system is not a straightforward task when exact figures are not available (power consumption of active components, control scheme etc). For this reason, the model incorporates a simple approach for estimating the cooling requirements, which can be easily altered in case data is available.

The model requires as input the rated installed power of the cooling system. It is assumed that the cooling requirements vary linearly with respect to the windings' temperature. The cooling system consumes 20% of its rated power when the windings' temperature is equal to the ambient temperature (dissipation of no-load losses) and varies linearly up to 100% of its rated power at maximum windings' temperature:

$$P_{cool} = \frac{20}{100} P_{cool,Nom} + \frac{\theta_t - \theta_{t,Amb}}{\theta_{t,Max} - \theta_{t,Amb}} P_{cool,Nom} \tag{5.7.10}$$

Where:

- P_{cool}: Cooling system power requirement (W)
- $P_{cool,Nom}$: Nominal installed power of the cooling system (W)
- θ_t: Windings' temperature (°C)
- $\theta_{t,Amb}$: Ambient temperature (°C)
- $\theta_{t,Max}$: Maximum windings' temperature (°C)

5.7.3 Model Assessment

An assessment of the proposed transformer model, through examples, is conducted to showcase its operation. Unfortunately, transformer manufacturers do not publish data of the measuring and testing procedure of their products. Therefore, due to unavailability of information, the transformer used in the examples is designed using approximations based on figures found in literature. The most important parameters of this transformer are summarized in Table 5.4. A detailed list of all the model inputs is provided in Appendix C.1.

Transformer Properties		
Variable	Unit	Value
S_{Nom}	(VA)	$800 \cdot 10^6$
$V_{pr,Nom}$	(V)	$220 \cdot 10^3$
$V_{sec,Nom}$	(V)	$380 \cdot 10^3$
α	$(-)$	220/380
$R_{C,sec}$	(pu)	800
$X_{M,sec}$	(pu)	500
$R_{eq,sec}$	(pu)	0.003
$X_{eq,sec}$	(pu)	0.16
$P_{cool,Nom}$	(W)	$36 \cdot 10^3$

Table 5.4: Transformer properties of the numerical example

The pu values of the series and shunt impedances, are based on the three-phase transformer component which is included in the *Simscape.SimPowerSystems* library of Matlab Simulink. These values are slightly altered in order the efficiency of the transformer to be in the vicinity of the values documented in [30] and presented in Table 5.5 for convenience purposes. The cooling type of the transformer is assumed to be $ONAF$ and the rated power of the cooling fans for a transformer of this rating is in the range of $35 - 40$ kW [25].

Transformer type	**Rated Power**	**Efficiency at**		**Loss at**	
		100% Rated Load	50% Rated Load	100% Rated Load	50% Rated Load
Generator transformer	1100 MVA	99.60%	99.75%	4400 kW	1375 kW
Interbus transformer	400 MVA	99.60%	99.75%	1600 kW	500 kW
Substation transformer	40 MVA	99.40%	99.60%	240 kW	80 kW
Distribution transformer	1 MVA	98.60%	99.00%	14 kW	5 kW

Table 5.5: Efficiencies and losses of larger and smaller utility transformers [30]

Figure 5.13 shows the difference regarding the efficiency and losses of a Wye/Wye connected transformer for constant and variable temperature of the windings. The same comparisons for the Delta/Wye configuration are made in Figure 5.14.

As already explained in Section 5.7.2.2, the temperature impact is implemented through a correction of the series resistance R_{eqs} of the equivalent circuit. For the constant temperature scenario, this resistance has the value that is derived from the short-circuit test measurements, while for the variable temperature scenario, the temperature correction of the resistance (equation 5.7.7) is activated.

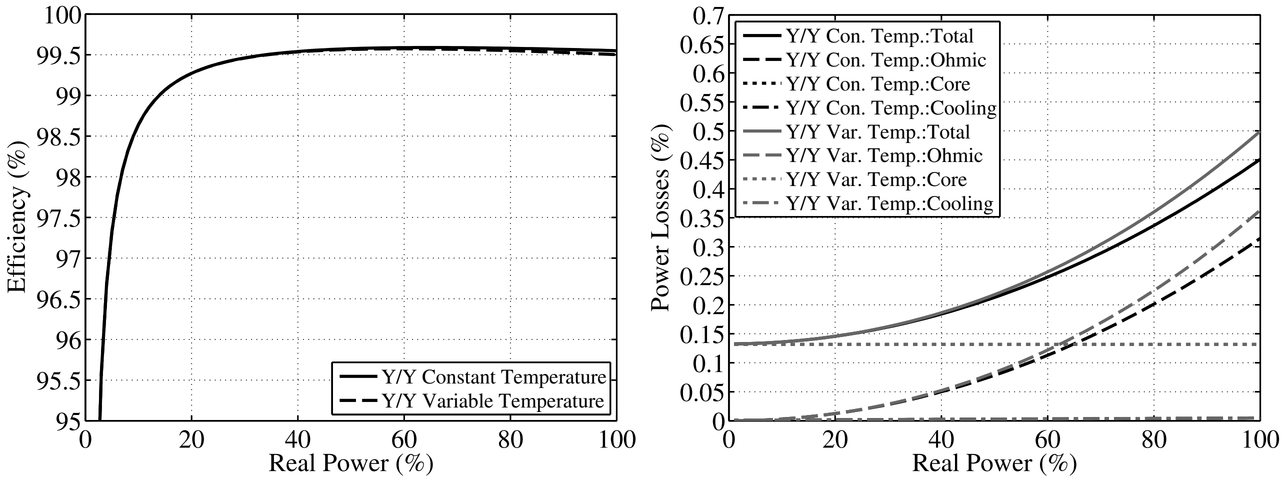

(A) (B)

FIGURE 5.13: Temperature impact for transformer in Wye/Wye connection (A) Comparison of efficiency curves (B) Comparison of losses curves

From Figure 5.13B, it is evident that the core losses stay constant irrespectively of the loading of the transformer, while the ohmic losses rise with increasing power and thus, current. Furthermore, it can be argued that the cooling requirements represent an insignificant fraction of the total losses.

In addition, it can be seen that the consideration of windings' temperature leads to higher ohmic losses especially for high values of power. As equation 5.7.7 suggests, this is expected due to the fact that the difference between the testing temperature θ_{Test} and the operating temperature θ becomes larger as the power rises (Equation 5.7.7). However, the implementation of the temperature variation does not have a drastic impact on the efficiency, as can be seen from Figure 5.13A.

Regarding the Delta/Wye configuration, it is clear from Figure 5.14 that the core losses are larger due to the higher phase voltage at the primary winding. Furthermore, the ohmic losses contribute less to the total losses since the phase current is lower. The lower phase current is also responsible for the fact that the windings' temperature consideration has a smaller impact on the ohmic losses.

Finally, from Figure 5.14A, it is seen that the efficiency of the transformer is lower especially for low values of power. This is an expected result since the always present core losses are much higher in the Delta/Wye configuration. Therefore, the losses are high even for low loading.

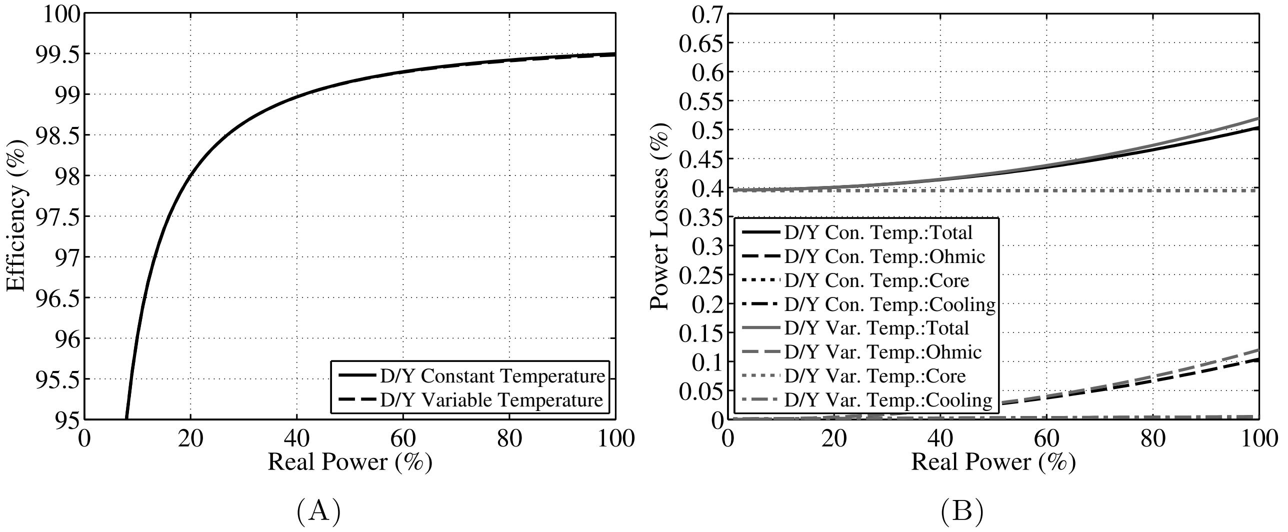

FIGURE 5.14: Temperature impact for transformer in Delta/Wye connection (A) Comparison of efficiency curves (B) Comparison of losses curves

Chapter 6

Case Study

6.1 Introduction

After analyzing and assessing individually each of the three proposed models, a case study is conducted. Its aim is to show how the models work together and how they perform under realistic scenarios. First of all, it assesses the sensitivity of the models regarding different values of some input variables (i.e. soil thermal resistivity, voltage level). In addition, it evaluates the difference in power losses between HVDC and HVAC transmission. Lastly, it assesses the impact of the implementation of the conductors' and semiconductors' temperature variation.

In this context, an OWF is designed and its power losses, between the output terminals of the wind turbines' transformers and the grid connection point, are determined. Multiple scenarios with different input variables are performed and comparisons between them are presented.

In Section 6.2 the layout of the OWF is explained. Consequently, Section 6.3 gives insights regarding preliminary calculations (i.e. wind resource, implementation of the wake effect etc) and includes the methodology according to which the power losses are derived. Section 6.4 gives an overview of the different sets of scenarios that are realized. Finally, the results are presented in Section 6.5.

6.2 OWF Layout

The hypothetical OWF of the case study is designed in order to resemble a typical OWF of the near future. Its inter-array layout is shown in Figure 6.1.

It is equipped with 80 wind turbines with rated power equal to 8 MW (Figure 6.2). The turbines are installed in 8 lines with every line having two strings (upper and lower) of 5 units each. The distance between the turbines of the same line is 1 km while the distance between lines is 1.5 km. In addition, the wind turbines are organized in two clusters of 40 units and each cluster is served by its personal offshore transformer substation.

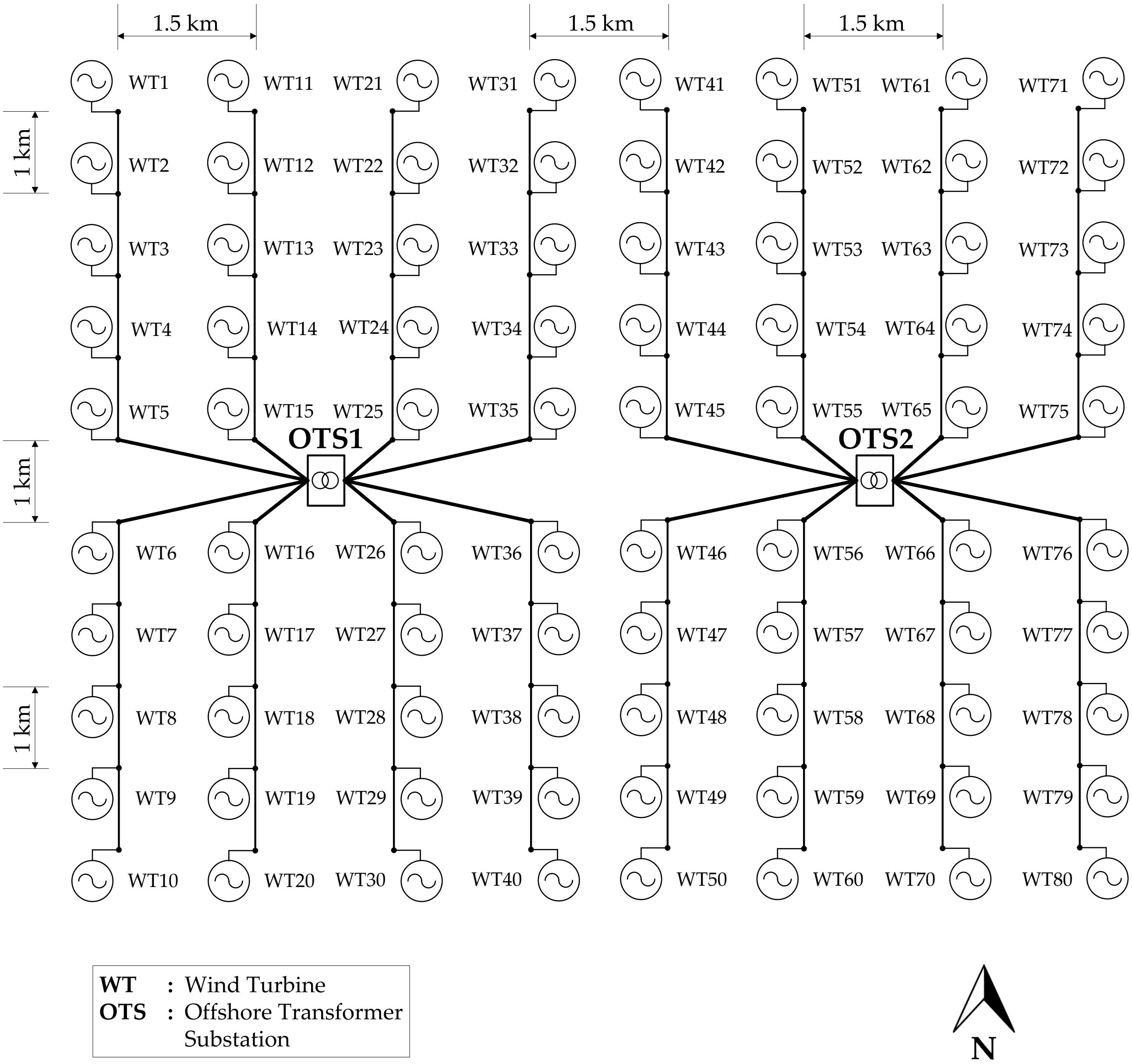

FIGURE 6.1: Graphical representation of the inter-array layout of the OWF

As already mentioned, two different transmission schemes are considered: HVDC and HVAC transmission. Figure 6.3 shows how these schemes are realized. In case of HVDC transmission, the produced power is directed from the two offshore transformer substations to a third offshore substation which houses the power rectifier. Consequently, the power is transmitted to the onshore substation by means of two HVDC cables. The onshore substation includes the power inverter and the step-up transformer which delivers the power of the OWF to the grid.

Regarding the HVAC scheme, the transmission system has fewer components. The produced power is transmitted directly from the two offshore transformer substations to the onshore

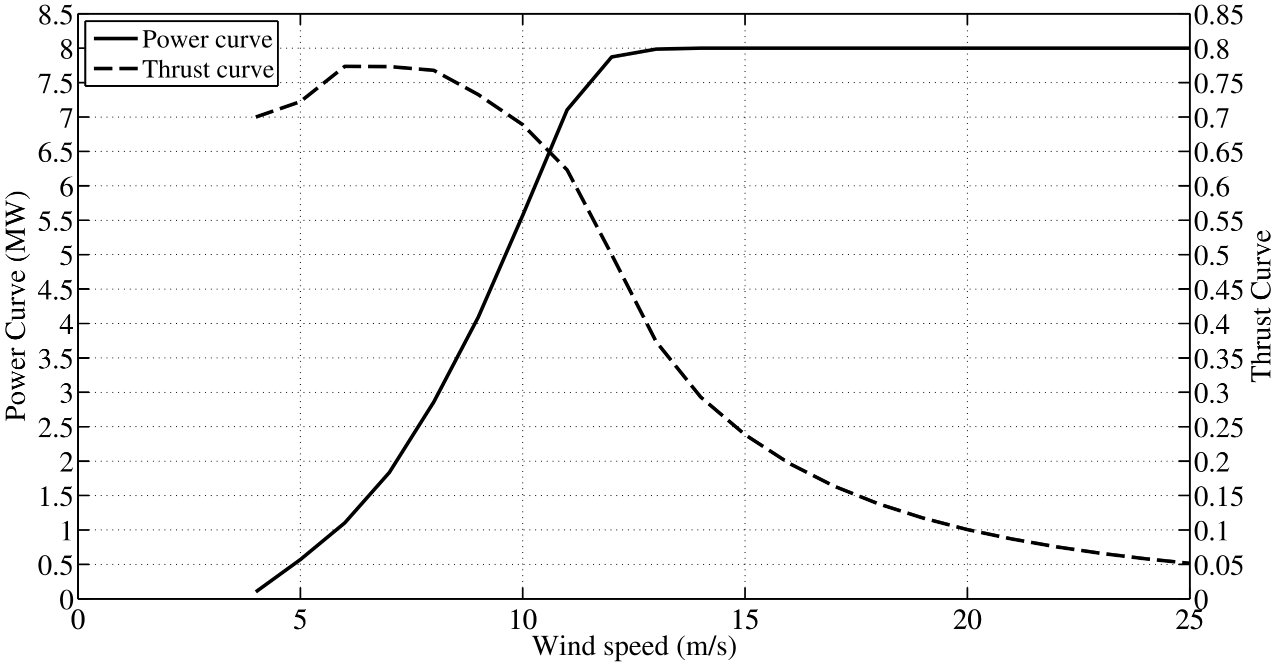

Figure 6.2: Power and thrust curves of wind turbine

substation by means of two separate HVAC cables. The onshore substation houses the step-up transformer. Finally, in case of HVAC transmission, reactive power compensation is realized at both ends of the two HVAC export cables.

6.3 Calculations' Methodology

In order to develop a realistic framework for assessing the proposed models, the power production of the OWF of the case study is determined using collected data and relevant software tools. In this section, initially, a brief description about the derivation of the wind rose and the implementation of the wake effect is given. Consequently, the methodology for the calculation of the OWF power losses is explained.

6.3.1 Wind Resource

As already mentioned, the North Sea is Europe's region of focus regarding the development of offshore wind energy projects. For this reason, the wind rose used in the case study is derived using data collected during 4 years in the platform Fino 1 located in the German waters of the North Sea. More information regarding the measurements can be found in [88]. The wind rose is shown in Figure 6.4.

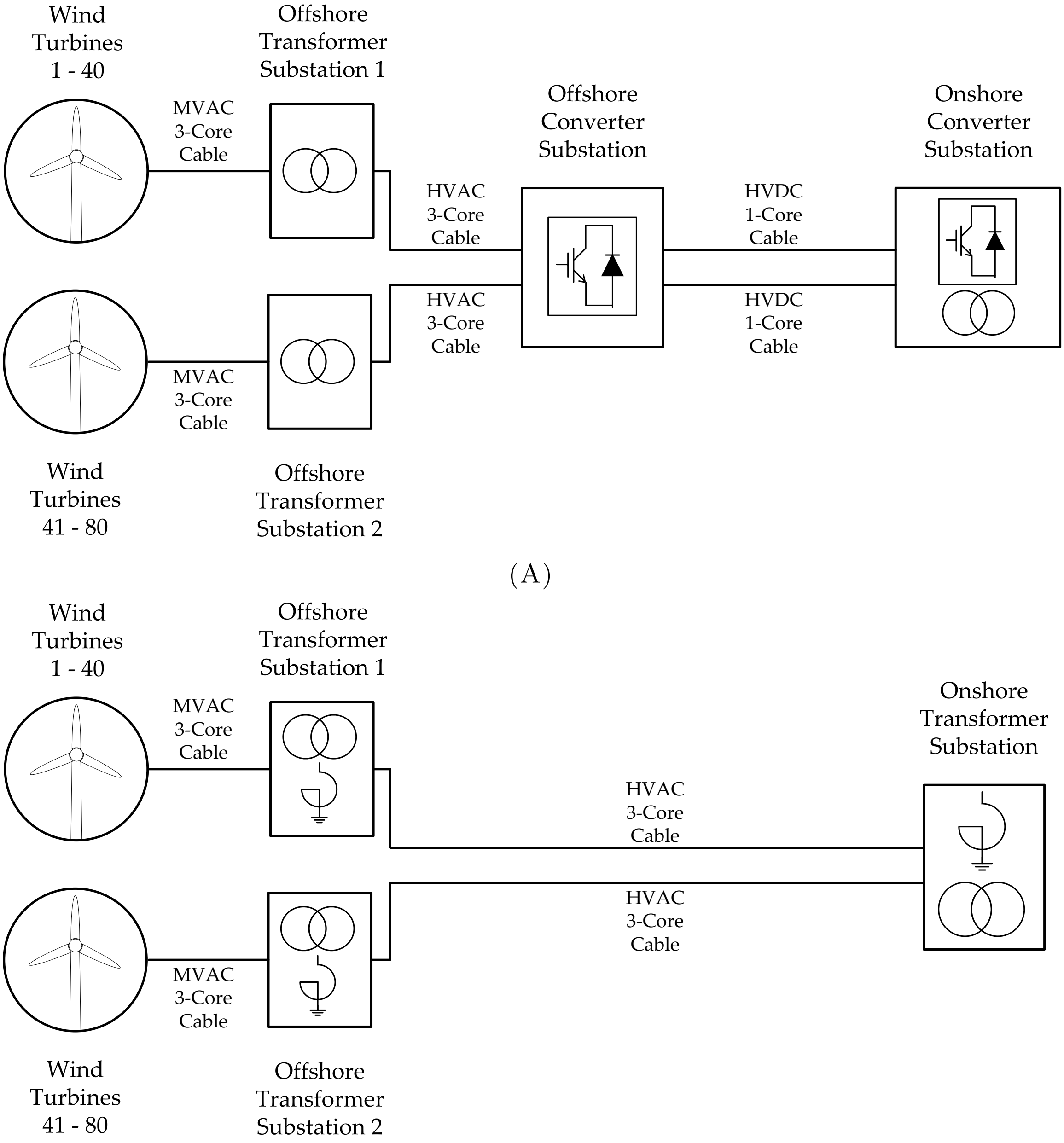

(A)

(B)

FIGURE 6.3: Graphical representation of power transmission schemes (A) HVDC (B) HVAC

6.3.2 Wake Effect and Energy Production

Having determined the inter-array layout and the wind resource of the OWF, the implementation of the wake effect leads to the derivation of the power production of each wind turbine for each wind direction of the rose (Figure 6.5). The wake effect impact is calculated using FarmFlow.

FarmFlow is a software developed by the Energy Research Centre of the Netherlands (ECN) [89]. It is an improved version of the UPMWAKE model [90], that calculates wake effects in wind farms by solving the parabolized Navier-Stokes equations in all three dimensions, while the turbulent processes in the wake are modeled with a k-ϵ turbulence model. The performance

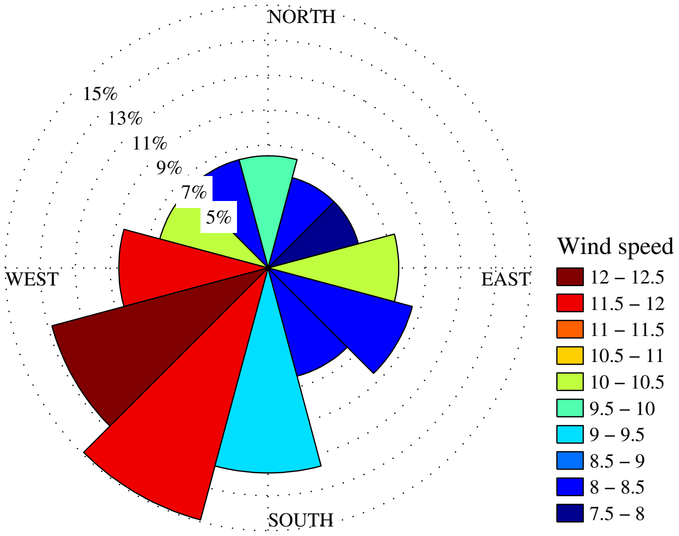

FIGURE 6.4: Wind Rose

of FarmFlow has been evaluated and compared to the commonly used models for predicting wind speed decrease inside turbines wakes [91] [92].

The losses though the drive-train of the wind turbines are not taken into account. Therefore, the calculated power production is assumed to be present at the output terminals of the generators' transformers.

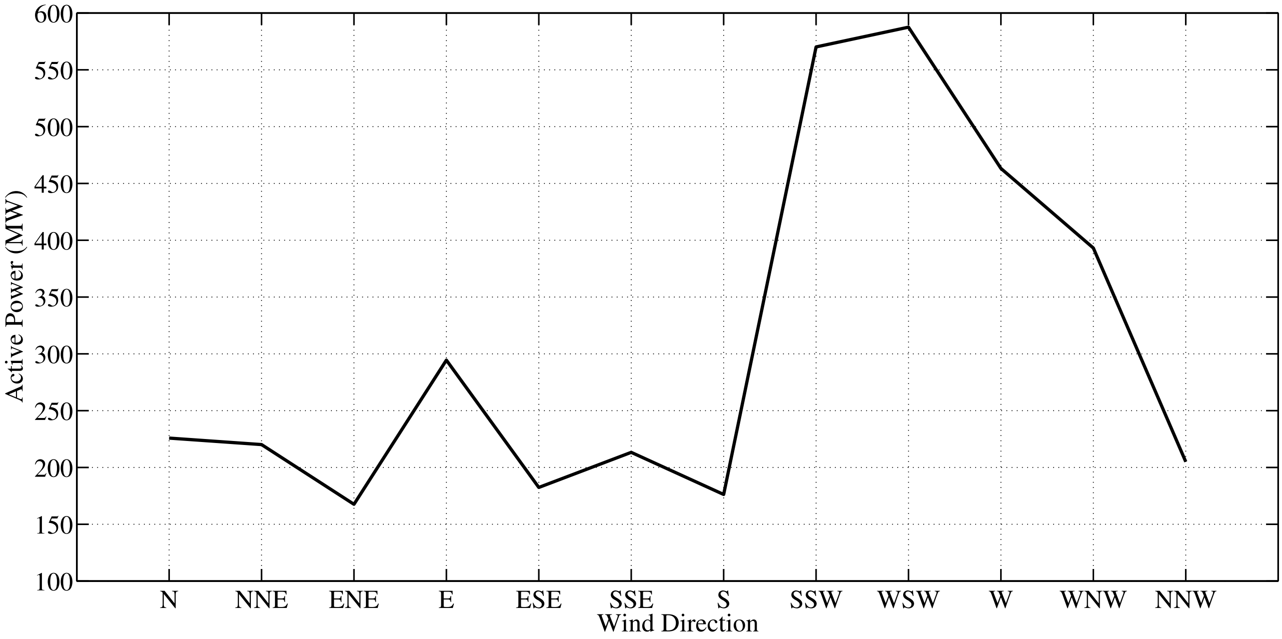

FIGURE 6.5: Wind farm power production per wind direction

6.3.3 Load Flow Calculation

The calculation of the power losses is conducted in two steps. Initially, it is assumed that the voltage at the output of the turbines is equal to 1 *pu*. An initial round of calculations determines the ohmic AC or DC resistance of the several cables used in the OWF. This is necessary since the resistance depends on the temperature of the conductor which in turn depends on the current loading of the conductor.

After having determined the resistance of all cables, a second round of calculations is realized using a load flow solver. The solver determines the voltage magnitude and angle of every wind generator in order the voltage at the control node of the system to be equal to 1 *pu*. Consequently, the power loss calculations are conducted again.

This procedure is followed for both HVDC and HVAC transmission. However there are some minor differences which are explained in the following sections.

6.3.3.1 HVDC Transmission

In case of HVDC transmission the voltage control node is at the AC terminal of the rectifier [93]. Therefore, this is the reference voltage which takes the 1 *pu* value in the power flow solver. In addition, the voltage at the AC terminal of the onshore inverter is controlled in order the OWF to deliver only active power to the grid ($cos\phi = 1$).

6.3.3.2 HVAC Transmission

Regarding the HVAC transmission, the control node is the connection point to the grid. Thus, the node that takes the 1 *pu* value is the one at the output terminal of the onshore step-up transformer. Furthermore, the AC transmission requires compensation of the HVAC line. Since the SPCs generate reactive power, shunt reactors are assumed to be installed at both ends of the HVAC lines at the offshore and onshore substations. The amount of compensation is accordingly chosen in order only active power to be delivered to the grid ($cos\phi = 1$). In this way, the two transmission schemes are compared on equal terms. Details about the amount of compensation can be found in Appendix D.2.

6.4 Scenarios Overview

Several scenarios, organized in four distinct sets of comparisons, are conducted. The first set shows the impact of soil thermal resistivity and collection voltage level on the power losses, when HVDC transmission is employed. The second set includes the same comparisons as the first one but for HVAC transmission.

Furthermore, the third set shows the difference in power losses for both transmission schemes with respect to the transmission length. Lastly, the fourth set is an expansion of the third set. The same scenarios are conducted again using standard models that do not take into consideration the dependency of power losses on temperature. In other words, the calculations are realized at maximum operation temperature for all components. Consequently, the calculated power losses are compared to the ones derived by using the proposed models.

The following tables give an overview of the most important input data for the three first sets. The fourth set's inputs are identical to the ones of the third set.

First Set of Comparisons: HVDC Transmission				
Variable	Unit	Main Scenario	Soil Resistivity Impact	Voltage Level Impact
MVAC Cable Cross-Section	(mm^2)	150	150	400
HVAC Cable Cross-Section	(mm^2)	1400	1400	1400
HVDC Cable Cross-Section	(mm^2)	630	630	630
MVAC Voltage Level	(kV)	66	66	33
HVAC Voltage Level	(kV)	220	220	220
HVDC Voltage Level	(kV)	640	640	640
Wet/Dry Soil Resistivity	$(K\ m/W)$	0.6/1.8	1.2/3.6	0.6/1.8
Export Cables' Length	(km)	100	100	100

Table 6.1: First set of comparisons: Assessment of the soil thermal resistivity and collection system voltage level impact on power losses for HVDC transmission

Second Set of Comparisons: HVAC Transmission				
Variable	Unit	Main Scenario	Soil Resistivity Impact	Voltage Level Impact
MVAC Cable Cross-Section	(mm^2)	150	150	400
HVAC Cable Cross-Section	(mm^2)	1400	1400	1400
MVAC Voltage Level	(kV)	66	66	33
HVAC Voltage Level	(kV)	220	220	220
Wet/Dry Soil Resistivity	$(K\ m/W)$	0.6/1.8	1.2/3.6	0.6/1.8
Export Cables' Length	(km)	50	50	50

Table 6.2: Second set of comparisons: Assessment of the soil thermal resistivity and collection system voltage level impact on power losses for HVAC transmission

6.5 Results

The results, organized per set of comparisons, are presented in the following sections.

Third and Forth Sets of Comparisons: HVDC vs HVAC Transmission			
Variable	Unit	HVDC Scenario	HVAC Scenario
MVAC Cable Cross-Section	(mm^2)	150	150
HVAC Cable Cross-Section	(mm^2)	800	800
HVDC Cable Cross-Section	(mm^2)	630	-
MVAC Voltage Level	(kV)	66	66
HVAC Voltage Level	(kV)	220	220
HVDC Voltage Level	(kV)	640	-
Wet/Dry Soil Resistivity	$(K\ m/W)$	0.6/1.8	0.6/1.8
Export Cables' Length	(km)	50, 100, 150	50, 100, 150

Table 6.3: Third and forth sets of comparisons: HVDC versus HVAC transmission with respect to the transmission line's length

6.5.1 First Set of Comparisons

Figure 6.6A shows how the efficiency of the OWF changes after each component while Figure 6.6B shows the power losses per component for the three scenarios. Initially, from the efficiency graph, it can be observed that the main scenario achieves the highest total efficiency. The scenario with the high soil thermal resistivity comes second with a relatively small difference from the first. The low collection voltage scenario has the highest losses.

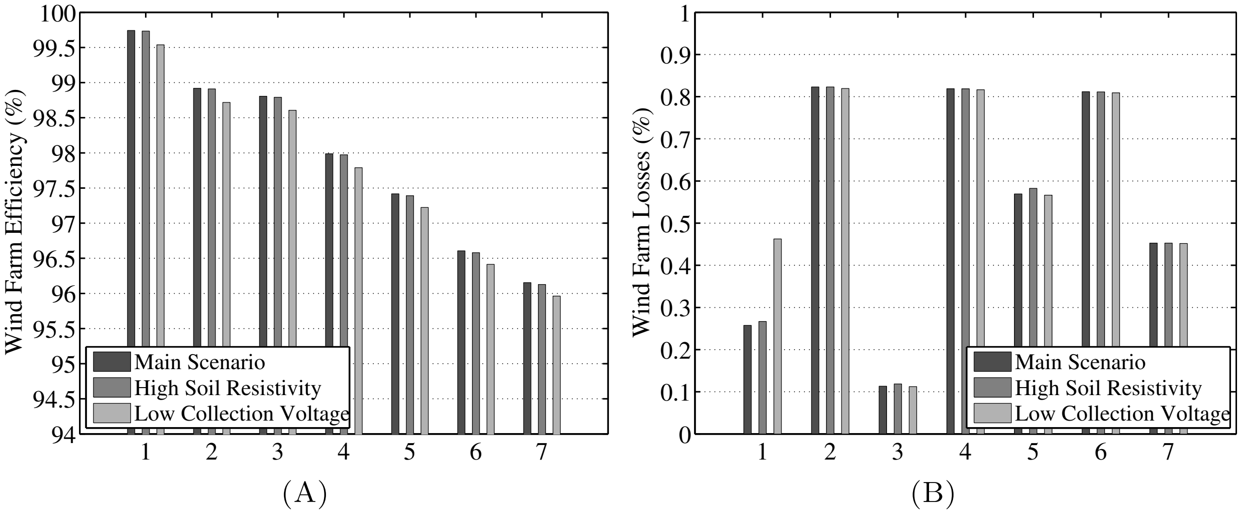

Figure 6.6: First set of comparisons: (A) Efficiency (B) Losses (1:Collection System 2:Offshore Transformers 3:HVAC Line 4:Rectifier 5:HVDC Line 6:Inverter 7:Onshore Transformer)

A better insight is given from the losses graph. It is seen that the difference in efficiency is mainly due to the difference in losses at the cables of the system. Comparing the first two scenarios, it is observed that although the high soil thermal resistivity leads to higher losses, it does not affect them significantly. On the contrary, the low collection voltage almost doubles the losses at the cables of the collection system.

Furthermore, the losses at the HVAC cables are very similar for the three scenarios with the high soil thermal resistivity scenario suffering the higher ones. It should be mentioned that these cables have a short length (approximately 8 km). Therefore the difference in losses is not very noticeable.

Regarding the HVDC cables, it is evident that the second scenario has the highest losses. The third scenario has a slightly better efficiency than the first one. In the third scenario, there are high losses at the collection system. Thus, the power that the HVDC cables have to transmit is lower. Since the HVDC voltage is the same at both scenarios, the current at the third scenario is lower which leads to lower losses.

The rest of the components of the system have approximately the same efficiency for all scenarios.

Table 6.4 shows the efficiency of the OWF and its lifetime energy yield for the three scenarios. The same trends can be seen once again. The first two scenarios have similar total efficiencies and therefore energy production. The third scenario comes last in energy yield because of its lower efficiency.

It should be underlined that although the high soil resistivity does not have a large impact on the power losses, it affects significantly the current carrying capacity of the cable as it was shown in Figure 3.18. This means that for transmitting the same amount of current a cable of larger cross section is necessary when it is buried in soil with higher thermal resistivity. For example, the HVAC cables need to have a cross section of 800 mm^2 when the soil resistivity is 0.6 $K\ m/W$. This cross section has to increase to 1400 mm^2 when doubling the soil thermal resistivity.

First Set of Comparisons: HVDC Transmission				
Variable	Unit	Main Scenario	Soil Resistivity Impact	Voltage Level Impact
Wind Farm Efficiency	(%)	96.15	96.13	95.96
Lifetime Energy Yield	(TWh)	57.494	57.478	57.379

Table 6.4: First set of comparisons: Efficiency and energy yield

6.5.2 Second Set of Comparisons

The same graphs are presented for the second set of comparisons in Figure 6.7. It is evident that the results are quite similar to the ones of the first set and that the same trends are present. It is observed that the third scenario is again the one with the lowest efficiency mainly due to the high losses of the collection system.

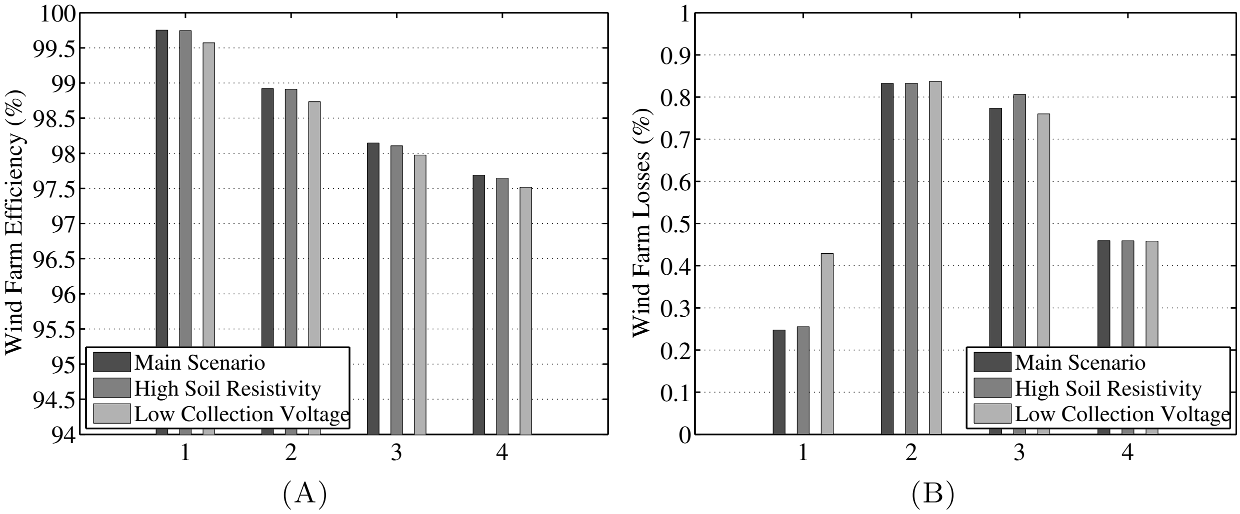

FIGURE 6.7: Second set of comparisons: (A) Efficiency (B) Losses
(1:Collection System 2:Offshore Transformers 3:HVAC Line 4:Onshore Transformer)

Regarding the transmission line, the losses of the HVAC cable in the third scenario are lower than the ones in the first scenario. The high collection system losses of the third scenario, which lead to lower current at the transmission line, are again responsible for this result.

Table 6.5 summarizes the efficiency and the lifetime energy yield for the three scenarios of the second set of comparisons.

Second Set of Comparisons: HVAC Transmission				
Variable	Unit	Main Scenario	Soil Resistivity Impact	Voltage Level Impact
Wind Farm Efficiency	(%)	97.69	97.65	97.52
Lifetime Energy Yield	(TWh)	58.411	58.387	58.308

TABLE 6.5: Second set of comparisons: Efficiency and energy yield

6.5.3 Third Set of Comparisons

Figure 6.8 presents the total OWF efficiency and Figure 6.9 shows the OWF efficiency per wind direction for both transmission schemes and for three different transmission lengths.

From the first graph, it is evident that the HVAC scheme is more efficient for short transmission lengths. As the length increases, the OWF efficiency decreases more rapidly using HVAC than HVDC transmission. After a specific length the HVDC option becomes more efficient. For the particular components used in this case study, this length is approximately 115 km.

In Figure 6.9, it can be noted once more that the transmission length has a greater impact on the efficiency when HVAC transmission is employed (i.e the lines corresponding to HVDC

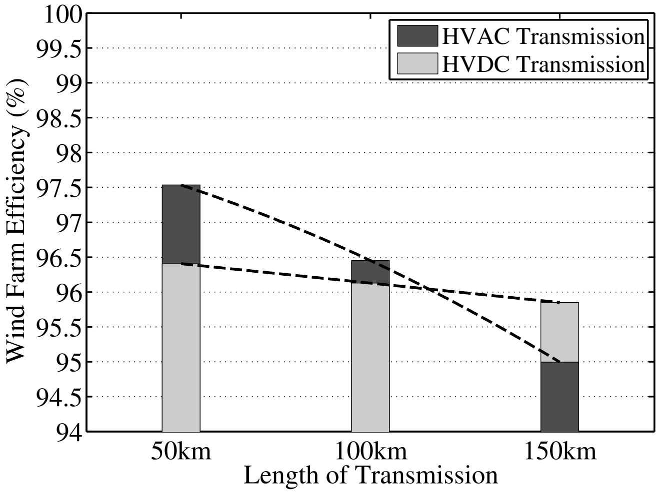

Figure 6.8: Third set of comparisons: Impact of HVDC and HVAC transmission on wind farm efficiency

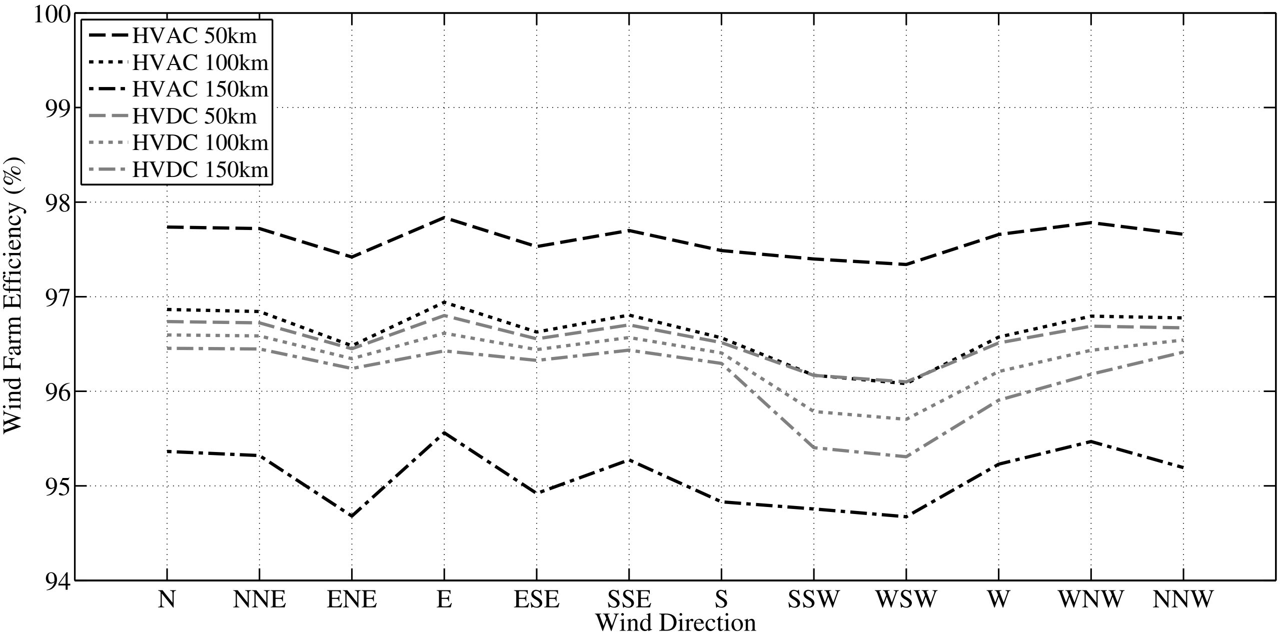

Figure 6.9: Third set of comparisons: Wind farm efficiency per wind direction

transmission are closer together than the ones of the HVAC transmission). Furthermore, it should be mentioned that the shape of the lines depends on the power production for each wind direction (Figure 6.5). Different amounts of power lead to different operation points on the efficiency curves of the transformers and/or the converters. This means that the efficiency of these components varies per wind direction which affects the shape of the lines accordingly.

Furthermore, Figure 6.10 shows the losses per component for both transmission schemes and for the same three transmission lengths. Regarding the HVDC transmission scheme, it can be argued that the losses of the export cables are only a fraction of the total losses since the transformers and the converters are responsible for the largest part of them. In addition, as the length increases from 50 to 100 to 150 km the transmission line losses increase approximately by 0.3%.

The transmission line is the major contributor to the total power losses when using HVAC transmission. In addition, the losses of the line increase more steeply with increasing transmission length from almost 1% at 50 km, to 2% at 100 km and to 3.5% at 150 km.

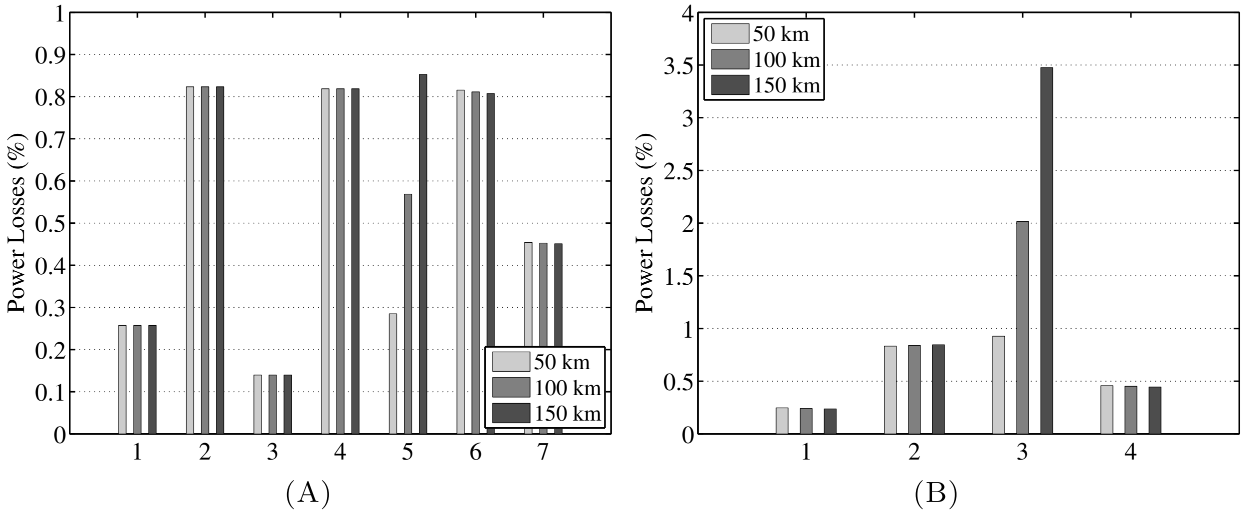

Figure 6.10: Third set of comparisons: (A) HVDC Transmission Losses (1:Collection System 2:Offshore Transformers 3:HVAC Line 4:Rectifier 5:HVDC Line 6:Inverter 7:Onshore Transformer) (B) HVAC Transmission Losses (1:Collection System 2:Offshore Transformers 3:HVAC Line 4:Onshore Transformer)

Table 6.6 summarizes the OWF efficiency and lifetime energy production for both HVDC and HVAC transmission and for the three lengths. As expected, the efficiency and thus the energy yield suffer a larger decrease as the transmission length increases in case of HVAC transmission.

Third Set of Comparisons: HVDC vs HVAC Transmission							
Variable	Unit	HVDC Scenario			HVAC Scenario		
Export Cables' Length	(km)	50	100	150	50	100	150
Wind Farm Efficiency	(%)	96.41	96.13	95.85	97.53	96.45	94.99
Lifetime Energy Yield	(TWh)	57.645	57.479	57.312	58.320	57.672	56.801

Table 6.6: Third set of comparisons: Efficiency and energy yield

6.5.4 Fourth Set of Comparisons

In the fourth set, which is an expansion of the third set, the proposed models are compared against standard models (i.e. they assume that conductors and semiconductors operate at maximum temperature). Figure 6.11 shows the difference in losses between the proposed and standard models for both transmission options. The three bars for each component correspond to the three aforementioned transmission lengths with ascending order (i.e. the first bar corresponds to 50 km, the second to 100 km and the third to 150 km).

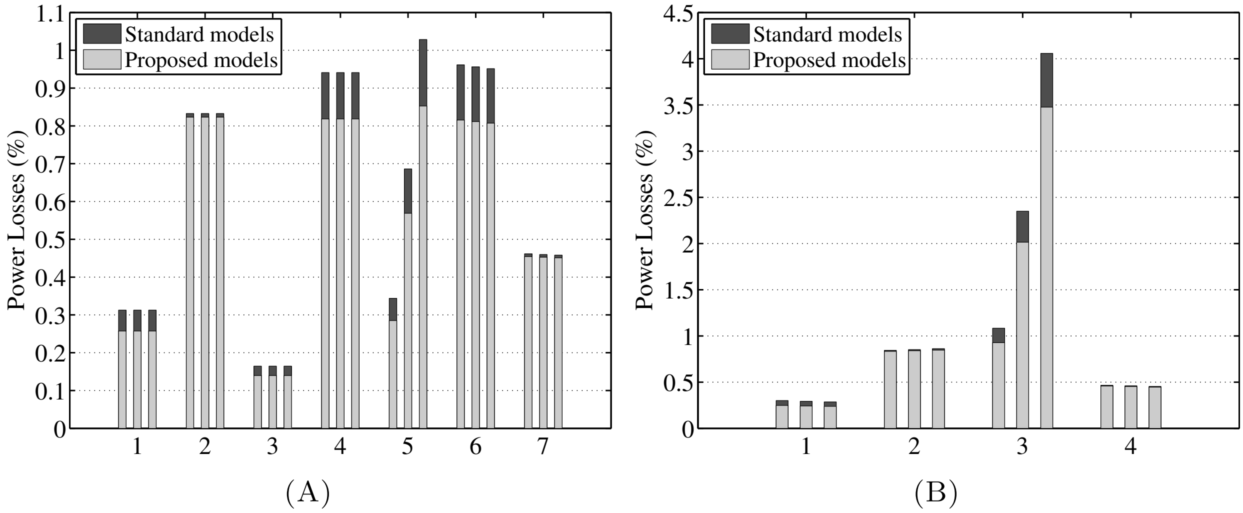

FIGURE 6.11: Fourth set of comparisons: (A) HVDC Transmission Losses (1:Collection System 2:Offshore Transformers 3:HVAC Line 4:Rectifier 5:HVDC Line 6:Inverter 7:Onshore Transformer) (B) HVAC Transmission Losses (1:Collection System 2:Offshore Transformers 3:HVAC Line 4:Onshore Transformer)

Regarding the HVDC transmission, it can be noted that the standard models calculate higher power losses mainly for the cables and the converters. More specifically, The collection system losses are approximately 0.05% higher when using standard models. In addition, although the difference at the HVAC cables is inconsiderable due to their short length, it grows larger at the transmission line and reaches almost 0.2% for a length of 150 km. Furthermore, the converters have approximately 0.1% higher losses when the temperature effect is not considered. Finally, it is evident that the transformers' losses do not change significantly.

For HVAC transmission, the difference between proposed and standard models is evident at the cables. The loss difference for the collection system is the same as for HVDC transmission but it is not that clearly seen due to the larger Y-axis scale. The difference increases significantly at the export cables and surpasses the 0.5% for 150 km. Lastly, similarly to the HVDC option, the difference regarding the transformers' losses is negligible.

Figure 6.12 presents the total OWF efficiency calculated by the proposed and the standard models for both transmission schemes and for the three transmission lengths. As expected, the efficiency is higher when using the proposed models for both HVDC and HVAC options. In addition, it can be observed that the point where the HVDC transmission becomes more efficient than the HVAC one is approximately the same (i.e. approximately 115 km). This means that the proposed models derive the same trend between HVDC and HVAC transmission as the standard models.

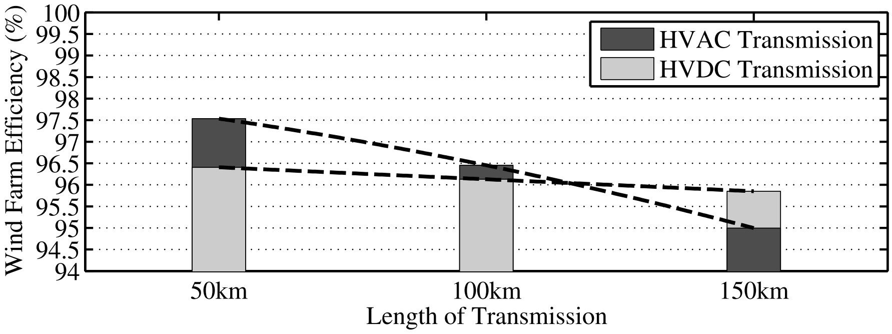

(A)

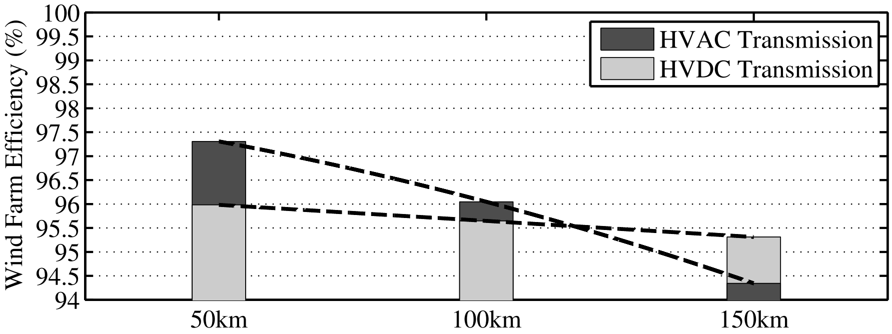

(B)

FIGURE 6.12: Fourth set of comparisons: (A) OWF efficiency using proposed models (B) OWF efficiency using standard models

Chapter 7

Conclusions and Future Work

The work described in this thesis has aimed to the development of models for the calculation of the collection and transmission losses of OWFs. Such models are vital for optimizing the process of FEED of OWFs and ultimately decreasing the cost of offshore wind energy. Models calculating the power losses of AC and DC SPCs, MMCs and power transformers have been introduced and assessed.

The models have met the initial requirements of high computational speed, capture of averaged steady-state operation, modularity and exclusive use of code. Furthermore, they have included a number of model-sensitive features. The SPC models has taken into account the fluctuation of characteristics of the surrounding soil (temperature, thermal resistivity) across the cable's length. The converter model has been built in order to take into consideration the IGBT module's datasheet and incorporate the impact of the operating temperature on the power losses. In addition, the transformer model has included the windings' operating temperature impact.

More specifically, the core of the SPC model has been based on the methodology presented by Anders and Brakelmann in [28]. However, several additional elements have been introduced. Initially, the cable has been divided in segments which have been modeled as pi models. Every segment has been provided with its own inputs (i.e. soil resistivity and temperature) and thus the losses have been calculated by using high resolution of the space varying soil properties. Furthermore, the use of simulation software for calculating the rated current of the cable (varies with the surrounding soil characteristics) and the current limit above which drying-out of the soil occurs has been eliminated by the introduction of iterative procedures. The results of the model have been compared with the results presented in [28] and the model's accurate operation has been proved.

Regarding the MMC model, taking into account the existing gap in the literature, a novel loss model has been described. The model has captured the main sources of power losses (conduction, switching and gate drivers' losses) and has included additional loss sources (inductor's losses and cooling requirements) while incorporating the effect of the conductors' and semiconductors' temperature variation. The model's operation has been compared against another averaged model developed by Allebrod, Hamerski and Marquardt and presented in [23]. Since the later, only takes into consideration the main loss sources and assumes that the converter always operates at maximum temperature, comparisons have been performed on the same basis by deactivating all the additional features from the proposed model. It has been shown that the models give similar results. Consequently, several assessments of the model have been conducted by gradually activating its novel features.

Power transformers are an established technology. The loss model has been based on the well-known simplified equivalent circuit of a power transformer. Additions have been made to approximate the impact of the winding's temperature on the losses and to take into consideration the cooling requirements. The model has been assessed using a hypothetical transformer based on figures found in literature. Comparisons have been performed between different windings' configurations and it has been shown that the results agree with the literature.

After presenting and assessing each model individually, a case study has been conducted to show how the models perform under realistic conditions. For this reason, an OWF has been designed and its losses have been calculated for a variety of different scenarios for both HVDC and HVAC transmission. The impact of variables such as the soil thermal resistivity and the collection system voltage has been assessed. In addition, comparisons between the power losses of HVAC and HVDC transmission with respect to the transmission length have been conducted. Lastly, the proposed models have been compared against standard models (in which temperature dependence is not considered) in order to assess the impact of the implementation of the conductors' and semiconductors' temperature variation.

Models are, essentially, tools that aim to capture the operation or behavior of a system according to some set criteria. In this context, there are always improvements that can be implemented in order to further refine them and produce results closer to reality. Some of these improvements are the following:

- Regarding the MMC model, it has been assumed that the semiconductors' temperature varies linearly with respect to the current flowing through them. Investigating and implementing a more accurate relationship between semiconductors' temperature and current would yield an even more realistic estimation of the converter losses.

- The same linear relationship has been used for computing the windings' temperature for the transformer model. Similarly, the derivation and application of a more accurate relationship would result in more realistic loss calculation.

- Regarding the case study, more detailed wind data could be used. For the power production of the OWF, an average value per wind direction is considered. Using the wind speed distribution per wind direction and calculating the power production of the OWF in greater detail would improve the results since the losses depend on the square of the current.

- The models presented and assessed in this thesis have focused on the collection and transmission losses. Therefore, the case study's results have not included the losses occurring in the drive-train of the wind generators. Including these losses would give more accurate estimations in terms of absolute values of the power losses.

- Another area for improvement of the case study's results could be a more accurate modeling of the reactive compensation. When using HVAC transmission, reactive power compensation has been applied at both ends of the transmission lines to balance the produced reactive power from the inherent capacitance of the SPCs. This reactive compensation has been modeled as a pure reactive load. In reality, the shunt reactors, that are used for this purpose, have power losses. Taking these losses into consideration would lead to a more accurate estimation of the total losses of the OWF.

Appendix A

Cabling Model

A.1 Thermal Resistance of Power Cables

The equations, for calculating the thermal resistance of some types of power cables used for submarine applications, are given below. Normally, the equations corresponding to every possible power cable assembly cannot be presented in the context of this thesis and the reader is encouraged to refer to the *IEC* 60287 standard for further information.

In case of a cable having screening layers, metallic tapes are considered to be part of the conductor or the sheath while semi-conducting layers (including metallized carbon paper tapes) are considered as part of the insulation. The appropriate component dimensions must be modified accordingly [27].

A.1.1 Thermal Resistance T_1

The T_1 thermal resistance is the one between one conductor and the sheath of the cable. For a single-core cable, AC or DC, it can be calculated as follows [27] [39]:

$$T_1 = \frac{\rho_i}{2\pi} \ln\left(1 + \frac{2t_1}{d_c}\right) \tag{A.1.1}$$

Where:

- ρ_i: Thermal resistivity of insulation $(K\ m/W)$
- d_c: Conductor diameter (mm)
- t_1: Thickness of insulation between conductor and sheath (mm)

Regarding three-core cables with a common metallic sheath over all three cores, T_1 can be determined by the following equation:

$$T_1 = K\frac{\rho_i}{2\pi}G + 0.031(\rho_f - \rho_i)e^{0.67\frac{t}{d_c}} \tag{A.1.2}$$

Where:

- ρ_i: Thermal resistivity of insulation $(K\ m/W)$
- ρ_f: Thermal resistivity of the filler material $(K\ m/W)$
- G: Geometric factor $(-)$
- d_c: Conductor diameter (mm)
- t: Insulation thickness between conductors (mm)

The geometric factor G can be determined by the graph in Figure A.1 [27]:

Concerning three-core cables that have individual metallic screens/sheaths over each core, T_1 is calculated using the same formula as for single-core cables [27] [39].

A.1.2 Thermal Resistance T_2

The second thermal resistance corresponds to the part of the cable between the sheath and the armour. For a single-core AC or DC cable and for a three-core cable having a common metallic sheath over its cores, T_2 is determined by the equation given below [27] [39]:

$$T_2 = \frac{\rho_{sa}}{2\pi}\ln\left(1 + \frac{2t_2}{D_s}\right) \tag{A.1.3}$$

Where:

- ρ_{sa}: Thermal resistivity of the material between the sheath and the armour $(K\ m/W)$
- D_s: Outer diameter of the sheath (mm)
- t_2: Thickness of the bedding between the sheath and the armour (mm)

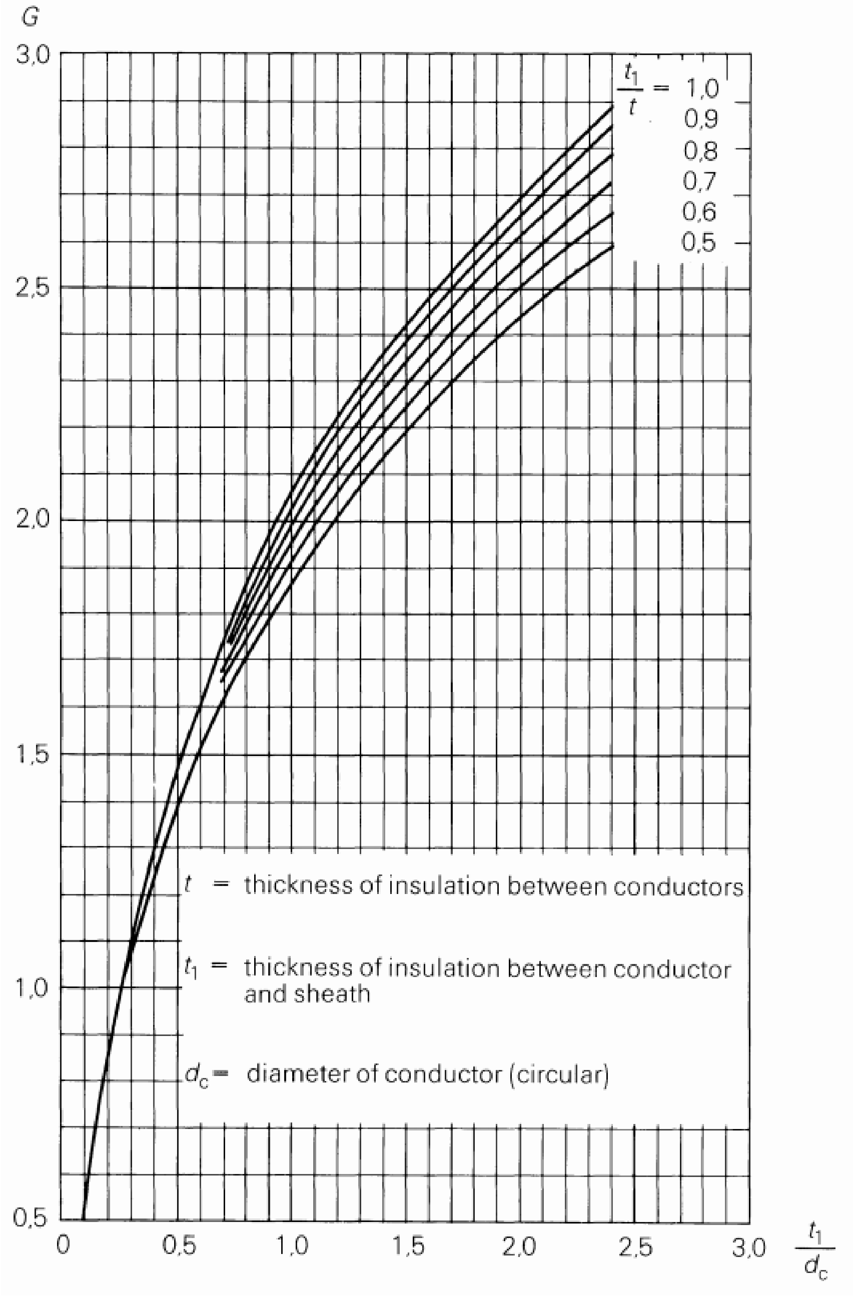

FIGURE A.1: The Geometric Factor G, [27]

Regarding three-core power cables bearing individual metallic screens/sheaths over each core, the thermal resistance T_2 can be calculated by the following expression [27] [39]:

$$T_2 = \frac{\rho_{sa}}{6\pi}\bar{G} \tag{A.1.4}$$

Where:

- ρ_{sa}: Thermal resistivity of the material between the sheath and armour $(K\ m/W)$
- $\bar{G}$: Geometric factor $(-)$

The geometric factor $\bar{G}$ can be determined graphically by using the corresponding graph provided shown in Figure A.2 [27]:

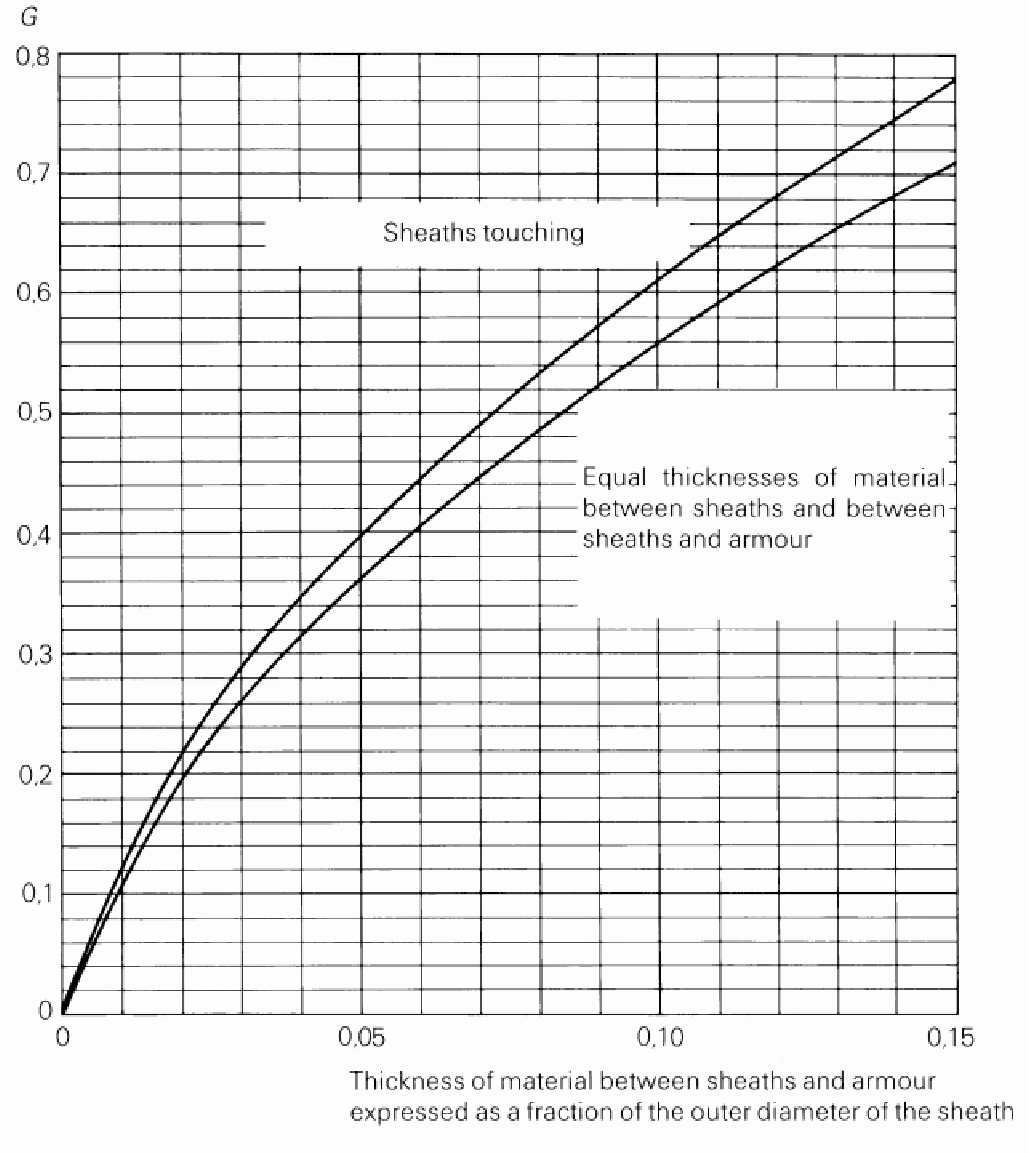

FIGURE A.2: The Geometric Factor $\bar{G}$ [27]

A.1.3 Thermal Resistance T_3

The thermal resistance T_3 relates to the external serving of the cable and can be calculated by the same formula for all cable types under consideration [27] [39]:

$$T_3 = \frac{\rho_{se}}{2\pi} \ln\left(1 + \frac{2t_3}{D_\alpha}\right) \tag{A.1.5}$$

Where:

- ρ_{se}: Thermal resistivity of the material of the serving $(K\ m/W)$

- D_a: Outer diameter of the armour (mm)
- t_3: Thickness of the serving (mm)

A.1.4 Thermal Resistance T_4

The forth and last thermal resistance refers to the immediate surroundings of the cable. For a single isolated buried cable, such as a three-core cable, it is given by the following expression [27]:

$$T_4 = \frac{1}{2\pi}\rho \ln\left(u + \sqrt{u^2 - 1}\right) \tag{A.1.6}$$

$$u = \frac{2L_1}{D_e} \tag{A.1.7}$$

Where:

- ρ: Thermal resistivity of the surrounding soil ($K\ m/W$)
- L_1: Distance from the surface of the ground to the cable axis (mm)
- D_e: External diameter of the cable (mm)

When $u > 10$, the expression A.1.6 can be simplified as follows [27]:

$$T_4 = \frac{1}{2\pi}\rho \ln(2u) \tag{A.1.8}$$

However, for a HVDC installation, there are two cables equally loaded, laid at the same depth and spaced apart. In this case the expression becomes [27] [11]:

$$T_4 = \frac{1}{2\pi}\rho \left\{ \ln\left(u + \sqrt{u^2 - 1}\right) + \frac{1}{2}\ln\left[1 + \left(\frac{2L_1}{s_1}\right)^2\right] \right\} \tag{A.1.9}$$

$$u = \frac{2L_1}{D_e} \tag{A.1.10}$$

Where:

- ρ: Thermal resistivity of the surrounding soil ($K\ m/W$)

- L_1: Distance from the surface of the ground to the cable axis (mm)
- D_e: External diameter of the cable (mm)
- s_1: Axial separation between the two cables (mm)

Lastly, in case of an installation including three single-core power cables buried together in trefoil formation, the thermal resistance T_4 can be calculated as follows [27]:

$$T_4 = \frac{1.5}{\pi}\rho\left[\ln\left(2u\right) - 0.630\right] \tag{A.1.11}$$

$$u = \frac{2L_2}{D_e} \tag{A.1.12}$$

Where:

- ρ: Thermal resistivity of the surrounding soil ($K\ m/W$)
- L_2: Distance from the surface of the ground to center of the trefoil group (mm)
- D_e: External diameter of one cable (mm)

In addition, for a trefoil formation, the T_3 thermal resistance calculated by the formulation given in section A.1.3 has to be multiplied by a factor equal to 1.6.

A.2 AC Resistance of the Conductor: Skin and Proximity Effect Factors

The skin and proximity effect factors for a three-core cable or three single-core cables with round conductors in flat or trefoil formation are given below. For other cable configurations (two-core cables, shaped conductors, pipe-type cables) the reader is referred to the *IEC* 60287 standard.

A.2.1 Skin Effect Factor

The skin effect factor is calculated as shown below [27]:

$$y_s = \frac{x_s^4}{192 + 0.8x_s^4} \tag{A.2.1}$$

$$x_s^2 = \frac{8\pi f}{R_{DC}^{\theta_{c,Max}}} 10^{-7} k_s \tag{A.2.2}$$

Where:

- f: Supply frequency (Hz)
- $R_{DC}^{\theta_{c,Max}}$: DC resistance per m of the conductor at $\theta_{c,Max}$ (°C) (Ω/m)

The coefficient k_s depends on the shape and the material of the conductor and is tabulated in the IEC 60287 standard.

A.2.2 Proximity Effect Factor

The proximity factor corresponding to three-core cables or three single-core cables, can be derived by the following equations:

$$y_p = \frac{x_p^4}{192 + 0.8x_p^4}\left(\frac{d_c}{s_0}\right)^2 \left[0.312\left(\frac{d_c}{s_0}\right)^2 + \frac{1.18}{\frac{x_p^4}{192+0.8x_p^4} + 0.27}\right] \tag{A.2.3}$$

$$x_p^2 = \frac{8\pi f}{R_{DC}^{\theta_{c,Max}}} 10^{-7} k_p \tag{A.2.4}$$

Where:

- d_c: Diameter of the conductor (mm)
- s_0: Distance between the conductor axes (mm)
- f: Supply frequency (Hz)
- $R_{DC}^{\theta_{c,Max}}$: DC resistance per m of the conductor at $\theta_{c,Max}$ (°C) (Ω/m)

The coefficient k_p is also tabulated in the IEC 60287 standard.

A.3 Inductance of Power Cables

Regarding a flat or trefoil formation of three single-core cables, their inductance per m (H/m) can be calculated according to equation A.3.1, with $N = 1$ corresponding to a trefoil formation and $N = 1.26$ to a flat formation as shown in Figure A.3 [31][94]. The same formula can be used also for the calculation of the inductance of a three-core cable [31]. Table A.1 summarizes some typical values of the constant K for different conductors.

$$L = (K + 0.2 \ln \left(\frac{2Ns_0}{d_c} \right))10^{-6} \tag{A.3.1}$$

Where:

- K: Constant depending on the number of wires in the conductor ($-$)
- d_c: Diameter of the conductor (mm)
- s_0: Distance between the conductor axes (mm)

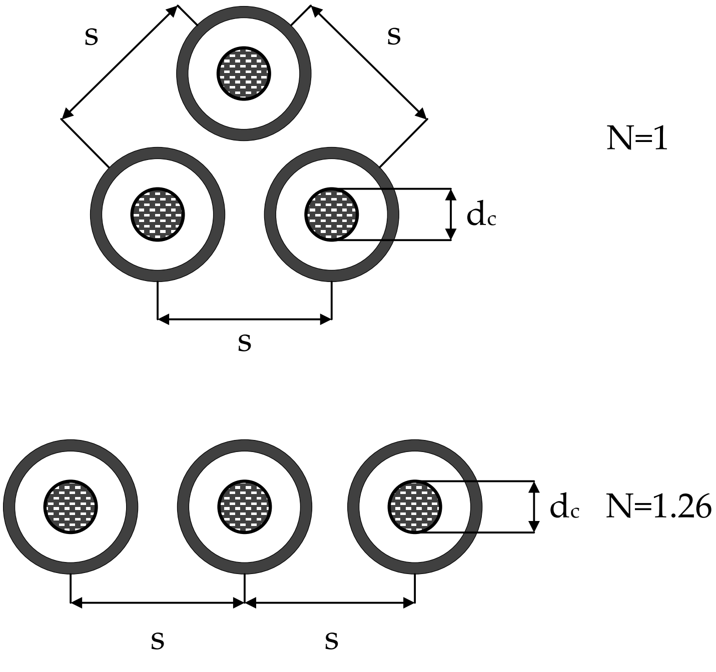

Figure A.3: Trefoil and Flat formation of three single-core cables

A.4 Capacitance and Dielectric Losses of Power Cables

The insulation of the cable can be modeled by a capacitance and a resistance connected in parallel between the conductor and the metallic screen/sheath.When the cable is energized, a

Typical values for constant K	
Number of wires in conductor	K
3	0.0778
7	0.0642
19	0.0554
37	0.0528
61 and over	0.0514
1 (solid)	0.0500
Hollow-core conductor, $12mm$ duct	0.0383

TABLE A.1: Typical values for constant K for different stranded conductors at $50Hz$ [31]

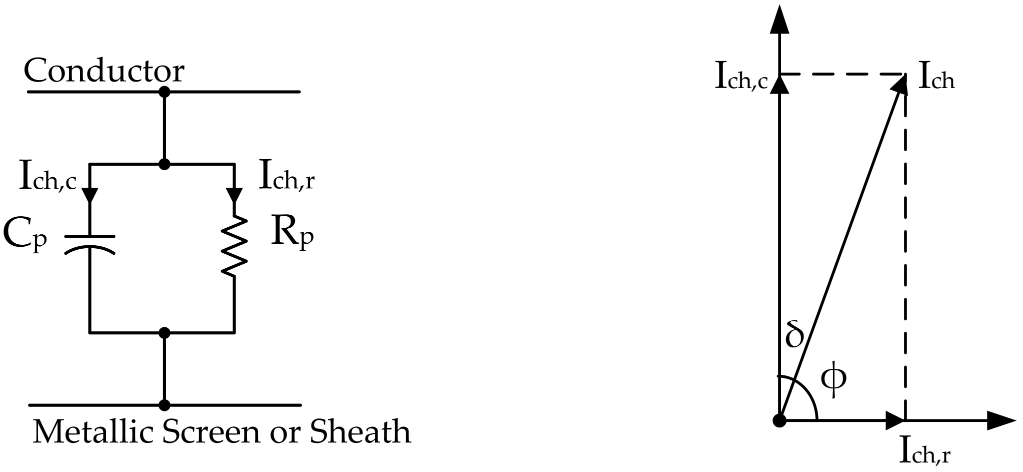

(A)

(B)

FIGURE A.4: MMC SMs: (A) Graphical representation of the insulation (B) Phasor diagram of the charging current

capacitive current, whose phase is shifted 90 ° ahead of the voltage phase, flows through the capacitance. In addition a resistive current, whose phase is in line with the voltage phase, flows through the resistance. The charging current $\overline{I}_{ch}$ is the sum of these individual currents:

$$\overline{I}_{ch} = \overline{I}_{ch,r} + \overline{I}_{ch,c} \tag{A.4.1}$$

The resistive and capacitive currents can be given by the following expressions:

$$\overline{I}_{ch,r} = \frac{\overline{U}_0}{R_p} \tag{A.4.2}$$

$$\overline{I}_{ch,c} = j\omega C_p \overline{U}_0 \tag{A.4.3}$$

Where $\overline{U_0}$ is the voltage across the insulation or in other words the conductor voltage to earth. From Figure A.4, it can be seen that the ratio between the magnitudes of the resistive and the capacitive current is equal to the tangent of angle δ. This tangent is called the loss factor:

$$\tan\delta = \frac{\left|\overline{I}_{ch,r}\right|}{\left|\overline{I}_{ch,c}\right|} = \frac{1}{R_p C_p \omega} \tag{A.4.4}$$

The magnitude of the charging current can also be expressed in term of the loss factor as follows:

$$\left|\overline{I}_{ch}\right| = \sqrt{I_{ch,r}^2 + I_{ch,c}^2} = \sqrt{I_{ch,c}^2(1+\tan\delta)} = \left|\overline{I}_{ch,c}\right| \sqrt{(1+\tan\delta)} \tag{A.4.5}$$

The dielectric loss is expressed as a consumption of real power on the resistance R_p. Therefore, using the expression of the loss factor the dielectric loss per m (W/m) can be calculated as follows:

$$W_d = \left|\overline{U}_0\right| \left|\overline{I}_{ch,r}\right| = \left|\overline{U}_0\right| \left|\overline{I}_{ch,c}\right| \tan\delta = \omega C_p U_0^2 \tan\delta = 2\pi f C_p U_0^2 \tan\delta \tag{A.4.6}$$

Where:

- f: System frequency (Hz)
- C_p: Shunt capacitance per m (F/m)
- U_0: Conductor phase voltage (V)

The capacitance per m in F/m can be derived by the equation shown below [27]:

$$C = \frac{\varepsilon}{18\ln\left(\frac{D_i}{d_c}\right)} 10^{-9} \tag{A.4.7}$$

Where:

- ε: Relative permittivity of the insulation material ($-$)
- D_i: External diameter of the insulation (excluding screen) (mm)
- d_c: Diameter of conductor (including screen, if any) (mm)

A.5 Screen/Sheath and Armour Loss Factors

The *IEC* 60287 standard includes formulas for the calculation of the screen/sheath loss factor for a variety of different cable assemblies and installations. It's impossible for all these cases to be presented in the context of this report. Therefore only some of them will be given mainly as an indication of the parameters on which the factor depends on. The reader is referred to the actual standard for further information.

A.5.1 Screen/Sheath Loss Factor

For three single-core cables in trefoil formation with sheaths bonded at both ends, the loss factor is given as follows in A.5.1.

$$\lambda_1^{'} = \frac{R_{sh}^{\theta_{sh,Max}}}{R_{AC}^{\theta_{c,Max}}} \frac{1}{1 + \left(\frac{R_{sh}^{\theta_{sh,Max}}}{X_{sh}} \right)^2} \tag{A.5.1}$$

$$\lambda_1^{''} = 0 \tag{A.5.2}$$

$$X_{sh} = 2\omega \ln \left(\frac{2s}{d_s} \right) 10^{-7} \tag{A.5.3}$$

In case of a three-core cable whose cores have an individual lead sheath (SL-type cables), the sheath loss factor is given by a similar relation as shown in A.5.4.

$$\lambda_1^{'} = \frac{R_{sh}^{\theta_{sh,Max}}}{R_{AC}^{\theta_{c,Max}}} \frac{1.5}{1 + \left(\frac{R_{sh}^{\theta_{sh,Max}}}{X_{sh}} \right)^2} \tag{A.5.4}$$

$$\lambda_1^{''} = 0 \tag{A.5.5}$$

$$X_{sh} = 2\omega \ln \left(\frac{2s_0}{d_s} \right) 10^{-7} \tag{A.5.6}$$

Where:

- $R_{sh}^{\theta_{sh,Max}}$: AC resistance per m of the sheath at $\theta_{sh,Max}$ (°C) (Ω/m)
- $R_{AC}^{\theta_{c,Max}}$: AC resistance per m of the conductor at $\theta_{c,Max}$ (°C) (Ω/m)
- X_{sh}: Reactance per m of the sheath (Ω/m)

- ω: Angular speed of the system (rad/s)
- s_0: Distance between conductor axes (mm)
- d_s: Mean diameter of the sheath (mm)

For a three-core unarmoured cable where the cores are contained in a common metallic sheath, $\lambda_1^{'}$ is negligible and the loss factor equals the $\lambda_1^{''}$. In case that the cable has round or oval conductors and the sheath resistance $R_{sh}^{\theta_{sh,Max}}$ is lower than $100\mu\Omega/m$ the loss factor is determined according to A.5.7.

$$\lambda_1^{''} = \frac{3R_{sh}^{\theta_{sh,Max}}}{R_{AC}^{\theta_{c,Max}}} \left[\left(\frac{2c}{d_s}\right)^2 \frac{1}{1+\left(\frac{R_{sh}^{\theta_{sh,Max}}}{\omega}10^7\right)^2} + \left(\frac{2c}{d_s}\right)^4 \frac{1}{1+4\left(\frac{R_{sh}^{\theta_{sh,Max}}}{\omega}10^7\right)^2} \right] \tag{A.5.7}$$

Whereas, when the cable, for the same round or oval conductors, has a sheath resistance $R_s^{\theta_{s,max}}$ which is greater than $100\mu\Omega/m$ the equation is as shown in A.5.8.

$$\lambda_1^{''} = \frac{3.2\omega^2}{R_{AC}^{\theta_{c,Max}} R_{sh}^{\theta_{sh,Max}}} \left(\frac{2c}{d_s}\right)^2 10^{-14} \tag{A.5.8}$$

Where:

- c: The distance between the axis of one conductor and the axis of the cable (mm)

The addition of a steel armour increases the loss in the sheath related to eddy currents. Therefore, in this case the relations A.5.7 and A.5.8 need to be multiplied by a factor given in

$$\left[1+\left(\frac{d_s}{d_a}\right)^2 \frac{1}{1+\frac{d_a}{\mu_{st}\delta_a}}\right] \tag{A.5.9}$$

$$\delta_a = \frac{A_a}{\pi d_a} \tag{A.5.10}$$

Where:

- d_a: Mean diameter of the armour (mm)
- μ_{st}: Relative permeability of the steel $(-)$
- δ_a: Equivalent thickness of the armour (mm)
- A_a: Cross-sectional area of the armour (mm^2)

A.5.2 Armour Loss Factor

Similarly to the screen/sheath loss factor, the *IEC* 60287 gives formulations for the armour loss factor of different cabling configurations. Indicatively, for a three-core cable of round conductors bearing a steel wire armour, the lass factor λ_2 is given from A.5.11.

$$\lambda_2 = 1.23\frac{R_a^{\theta_{a,Max}}}{R_{AC}^{\theta_{c,Max}}}\left(\frac{2c}{d_a}\right)^2\frac{1}{\left(\frac{2.77R_a^{\theta_{a,Max}}10^6}{\omega}\right)^2+1} \tag{A.5.11}$$

In case of an SL-type cable with armour, the screening effect of the sheath currents reduces the armour loss. Therefore, in this case the loss factor can be determined as shown in A.5.12.

$$\lambda_2 = 1.23\frac{R_a^{\theta_{a,Max}}}{R_{AC}^{\theta_{c,Max}}}\left(\frac{2c}{d_a}\right)^2\frac{1}{\left(\frac{2.77R_a^{\theta_{a,Max}}10^6}{\omega}\right)^2+1}\left(1-\frac{1}{1+\left(\frac{R_{sh}^{\theta_{sh,Max}}}{X_{sh}}\right)^2}\right) \tag{A.5.12}$$

- $R_a^{\theta_{a,Max}}$: AC resistance per m of the armour at $\theta_{a,Max}$ (°C) (Ω/m)
- d_a: Mean diameter of the armour (mm)
- c: Distance between the axis of one conductor and the axis of the cable (mm)

A.6 Screen/Sheath and Armour Temperature and Resistance

The calculations of screen/sheath and armour loss factors require the screen/sheath and armour resistance respectively. However, these resistances are temperature depended. According to *IEC* 60287, the temperature and the resistance of the screen/sheath are derived by the following relations, respectively:

$$\theta_{sh} = \theta_c - (I_c^2 R_{AC}^{\theta_c} + 0.5W_d)T_1 \tag{A.6.1}$$

Where:

- θ_c: Temperature of the conductor (°C)

- I_c: Current of conductor (A)
- $R_{AC}^{\theta_c}$: AC resistance per m of the conductor at θ_c (°C) (Ω/m)
- W_d: Dielectric loss per m for the insulation surrounding one conductor (W/m)
- T_1: Thermal resistance per m between one conductor and the sheath $(K\ m/W)$

$$R_{sh}^{\theta_{sh}} = R_{sh}^{20}[1 + \alpha_{20}(\theta_{sh} - 20)] \tag{A.6.2}$$

Where:

- R_{sh}^{20}: AC resistance of the screen/sheath at at 20 °C (Ω/m)
- α_{20}: Constant mass temperature coefficient at 20 °C (K^{-1})
- θ_{sh}: Temperature of the screen/sheath (°C)

In addition, similar equations are given for the calculation of the temperature and the resistance of the armour:

$$\theta_a = \theta_c - (I_c^2 R_{AC}^{\theta_c} + 0.5W_d)T_1 - \left[I_c^2 R_{AC}^{\theta_c}(1 + \lambda_1) + W_d\right] nT \tag{A.6.3}$$

Where:

- θ_c: Temperature of the conductor (°C)
- I_c: Current flowing in one conductor (A)
- $R_{AC}^{\theta_c}$: AC resistance per m of the conductor at θ_c °C (Ω/m)
- W_d: Dielectric loss per m for the insulation surrounding one conductor (W/m)
- T_1: Thermal resistance per m between one conductor and the sheath $(K\ m/W)$
- T_2: Thermal resistance per m between the sheath and the armour $(K\ m/W)$
- n: Number of load-carrying conductors in the cable $(-)$
- λ_1: Loss factor for the sheath or screen $(-)$

$$R_a^{\theta_a} = R_a^{20}[1 + \alpha_{20}(\theta_a - 20)] \tag{A.6.4}$$

Where:

- R_a^{20}: AC resistance per m of the armour at at 20 °C (Ω/m)
- α_{20}: Constant mass temperature coefficient at 20 °C (K^{-1})
- θ_a: Temperature of the armour (°C)

A.7 SPC Power Losses by Anders and Brakelmann

The equation 3.3.2 can be altered to give the relation between the conductor temperature and a current that is lower than the maximum permissible current of the conductor:

$$I_c = \left[\frac{\Delta\theta_c - W_d\left[\frac{1}{2}T_1 + n(T_2 + T_3 + T_4)\right]}{R_{AC}^{\theta_c}T_1 + nR_{AC}^{\theta_c}(1 + \lambda_1)T_2 + nR_{AC}^{\theta_c}(1 + \lambda_1 + \lambda_2)(T_3 + T_4)}\right]^{0.5} \tag{A.7.1}$$

Where:

- I_c: Current of conductor (A)
- $\Delta\theta_c$: Conductor temperature rise above the ambient temperature (K)
- $R_{AC}^{\theta_c}$: AC resistance per m of the conductor at θ_c °C (Ω/m)

From this equation, it can be seen that the temperature rise because of the dielectric losses can be expressed as follows:

$$\Delta\theta_d = W_d\left[\frac{1}{2}T_1 + n(T_2 + T_3 + T_4)\right] \tag{A.7.2}$$

In addition, the total ohmic losses per m of the cable are given by the following equation:

$$W_I = nR_{AC,t}^{\theta_c}I_c^2 \tag{A.7.3}$$

Where:

- n: Number of load-carrying conductors in the cable $(-)$
- $R^{\theta_c}_{AC,t}$: Total AC resistance per m of the cable at θ_c°C (Ω/m)
- I_c: Current of conductor (A)

Using the equations 3.3.8 and 3.3.12, the total AC resistance of the cable at temperature θ_c is can be expressed as follows:

$$R^{\theta_c}_{AC,t} = R^{20}_{AC,t}[1 + \alpha_{20}(\theta_c - 20)] \tag{A.7.4}$$

Therefore the total ohmic losses can be written as:

$$W_I = nR^{\theta_c}_{AC,t}I_c^2 = nR^{\theta_c}_{AC}(1 + \lambda_1 + \lambda_2)I_c^2 = nR^{20}_{AC,t}[1 + \alpha_{20}(\theta_c - 20)]I_c^2 \tag{A.7.5}$$

Furthermore, if the total thermal resistance of the cable is expressed as:

$$T_t = \frac{T_1}{n(1 + \lambda_1 + \lambda_2)} + \frac{(1 + \lambda_1)T_2}{(1 + \lambda_1 + \lambda_2)} + (T_3 + T_4) \tag{A.7.6}$$

Then, the equation A.7.1 can be reshaped as follows:

$$\Delta\theta_c = W_I T_t + \Delta\theta_d \tag{A.7.7}$$

In a completely analogous procedure, a similar relations can be derived in case there is drying-out of the soil. Having in mind that v_x is the ratio of the thermal resistivities of the dry and moist soil zones while $\Delta\theta_{cr}$ is the critical temperature rise of the soil, the equation A.7.1 is modified as follows:

$$I_c = \left[\frac{\Delta\theta_c - W_d\left[\frac{1}{2}T_1 + n(T_2 + T_3 + v_x T_4)\right] + (v_x - 1)\Delta\theta_{cr}}{R^{\theta_c}_{AC}T_1 + nR^{\theta_c}_{AC}(1 + \lambda_1)T_2 + nR^{\theta_c}_{AC}(1 + \lambda_1 + \lambda_2)(T_3 + v_x T_4)}\right]^{0.5} \tag{A.7.8}$$

While the temperature rise because of the dielectric losses is the following:

$$\Delta\theta_{d,x} = W_d\left[\frac{1}{2}T_1 + n(T_2 + T_3 + v_x T_4)\right] \tag{A.7.9}$$

Furthermore, a slightly different relation expresses the total thermal resistance:

$$T_{t,x} = \frac{T_1}{n(1+\lambda_1+\lambda_2)} + \frac{(1+\lambda_1)T_2}{(1+\lambda_1+\lambda_2)} + (T_3 + v_x T_4) \tag{A.7.10}$$

Finally, using the substitution: $\theta_x = (v_x - 1)\Delta\theta_{cr}$, the temperature rise is written as follows:

$$\Delta\theta = W_I T_{t,x} + \Delta\theta_{d,x} - \theta_x \tag{A.7.11}$$

It can be seen that the first set of equations, which correspond to the case when no drying-out of the soil occurs, can be derived from the second set of equations (drying-out occurs) by giving the appropriate values to the v_x and θ_x variables:

When drying-out occurs:

$$v_x = \frac{\rho_{dry}}{\rho_{moist}} \tag{A.7.12}$$

$$\theta_x = (v_x - 1)\Delta\theta_{cr} \tag{A.7.13}$$

When drying-out does not occur:

$$v_x = 1 \tag{A.7.14}$$

$$\theta_x = 0 \tag{A.7.15}$$

From now on, only the second set of equations is treated, since it is applicable whether drying-out occurs or not. Using the equation A.7.5 and having in mind that $\Delta\theta_c = \theta_c - \theta_{c,Amb}$, the A.7.11 can be expressed as:

$$\Delta\theta_c = T_{t,x} n R^{20}_{AC,t}[1+\alpha_{20}(\theta_c - 20)]I_c^2 + \Delta\theta_{d,x} - \theta_x = T_{t,x} n R^{20}_{AC,t}(\alpha_{20}\Delta\theta_c + c_a)I_c^2 + \Delta\theta_{d,x} - \theta_x \tag{A.7.16}$$

Where:

$$c_a = 1 + \alpha_{20}(\theta_{c,Amb} - 20) \tag{A.7.17}$$

During the rated loading, the conductor reaches its maximum temperature. In this case the equations A.7.11 and A.7.5 are respectively written as follows:

$$\Delta\theta_{c,Max} = W_{I,R} T_{t,R} + \Delta\theta_{d,R} - \theta_{x,R} \tag{A.7.18}$$

$$W_{I,R} = nR^{20}_{AC,t}[1 + \alpha_{20}(\theta_{c,Max} - 20)]I^2_{c,R} = nR^{20}_{AC,t}c_m I^2_{c,R} \tag{A.7.19}$$

Where:

$$c_m = 1 + \alpha_{20}(\theta_{c,Max} - 20) \tag{A.7.20}$$

Now, the resistance $R^{20}_{AC,t}$ in equation A.7.16 can be substituted by combining the equations A.7.18 and A.7.19. The result is the following:

$$\begin{aligned} \Delta\theta - \Delta\theta_{d,x} + \theta_x = T_{t,x} n R^{20}_{AC,t}(\alpha_{20}\Delta\theta + c_a)I^2_c = \\ = (\Delta\theta_{c,Max} - \Delta\theta_{d,R} + \theta_{x,R})\frac{v_T}{c_m}\left(\frac{I_c}{I_{c,R}}\right)^2(\alpha_{20}\Delta\theta + c_a) \end{aligned} \tag{A.7.21}$$

Where:

$$v_T = \frac{T_{t,x}}{T_{t,R}} \tag{A.7.22}$$

Three different cases may arise regarding the interpretation of equation A.7.22. If drying-out of the soil occurs for current I_c which is assumed to be lower than the rated current, then naturally there is also drying-out for the rated current. In this case $v_T = 1$. If there is no drying-out for current I_c but the soil dries out under its rated loading then the numerator of v_T is the total thermal resistance of the cable that corresponds to moist soil ($v_x = 1$) and the denominator is the one that corresponds to dried soil. Finally, if the soil does not dry out at the cable's rated loading then it is assumed that it never dries out for any current. In this case $v_T = 1$ too. In this context, the assumption that the loss factors λ_1 and λ_2, which are needed for the calculation of the total thermal resistance, are not dependent on the current values. This is not correct but the error which is introduced by this assumption is negligible [28].

Solving the equation A.7.21 with respect to the temperature rise, the following relation is derived:

$$\Delta\theta = \frac{v_T c_a(\Delta\theta_{c,Max} - \Delta\theta_{d,R} + \theta_{x,R})\left(\frac{I_c}{I_{c,R}}\right)^2 + c_m(\Delta\theta_{d,x} - \theta_x)}{c_m - v_T\alpha_{20}(\Delta\theta_{c,Max} - \Delta\theta_{d,R} + \theta_{x,R})\left(\frac{I_c}{I_{c,R}}\right)^2} \tag{A.7.23}$$

After making the following substitutions:

$$\theta_1 = v_T c_a(\Delta\theta_{c,Max} - \Delta\theta_{d,R} + \theta_{x,R}) \tag{A.7.24}$$

$$\theta_2 = c_m(\Delta\theta_{d,x} - \theta_x) \tag{A.7.25}$$

$$c_1 = 1 + \alpha_{20}(\theta_{c,Amb} - 20 + \Delta\theta_{d,R} - \theta_{x,R}) \tag{A.7.26}$$

$$c_2 = \alpha_{20}(\Delta\theta_{c,Max} - \Delta\theta_{d,R} + \theta_{x,R}) \tag{A.7.27}$$

the equation A.7.23 is reshaped as follows:

$$\Delta\theta = \frac{\theta_1\left(\frac{I_c}{I_{c,R}}\right)^2 + \theta_2}{c_1 + c_2\left[1 - v_T\left(\frac{I_c}{I_{c,R}}\right)^2\right]} \tag{A.7.28}$$

Finally, the total cable losses under current I_c can be calculated. The losses consist of two parts: the dielectric and the ohmic losses. Using the relations A.7.5, A.7.19 and A.7.28, the total cable losses are expressed as follows:

$$W_t = W_d + W_{I,R}\left(\frac{I_c}{I_{c,R}}\right)^2\left[\frac{c_a}{c_m} + \frac{\alpha_{20}}{c_m}\Delta\theta\right] = W_d + W_{I,R}\left(\frac{I_c}{I_{c,R}}\right)^2 v_\theta \tag{A.7.29}$$

Where:

$$v_\theta = \frac{c_3}{c_1 + c_2\left[1 - v_T\left(\frac{I_c}{I_{c,R}}\right)^2\right]} \tag{A.7.30}$$

and:

$$c_3 = 1 + \alpha_{20}(\theta_{c,Amb} - 20 + \Delta\theta_d - \theta_x) \tag{A.7.31}$$

Appendix B

MMC Model

B.1 MMC Model Preliminary Calculations

Initially, the algorithm calculates the number and the configuration (series and/or parallel connected) of IGBT switches that are needed for every SM, taking into account the characteristics of the IGBT module. As explained in 4.3.1, the nominal average capacitors' voltage is:

$$V_{CAv,Nom} = \frac{V_{DC,Nom}}{N_{SM}} \tag{B.1.1}$$

Where:

- $V_{CAv,Nom}$: Average capacitors' voltage (V)
- $V_{DC,Nom}$: Nominal voltage at the DC side of the converter (V)
- N_{SM}: Number of SMs per arm $(-)$

Both of the IGBT switches of a SM have to be able to withstand this voltage. Although a capacitors' voltage balancing scheme is assumed to keep the capacitors' voltages at this value, some voltage rippling is unavoidable. Therefore, a voltage ripple is taken into account for the dimensioning procedure. The number of IGBT modules in series per switch can be calculated according to:

$$N_{series} = ceil\left[\frac{V_{CAv,Nom}(1+v_{rip})}{V_{CE,Nom}}\right] \tag{B.1.2}$$

Where:

- N_{series} Number of IGBT modules in series per SM switch $(-)$
- $V_{CAv,Nom}$: Average capacitors' voltage (V)
- v_{rip} Allowed percent arm voltage ripple (%)
- $V_{CE,Nom}$ Nominal off-state collector-emitter voltage of the IGBT module (V)

The procedure of determining the number of strings of switches in parallel is more complicated. An IGBT dissipates heat at a specific rate that depends on the thermal resistance and the temperature difference between the junction and the case according to expression B.1.3. The same expression can be used for calculating the heat dissipation between other layers of the IGBT module such as the case to heatsink and heatsink to ambient environment layers. A graphical representation of the thermal circuit of an IGBT module is shown in Figure B.1.

$$P_{heat} = \frac{\theta_J - \theta_C}{R_{th,J-C}} \tag{B.1.3}$$

Where:

- P_{heat} Dissipated power per module (W)
- θ_J: Junction temperature (°C)
- θ_C Case temperature (°C)
- $R_{th,J-C}$ Junction to case thermal resistance per m^2 (K/W)

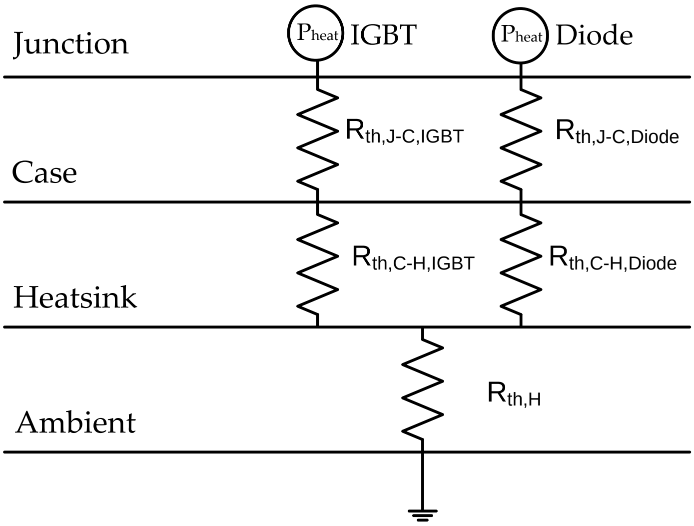

FIGURE B.1: Thermal diagram of an IGBT module

The datasheet gives the value of the junction to case and case to heatsink thermal resistance for both the IGBT and the diode. The user provides the minimum achievable heat resistance of the liquid cooled heatsink and the maximum junction and the ambient temperature.

Using this data, the maximum achievable heat dissipation is determined. The heat generated by conduction and switching losses needs to be lower than this achievable limit. Therefore, the derivation of the number of strings is based on the maximum heat that the IGBT has to dissipate which occurs during its nominal loading.

The IGBTs of a SM are not equally loaded during the MMC operation. This means that either the upper or the lower switch of a SM dissipates more heat depending on the type of MMC operation (inverter or rectifier). The dimensioning has to be conducted with respect to the maximum amount of generated heat. In order to do that the losses at rated loading are needed. Therefore, initially, it is assumed that one string is adequate.

$$N_{parallel} = 1 \tag{B.1.4}$$

The losses of an IGBT module of each of the two switches of a SM are calculated for the rated values of the MMC. The module that experiences the highest losses is used for the dimensioning. Due to the fact that the IGBT and the diode have different thermal resistances, an equivalent thermal resistance is calculated by taking into account the percentage of power that is dissipated through the IGBT and the diode. For example, the equivalent junction to case thermal resistance is derived according to equation B.1.5. The same expression is used for the calculation of the thermal resistance between case and heatsink. The maximum achievable heat dissipation of the module is derived using expression B.1.6.

$$R_{th,J-C,eq} = \frac{P_{heat,IGBT}}{P_{heat,Nom}} R_{th,J-C,IGBT} + \frac{P_{heat,Diode}}{P_{heat,Nom}} R_{th,J-C,Diode} \tag{B.1.5}$$

Where:

- $R_{th,J-C,eq}$: Equivalent junction to case thermal resistance per m^2 (K/W)
- $P_{heat,IGBT}$ Dissipated power from the IGBT (W)
- $P_{heat,Nom}$: Maximum dissipated power at nominal loading of a module (W)
- $R_{th,J-C,IGBT}$ IGBT junction to case thermal resistance per m^2 (K/W)
- $P_{heat,Diode}$ Dissipated power from the diode (W)
- $R_{th,J-C,Diode}$ Diode junction to case thermal resistance per m^2 (K/W)

$$P_{heat,Max} = \frac{\theta_J - \theta_{m,Amb}}{R_{th,J-C,eq} + R_{th,C-H,eq} + R_{th,H}} \tag{B.1.6}$$

Where:

- $P_{heat,Max}$ Maximum achievable dissipated power of a module (W)
- θ_J: Junction temperature (°C)
- $\theta_{m,Amb}$ MMC ambient temperature (°C)
- $R_{th,J-C,eq}$: Equivalent junction to case thermal resistance per m^2 (K/W)
- $R_{th,C-H,eq}$: Equivalent case to heatsink thermal resistance per m^2 (K/W)
- $R_{th,H}$: Heatsink thermal resistance per m^2 (K/W)

Consequently, for a user specified junction to case temperature difference the maximum achievable heat dissipation is derived. The number of strings is updated according to the following equation:

$$N_{parallel} = ceil\left[\frac{P_{heat,Nom}}{P_{heat,Max}}\right] \tag{B.1.7}$$

Where:

- $N_{parallel}$ Number of IGBT modules in parallel per SM switch $(-)$
- $P_{heat,Nom}$: Maximum dissipated power at nominal loading of a module (W)
- $P_{heat,Max}$ Maximum achievable dissipated power of a module (W)

B.2 IGBT Module Conduction Losses

The conduction losses of an IGBT can be calculated by considering an approximation of a series connection of a DC voltage source (V_{ce0}), representing the IGBT's on-state zero-current collector-emitter voltage, and a collector-emitter on-state resistance (R_{ce}) [95]:

$$v_{ce} = V_{ce0} + R_{ce} i_c \tag{B.2.1}$$

The same approximation can be used for the antiparallel diode connected to the IGBT [95]:

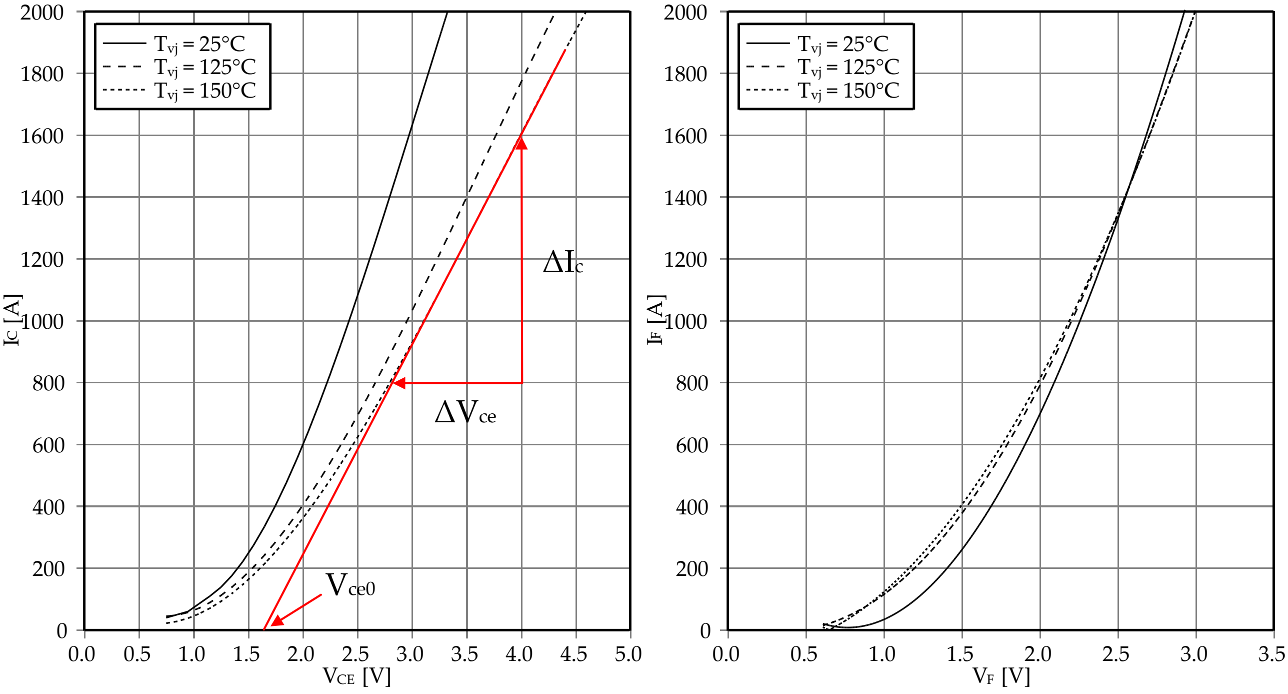

(A) (B)

Figure B.2: FZ1000R33HL3: (A) Collector current vs collector-emitter voltage characteristic (B) Diode current vs diode voltage characteristic [22]

$$v_d = V_{d0} + R_d i_d \tag{B.2.2}$$

These important parameters may be found directly from the IGBT datasheet. Figure B.2A shows the relationship between the collector current and the collector-emitter voltage for the Infineon IGBT. Using, for example, the curve corresponding to 150^oC, the collector-emitter on-state resistance (R_{ce}) and the on-state zero-current collector-emitter voltage (V_{ce0}) can be derived. The (R_{ce}) is equal to the fraction $\frac{\Delta V_{ce}}{\Delta \mathrm{I}_{ce}}$, while (V_{ce0}) can be derived by extending the line of the slope towards the x-axis. The point where the line intersects the x-axis is the value of (V_{ce0}).

However, these values correspond to a temperature of 150^oC, therefore a correction has to be applied for the range of operation temperatures. This correction factor, for a specific value of the collector current, is equal to the v_{ce} that corresponds to the operation temperature T over the v_{ce} for the same current that corresponds to 150^oC. It is then multiplied with the expression B.2.1. The v_{ce} that corresponds to temperatures other than the three provided by the graph is derived by means of linear interpolation (or extrapolation) between the three given curves.

$$K_{t,T} = \frac{v_{ce,@T}}{v_{ce,@150^oC}} \tag{B.2.3}$$

Where:

- $v_{ce,@T}$: On-state collector-emitter voltage at operation temperature T (V)
- $v_{ce,@150^oC}$: On-state collector-emitter voltage at 150^oC (V)

Using equations B.2.1, B.2.3 the instantaneous value of the conduction losses can be expressed as [96]:

$$p_{con} = v_{ce} \cdot i_c = K_{t,T}(V_{ce0} + R_{ce} i_c) i_c \tag{B.2.4}$$

Where:

- v_{ce}: On-state collector-emitter voltage (V)
- i_c: Collector current (A)
- $K_{t,T}$: Temperature correction factor $(-)$
- V_{ce0}: On-state zero-current collector-emitter voltage at 150^oC (V)
- R_{ce}: On-state collector-emitter resistance at 150^oC (Ω)

Consequently, the dissipated energy due to conduction over a fundamental period is given by the relation B.2.5, while the conduction losses over a fundamental period are given in B.2.6.

$$E_{con} = \int_0^T K_{t,T}(V_{ce0} \cdot i_c + R_{ce0} \cdot {i_c}^2) dt \tag{B.2.5}$$

$$P_{con} = \frac{1}{T} \int_0^T K_{t,T}(V_{ce0} \cdot i_c + R_{ce0} \cdot {i_c}^2) dt \tag{B.2.6}$$

Using Figure B.2B and following the same procedure, similar expressions are derived regarding the antiparallel diode:

$$K_{d,T} = \frac{v_{d,@T}}{v_{d,@150^oC}} \tag{B.2.7}$$

Where:

- $v_{d,@T}$: On-state diode voltage at operation temperature T (V)
- $v_{d,@150^oC}$: On-state diode voltage at 150^oC (V)

$$p_{con} = v_d \cdot i_d = K_{d,T}(V_{d0} + R_d i_d) i_d \tag{B.2.8}$$

Where:

- v_d: On-state diode voltage (V)
- i_d: Diode current (A)
- $K_{d,T}$: Temperature correction factor $(-)$
- V_{d0}: On-state zero-current diode voltage at 150^oC (V)
- R_d: On-state diode resistance at 150^oC (Ω)

$$E_{con} = \int_0^T K_{d,T}(V_{d0} \cdot i_d + R_{d0} \cdot {i_d}^2) dt \tag{B.2.9}$$

$$P_{con} = \frac{1}{T} \int_0^T K_{d,T}(V_{d0} \cdot i_d + R_{d0} \cdot {i_d}^2) dt \tag{B.2.10}$$

B.3 IGBT Module Switching Losses

Since there are no simple analytical expressions that describe the voltage and current during a switching transient of an IGBT [96], the switching losses can be determined using data straight from the IGBT module's datasheet. More specifically, the curves of the switching losses with respect to the current and gate resistor are required for both the IGBT switch and the diode.

Figure B.3 shows the IGBT's switching losses and the diode's reverse recovery losses with respect to the current.

These graphs show the dependency of the switching losses with respect to the current while other variables are kept constant (junction temperature, gate resistor and collector-emitter DC voltage). Therefore, three correction factors have to be employed [96]:

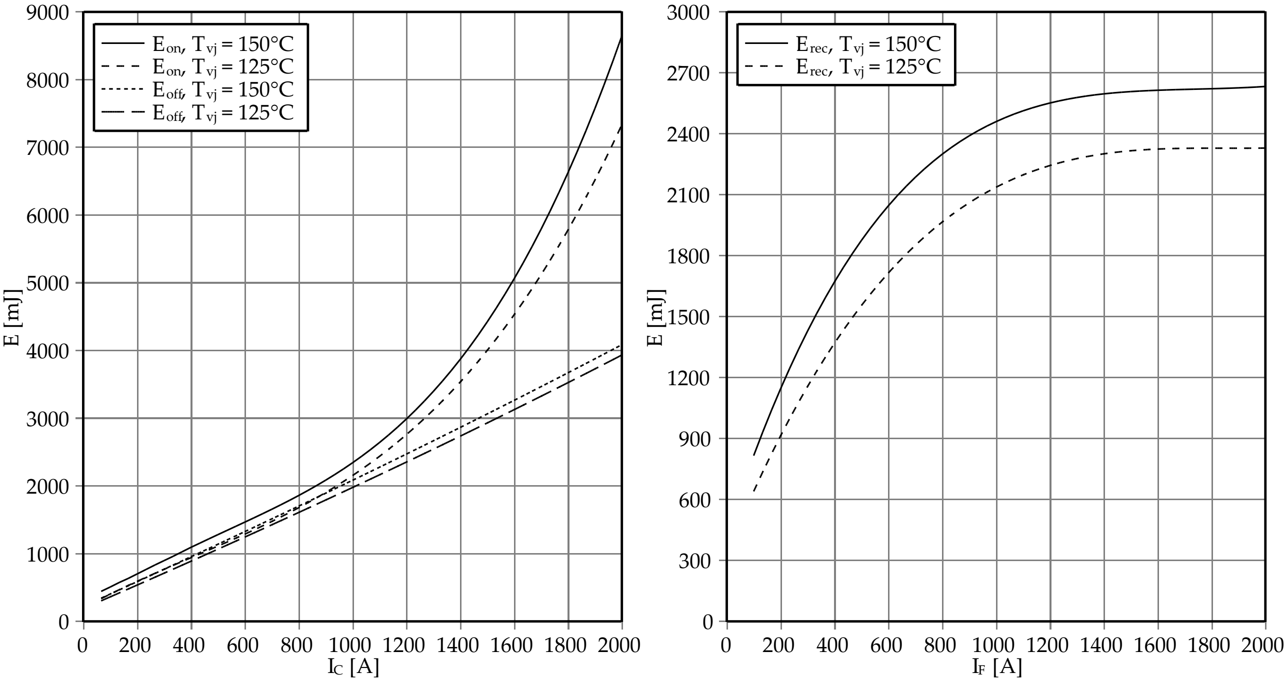

(A) (B)

FIGURE B.3: FZ1000R33HL3: (A) IGBT switching losses vs collector current characteristic (B) Diode reverse recovery losses vs diode current characteristic [22]

$$L_{t,T} = \frac{E_{sw,T}}{E_{sw,T_{Dts}}} \tag{B.3.1}$$

$$L_{t,R_G} = \frac{E_{sw,R_G}}{E_{sw,R_{G,Dts}}} \tag{B.3.2}$$

$$L_{t,V_{ceDC}} = \frac{V_{ceDC}}{V_{ceDC,Dts}} \tag{B.3.3}$$

Where:

- $E_{sw,T}$: Switch-on or off energy at a specific operation temperature (J)
- $E_{sw,T_{Dts}}$: Switch-on or off energy at the datasheet temperature (J)
- E_{sw,R_G}: Switch-on or off energy with a specific gate resistor (J)
- $E_{sw,R_{G,Dts}}$: Switch-on or off energy with the datasheet gate resistor (J)
- V_{ceDC}: Collector-emitter DC voltage (V)
- $V_{ceDC,Dts}$: Datasheet collector-emitter DC voltage (V)

Similar correction factors can be defined regarding the diode.

$$L_{d,T} = \frac{E_{rec,T}}{E_{rec,T_{Dts}}} \tag{B.3.4}$$

$$L_{d,R_G} = \frac{E_{rec,R_G}}{E_{rec,R_{G,Dts}}} \tag{B.3.5}$$

$$L_{d,V_{dDC}} = \frac{V_{ceDC}}{V_{ceDC,Dts}} \tag{B.3.6}$$

Where:

- $E_{rec,T}$: Reverse recovery energy at a specific operation temperature (J)
- $E_{rec,T_{Dts}}$: Reverse recovery energy at the datasheet temperature (J)
- E_{rec,R_G}: Reverse recovery energy with a specific gate resistor (J)
- $E_{rec,R_{G,Dts}}$: Reverse recovery energy with the datasheet gate resistor (J)

B.4 Arm Inductors Dimensioning

The ohmic resistance of four different arm inductances are calculated, namely 1 mH, 2 mH, 4 mH, 6 mH. The model requires as inputs the rated current and the DC and AC resistance of one of the inductors connected in parallel at each SM. Therefore the total inductance for every SM is the arm inductance divided by the number of SMs which is 38 for the new numerical example: 26.3 μH, 52.6 μH, 105.3 μH, 157.9 μH for 1 mH to 6 mH of arm inductance respectively.

The diameter of the conductor chosen for the inductors is equal to 7.35mm (AWG 1). According to [97] the ampacity of such a conductor at ambient temperature of 20 ^oC and maximum insulation temperature of 90 ^oC is 229 A. The dimensioning is conducted for rated RMS arm current which is equal to 760 A. Thus, 4 inductors need to be connected in parallel for every SM. Therefore, to maintain the previously calculated inductance per SM, each individual inductor has to be: 105.2 μH, 210.4 μH, 421.2 μH, 631.6 μH for 1mH to 6mH of arm inductance respectively.

The length of the conductor needed for each inductor is calculated using two different online inductor calculators: The 'Pronine Multilayer Air Core Inductor Calculator' [98] and the 'Coil32 Multilayer Coil Inductance Calculator' [99]. Both calculators require as inputs the diameter of the coil, the length of the winding and the diameter of the conductor. Coil32 also needs the

Inductor Characteristics	
Diameter of coil (cm)	7
Length of winding (cm)	20
Diameter of conductor (mm)	7.35
Diameter of conductor with insulation (mm)	8.5

Table B.1: Characteristics of each inductor in parallel at every SM

diameter of the conductor including its insulation. The values assigned to these variables are shown in Table B.1.

The average value of the length of conductor calculated by the two calculators is: 16.480 m, 24.010 m, 34.795 m, 43.370 m for 1 mH to 6 mH of arm inductance respectively. According to IEC 60228 the DC resistance of a copper conductor of a diameter equal to 7.35 mm at 20 ^oC is approximately 0.456 Ω/km [100]. Consequently, the DC resistance at 20 ^oC of the inductor is calculated: 7.515 $m\Omega$, 10.949 $m\Omega$, 15.867 $m\Omega$, 19.777 $m\Omega$ for 1 mH to 6 mH of arm inductance respectively. The resistance of the total arm inductance can be calculated by dividing these values by 4 (the number of inductors in parallel at each SM) and then multiplying by 38 (the number of the SMs of each arm).

The AC resistance can be derived from the DC resistance by taking into account the skin effect. However according to [101] the skin depth for copper at 50 Hz is approximately 9.22 mm which is well above the diameter of the wire of the inductor. Therefore, the AC resistance can be taken equal to the DC resistance. The calculations are summarized in Table B.2.

Inductors Calculations				
Total Arm Inductance (mH)	1	2	4	6
Total SM Inductance (μH)	26.3	52.6	105.3	157.9
Individual Inductor's Inductance (μH)	105.2	210.4	421.2	631.6
Individual Inductor's wire length (m)	16.480	24.010	34.795	43.370
Individual Inductor's DC Resistance at 20^oC ($m\Omega$)	7.515	10.949	15.867	19.777
Individual Inductor's DC Resistance at 20^oC ($m\Omega$)	7.515	10.949	15.867	19.777
Total Arm DC Resistance at 20^oC ($m\Omega$)	71.393	104.015	150.737	187.88
Total Arm AC Resistance at 20^oC ($m\Omega$)	71.393	104.015	150.737	187.88

Table B.2: Calculations of the arm inductors for different values of arm inductance

B.5 MMC Example

The inputs of the numerical example of the 510 MVA MMC presented in Section 4.4.3.2 are shown in detail in the following table B.3. The inputs originate from either design decisions or manuals and standards as explained in the main body of the thesis. Their origin is included here for the sake of convenience. An input, whose origin has not been mentioned so far, is the thermal resistance of the heatsink. The value of this resistance was chosen to be in the vicinity of typical liquid-cooled heatsink thermal resistances [102].

Inputs			
Variable	Unit	Value	Reference
$P_{DC,Nom}$	(W)	$500 \cdot 10^6$	Design decision
$P_{AC3ph,Nom}$	(W)	$500 \cdot 10^6$	Design decision
$Q_{AC3ph,Nom}$	(VAr)	$100 \cdot 10^6$	Design decision
$IRopFlag$	$(-)$	$Misc$	Design decision
V_{DC}	(V)	$450 \cdot 10^3$	Design decision
m	$(-)$	0.8	Design decision
P_{DC}	(W)	$5 \cdot 10^6$	Design decision
P_{AC3ph}	(W)	$5 \cdot 10^6$	Design decision
$Step$	(W)	$5 \cdot 10^6$	Design decision
phi	(rad)	0.1974	Design decision
f	(Hz)	50	Design decision
f_{sw}	(Hz)	150	Design decision
N_{SM}	$(-)$	38	Design decision
v_{rip}	(%)	0.1	Design decision
$V_{CE,Nom}$	(V)	3300	[22]
$R_{th,J-C,IGBT}$	(k/W)	$11 \cdot 10^{-3}$	[22]
$R_{th,J-C,Diode}$	(k/W)	$20 \cdot 10^{-3}$	[22]
$R_{th,C-H,IGBT}$	(k/W)	$14.5 \cdot 10^{-3}$	[22]
$R_{th,C-H,Diode}$	(k/W)	$16.5 \cdot 10^{-3}$	[22]
$R_{th,H}$	(k/W)	$9 \cdot 10^{-3}$	[102]
$\theta_{m,Max}$	(°C)	90	Design decision
$\theta_{m,Amb}$	(°C)	20	Design decision
$\theta_{i,Max}$	(°C)	90	Design decision
$I_{ind,Nom}$	(A)	229	See Appendix B.4
R^{20}_{indDC}	(Ω)	$Misc$	See Appendix B.4
R^{20}_{indAC}	(Ω)	$Misc$	See Appendix B.4
α_{20}	(K^{-1})	$3.93 \cdot 10^{-3}$	[27]
COP	$(-)$	20	[77]
R_{Gon}	(Ω)	0.75	[22]
R_{Goff}	(Ω)	4	[22]
R_{Grec}	(Ω)	0.75	[22]
$I_C = f(V_{CE})$	$(-)$	$Curve$	[22]
$E_{on} = f(I_C)$	$(-)$	$Curve$	[22]
$E_{off} = f(I_C)$	$(-)$	$Curve$	[22]
$E_{on} = f(R_G)$	$(-)$	$Curve$	[22]
$E_{off} = f(R_G)$	$(-)$	$Curve$	[22]
$I_D = f(V_D)$	$(-)$	$Curve$	[22]
$E_{rec} = f(I_D)$	$(-)$	$Curve$	[22]
$E_{rec} = f(R_G)$	$(-)$	$Curve$	[22]

Table B.3: Model Inputs

Appendix C

Transformer Model

C.1 Transformer Example

The transformer model inputs of the numerical example are listed in Table C.1.

Inputs			
Variable	Unit	Value	Reference
$R_{C,sec}$	(pu)	800	Design decision
$X_{M,sec}$	(pu)	500	Design decision
$R_{eq,sec}$	(pu)	0.003	Design decision
$X_{eq,sec}$	(pu)	0.16	Design decision
α	$(-)$	220/380	Design decision
S_{Nom}	(VA)	$800 \cdot 10^6$	Design decision
S_{in}	(VA)	$8 \cdot 10^6$	Design decision
$Step$	(VA)	$8 \cdot 10^6$	Design decision
$\overline{V}_{in,LL}$	(V)	$220 \cdot 10^3$	Design decision
ϕ	(rad)	0.3175	Design decision
$\theta_{t,Amb}$	(°C)	15	Design decision
$\theta_{t,Test}$	(°C)	25	Design decision
$\theta_{t,Rise}$	(°C)	65	Design decision
a_{20}	(K^{-1})	$3.93 \cdot 10^{-3}$	[27]
$P_{cool,Nom}$	(W)	$36 \cdot 10^3$	Design decision

Table C.1: Model Inputs

Appendix D

Case Study

D.1 Cables' Characteristics

In this section, the types of cables that were used in the case study are presented in detail. These are a 17.3/30 kV and a 38/66 kV three-core MVAC SPCs, a 127/220 kV three-core HVAC SPC of two different cross-sections and a 320 kV single-core HVDC SPC. Their characteristics are listed in the following table:

Cable Properties							
Variable	**Unit**	**MVAC**		**HVAC**		**HVDC**	**Reference**
V_0/V	(kV)	17.3/30	38/66	127/220	127/220	320	
A	(mm^2)	400	150	800	1400	630	[27][103]
C	$(\mu F/km)$	0.2900	0.1900	0.1700	0.2000	-	[27][103]
L	(mH/km)	0.3500	0.4100	0.4000	0.3500	-	[27][103]
R_{AC20}	(Ω/km)	0.0494	0.1246	0.0246	0.0169	0.0273	[27][103]
$tan(\delta)$	$(-)$	0.0040	0.0010	0.0010	0.0010	-	[27][103]
θ_{max}	(°C)	90	90	90	90	90	[27][103]
λ_1	$(-)$	0.0339	0.0119	0.3101	0.5005	-	[27][103]
λ_2	$(-)$	0.1507	0.0587	0.2051	0.2832	-	[27][103]
T_1	$(K\ m/W)$	0.3253	0.4961	0.5028	0.4175	0.6643	[27][103]
T_2	$(K\ m/W)$	0.0525	0.0642	0.0408	0.0321	0.0329	[27][103]
T_3	$(K\ m/W)$	0.0455	0.0494	0.0313	0.0284	0.0388	[27][103]
T_4air	$(K\ m/W)$	0.2126	0.2359	0.1310	0.1173	0.2511	[27][103]
T_4soil	$(K\ m/W)$	0.5456	0.5582	0.4523	0.4375	0.5421	[27][103]

Table D.1: Properties of SPC used in the case study

D.2 Compensation

The following tables show the amount of compensation for each wind direction and for every scenario of the case study that includes HVAC transmission.

Compensation (MVAr)				
Line Length (km)	50		100	150
Cable Cross-section (mm^2)	800	1400	800	800
North	65	75	133	200
	65	75	133	200
	65	81	133	203
	65	81	133	203
North North East	65	75	133	200
	65	75	133	200
	68	82	133	203
	68	82	133	203
East North East	70	80	133	200
	70	80	133	200
	67	79	137	205
	67	79	137	205
East	63	73	130	195
	63	73	130	195
	63	73	130	200
	63	73	130	200
East South East	70	80	135	200
	70	80	135	200
	65	78	135	205
	65	78	135	205
South South East	70	80	130	200
	70	80	130	200
	65	75	135	205
	65	75	135	205

Table D.2: Amount of compensation for each scenario for wind directions from North to South South East

Compensation (MVAr)				
Line Length (km)	50		100	150
Cable Cross-section (mm^2)	800	1400	800	800
South	70	80	133	200
	70	80	133	200
	65	79	135	205
	65	79	135	205
South South West	40	50	110	175
	40	50	110	175
	40	50	100	180
	40	50	100	180
West South West	40	50	103	175
	40	50	103	175
	40	50	105	175
	40	50	105	175
West	50	60	115	185
	50	60	115	185
	45	63	120	185
	45	63	120	185
West North West	60	70	120	190
	60	70	120	190
	55	65	125	190
	55	65	125	190
North North West	65	75	133	200
	65	75	133	200
	70	80	135	204
	70	80	135	204

Table D.3: Amount of compensation for each scenario for wind directions from South to North North West

Bibliography

[1] IPCC Working Group I. Climate Change 2013: he Physical Science Basis. Technical report, Intergovernmental Panel on Climate Change, 2013.

[2] REN21. Renewables 2014 Global Status Report. Technical report, Renewable Energy Policy Network for the 21st Century, 2014.

[3] IPCC. Renewable Energy Sources and Climate Change Mitigation. Technical report, Intergovernmental Panel on Climate Change, 2012.

[4] WWEA. Half-year Report 2014. Technical report, World Wind Energy Association, 2014.

[5] WEC. World Energy Resources 2013 Survey. Technical report, World Energy Council, 2013.

[6] LORC. List of Offshore Wind Farms, 2014. URL `www.lorc.dk/offshore-wind-farms-map/list`. [Last accessed 29th September 2014].

[7] 4C Offshore. Offshore Wind Farms Database. URL `www.4coffshore.com/windfarms/`. [Last accessed 29th September 2014].

[8] The Wind Power. Wind Turbines and Wind Farms Database, 2014. URL `www.thewindpower.net/windfarms_offshore_en.php`. [Last accessed 29th September 2014].

[9] J.H. Larsen. The World's Largest Offshore Windfarm, Middelgrunden 40 MW. Technical report, Copenhagen Environment and Energy Office (CEEO), 2001.

[10] The Crown Estate. Offshore Wind Cost Reduction - Pathways Study. Technical report, The Crown Estate, 2012.

[11] T. Worzyk. *Submarine Power Cables: Design, Installation, Repair, Environmental Aspects*. Springer, 2009.

[12] W. Thue. *Electrical Power Cable Engineering*. CRC Press, 3rd edition, 2011.

[13] Nexans. Submarine Cable 19/33 (36)kV 3-core Copper XLPE, 2014. URL `http://www.nexans.de/eservice/Germany-en/navigate_184924/2XS_FL_2YRAA_RM_19_33_36_kV.html#description`. [Last accessed 16th October 2014].

[14] ABB. HVDC Extruded Submarine Cables, 2014. URL `http://new.abb.com/systems/high-voltage-cables/cables/hvdc-extruded-cables/hvdc-submarine-cables`. [Last accessed 16th October 2014].

[15] E. Zaccone. HVDC Transmission Cable Systems - State of the Art and Future Trends, 2009. URL `http://www.pesicc.org/iccwebsite/subcommittees/subcom_c/Presentations/2009Spring/C-4-HVDCTransmissionCableSystems-Zaccone.pdf`. [Last accessed 16th October 2014].

[16] M.H. Rashid. *Power Electronics Handbook*. Academic Press / Elsevier, 2nd edition, 2006.

[17] C.C. Davidson and D.R. Trainer. Innovative concepts for hybrid multi-level converters for hvdc power transmission. In *9th IET International Conference on AC and DC Power Transmission*, 2010.

[18] Siemens. Siemens installs two offshore platforms for TenneT in the North Sea in July, July 2014. URL `http://www.siemens.com/press/en/feature/2013/energy/2013-08-x-win.php?content[]=E&content[]=ES&content[]=ET&content[]=EW&stop_mobi=true`. [Last accessed 20th October 2014].

[19] Allianz. Global Risk Dialogue: Energized, 2013. URL `http://www.agcs.allianz.com/insights/expert-risk-articles/energized/`. [Last accessed 20th October 2014].

[20] M. Guan, Z. Xu, and H. Chen. Control and modulation strategies for modular multilevel converter based HVDC system. In *37th Annual Conference on IEEE Industrial Electronics Society (IECON)*, 2011.

[21] A. Antonopoulos. Control, Modulation and Implementation of Modular Multilevel Converters. Master's thesis, KTH Royal Institute of Technology, 2011.

[22] Infineon. *Technical Information of IGBT module FZ1000R33HL3*, 2013.

[23] S. Allebrod, R. Hamerski, and R. Marquardt. New Transformerless, Scalable Modular Multilevel Converters for HVDC-Transmission. In *Power Electronics Specialists Conference*, pages 174 – 179, 2008.

[24] S.J. Chapman. *Electric Machinery Fundamentals*. Elizabeth A. Jones, 4th edition edition, 2005.

[25] M. Heathcote. *J & P Transformer Book*. Newnes, 13th edition edition, 2007.

[26] J.J. Winders. *Power Transformers Principles and Applications*. Marcel Dekker Inc, 2002.

[27] International Electrotechnical Commission. IEC 60287: Electric cables - Calculation of the current rating, 2006.

[28] G. J. Anders and H. Brakelmann. Improvement in Cable Rating Calculations by Consideration of Dependence of Losses on Temperature. *IEEE Transactions on Power Delivery*, 19(3):919–925, July 2004.

[29] J. Glasdam, J. Hjerrild, L.H. Kocewiak, and C.L Bak. Review on multi-level voltage source converter based HVDC technologies for grid connection of large offshore wind farms. In *Power System Technology (POWERCON), 2012 IEEE International Conference*, 2012.

[30] S. Fassbinder. Application Note: Efficiency and Loss Evaluation of Large Power Transformers. Technical report, European Copper Institute, 2013.

[31] G.F. Moore. *Electric Cables Handbook*. Blackwell Science, 3rd edition, 1997.

[32] IPCC Working Group III. Climate Change 2014: Mitigation of Climate Change. Technical report, Intergovernmental Panel on Cliamate Change, 2014.

[33] BVG associates. Offshore Wind Technology Pathways for Scotland. Technical report, BVG associates, 2012.

[34] IPCC Working Group II. Climate Change 2014: Impacts, Adaptation and Vulnerability. Technical report, Intergovernmental Panel on Cliamate Change, 2014.

[35] M. Scott. We Are Not Alone: Climate Change Laws Span The World, February 2014. URL `http://www.forbes.com/sites/mikescott/2014/02/27/we-are-not-alone-climate-change-laws-span-the-world/`. [Last accessed 20th September 2014].

[36] GWEC. Global Wind Report - Annual Market Update 2013. Technical report, Global Wind Energy Council, 2013.

[37] EWEA. Deep Water - The next step for offshore wind energy. Technical report, European Wind Energy Association, 2013.

[38] NKT Cables. *High Voltage Cable Systems*, 2009.

[39] G. J. Anders. *Rating of Electric Power Cables in Unfavourable Thermal Conditions*. John Wiley & Sons, 2005.

[40] H. Brakelmann. Loss Determination for Long Three-Phase High-Voltage Submarine Cables. *European Transactions on Electrical Power*, 13(3):193–197, June 2003.

[41] D.H. Young and R.A Freedman. *Sears and Zemansky's University Physics: With Modern Physics*. Addison-Wesley, 2011.

[42] L.L. Grigsby. *Electric Power Generation, Transmission and Distribution.* CRC, 2nd edition edition, 2006.

[43] K.N.Md Hasan, K. Rauma, A. Luna, J. I. Candela, and P. Rodriguez. Harmonic Resonance Study for Wind Power Plant. In *International Conference on Renewable Energies and Power Quality*, 2012.

[44] A. Madariaga, J. L. Martin, I. Zamora, S. Ceballos, and O. Anaya-Lara. Effective Assessment of Electric Power Losses in Three-Core XLPE Cables. *IEEE Transactions on Power Systems*, 28(4):4488–4495, November 2013.

[45] E. N. Abildgaard and M. Molinas. Modelling and Control of the Modular Multilevel Converter (MMC). *Energy Procedia*, 20:227–236, 2012.

[46] T.M. Iversen. Multilevel Converters for a 10 MW, 100 kV Transformer-less Offshore Wind Generator System. Master's thesis, Norwegian University of Science and Technology, 2012.

[47] M.F. Escalante, J.C. Vannier, and A. Arzande. Flying Capacitor Multilevel Inverters and DTC Motor Drive Applications. *IEEE Transactions on Industrial Electronics*, 49: 809–815, 2002.

[48] A. Lesnicar and R. Marquardt. An Innovative Modular Multilevel Converter Topology Suitable for a Wide Power Range. In *IEEE Power Tech Conference Proceedings, Bologna*, 2003.

[49] A. Arman Hassanpoor, K. Ilves, S. Norrga, L. Angquist, and H.P. Nee. Tolerance Band Modulation Methods for Modular Multilevel Converters. *IEEE Transactions on Power Electronics*, PP:1, 2014.

[50] G.P. Adam, S.J. Finney, B.W. Williams, D.R. Trainer, C.D.M. Oates, and D.R Critchley. Network fault tolerant voltage-source-converters for high-voltage applications. In *9th IET International Conference on AC and DC Power Transmission*, 2010.

[51] A.M. Cross, D.R Trainer, and R.W. Crookes. Chain-link based HVDC Voltage Source Converter using current injection. In *9th IET International Conference on AC and DC Power Transmission*, 2010.

[52] R. Feldman, M. Tomasini, J.C. Clare, and P. Wheeler. A low loss modular multilevel voltage source converter for HVDC power transmission and reactive power compensation. In *9th IET International Conference on AC and DC Power Transmission*, 2010.

[53] M.M.C Merlin, T.C. Green, P.D. Mitcheson, D.R. Trainer, D.R. Critchley, and R.W. Crookes. A New Hybrid Multi-Level Voltage-Source Converter with DC Fault Blocking Capability. In *9th IET International Conference on AC and DC Power Transmission*, 2010.

[54] B. Jacobson, P. Karlsson, G. Asplund, L. Harnefors, and T. Jonsson. VSC-HVDC Transmission with Cascaded Two-Level Converters. In *43rd CIGRE*, 2010.

[55] D.G. Holmes and T.A. Lipo. *Pulse Width Modulation for Power Converters*. John Wiley & Sons, 2003.

[56] M Saeedifard and R. Iravani. Dynamic Performance of a Modular Multilevel Back-to-Back HVDC System. *IEEE Transactions on Power Delivery*, 25:2903 – 2912, 2010.

[57] E. Solas, G. Abad, J.A. Barrena, A. Carcar, and S. Aurtenetxea. Modulation of Modular Multilevel Converter for HVDC Application. In *14th International Power Electronics and Motion Control Conference (EPE/PEMC)*, 2010.

[58] G. Ding, G. Tang, Z. He, and M. Ding. New technologies of voltage source converter (VSC) for HVDC transmission system based on VSC. In *IEEE Power and Energy Society General Meeting - Conversion and Delivery of Electrical Energy in the 21st Century*, 2008.

[59] H. Saad, J. Peralta, S. Dennetire, J. Mahseredjian, J. Jatskevich, J. A. Martinez, A. Davoudi, M. Saeedifard, V. Sood, X. Wang, J. Cano, and A. Mehrizi-Sani. Dynamic Averaged and Simplified Models for MMC-Based HVDC Transmission Systems. *IEEE Transactions on Power Delivery*, 28:1723 – 1730, 2013.

[60] J. Peralta, S. Dennetire, J. Mahseredjian, and S. Nguefeu. Detailed and Averaged Models for a 401-Level MMC-HVDC System. *IEEE Transactions on Power Delivery*, 27:1501–1508, 2012.

[61] D. Siemaszko, A. Antonopoulos, K. Ilves, M. Vasiladiotis, L. Angquist, and H.P. Nee. Evaluation of control and modulation methods for modular multilevel converters. In *International Power Electronics Conference (IPEC)*, 2010.

[62] K. Li and C. Zhao. New Technologies of Modular Multilevel Converter for VSC-HVDC Application. In *Asia-Pacific Power and Energy Engineering Conference (APPEEC)*, 2010.

[63] Q. Tu and Z. Xu. Impact of Sampling Frequency on Harmonic Distortion for Modular Multilevel Converter. *IEEE Transactions on Power Delivery*, 26:298–306, 2011.

[64] A. Antonopoulos, L. Angquist, and H.P. Nee. On dynamics and voltage control of the Modular Multilevel Converter. In *13th European Conference on Power Electronics and Applications* , 2009.

[65] L. Angquist, A. Antonopoulos, D. Siemaszko, K. Ilves, M. Vasiladiotis, and H.P. Nee. Inner control of Modular Multilevel Converters - An approach using open-loop estimation of stored energy. In *International Power Electronics Conference (IPEC)*, 2010.

[66] M. Hagiwara, R. Maeda, and H. Akagi. Control and Analysis of the Modular Multilevel Cascade Converter Based on Double-Star Chopper-Cells (MMCC-DSCC). *IEEE Transactions on Power Electronics*, 26:1649 – 1658, 2011.

[67] K. Ilves, A. Antonopoulos, S. Norrga, and H.P. Nee. A New Modulation Method for the Modular Multilevel Converter Allowing Fundamental Switching Frequency. *IEEE Transactions on Power Electronics*, 27:991 – 998, 2012.

[68] M. Zygmanowski, B. Grzesik, and R. Nalepa. Capacitance and Inductance Selection of the Modular Multilevel Converter. In *Power Electronics and Applications (EPE)*, 2013.

[69] K. Ilves, A. Antonopoulos, L. Harnefors, S. Norrga, and H.P. Nee. Circulating Current Control in Modular Multilevel Converters with Fundamental Switching Frequency. In *7th International Power Electronics and Motion Control Conference - ECCE Asia*, 2012.

[70] K. Ilves, A. Antonopoulos, S. Norrga, and H.P. Nee. Steady-State Analysis of Interaction Between Harmonic Components of Arm and Line Quantities of Modular Multilevel Converters. *IEEE Transactions on Power Electronics*, 27:57–68, 2012.

[71] Q. Tu, Z. Xu, and L. Xu. Reduced Switching-Frequency Modulation and Circulating Current Suppression for Modular Multilevel Converters. *IEEE Transactions on Power Delivery*, 26:2009–2017, 2011.

[72] K. Ilves. Modeling and Design of Modular Multilevel Converters for Grid Applications. Master's thesis, KTH Royal Institute of Technology, 2012.

[73] Y. Zhang, G.P. Adam, Lim T.C., Finey S.J., and B.W. Williams. Analysis of modular multilevel converter capacitor voltage balancing based on phase voltage redundant states. *IET Power Electronics*, 5:726–738, 2012.

[74] Alstom. *Voltage Source Converter Cooling Plant*, 2010.

[75] R.K. Rajput. *Engineering Thermodynamics.* Laxmi Publications, 3rd edition edition, 2007.

[76] Q. Tu, Z. Xu, H. Huang, and J. Zhang. Parameter Design Principle of the Arm Inductor in Modular Multilevel Converter based HVDC . In *International Conference on Power System Technology (POWERCON)*, 2010.

[77] Emerson Network Power. *Liebert CRV - Efficient Cooling for IT Equipment*, 2014.

[78] Semikron. *Gate Resistor - Principles and Applications*, 2007.

[79] W. Ziomek. Editorial: Transformer electrical Insulation. *IEEE Transactions on Dielectrics and Electrical Insulation*, 19:1841–1842, 2012.

[80] O. Sarneroth. Insulation Materials, January 2001. URL `http://www05.abb.com/global/scot/scot252.nsf/veritydisplay/d5b8bcd1a42b581885256d9100611f34/$file/insulation%20materials.pdf`. [Last accessed 20th October 2014].

[81] ABB. *Dry-type transformers and reactors: Safe, reliable and energy-efficient*, 2013.

[82] H. Al-Almin, J. O'Brien, and M. Lashbrook. Synthetic ester transformerfluid: A total solution to windpark transformer technology. *Renewable Energy*, 49:33–38, 2013.

[83] K. Lane. The Basics of Large Dry-Type Transformers, June 2007. URL `http://ecmweb.com/content/basics-large-dry-type-transformers`. [Last accessed 20th October 2014].

[84] S.V. Kulkarni and S.A. Khaparde. *Transformer Engineering Design and Practice*. Marcel Dekker Inc, 2004.

[85] J. Declercq and R. Van Schevensteen. Transformers for offshore multi-megawatt turbines: discussions on specifications, safety and environment. In *European Offshore Wind Conference & Exhibition, Copenhagen*, 2005.

[86] J. Declercq and R. Van Schevensteen. Challenges for Reliable Offshore Transformers. *Windtech International*, January-February, 2008.

[87] J.H Dellinger. The temperature coefficient of resistance of copper. *Bulletin of the Bureau of Standards*, 7:71–101, 1911.

[88] E. Berge, O. Byrkjedal, Y. Ydersbond, and D. Kindler. Modelling of offshore wind resources. Comparison of a mesoscale model and measurements from FINO 1 and North Sea oil rigs. In *European Wind Energy Conference and Exhibition (EWEC)* , 2009.

[89] E.T.G. Bot. FarmFlow - Improved near wake modelling and validation against four full scale wind farms. Technical report, Energy Research Centre of the Netherlands, 2012.

[90] A. Crespo, J. Hernandez, E. Fraga, and C. Andreu. Experimental validation of the UPM computer code to calculate wind turbine wakes and comparison with other models. *Journal of Wind Engineering and Industrial Aerodynamics* , 27:77–88, 1988.

[91] L.J. Vermeer, J.N. Sorensen, and A. Crespo. Wind turbine wake aerodynamics. *Progress in Aerospace Sciences*, 39:467–510, 2003.

[92] R.J. Barthelmie, G.C. Larsen, S.T. Frandsen, L. Folkerts, K. Rados, S.C. Pryor, B. Lange, and G. Schepers. Comparison of Wake Model Simulations with Offshore Wind Turbine Wake Profiles Measured by Sodar. *Journal of Atmospheric and Oceanic Technology*, 23: 888–901, 2006.

[93] R. Teixeira Pinto, S. Rodrigues, E. Wiggelinkhuizen, R. Scherrer, P. Bauer, and J. Pierik. Operation and Power Flow Control of Multi-Terminal DC Networks for Grid Integration of Offshore Wind Farms Using Genetic Algorithms. *Energies*, 6:1–26, 2012.

[94] ABB. *XLPE Land Cable Systems User's Guide - Revision 5*, 2006.

[95] D. Graovac and M. Purschel. *IGBT Power Losses Calculation Using the Data-Sheet Parameters.* Infineon, 2009.

[96] Infineon. *Calculation of Major IGBT Operating Parameters.* Infineon, 1999.

[97] National Fire Protection Association. NFPA 70 National Electrical Code 2008 Edition, 2008.

[98] Pronine Electronics Design. Pronine Multilayer Air Core Inductor Calculator, 2004. URL `http://www.pronine.ca/multind.htm`. [Last accessed 19th October 2014].

[99] Coil32. Coil32 multilayer coil inductance calculator. URL `http://coil32.narod.ru/calc/multi_layer-en.html`. [Last accessed 19th October 2014].

[100] International Electrotechnical Commission. IEC 60228: Electric cables - Conductors of insulated cables, 2004.

[101] Chemandy Electronics. Calculator for Skin Effect Depth, 2014. URL `http://chemandy.com/calculators/skin-effect-calculator.htm`. [Last accessed 19th October 2014].

[102] Westcode. *Water Cooled Heatsink Type XW180GA34#*. IXYS, November 2009.

[103] ABB. *XLPE Submarine Cable Systems - Attachment to XLPE Land Cable Systems - User's Guide*, 2010.